

Studies of a Quantum Degenerate Fermionic Lithium Gas

by

Zoran Hadzibabic

Submitted to the Department of Physics
in partial fulfillment of the requirements for the degree of

Doctor of Philosophy

at the

MASSACHUSETTS INSTITUTE OF TECHNOLOGY

August 2003

© Massachusetts Institute of Technology 2003. All rights reserved.

Author
Department of Physics
August 31, 2003

Certified by
Wolfgang Ketterle
John D. MacArthur Professor of Physics
Thesis Supervisor

Accepted by
Thomas J. Greytak
Professor of Physics, Associate Department Head for Education

Studies of a Quantum Degenerate Fermionic Lithium Gas

by

Zoran Hadzibabic

Submitted to the Department of Physics
on August 31, 2003, in partial fulfillment of the
requirements for the degree of
Doctor of Philosophy

Abstract

The work described in this thesis can be divided into two parts. The first part is concerned with the production of degenerate Fermi gases and Bose-Fermi mixtures. The second part of the thesis describes studies of strongly interacting spin-mixtures of ultracold fermions.

We have cooled a magnetically trapped spin-polarized ${}^6\text{Li}$ Fermi gas into quantum degeneracy by sympathetic cooling with bosonic ${}^{23}\text{Na}$. In order to do this, we have converted our previously developed apparatus for Bose-Einstein condensation of ${}^{23}\text{Na}$ into a two-species cooling facility. We have produced ${}^6\text{Li}$ samples with up to 7×10^7 atoms at temperatures below $0.5 T_F$, and up to 3×10^7 atoms at temperatures as low as $0.05 T_F$. Further, we have also produced stable quantum degenerate mixtures of ${}^{23}\text{Na}$ and ${}^6\text{Li}$, with several million atoms of each species.

In a second set of experiments, we have studied strongly interacting spin-mixtures of ${}^6\text{Li}$. The strength of interactions was resonantly controlled by applying a magnetic field and tuning to “Feshbach resonances”, which occur when the total energy of the colliding particles coincides with the energy of a bound molecular state. These studies are relevant for the continuing quest for a superfluid transition in a Fermi gas.

By studying the inelastic decay of the cloud, we have experimentally identified two Feshbach resonances for the inter-state interactions of the two lowest ground states of ${}^6\text{Li}$. Most importantly, we found that the lifetime of the strongly interacting system is long enough to observe a superfluid transition in the future.

The effects of the coherent collisions in ${}^6\text{Li}$ spin-mixtures were studied using radio-frequency (RF) spectroscopy. We demonstrated the absence of mean field “clock shifts” in a two-state mixture of fermions, and have introduced a three-level method to observe the interaction energy shifts. In the strongly interacting regime, near a Feshbach resonance, we have observed universal behavior of the interaction energy, independent of the value of the scattering length.

Finally, we have theoretically studied the effects of Pauli blocking during a free expansion of a degenerate Fermi gas. We have concluded that a strongly interacting normal gas will undergo a hydrodynamic expansion even at zero temperature, due to inefficiency of the Pauli suppression of collisions. Therefore, the already observed hydrodynamic expansion cannot be conclusively interpreted as a signature of superfluidity.

Thesis Supervisor: Wolfgang Ketterle

Title: John D. MacArthur Professor of Physics

To my parents, Borislav and Ljiljana

and my sister Selena

Acknowledgments

*we took me and D. Boon's and George's stench
and put them up on stage
watt, Tour Spiel*

During my years at MIT, I was indebted both professionally and personally to more people than I could possibly list here. While some have directly contributed to my work, others have made life outside lab worth living. I was particularly fortunate to have as my immediate collaborators the sort of people who fall into both categories. Faced with the knowledge that I cannot do justice to everyone, I merely mention some of those whose impact on my life was the greatest.

First of all, I would like to thank Wolfgang Ketterle for having faith in me and giving me a chance to work in his lab at a time when it was not clear that I had any experimental talents. Secondly, I would like to thank Wolfgang Ketterle for having faith in me in my early days and months in the group, when it was still not clear that I had any experimental talents. Over the years, Wolfgang has provided not only brilliant scientific advice, but also moral guidance in times of hardship. Dave Pritchard has acted as an unofficial second advisor, partially because he cannot really help it, and partially because I would have bullied him into it if he could. Dave has offered council beyond the call of duty, and his shoot-from-the-hip approach to discussing anything, sometimes physics, has been greatly appreciated.

Next I would like to express my eternal gratitude to the other graduate students on the lithium crew, with whom I have shared many a day and night - (Subha)Deep Gupta (who jams econo), Claudiu Stan, Martin Zwierlein and Christian Schunck. None of the work described in this thesis would have been possible without them. Nor would all the hard work be half as enjoyable without the sense of camaraderie that surpassed anything I could have hoped for.

Deep and I arrived at MIT at the same time, taken all our exams at the same time, and defended our theses within a day of each other. Over the last few years, we have shared the office and worked together, or at least discussed both physics and life, almost every day. This thesis is his as much as it is mine. I could not have had a better partner on this journey. Deep is a constant source of ideas, both serious and bizarre and stupendously funny. He also has an impeccable taste in food, a profound understanding of the genius of Audrey Hepburn, and an agreeable taste in music. I should also admit that he is much better than me at oil wrestling.

With Claudiu, I have started off the lithium project as a two-man show, and we share a unique bond of entering a completely unknown territory together, uncertain whether our

efforts would ever bear fruition. Those early days were frustrating more than not, and Claudiu's unshakeable calmness has given me invaluable emotional support, probably more so than he might be aware. Not to mention that he has built all the hardest parts of the experiment, which would have taken me infinitely longer time.

Both Martin and Christian have initially joined us as "apprentices", to do their undergraduate theses under our guidance. Within months, this apprenticeship had turned into an equal partnership and a close friendship. We were fortunate to convince them to continue working in our group as graduate students. It gives me a great peace of mind to know that the future of this experiment lies in the hands of two such enthusiastic and brilliant young scientists.

Due thanks should also be given to the two experienced postdocs with whom we have worked at different times - Kai Dieckmann and Axel Görlitz. They have not only offered invaluable advice, but have also taken equal part in the sometimes miserable life of graduate students, doing the most mundane jobs and staying up with us all night, struggling with the experiment.

Outside the lithium group, there is a large AMO community at MIT, and I am indebted in various small and big ways to all of its members. Some of them simply cannot go unmentioned.

Before starting the lithium project, I was guided in my first steps into experimental atomic physics by the original BEC II group - Chandra Raman, Roberto Onofrio, Michael Köhl, Dallin Durfee and Chris Kuklewicz. I have learned a great deal from each and everyone of them, as well as from Dan Stamper-Kurn, Shin Inouye and Ananth Chikkatur, who had been running the original BEC machine, now converted into our sodium-lithium experiment.

Jamil Abo-Shaeer joined the group at about the same time as I did, and within 24 hours we had formed a friendship that has lasted and deepened over the years, and which has enriched me for the rest of my life. His ability to cheer me up at work, when cheering up is needed, and his selfless dedication to all of his friends, are second to none. Another veteran student whose stay at MIT has greatly overlapped with mine, and for whom I have developed a fondness reserved only for the most wonderful and genuine people, is Aaron Leanhardt. Aaron is also the single person, outside the lithium lab, whose physics help and advice I have sought most often.

Among the many younger students who have joined the group in the recent years, I would particularly like to mention Jit Kee Chin, Gretchen Campbell and Micah Boyd. I will cherish forever the times we have spent together, both in Cambridge and at an unforgettable conference in Orlando.

Last but not least, I would like to thank Carol Costa and everyone at RLE headquarters for keeping the show running. Carol in particular has helped me with all the little organizational things I would have forgotten or failed to do in time, or at all.

Outside MIT, I have had a home away from home at 63 Henry Street in Cambridgeport. There is no way for me to express how fortunate I was to live with Walter Rantner and Mirko & Natasa Ristivojevic, whom I have known and loved for more than a decade, and who have been my second family.

The part-time staff of the 63 is numbered in dozens. Everyone who has ever lived with us, visited us for a few weeks, or just came over for dinner and sat on our porch until the wee hours of the morning, has made me feel more at home. Bosiljka Tasic and Gojko Lalic have been over so many times, they could have just as well moved in. Particularly cherished were the visits by my sister Selena, who I have lately finally had a chance to spend more time with, after seeing her way too infrequently for seven years.

While I am in many (predictable) ways happy that I am now done with my PhD, it saddens me that the 63 crowd is being disbanded.

Finally, I would like to thank this lot for keeping it lit: Bluefin at Porter Sq., Will Oldham, Bill Calahan, Chan Marshall, David Gedge, Howe Gelb, Joey Burns & John Convertino, Miracle of Science on Mass. Ave., Ethan & Joel Coen, Jeff Bridges, John Goodman, Larry Sellers, Philip Seymour Hoffman, Major Tom, the couple that used to run Mars Records on Mass Ave., Guided By Voices, Yo La Tengo, Darkwood Dub, Jarboli, Edward Norton, David Fincher, Paul Auster, Mira Sorvino, anyone who ever reads these pages, John Lurie, Morrissey & Marr, Forster & McLennan, Michael Rapaport, Gwyneth Paltrow, Eliza Dushku, Nick Hornby, Jay McInerney, Dimitrios Cuisine & Pizza and Stefani's (both on Brookline St. in Cambridge), The Minutemen, Sacramento Kings, Dejan Bodiroga, Tom Stoppard, D. C. Berman, Drag City, Frank Miller, Alan Moore, Garth Ennis, Adam Green & Kimya Dawson, Other Music, Jack Rabid & the Big T, ventolin, Presing, Grant Hart, Steve Wynn, Neil Gaiman, Destiny, Death, Dream, Destruction, Desire, Despair & Delirium.

This work was supported by the National Science Foundation (NSF), the Office of Naval Research (ONR), the Army Research Office and the Joint Services Electronics Program (JSEP) of the Army Research Office (ARO), the National Aeronautics and Space Administration (NASA), and the David and Lucile Packard Foundation.

Contents

1	Introduction	12
1.1	Of Bosons and Fermions	12
1.1.1	Bose-Einstein condensates - a success story	13
1.1.2	Quantum degenerate fermions	14
1.1.3	Bose-Fermi mixtures	14
1.2	Trapped ultracold gases	15
1.2.1	How cold is cold enough?	15
1.2.2	The μK containers for atoms	15
1.3	Outline of this thesis	16
2	Two-species apparatus for cooling of ^6Li and ^{23}Na	17
2.1	Sympathetic cooling of fermions	17
2.1.1	Why two species?	17
2.1.2	Why a boson and a fermion?	18
2.1.3	Why ^{23}Na and ^6Li ?	19
2.2	Outline of our cooling strategy	19
2.3	Two-species oven	21
2.4	Laser cooling of ^6Li	23
2.4.1	Some laser cooling basics	23
2.4.2	Simultaneous Zeeman slowing of ^6Li and ^{23}Na	25
2.4.3	Differences between ^6Li and ^{23}Na MOTs	26
2.4.4	^6Li laser system	28
2.5	Two-species MOT for ^6Li and ^{23}Na	32
2.5.1	Single-species ^6Li MOT	32
2.5.2	Coexistence of the two MOTs	34
2.6	Conclusion	36
3	Production of coexisting ^6Li Fermi seas and ^{23}Na BECs	37
3.1	Choice of ^{23}Na and ^6Li hyperfine states for sympathetic cooling experiments	37
3.2	Sympathetic cooling with sodium in the $F = 1$ state	41
3.2.1	Some remaining confusions...	45

3.3	Condensation of ^{23}Na in the $F = 2$ hyperfine state	46
3.3.1	Magnetic trap loading	46
3.3.2	Avoiding three-body losses	49
3.4	Sympathetic cooling with sodium in the $F = 2$ state	50
3.4.1	Boost in the ^6Li atom number	50
3.4.2	Trading-in the ^6Li atom number for deeper quantum degeneracy . .	51
3.4.3	Two-species degenerate mixture	52
3.5	Summary of sympathetic cooling experiments	52
4	Interactions in ^6Li spin mixtures	54
4.1	Language of collisions	54
4.1.1	Inelastic, elastic, and coherent collisions	54
4.1.2	Elastic scattering amplitude	55
4.1.3	Weakly interacting limit	55
4.1.4	Strongly interacting limit	56
4.2	Feshbach resonances	57
4.2.1	Scattering resonances	57
4.2.2	Tuning the scattering length with a magnetic field	59
4.2.3	Strongly interacting limit revisited	61
4.2.4	Adiabatic creation of diatomic molecules	61
4.3	High temperature superfluidity of ^6Li ?	62
5	Experiments with ^6Li in the vicinity of Feshbach resonances	64
5.1	Prediction of Feshbach resonance(s) in ^6Li	64
5.2	Experimental methods	65
5.2.1	Generation of uniform high magnetic fields	65
5.2.2	Optical trapping	66
5.2.3	Preparation of interacting spin mixtures	66
5.2.4	Spin selective imaging at high magnetic fields	67
5.3	What to look for?	67
6	Inelastic losses near a Feshbach resonance	70
6.1	Note on the experimental procedure	71
6.2	Two decay resonances of the $ 1\rangle - 2\rangle$ spin mixture	71
6.3	Relative positions of the decay and the Feshbach resonances	72
6.4	The main good news	73
7	Elastic collisions and the expansion measurements	75
7.1	Hydrodynamic expansion of a classical gas	76
7.2	Superfluid <i>vs.</i> classical hydrodynamics in a degenerate Fermi gas	79
7.3	Pauli blocking of collisions during the expansion of a degenerate Fermi gas .	81

7.3.1	Effects of the Fermi surface deformation on Pauli blocking	81
7.3.2	Deformation of the Fermi surface during the expansion	83
7.4	Conclusions and one final thought	86
8	RF Spectroscopy of coherent collision energy shifts	87
8.1	Spectroscopic insensitivity to coherent collisions in a two-level system . . .	88
8.1.1	Bloch sphere representation of the RF transitions	90
8.1.2	Comparison with bosons	92
8.2	Spectroscopy of cold collisions in a three-level system	92
8.2.1	Strongly interacting and high density limit	95
9	Conclusions and outlook	98
A	^6Li laser system baedeker	101
A.1	Diode Lasers	101
A.1.1	Free Running Diode Lasers	101
A.1.2	Grating Stabilization	105
A.1.3	Injection Locking	106
A.2	Locking of the master laser to the ^6Li atomic resonance	108
A.3	Imaging frequencies at high magnetic fields	111
A.4	Layout of the ^6Li laser system	113
B	Two-Species Mixture of Quantum Degenerate Bose and Fermi Gases	115
C	Fifty-fold improvement in the number of quantum degenerate fermionic atoms	120
D	Radio-Frequency Spectroscopy of Ultracold Fermions	125
E	Spectroscopic insensitivity to cold collisions in a two-state mixture of fermions	130

List of Figures

1-1	Classical, Bose and Fermi gases	13
2-1	Outline of the ${}^6\text{Li}$ cooling strategy	20
2-2	Two-species oven for ${}^{23}\text{Na}$ and ${}^6\text{Li}$	22
2-3	Energy level diagram for laser cooling of ${}^6\text{Li}$	23
2-4	Outline of the ${}^6\text{Li}$ laser system	29
2-5	Frequencies of seeded slave lasers recorded by a Fabry-Perot spectrum analyzer	30
2-6	Tandem AOM for the ${}^6\text{Li}$ imaging light	31
2-7	Absorption monitor of a ${}^6\text{Li}$ MOT	32
2-8	Measurement of the ${}^6\text{Li}$ MOT temperature	33
2-9	Dependence of the ${}^6\text{Li}$ MOT temperature on the detuning of the cooling light	34
2-10	Inter-species light assisted collisions in a two-species MOT	35
3-1	Ioffe-Pritchard magnetic trap coils	38
3-2	Hyperfine structures of ${}^{23}\text{Na}$ and ${}^6\text{Li}$	39
3-3	${}^6\text{Li}$ cooling path	42
3-4	Onset of Fermi degeneracy	44
3-5	Loading of $ F = 2, m_F = 2\rangle$ sodium atoms into the magnetic trap	47
3-6	Frequencies for sodium optical pumping	48
3-7	Large and ultra-degenerate Fermi sea	52
3-8	Two-species mixture of degenerate Bose and Fermi gases	53
4-1	Cartoon of scattering resonances.	58
4-2	Shape scattering resonance.	59
4-3	Feshbach resonance.	60
5-1	Predicted Feshbach resonance in ${}^6\text{Li}$	65
5-2	High field imaging and mutual cooling of an optically trapped ${}^6\text{Li}$ spin mixture	68
6-1	Magnetic field dependence of inelastic losses in a ${}^6\text{Li}$ $ 1\rangle - 2\rangle$ spin mixture	72
6-2	Updated prediction of the ${}^6\text{Li}$ a_{12} Feshbach resonances	73
7-1	Ballistic and hydrodynamic expansion of a classical gas	77

7-2	Anisotropic expansion of a strongly interacting ^6Li spin mixture	78
7-3	Superfluid hydrodynamic expansion of a weakly interacting ^{23}Na BEC . . .	80
7-4	Opening up of final states for elastic scattering at zero temperature.	82
7-5	Local momentum-space Fermi surface of an expanding gas	84
7-6	Allowed and forbidden elastic collisions during the expansion.	84
7-7	Fraction of Pauli allowed elastic collisions during the expansion.	85
8-1	Equilibrium shifts of the energy levels in an interacting two-state mixture of fermions	88
8-2	Absence of the clock shift in a pure fermionic state	89
8-3	Absence of the clock shift in a decohered two-state mixture of fermions . . .	90
8-4	Bloch sphere representation of the RF transitions	91
8-5	RF spectroscopy in a three-level system	93
8-6	Spectroscopic measurement of the interaction energies	94
8-7	Spectroscopic frequency shifts as a function of the magnetic field	95
8-8	Expansion measurements of the interaction energy by Bourdel <i>et al.</i>	96
A-1	Grating stabilized laser system in a Littrow configuration	105
A-2	Summary of frequency scales in a grating stabilized laser	106
A-3	Seeding of a diode laser	107
A-4	Saturated absorption spectroscopy setup	108
A-5	Optical pumping Doppler free spectroscopy	109
A-6	Absorptive and dispersive Doppler free spectrum	111
A-7	Optical transitions in ^6Li at high magnetic fields	112
A-8	Layout of the ^6Li laser system	114

Chapter 1

Introduction

*I was one of seventeen children. We were all named Wilkinson...
I would've liked to've bin an only child.
That way when someone shouts Wilkinson, you know if it's you or not.*
Neil Gaiman, *A Game of you*

1.1 Of Bosons and Fermions

All particles in nature can be divided into two categories according to their “social behavior”. While identical *bosons* like to stick together, identical *fermions* avoid each other at all costs. Atoms fall into one of the two categories depending on the total number of protons, neutrons and electrons that they are made of. If this number is even, the atom is a boson; if it is odd, the atom is a fermion. In this thesis we will be mostly concerned with two atomic species, one fermionic - ${}^6\text{Li}$, and one bosonic - ${}^{23}\text{Na}$.

At a quantum mechanical level, the world is discrete, partitioned into unit cells of finite size. Alternatively, we say that a particle can occupy only a discrete set of “quantum mechanical states”, which correspond to different energies. While identical bosons like being in the same state, no more than one identical fermion can occupy the same unit cell.

Naturally, the question whether two particles like each other or not, arises only if they actually meet. The probability that this happens distinguishes “classical” from “quantum degenerate” gases. In a classical gas, such as the air around us, the meeting probability is low, and hence it is not important whether the particles are fermions or bosons. In this case, only a small fraction of energetically available quantum states in the system is occupied by atoms. The issue whether two atoms would want to (bosons), or could not (fermions) occupy the same state then rarely arises.

However, if we cool the gas to very low temperatures, this greatly reduces the energy available to the atoms, and hence the choice of states that they can occupy. The differences

between Bose and Fermi atomic gases become pronounced once the number of energetically available states in the system is reduced approximately to the number of particles.

In the quantum degenerate regime, bosons pile up in the lowest energy state and form a “Bose-Einstein condensate” (BEC). Fermions on the other hand are forced to occupy different states, and form a “Fermi sea”. This is illustrated in Fig. 1-1 for the case of atoms trapped in a parabolic potential well.

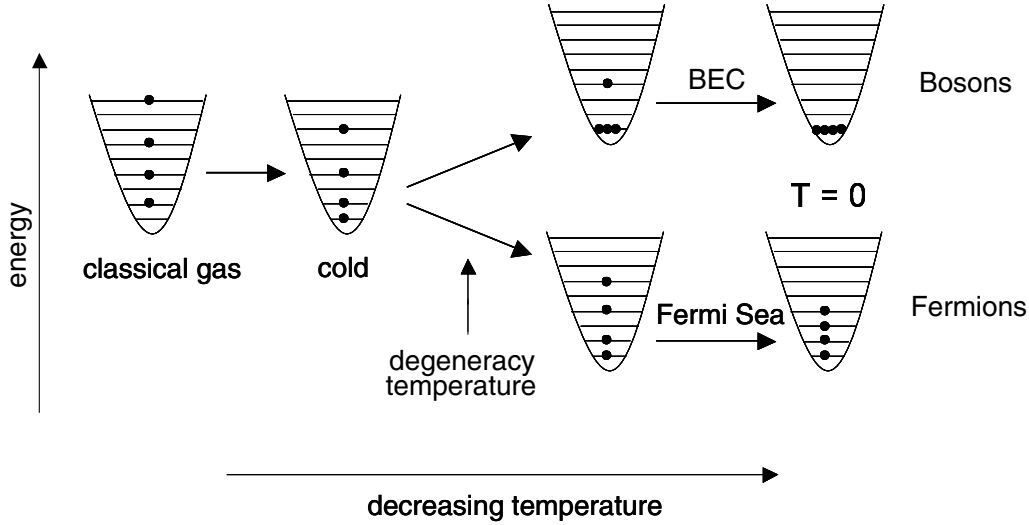


Figure 1-1: Classical, Bose and Fermi gases. The atoms occupy a discrete set of quantum states corresponding to different energies. At high temperatures, there is no distinction between Bose and Fermi gases. Here, the occupied states are few and far between. As we lower the temperature of the gas, the atoms fall into lower and lower energy states. A fork in the road occurs once neighboring states start being occupied. At this point, the atoms have to decide whether they want to move in together or not. Bosons decide to all pile up in the same state. Fermions on the other hand each keep a state to themselves, even though this is much more energetically expensive.

1.1.1 Bose-Einstein condensates - a success story

In 1995, atomic physicists have successfully cooled bosonic gases into quantum degeneracy [10–12]. The story of BEC is one of great success, and has by now been told many times. What started as the quest for the demonstration of the BEC, has lent itself to much broader research, both in conventional atomic physics and in what has traditionally been the area of condensed matter physics. A good summary of the BEC history is provided by the 2001 Nobel Prize lectures of Eric Cornell and Carl Wieman [13], and Wolfgang Ketterle [14].

Broadly speaking, atomic BECs are fascinating for two reasons. First, they give us an almost textbook example of a weakly interacting superfluid, much more amenable to theoretical calculations than the strongly interacting ^4He liquid. Further, in atomic systems

we can relatively easily manipulate the strength of the particle interactions, as well as change their nature from repulsive to attractive and vice versa. This makes BECs an ideal test bed for fundamental many-body theories.

Second, atomic BECs are truly macroscopic coherent matter waves. This makes them extremely bright sources for a range of atom optics applications¹, from precision measurements of fundamental constants, to development of novel navigation instruments.

1.1.2 Quantum degenerate fermions

A natural complement to BEC research is to produce and study a quantum degenerate gas of Fermi atoms. After the pioneering work by DeMarco and Jin in 1999 [15], this subfield has gained its own momentum, and it is now becoming increasingly obvious that it will provide (at least) as much excitement. So far, six experimental groups have achieved quantum degeneracy in either ^{40}K [15, 16] or ^6Li [1, 17–19].

Like their Bose counterparts, these systems offer a great flexibility in tuning the experimental parameters such as particle number, density, strength of interactions, spin compositions or the temperature.

One particularly interesting prospect of this research is the attainment of fermionic superfluidity in a gaseous system. In analogy with superconductors or superfluid ^3He , at low enough temperatures and for attractive effective interactions, fermionic atoms can pair up into bosonic Cooper pairs [20], and undergo a phase transition into a superfluid state. Due to the widely tunable experimental parameters, studies of superfluidity in an atomic Fermi gas could provide a more general understanding of the pairing mechanisms in a range of very different systems, from solids to neutron stars and the quark matter [21].

Experimental studies of ultracold Fermi systems in the regimes of strong and controllable interactions are already well underway [3, 5, 22–30]. According to some theories of superfluidity in a Fermi gas [31–42], the combination of the temperature and the attractive interactions required for the phase transition is already within experimental reach. One of the main current experimental challenges is to identify an effective way to observe the transition.

1.1.3 Bose-Fermi mixtures

Finally, given that all particles obey one of the only two types of quantum statistics, the scientific motivation for producing and studying quantum degenerate mixtures of Bose and Fermi atoms is obvious. A classic example of such a degenerate Bose-Fermi system is the strongly interacting ^4He – ^3He mixture.

A single experimental apparatus in which degenerate gases of either kind could be produced, as well as their mixtures, then seems like an omnipotent solution.

¹In the field of “atom optics”, we manipulate matter waves in the ways that we are used to manipulating light - reflect them off mirrors, focus them with lenses, interfere them, or diffract them off gratings.

This thesis describes the production of a degenerate Bose-Fermi mixture of ^{23}Na and ^6Li [1, 2]. In other current experiments, degenerate mixtures of ^7Li and ^6Li [17, 18], as well as ^{87}Rb and ^{40}K [16], are also being produced.

1.2 Trapped ultracold gases

To get a sense of scale, let us introduce some basic experimental parameters of ultracold atomic clouds.

1.2.1 How cold is cold enough?

We can quantify the level of quantum degeneracy in a gas in terms of the phase space density:

$$\rho = n\lambda_{\text{dB}}^3 \quad (1.1)$$

where n is the gas density, and $\lambda_{\text{dB}} = h/\sqrt{2\pi mk_B T}$ is the thermal deBroglie wavelength, which measures the size of the quantum wave packets describing individual atoms. For $\rho \ll 1$, there is no distinction between fermions and bosons. The cross-over to quantum degeneracy occurs at a temperature for which $\rho \sim 1$. At this point, the “size” of the atoms becomes comparable to the typical distance between two particles in the gas, and the atoms start “feeling each other” in real space. For an atomic gas with the same density as air, the degeneracy temperature would be about 10 mK.

However, an additional problem in producing an atomic quantum *gas* is that at such low temperatures, most substances will become solid, or at least liquid, before quantum degeneracy is reached. We cannot really solve this problem, but we can postpone it. In order to turn into a solid, an atomic gas starts off by creating molecules, which then combine into larger and larger clusters. For this process to start, several atoms must be found in the same place at the same time. If the gas density is very low, the probability of this happening is greatly reduced and the process is slowed down.

In order to perform our experiments, we must make sure that the gaseous state has a lifetime of seconds to minutes. This requires that the gas density is about a million times lower than the density of air. The typical degeneracy temperature is then reduced to about 1 μK , *i.e.* one millionth of a degree above absolute zero.

1.2.2 The μK containers for atoms

Ultracold atomic clouds are too fragile to be put in contact with any material object. The only place where they live long enough is in ultra high vacuum (UHV), levitating in free space electromagnetic traps. Even if it is not in contact with any material object, a trapped ultracold gas will eventually be destroyed by collisions with the background gas

in the chamber, which is at room temperature. In order to give our samples a respectable lifetime, of about one minute, the pressure inside the vacuum chamber must be kept below 10^{-11} Torr, about 10^{14} times lower than the atmospheric pressure.

Usual traps are parabolic, or *harmonic*, like those illustrated in Fig. 1-1. The characteristic trapping frequency, with which the atoms oscillate around the bottom of the trap, is $\omega \sim 2\pi \times 100$ Hz. The typical size of an ultracold, μ K atomic cloud is then $R = \sqrt{k_B T / (m\omega^2)} \sim 50 \mu\text{m}$.

In a cloud containing N atoms, the density in the center of the trap is approximately $n \sim N/R^3$, and we can rewrite Eq. 1.1 as $\rho \sim N(\hbar\omega/k_B T)^3$. We thus most commonly express the degeneracy criterion $\rho \sim 1$, as:

$$k_B T_{\text{DEG}} \sim \hbar\omega N^{1/3} \quad (1.2)$$

where the number of atoms in a degenerate gas is typically $N \sim 10^6$.

To summarize, a typical quantum degenerate atomic cloud is a million times thinner than air, and contains about a million atoms, at a temperature of one millionth of a degree above absolute zero.

1.3 Outline of this thesis

The first part of this thesis describes the production of degenerate Fermi gases and Bose-Fermi mixtures [1, 2]. In Chapter 2, I introduce our cooling strategy and all the technical developments which were needed in order to convert our previously built sodium BEC apparatus into a joint ^{23}Na – ^6Li experimental facility. Our results on simultaneous cooling of lithium and sodium into quantum degeneracy are summarized and discussed in Chapter 3.

The second part of the thesis, consisting of Chapters 4 - 8, is dedicated to interacting Fermi gases. Chapter 4 provides some theoretical background - I discuss the types of collisions which occur in spin-mixtures of fermions, how the interactions can be externally controlled near “Feshbach resonances”, and the possibility of achieving fermionic superfluidity. In Chapter 5, I briefly introduce the additional experimental techniques needed for studies of ^6Li in the strongly interacting regime. Chapters 6 - 8 describe our experimental and theoretical studies of different types of interactions in ultracold Fermi clouds [3–6]. Each of these three chapters is dedicated to one type of collisions - inelastic [3], incoherent elastic [4], and coherent [5, 6].

Finally, some more technical aspects of the ^6Li laser system, as well as the reprints or preprints of four publications [1, 2, 5, 6], are included in Appendices at the end of the thesis.

Chapter 2

Two-species apparatus for cooling of ^6Li and ^{23}Na

This chapter describes the “development” phase of our two-species experiment, namely our cooling strategy, the technical additions to the previously existing BEC apparatus, and the simultaneous production of laser cooled ^6Li and ^{23}Na samples. This is the starting point for the production of quantum degenerate Fermi and Bose-Fermi gases, which will be described in Ch. 3.

2.1 Sympathetic cooling of fermions

2.1.1 Why two species?

All experiments with quantum degenerate alkali gases rely on two classes of cooling methods - laser cooling, and evaporative cooling [43, 44]. Evaporative cooling of Bose gases is most commonly performed with magnetically trapped spin-polarized samples. As will soon become apparent, this simplistic approach cannot be taken in cooling of fermions into quantum degeneracy.

All laser cooling methods, such as Zeeman slowing, magneto-optical trapping, or polarization gradient cooling, are independent of the quantum statistics of the cooled atoms, and work equally well for bosons and fermions. The reason for this is that all these methods rely on fundamentally single-particle physics concepts - each atom interacts with the laser fields independently. Further, currently produced laser cooled atomic samples are almost always far away from quantum degeneracy, and the atoms are classical with respect to their external degrees of freedom.

Evaporative cooling on the other hand is fundamentally a two-particle physics concept. Most energetic atoms are selectively removed from the (magnetic or optical) trap, taking away more than their share of energy, and leaving the remaining atoms to rethermalize at a lower temperature. Both the population of the wings of the energy distribution,

and the subsequent thermalization of the sample, rely on binary collisions between atoms. At ultralow temperatures, this process does depend on quantum statistics. Specifically, evaporative cooling would not work in a spin polarized Fermi gas. The reason is obvious - since all particles are in the same spin state, the two-particle wave function is necessarily symmetrized in spin space, and hence must be anti-symmetric in real space. This prevents s -wave collisions, while higher order partial waves are suppressed at low temperatures by the centrifugal barrier. We can estimate the energy (or temperature) threshold for p -wave collisions to be $k_B T_{p\text{-wave}} \sim \hbar^2/(2mR^2)$. Here, R is the range of the inter-particle interaction, and hence the maximum allowed impact parameter. Without knowing the details of the molecular potential curves, we can estimate R to be on the scale of a “garden variety” s -wave scattering length, say a few nm¹. This implies a p -wave threshold on a mK scale, while a typical temperature of quantum degeneracy is on the μ K scale. Suppression of higher order partial waves is even more drastic. The collisions thus freeze out long before degeneracy can be reached. Recently, Regal and Jin [24] have demonstrated that p -wave interaction could be enhanced near a Feshbach resonance (see Chapter 4) sufficiently to enable evaporative cooling. However, this enhancement is accompanied by strong inelastic losses, and does not offer much promise for a practical cooling strategy.

The way to overcome these problems is to employ some form of “sympathetic” cooling between two distinguishable types of particles. In this scenario, thermalization of fermions is mediated by inter-species collisions. The two distinguishable species can be two spin states of the same atom [15, 19], two different isotopes of the same chemical element [17, 18], or two different chemical elements [1, 16]. Taking this approach, six experimental groups have thus far achieved quantum degeneracy in Fermi gases of either ⁴⁰K [15, 16] or ⁶Li [1, 17–19].

2.1.2 Why a boson and a fermion?

In addition to the obvious scientific appeal of allowing for studies of degenerate Bose-Fermi (BF) mixtures, BF sympathetic cooling has several advantages over its Fermi-Fermi (FF) counterpart. In general, cooling of fermions becomes less time-efficient as the temperature gets lower. The reason for this is that the scattering rate into low energy states is proportional to $1 - f$, f being the Fermi-Dirac occupation number. As the occupation of the low lying states becomes appreciable at $T \ll T_F$, the cooling rate is reduced. In a two fermion experiment, both species rely on each other for cooling, and neither can easily find its way down in temperature. On the other hand, if fermions are cooled in a bosonic thermal bath, which can rapidly achieve thermal equilibrium on its own, the problem should be reduced. Note that time-efficiency of the cooling process is not just a matter of convenience. Cooling is in competition with the timescale for heating and decay of the system, set for example by the collisions with the residual background gas in the vacuum chamber. Time efficiency therefore has fundamental implications on the final temperatures and size of the system [45].

¹See Ch. 4 for a reasonable justification of this estimate.

Further, FF cooling is most efficient if the heat capacities of the two species are comparable at all times. This means that both species must be actively evaporated, and the degenerate Fermi samples are much smaller than the initial samples prepared by laser cooling. In BF experiments, it is sufficient to evaporate the bosonic species. The sympathetic cooling can thus, at least in principle, be conservative in the fermion atom number. Therefore, it is possible to produce large degenerate Fermi samples without huge demands on the laser cooling of the fermionic species.

2.1.3 Why ^{23}Na and ^6Li ?

The criteria for designing BF sympathetic cooling experiments include the heat capacity of the “refrigerator”, and the inter-species collisional properties, both elastic and inelastic. ^{23}Na offers the largest, stable Bose-Einstein condensates [46], which makes it a very appealing choice for sympathetic cooling of fermions. Of course, in our case, the choice of ^{23}Na was further motivated by the fact that we already had a functioning BEC apparatus.

Experiments with degenerate alkali fermions have thus far used either ^{40}K or ^6Li . Both species are promising candidates for the observation of a BCS-like superfluid transition (see Chapter 4). However, while ^6Li is abundant in nature, ^{40}K is scarce. This makes only ^6Li suitable for our particular cooling strategy. In our ^{23}Na experiments, the atomic source is based on an oven and a Zeeman slower (see Fig. 2-1 below). This approach yields large ultracold samples, but also uses the atomic resources inefficiently. Since we wanted to use the same atomic source for both species, in order to minimize the modifications to our ^{23}Na BEC apparatus, ^{40}K was not a viable choice for practical reasons.

Further, it is favorable that the fermion mass is lower than the boson mass. When the two are held in the same magnetic trap, lower mass enhances the fermion trapping frequency, $\propto 1/\sqrt{m}$, and hence the ratio of Fermi temperature to the BEC transition temperature. Therefore, given the same characteristic temperature of the bosonic refrigerator, a lighter fermion can be cooled deeper into quantum degeneracy.

Finally, the inter-species collisional properties are generally not predictable, and have to be tested experimentally. In this regard, one often has to take a chance in designing a sympathetic cooling experiment, but as we will see in Chapter 3, ^{23}Na - ^6Li combination has proven to be rather fortuitous.

2.2 Outline of our cooling strategy

Our ^6Li cooling strategy is designed around the previously established protocol for production of ^{23}Na BECs [47], outlined in Fig. 2-1. An effusive ^{23}Na atomic beam is produced by evaporating sodium metal in the oven. Zeeman slowed atoms are loaded from the atomic beam into a dark-SPOT magneto-optical trap (MOT) [48]. The atoms are then loaded into a Ioffe-Pritchard magnetic trap and evaporatively cooled to BEC. A detailed descrip-

tion of our ^{23}Na BEC apparatus, including the laser system, vacuum chamber, magnetic trap, standard detection methods and computer control of the experiment, is given in the previous PhD theses from this group [7].

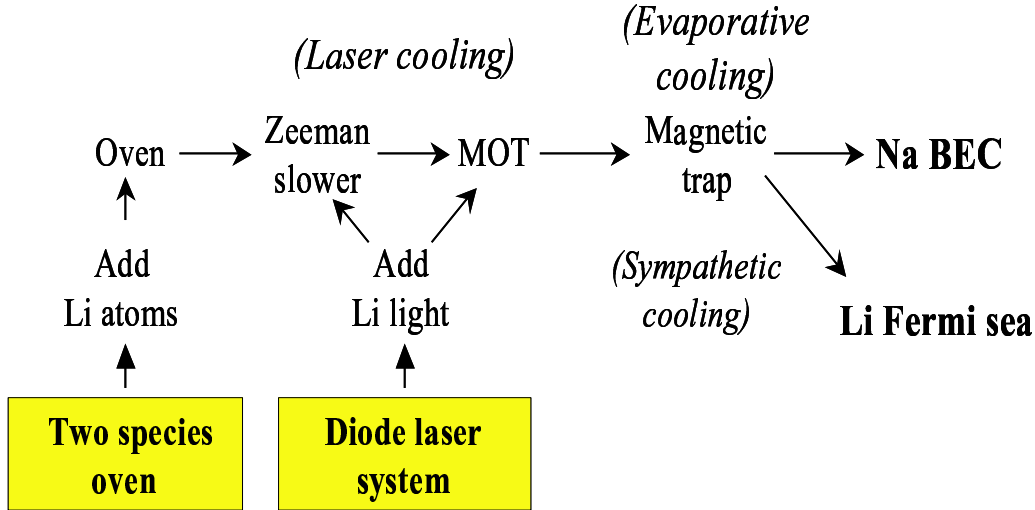


Figure 2-1: Outline of the ^6Li cooling strategy.

The extension to a two-species cooling experiment is then conceptually straightforward (Fig. 2-1). A two-species atomic beam is produced in a common oven, and slowed in a common Zeeman slower. The slowed atoms are then collected in a common two-species MOT, and transferred into a common magnetic trap. At this point, only sodium atoms are actively evaporated and cooled to BEC in the same way as in our traditional single-species experiments. At the end of the evaporative cooling cycle, in addition to a sodium BEC, we get a lithium Fermi sea “for free”. During the evaporative cooling, the lithium number ideally stays constant, which means that we need to load the magnetic trap with only as many atoms as we want to, or can, cool into quantum degeneracy.

As indicated in Fig. 2-1, only two major hardware additions were needed in order to convert our sodium BEC apparatus into a two-species experiment - a two-species oven which produces a combined ^{23}Na - ^6Li atomic beam, and a laser system for laser cooling of lithium.

Let us estimate the potential of this strategy, and the requirements for its implementation. In our ^{23}Na BEC experiments, the flux of hot atoms from the oven into the solid angle subtended by the MOT is about $2 \times 10^{12} \text{s}^{-1}$. About 10^{10} Zeeman slowed atoms are collected in the MOT, 30% of which are transferred into the magnetic trap. After evaporative cooling, pure BECs of $\sim 10^7$ atoms are produced. The number of atoms at the BEC transition is higher, typically $0.5 - 1 \times 10^8$.

Now, sympathetic cooling is efficient only as long as the heat capacity of the cooling body is larger or equal to the heat capacity of the body to be cooled. Below the condensation temperature, heat capacity of a Bose gas starts dropping rapidly ($\propto T^3$). In fact,

thermodynamic calculation with the constraint of constant particle number would tell us that the BEC itself has a vanishing heat capacity, which would make it completely useless as a refrigerant [17]. I believe this conclusion is a bit oversimplified, and is not trivially applicable to the case of an evaporatively cooled cloud, since in the latter case, heating can always be converted into particle loss. For example, suppose we immerse a small and hot lithium cloud into a really large (zero temperature) sodium BEC. Each inter-species collision will take energy out of the lithium cloud and create a high energy sodium particle. If such a particle stays in the trap, this would indeed lead to drastic heating of the sodium reservoir. However, if every thermal sodium atom is immediately removed from the trap, cooling of lithium can continue with the sodium thermal bath still being at zero temperature. Nonetheless, it is reasonable to assume that cooling is efficient only as long as the numbers of sodium and lithium atoms are at least comparable. We conclude that the maximum number of ^6Li atoms we could possibly cool deep into quantum degeneracy is in the range $10^7 - 10^8$. This is of course still very good news, as these numbers are comparable to the largest alkali BECs ever produced [46].

From a practical point of view, this also means that our two-species apparatus does not need to provide us with more than $10^7 - 10^8$ laser cooled ^6Li atoms. In other words, on the way from the MOT to a BEC we lose about a factor of 200 in the sodium atom number. For lithium, we can afford to do that much worse in the laser cooling stage². Further, the large sodium MOT is density limited [48], so we can do even worse in terms of the loading rate of the lithium MOT. This moderate goal allowed for two major simplifications. Firstly, all the lithium laser cooling light could be generated by cheap, low power diode lasers. Secondly, we could load the ^6Li MOT using a Zeeman slower which is actually optimized for ^{23}Na .

2.3 Two-species oven

The main difficulty in having a joint ^6Li and ^{23}Na atomic source is that the two metals have rather different vapor pressures. The conventional sodium oven is operated at $\sim 260^\circ\text{C}$. At the same temperature, lithium has a vapor pressure lower by about three orders of magnitude, and needs to be heated to $\sim 400^\circ\text{C}$ to achieve a decent atomic flux. (As a rough guide for both metals at these temperatures, a 20°C temperature increase corresponds to an increase in vapor pressure by about a factor of two.) Our solution to this problem is sketched in Fig. 2-2. More technical details of the oven design will be given in the PhD thesis of Claudiu Stan.

The oven has two chambers connected by a transfer nozzle of low conductance $\sigma_1 = 0.06$ l/s (for ^{23}Na ³). In the first (left) chamber, sodium is heated to $T_1 = 380^\circ\text{C}$. This produces

²The 30% transfer efficiency of sodium atoms from the MOT into the magnetic trap is limited by the fact that optical pumping into a single Zeeman state is difficult in dense laser cooled samples. For small lithium samples this factor of 3 loss is also absent.

³Conductance expressed in l/s is a function of atomic velocity, and hence it depends on both the atomic

an unusually high vapor pressure, but the small nozzle conductance limits the rate at which sodium is evaporated. In the second chamber, sodium is mixed with lithium heated up to $T_2 = 400$ °C, and they both leave through the main nozzle, which has a much higher conductance $\sigma_2 = 2.4$ l/s for ^{23}Na , 4.5 l/s for ^6Li . Both nozzles are heated to 450 °C. The nozzles are kept hot even when the experiment is not running, in order to insure that they remain the hottest spots in the oven at all times, and no clogging can occur.

At these settings, the atom fluxes into the solid angle subtended by the MOT region are $3 \times 10^{11} \text{ s}^{-1}$ for ^6Li , and $2 \times 10^{12} \text{ s}^{-1}$ for ^{23}Na . Since $\sigma_2/\sigma_1 \approx 40$, practically all the lithium goes into the experiment, and the amount distilled into the sodium chamber can be neglected.

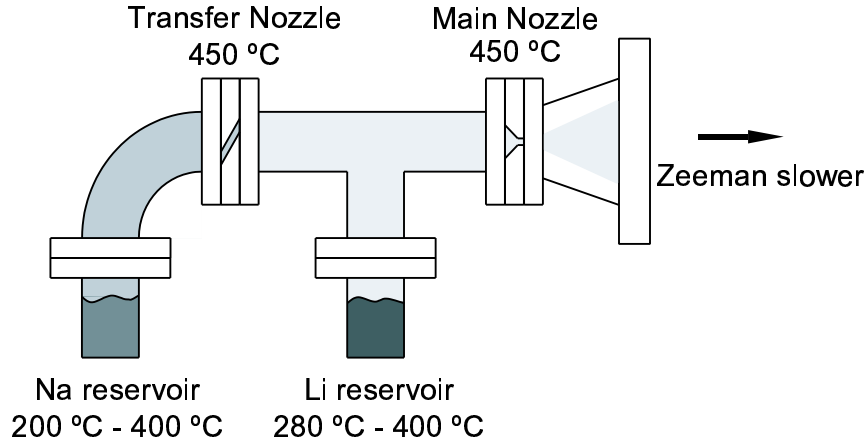


Figure 2-2: Two-species oven. ^{23}Na and ^6Li vapors are produced in separate chambers to allow for independent control of the atom fluxes. The two species are mixed in the lithium chamber. The transfer nozzle has a conductance 40 times lower than the main nozzle, and limits the undesirable diffusion of lithium into the sodium chamber.

However, it is important that the oven can also be operated in a single-species mode. Lithium-only operation is trivial and consists of heating only the second chamber. The small fraction of atoms that takes the wrong turn and ends up in the first chamber will condense there, but that is a small loss. Sodium-only operation requires a bit more care. If the fluxes of sodium through the two nozzles are to be equal, its equilibrium vapor pressure in the second chamber should be

$$P_2 = P_1 \frac{\sigma_1}{\sigma_2} \approx \frac{1}{40} P_1 \quad (2.1)$$

where P_1 is the vapor pressure in the first chamber.

The real vapor pressure is given by either this value, or the vapor pressure corresponding to the second chamber temperature, whichever is lower. The factor of 40 in the vapor mass, and the temperature. All conductances are calculated for the nozzle temperature of 450 °C.

pressure corresponds to a temperature difference of about 100 °C. Therefore, as long as $T_2 \geq 280$ °C, there will be no build up of sodium in the second chamber. For $T_2 < 280$ °C, sodium will start condensing in the second chamber, rather than going into the slower and the experiment. At this point, the flux of atoms is completely determined by the vapor pressure given by T_2 , and heating the first chamber even further would not increase it. Therefore, when running in sodium-only mode we heat up the lithium reservoir to 280 °C as well. This means that some lithium atoms are wasted, but these numbers are negligible.

This oven has now replaced the sodium oven on our BEC apparatus, and in sodium-only experiments it gives the same results as the old one.

2.4 Laser cooling of ^6Li

2.4.1 Some laser cooling basics

In our experiments we use standard techniques of atom beam slowing and magneto-optical trapping [43]. Here I will briefly mention the relevant experimental methods and parameters only in as much detail as is needed to compare and contrast the laser cooling of ^{23}Na and ^6Li .

The ground state of alkali atoms has one unpaired electron in the S shell, $2^2S_{1/2}$ in lithium, $3^2S_{1/2}$ in sodium. The first excited state is of the $(2,3)^2P_J$ form, and is split by $\vec{L} \cdot \vec{S}$ coupling into $J = 1/2$ and $J = 3/2$ states. Laser cooling is done on the D_2 line, connecting the ground state and the $^2P_{3/2}$ excited state. The wavelength of this transition is 671 nm in ^6Li , and 589 nm in ^{23}Na . The diagram of relevant energy levels is shown for ^6Li in Figure 2-3.

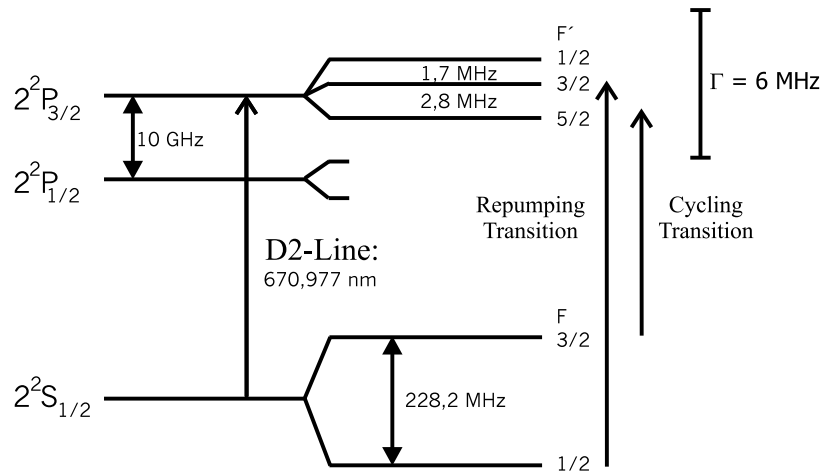


Figure 2-3: Energy level diagram for laser cooling of ^6Li

Both the ground and the excited state are further split into different hyperfine states by the $\vec{I} \cdot \vec{J}$ interaction between the electron and the nuclear spin I . At low magnetic fields,

good quantum numbers are therefore $\vec{F} = \vec{J} + \vec{I}$, and its projection along the quantization axis, m_F . The value of the nuclear spin is $I = 1$ in ${}^6\text{Li}$, and $I = 3/2$ in ${}^{23}\text{Na}$. The hyperfine splitting of the two ground states is 228 MHz in ${}^6\text{Li}$, and 1.77 GHz in ${}^{23}\text{Na}$.

The stretched ground and excited states, with $m_F = -F = -(I + J) = -(I + L + S)$, connected by σ^- polarized light, form a cycling transition which is used for laser slowing and cooling in our experiments. In these states all the angular momenta are fully aligned with the quantization axis, so at all values of the magnetic field the magnetic moment in the ground state is simply one Bohr magneton, μ_B , and in the excited state it is $2\mu_B$. The Zeeman shift of the cooling transition is thus $-\mu_B/h = -1.4 \text{ MHz/G}$, for both ${}^6\text{Li}$ and ${}^{23}\text{Na}$.

The spontaneous light force on an atom absorbing photons with wavevector \vec{k} at a rate γ_s is simply:

$$\vec{F} = \hbar \vec{k} \gamma_s \quad (2.2)$$

For an atom moving with velocity \vec{v} , in presence of a spatially varying magnetic field $B(\vec{r})$, the scattering rate is:

$$\gamma_s = \frac{\Gamma}{2} \frac{s}{1 + s + (2\delta/\Gamma)^2} \quad (2.3)$$

where the effective detuning:

$$\delta(\vec{v}, \vec{r}) = \omega - \omega_0 - \vec{k} \cdot \vec{v} + B(\vec{r})\mu_B/\hbar \quad (2.4)$$

includes the Doppler and Zeeman shifts. Here, Γ is the natural linewidth of the excited state, and the saturation parameter $s \equiv 2\Omega_R^2/\Gamma^2$ is the dimensionless measure of the intensity of the laser light, Ω_R being the corresponding Rabi frequency.

The dependance of scattering rate γ_s on the velocity and the position of the atom is the source of coupling between internal and external degrees of freedom, and the basis of laser cooling and trapping. For example, a moving atom interacting with isotropic light red detuned from the resonance will preferentially be kicked in the direction opposite to its motion and hence slowed down.

Natural linewidths in lithium and sodium are $2\pi \times 6 \text{ MHz}$ and $2\pi \times 10 \text{ MHz}$, respectively. The recoil velocity, $v_{rec} = \hbar k/m$, is about 10 cm/s in ${}^6\text{Li}$, and about 3 cm/s in ${}^{23}\text{Na}$. The saturation intensity (corresponding to $s = 1$) is approximately 2.5 mW/cm² for lithium, and 6.4 mW/cm² for sodium. Saturation intensity sets the natural scale for all laser intensities used for cooling. Therefore, we already see that, other things being equal, about 2.5 less laser power should be needed for lithium laser cooling.

2.4.2 Simultaneous Zeeman slowing of ^6Li and ^{23}Na

An important question in the design of our experiment was whether our existing sodium Zeeman slower could be used for simultaneous slowing of lithium. Changing the slower itself would have involved breaking the vacuum in the system, something that has not been done since 1996. Keeping the same slower, but changing the currents running through it would not have been as drastic, but could have compromised efficient loading of sodium into the dark-SPOT. Fortunately, neither was needed.

In our “increasing field” Zeeman slower (see Eq. 2.7), sodium atoms are slowed by a counter-propagating σ^- polarized beam detuned ≈ 1 GHz from the cycling transition. The capture velocity of our slower (for ^{23}Na atoms) is $v_0 \approx 589$ m/s, and the deceleration rate is $a \approx 4 \times 10^5$ m/s². Longitudinal velocity distribution in an effusive beam has the form:

$$\rho(v) \propto v^3 e^{-\frac{mv^2}{2k_B T}} \quad (2.5)$$

The average velocity of atoms coming out of the oven at a temperature of 450 °C is

$$v_{th} = \frac{3}{4} \sqrt{\frac{2\pi k_B T}{m}}, \quad (2.6)$$

equal to ≈ 940 m/s for ^{23}Na , and 1840 m/s for ^6Li .

The spatial dependence of the DC magnetic field used to compensate for the changing Doppler shift of slowing atoms, derived from the condition that $\delta = \text{const}$ in Eq. 2.4, has the form:

$$B = B_0 \left(1 - \sqrt{1 - \frac{x}{L}} \right) \quad (2.7)$$

where $L = v_0^2/a \approx 40$ cm is the length of the slower, and $B_0 = (\hbar/\mu_B)kv_0 \approx 700$ G corresponds to the Zeeman shift equal to the Doppler shift at v_0 .

The atoms coming out of the oven are distributed over the two hyperfine ground states with probabilities proportional to their (zero magnetic field) degeneracies, $2(I \pm 1/2) + 1$. In order to prepare the atoms for slowing, a σ^- “repumping” laser beam, resonant with the lower hyperfine state, is added to the slowing beam. At zero magnetic field, before the atoms enter the slower, the combination of the slowing and the repumping beam optically pumps the atoms into the stretched ground state⁴.

Using a slowing laser beam of 50 – 100 mW power, we typically slow a flux of few times 10^{10} ^{23}Na atoms/s, to a velocity of few tens of m/s. The repumping frequency, detuned 1.77 GHz to the blue of the slowing frequency, is provided by a sideband generated by passing the slowing beam through an electro-optical modulator. The repumping laser power is about 1/3 of slowing power.

⁴Repumping of the atoms which fall into the lower hyperfine state during the slowing cannot be very efficient, as different transitions have different Zeeman shifts, and keeping the cycling transition on resonance will in general not keep the repumper on resonance as well.

If two different alkali species are slowed using the same magnetic field profile (Eq. 2.7), then:

$$v_0 = \frac{\mu_B B_0}{\hbar k} \propto 1/k \quad \text{and} \quad a = \frac{v_0^2}{2L} \propto 1/k^2 \quad (2.8)$$

For our case this gives:

$$\frac{a_{Li}}{a_{Na}} = \left(\frac{671}{589} \right)^2 = 1.3 \quad (2.9)$$

On the other hand, the maximum deceleration rate, at infinite light intensity, is:

$$a_{max} = v_{rec} \Gamma / 2 \quad (2.10)$$

equal to 18×10^5 m/s² in ⁶Li, and 9×10^5 m/s² in ²³Na, so $a_{max}^{Li}/a_{max}^{Na} = 2$.

This means that in a slower (magnetic field profile) optimized for ²³Na, ⁶Li atoms will be slowed at a smaller fraction of the maximum deceleration. A slower optimized for ²³Na can thus be used for ⁶Li, and it will only be more conservative. This also means that a lower power of the slowing laser beam is needed to keep it working⁵.

One drawback is that a smaller fraction of the thermal velocity distribution is efficiently slowed down for ⁶Li than for ²³Na. The capture velocities of the slower for the two species are comparable (Eq. 2.8), while ⁶Li thermal velocity at the slower entrance is almost twice higher (Eq 2.6). Since the capture velocity of our slower is smaller than the most probable velocity, $\sqrt{3k_B T/m}$, we can conservatively estimate that the successfully slowed fraction of the hot atomic flux will be proportional to

$$\left(\frac{v_0}{v_{th}} \right)^4 \propto \frac{m^2}{k^4} \quad (2.11)$$

This comes out to ~ 9 times lower fraction for lithium than for sodium. This may seem rather inefficient, but even combined with the ~ 7 smaller total flux of hot atoms, it still keeps us on the right track for collecting $\sim 10^8$ lithium atoms in a MOT.

2.4.3 Differences between ⁶Li and ²³Na MOTs

We collect sodium atoms into a standard dark-SPOT MOT [48], which uses three pairs of counter propagating laser beams, and a three-dimensional quadrupole magnetic field, created by two magnetic coils in anti-Helmholtz configuration.

Operation of the MOT fundamentally depends on constant optical repumping of atoms out of the lower hyperfine state. Off-resonant excitations of the atoms into the $F' < I + 3/2$ excited hyperfine states allows the atoms to fall into the lower hyperfine ground state and become invisible to the cooling light. In a dark-SPOT, the repumping light is (mostly)

⁵A more practical upper bound on the deceleration rate is $a_{max}^s = s a_{max} / (1 + s)$, the maximum deceleration for the available light intensity.

confined to the edges of the cloud, and the atoms in the center of the trap sit in the dark of the lower hyperfine state⁶. The probability that the atoms are pumped into the upper hyperfine is therefore high only if they attempt to escape from the trap, and need to be pushed back by the trapping light. This approach reduces the adverse effects of light-assisted collisions between ground and excited state atoms, and the radiation pressure arising from the fact that a photon spontaneously radiated by one atom can be reabsorbed by another, leading to mutual repulsion between the two. This allows for storing of cold atoms in the dark at much higher densities, in our sodium case giving an enhancement by a factor of order 10.

In our setup, the $1/e^2$ diameter of the ^{23}Na MOT beams is about 1 inch, and the laser power is about 30 mW per beam, giving a peak intensity comparable to the saturation intensity. The cooling laser frequency is tuned ~ 20 MHz to the red of the cycling transition $F = 2 \rightarrow F' = 3$. Typical magnetic field gradients in our MOT are 20 G/cm in the axial, and half that in the radial direction. The repumping is done with a single 30 mW beam which is spatially tailored by a dark spot imaged onto the center of the trap. The diameter of the dark spot image, and hence the size of the high density cloud, is 10 mm. We typically collect $\sim 10^{10}$ ^{23}Na atoms in the dark-SPOT, in about 4 s, at peak density of $> 10^{11} \text{ cm}^{-3}$.

Typical temperature in our ^{23}Na MOT is ~ 1 mK. Two-level theory of Doppler cooling predicts a cooling limit of $k_B T_D = (1/2)\hbar\Gamma = 240 \mu\text{K}$ for ^{23}Na , and $140 \mu\text{K}$ for ^6Li . However, this temperature is (theoretically) achieved for a light detuning of $\delta = -\Gamma/2$. Such a small detuning leads to a small effective trap volume and is not compatible with maximizing the atom number. Historically, the dark-SPOT stage was followed by about 5 ms of polarization gradient cooling, which resulted in sub-Doppler temperatures of $\sim 100 \mu\text{K}$. We have since found this cooling stage unnecessary, and have omitted it from the experimental procedure.

One peculiarity of ^6Li is that the excited state hyperfine splitting is smaller than the $\Gamma = (2\pi) \times 6$ MHz natural linewidth (see Fig. 2-3). Different lines are thus unresolved, and we can treat ^6Li as essentially a three level system, with both ground states being coupled to the single excited state by light of any polarization.

One adverse consequence of the unresolved excited electronic state is that polarization gradient cooling methods are inefficient in ^6Li [49]. Another important consequence is that the repumping of atoms out of the lower hyperfine state is more demanding. Off-resonant excitations into the $F' < 5/2$ hyperfine state are quite likely, and the atoms “fall off” the cycling transition more easily. In order to keep rescuing them, the best results are obtained with about equal amounts of laser power in the cooling and repumping MOT beams. Further, Schreck *et al.*[18] have found that the MOT functions properly only if the repumping light is arranged in a six beam MOT configuration. This also means that setting up a dark-SPOT configuration for ^6Li would be technically more demanding than for ^{23}Na .

⁶Some repumping light might be scattered into the center of the trap by the atoms on the edge of the cloud

Since for the targeted lithium atom number in the MOT, $\sim 10^8$, density limitations do not play a role anyway [49], we have not attempted to do this.

2.4.4 ^6Li laser system

Outline of the System

The whole laser system for cooling and trapping of ^6Li is based on inexpensive low power diode lasers in a Master-Slave configuration. To avoid obscuring the main storyline, we summarize only the main points here. Appendix A is written up as a more comprehensive companion to this section.

There are four principal frequencies needed for the experiment:

1. MOT trapping light, detuned ~ 25 MHz to the red of the $F = 3/2 \rightarrow F' = 5/2$ cycling transition.
2. MOT repumping light, detuned ~ 25 MHz to the red of the $F = 1/2 \rightarrow F' = 3/2$ transition.
3. Slowing light, detuned ~ 1 GHz to the red of the $F = 3/2 \rightarrow F' = 5/2$ cycling transition.
4. Slower repumping light, detuned ~ 1 GHz to the red of the $F = 1/2 \rightarrow F' = 3/2$ transition.

Figure 2-4 summarizes the “topology” of our laser system. One laser is used as the master oscillator and is referenced to a ^6Li atomic line. Acousto-optic modulators (AOMs) are used to generate four beams with the frequencies needed for the experiment. Each of these beams is then amplified in a dedicated slave laser by injection locking. Outputs of the slave lasers have the spectral characteristics, tunability, and long term stability of the injection light, and the power of a free running laser diode, 30 – 50 mW. The total laser power in the system is thus 120 – 200 mW ⁷. To give a sense of scale, the dye laser system used for our ^{23}Na experiment puts out about 1.6 W of power. Initial inspiration for our diode laser system came from the work done in the group of Rudi Grimm [49].

Frequency stabilized Master Laser

The starting point of our laser system is a TuiOptics DL100 grating stabilized diode laser. The grating setup is a Littrow configuration, based on a laser developed in the group of Ted Hänsch [50]. A 30 mW diode placed in this setup gives us an output of 12 – 15 mW with a laser linewidth of about 1 MHz (see Appendix A.1 for details).

Once the grating feedback, temperature, and the current of the laser are optimized for the desired wavelength, frequency can be electronically scanned over up to 10 GHz without a mode hop. This is achieved by applying voltage to the piezoelectric transducer mounted

⁷Typical lifetime of a diode is on the order of few months, and the total power output of our laser system fluctuates with the fluctuating market for 671 nm diodes.

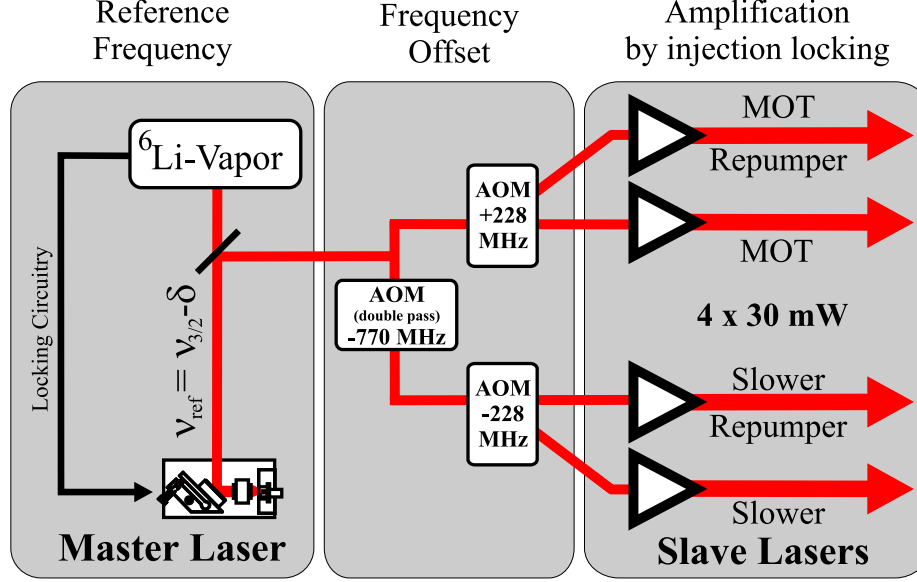


Figure 2-4: Topology of the ^6Li laser system. (1) The master laser is locked to the ^6Li D_2 resonance. (2) Three AOMs generate the four frequencies needed for slowing and magneto-optical trapping. Vertical ordering indicates the relative ordering of frequencies. (3) This light is then amplified by injection locking of four slave lasers.

at the back of the grating. We found the slow drift of the laser frequency to be about 500 kHz/s. This is in fact enough to obtain a MOT, stable over several seconds. For long term stability, the master laser is locked to the atomic resonance of a ^6Li vapor. The details of the locking method, setup, and results are explained in Appendix A.2. Briefly, we use Doppler free optical pumping (saturated absorption) spectroscopy, and lock to the crossover feature, 114 MHz to the blue of the cycling transition. We achieve long term frequency stability of about 1 MHz.

Generation of frequencies

Master laser light is split into two beams using a polarizing beam splitter cube. The splitting ratio is about 80/20%. The stronger beam is shifted to the red by about 770 MHz in a double pass AOM with total efficiency of 25%. The (first pass) zeroth order of the AOM is used for locking the master, and for monitoring its spectral characteristics with a wavemeter and a Fabry-Perot spectrum analyzer.

The two beams, now carrying about equal laser powers, define the MOT and the slower manifolds. Each of them is further split into two, using 228 MHz AOMs working at 50% efficiency. Both orders of the AOMs are used, and the four beams then define our four principal frequencies, each carrying about 1 mW of power.

Injection locked Slave Lasers

Once light at the four primary frequencies is generated, each of them is amplified in a dedicated slave laser diode by injection locking, or seeding (see Appendix A.1). With 1 mW of seeding power, a 30 – 50 mW slave laser can be injection locked up to 3 nm away from its free running wavelength.

For our slave lasers, we use commercial ThorLabs diode mounts and temperature and current controllers. Single stage optical isolators used for protecting the diodes from unwanted feedback are purchased from Optics for Research, and provide about 40 dB isolation.

Small fractions of all four slave outputs are multiplexed into a single beam using beam splitter cubes, so that the seeding can be constantly monitored with a single Fabry-Perot spectrum analyzer. A typical spectrum is shown in Fig. 2-5.

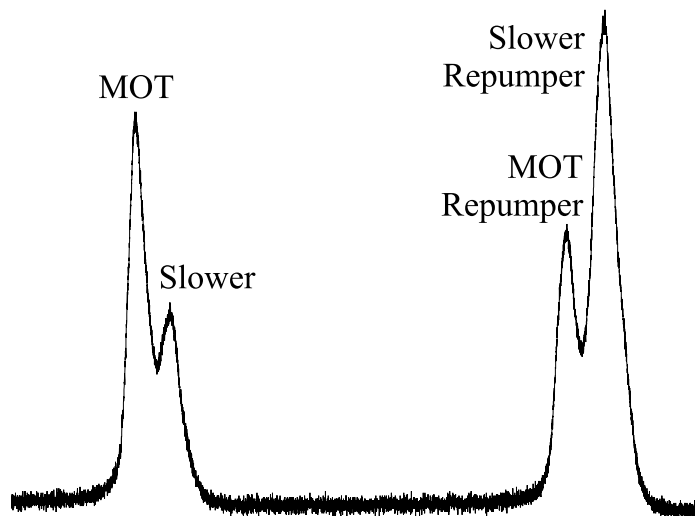


Figure 2-5: Frequencies of the four seeded slave lasers recorded by a Fabry-Perot spectrum analyzer. The analyzer has a free spectral range of 1 GHz, and thus the MOT and the slower manifolds are aliased almost on top of each other. The apparent laser linewidth is limited to about 10 MHz by the resolution of the spectrum analyzer.

Imaging and optical pumping light

In addition to the four slowing and trapping frequencies, two independently tunable frequencies are needed for imaging the $F = 1/2$ and $F = 3/2$ ground state lithium atoms. The same light is used for optical pumping of atoms between the two hyperfine ground states. Since only sub mW powers are needed, the light is split off the MOT and MOT repumper slaves' outputs. The two imaging light beams are combined on a polarizing beam splitter cube with opposite linear polarizations and sent through a common “tandem AOM”, consisting of two AOMs shifting the light up by 200 MHz $+\delta$, and then down by 200 MHz

$-\delta$. The frequencies can thus be shifted by an arbitrary amount 2δ . The two AOMs are set up in such a way that changing the detuning δ has a minimal effect on the direction of the output beam (Fig. 2-6). One of the AOMs in the pair is also used for fast ($< \mu s$) externally controlled switching of the light. Polarization encoding of the frequencies allows us to separate the two imaging light beams after the tandem AOM, again using a polarizing beam splitter cube.

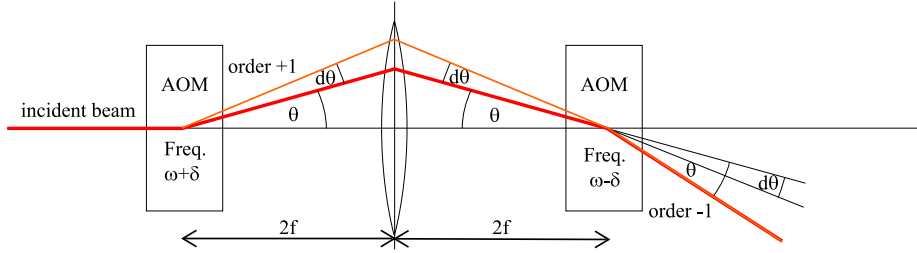


Figure 2-6: Tandem AOM for the ${}^6\text{Li}$ imaging light.

The complete setup of the lithium laser system is given in Appendix A.4.

Merging of the two laser systems

The laser systems for ${}^6\text{Li}$ and ${}^{23}\text{Na}$ are built on separate optical tables, and in separate rooms. All the different laser beams are separately brought to the experiment via optical fibers. The efficiency of light coupling into the fibers is 60 – 70%.

The two colors (for lithium and sodium) are merged on the experimental table using dichroic beam splitters, which are transparent for 589 nm and reflective for 671 nm light, or vice versa. However, due to relatively small difference in the two wavelengths, available dichroics are not perfect and a power loss of about 10% is unavoidable. Therefore, in places where the two overlapping beams (initially) have opposite polarizations, we combine them on polarizing beam splitter cubes.

After the two colors are overlapped, polarizations need to be manipulated simultaneously and identically for both wavelengths. To this end, we have replaced all half and quarter waveplates on the experiment with zero order waveplates designed for 633 nm.⁸ To illustrate the validity of this approach, we calculate the effect of such a quarter waveplate on linear polarization, aligned at 45° to the plate's axis. Projecting the result onto the “wanted” and “unwanted” circular polarizations, we find that the fraction of light power in the wrong polarization is $(\pi/4)^2(1 - 633 \text{ nm}/\lambda)^2$. Both for sodium and for lithium this is less than 1%. Results for the half waveplate depend on the desired angle of rotation, but are generally

⁸In general, a half (and likewise for quarter) waveplate has a retardation of $n + 1/2$ wavelengths. The order of the plate, n , is an arbitrary integer, usually around 10. Except for specific, commensurate values of n , such a plate can not be used for two different wavelengths since the error in retardation scales with the order of the plate.

comparable or better. Operation of the MOT is too robust for this to present a serious problem. Still, in order to have more tuning freedom, we also installed “full” waveplates for one of the wavelengths. These basically consist of two consecutive half waveplates, with their primary axes parallel. They are used to affect one wavelength without affecting the other one.

2.5 Two-species MOT for ^6Li and ^{23}Na

2.5.1 Single-species ^6Li MOT

After the optical fibers, the laser power available for each of the six lithium MOT beams is about 5 mW, both for cooling and for repumping. The beams are collimated to an $1/e^2$ diameter of about 1 cm. The powers in the slowing and slowing repumping laser beams are ~ 20 mW and ~ 5 mW respectively.

The loading of the MOT is monitored either by an absorption monitor (Figure 2-7), or simply by collecting the fluorescence of the MOT on a photodiode. Only in the development stages of the experiment, we performed some more quantitative analysis of the MOT by absorption imaging.

We can collect $\sim 2 \times 10^8$ ^6Li atoms in a single species MOT in about 10 s. Our oven will allow an increase of the atom flux by at least another factor of 4. However, at present we do not seem to be limited by the atom number. Our estimate of the peak MOT density is $\leq 10^{10} \text{ cm}^{-3}$. At this density, we do not expect that implementing a dark-SPOT would yield any benefits.

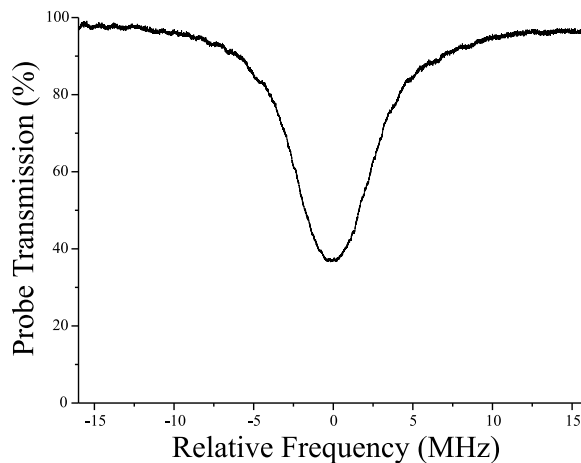


Figure 2-7: Absorption monitor of a ^6Li MOT. A weak probe beam is sent through the MOT, and its frequency is continuously scanned over the resonance for one of the two ground states. The transmission of the probe is recorded on a photo diode.

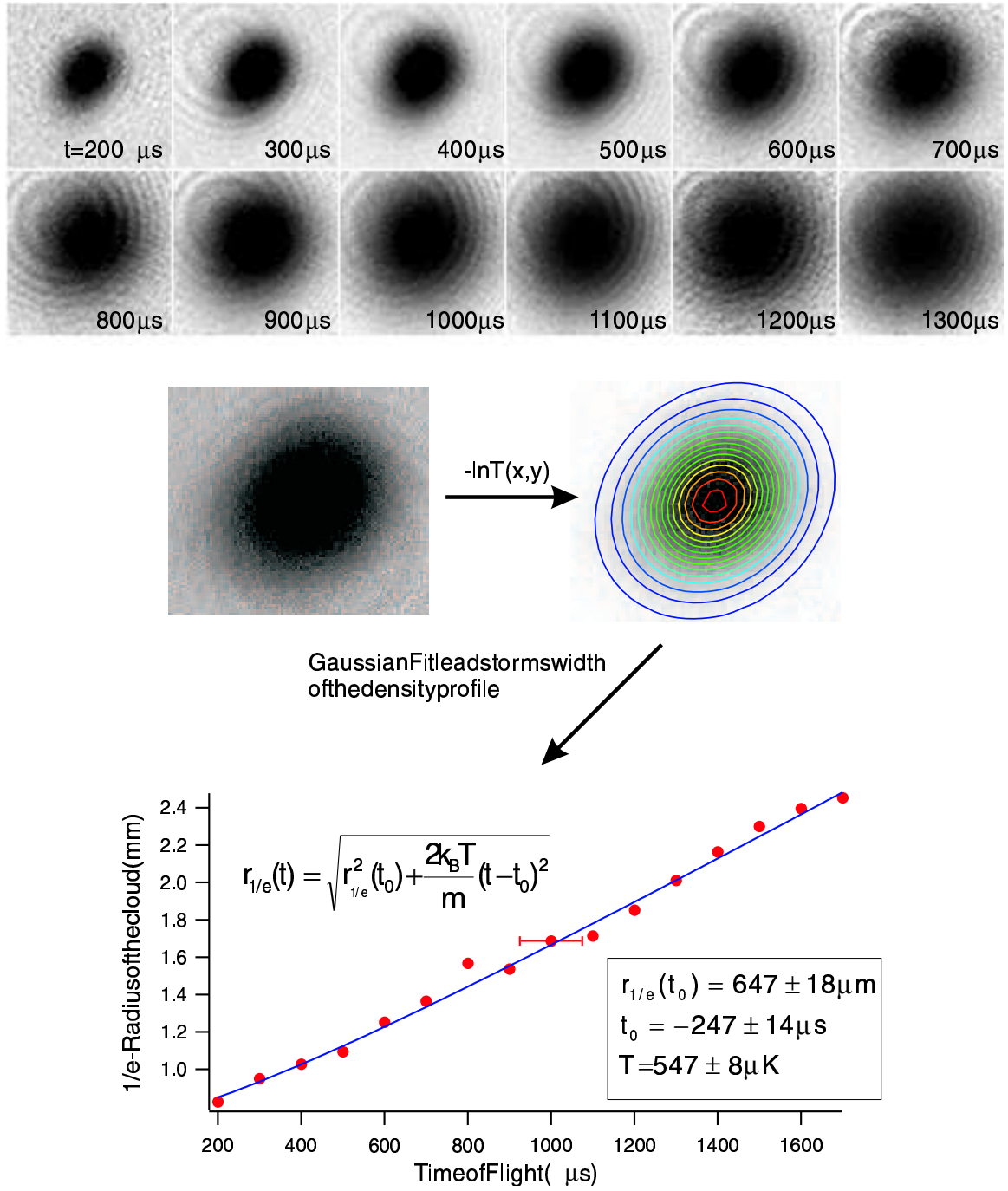


Figure 2-8: Measurement of the ^6Li MOT temperature. Absorption images were taken after a variable time of free expansion of the cloud, after the MOT light and magnetic field have been turned off. We also allow for an offset in the release time of the cloud.

Analysis of the MOT temperature from the free expansion of the cloud is shown in Figure 2-8. We have also studied the dependence of the MOT temperature with the detuning of the cooling light (Figure 2-9). The lowest temperature was achieved at $\delta = -2.5\Gamma$. However, the highest number of atoms was achieved at about $\delta = -4\Gamma$.

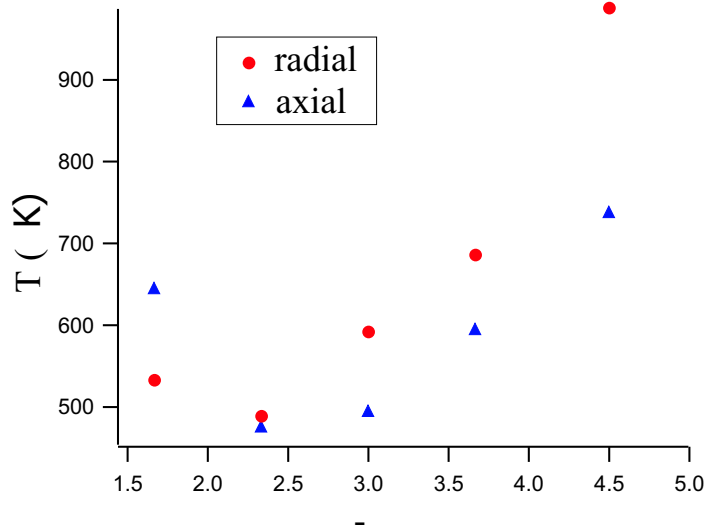


Figure 2-9: Dependence of the ^6Li MOT temperature on the detuning of the cooling light. Note that there is no good reason for the MOT temperature to be perfectly isotropic. Due to the separation of time scales for atomic collisions and laser cooling, atoms are primarily in thermal equilibrium with the laser beams, and not with each other.

2.5.2 Coexistence of the two MOTs

In loading ^6Li and ^{23}Na simultaneously into a two-species MOT, we encountered the first true unknown in our experiment - do they like each other? It turned out that they do not mind each other too much.

The main additional source of trap loss in a two-species MOT are light assisted collisions between ground and excited state atoms [51] (Figure 2-10). The small number of lithium atoms does not affect the sodium MOT, while our largest sodium MOT clouds reduce lithium atom number by not more than a factor of 4. The effect can be reduced if the two MOTs are deliberately displaced with respect to each other. This is easily achieved using the “full” waveplates for one of the species. Along one direction (horizontal in our experiments), the power in the two counter-propagating MOT laser beams is deliberately imbalanced in order to push the cloud away from the center of the quadrupole magnetic field. In our experiments, we displace the ^6Li MOT. The reason is that atoms from such an “off-balanced” MOT are not optimally transferred into the magnetic trap, and the cloud is likely to be heated during the transfer. Therefore, we prioritize the ^{23}Na temperature,

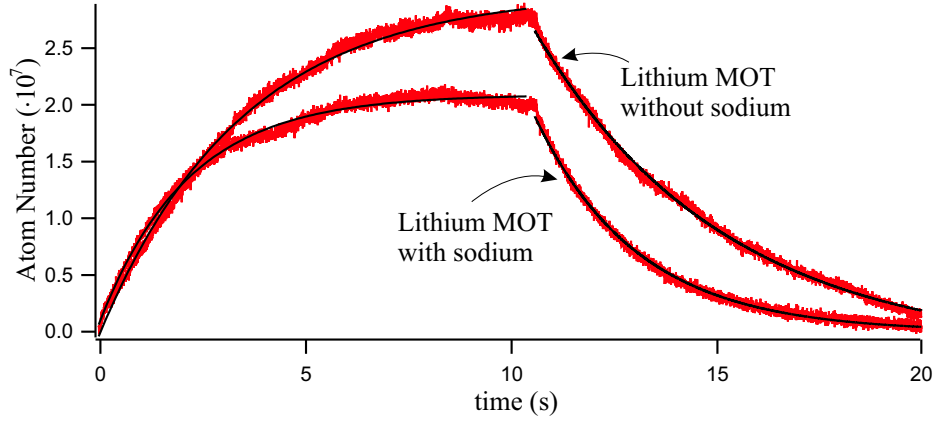


Figure 2-10: Inter-species light assisted collisions in a two-species MOT. Loading is monitored by collecting the fluorescence from the MOT on a photodiode. The absolute atom number was calibrated by comparison with absorption images. This particular data was taken using relatively small atom numbers of either species.

while the small ${}^6\text{Li}$ cloud thermalizes with sodium in the magnetic trap in any case. Note that these results hold for a “DC” two-species MOT. In the complete cooling cycle, further tricks can be played by varying the loading times of the two MOTs before transfer into the magnetic trap. We find that the characteristic timescale for loading of a well aligned sodium MOT can be shorter than the timescale for light-assisted losses in a displaced lithium MOT. By turning on the sodium light only during the last 2 s of lithium loading, we can have $\sim 10^8$ lithium atoms at the end of the MOT stage. This is already within a factor of ~ 2 of the maximum atom number in a DC single-species lithium MOT. Finally, note that the effect of light -assisted collisions could be minimized further if lithium was collected in a dark-SPOT. However, at this point, the potential benefits do not seem worth the effort.

Studying trap losses in two species MOTs is interesting in its own right (see [52] and references therein). However, this was not our primary area of interest, and for the most part we just concluded that the losses are perfectly acceptable, and moved on. Below I present a crude semi-quantitative study of the inter-species inelastic collision rate. In the limit of a small lithium cloud being immersed in a large and unaffected sodium cloud of approximately uniform density, we can write down a simple heuristic model for loading rate and final lithium atom number in the MOT:

$$\dot{N}_{Li} = L - \alpha N_{Li} - \beta n_{Na} N_{Li} \quad (2.12)$$

where L is the loading rate, α summarizes all the losses in a single species ${}^6\text{Li}$ MOT, and β characterizes the additional losses in the presence of a large ${}^{23}\text{Na}$ MOT. The loading of the MOT is then given by:

$$N_{Li} = \frac{L}{\alpha + \beta n_{Na}} \left(1 - e^{-(\alpha + \beta n_{Na})t} \right) \quad (2.13)$$

If the loading is interrupted, the atom number decays with the same time constant. An example of such loading and decay curve is given in Figure 2-10. We estimate $\alpha \sim 0.3 \text{ s}^{-1}$, and assume that in a temperature limited MOT α is independent of the loading rate. (In this experiment $L \sim 10^7 \text{ s}^{-1}$.) Since our largest sodium MOTs have a peak density of $\geq 10^{11} \text{ cm}^{-3}$ and reduce lithium atom number by not more than a factor of 4, we can estimate an upper bound on β of about $10^{-11} \text{ cm}^3/\text{s}$. This crude estimate agrees quite well with the more detailed study reported in [51].

2.6 Conclusion

Modifying our ^{23}Na BEC apparatus to the point where we could simultaneously collect $\sim 10^{10}$ sodium and $\sim 10^8$ lithium atoms in a two-species MOT completed the development phase of our experiment. These numbers were more than sufficient for the experiments on sympathetic cooling of ^6Li into quantum degeneracy, which are described in the following chapter. This is where real science began...

Chapter 3

Production of coexisting ^6Li Fermi seas and ^{23}Na BECs

This chapter describes the sympathetic cooling experiments in which we produce quantum degenerate ^6Li Fermi gases, and quantum degenerate Bose-Fermi mixtures of ^{23}Na and ^6Li gases. The experiments discussed here were reported in the following publications:

*Z. Hadzibabic, C. A. Stan, K. Dieckmann, S. Gupta, M. W. Zwierlein, A. Görlitz, and W. Ketterle, “Two-Species Mixture of Quantum Degenerate Bose and Fermi Gases,” Phys. Rev. Lett. **88**, 160401 (2002) [1].* Included in Appendix B.

Z. Hadzibabic, S. Gupta, C. A. Stan, C. H. Schunck, M. W. Zwierlein, K. Dieckmann, and W. Ketterle, “Fifty-fold improvement in the number of quantum degenerate fermionic atoms,” cond-mat/0306050 (2003) [2]. Included in Appendix C.

3.1 Choice of ^{23}Na and ^6Li hyperfine states for sympathetic cooling experiments

We perform evaporative (sympathetic) cooling of ^{23}Na (^6Li) atoms in a cylindrically symmetric Ioffe-Pritchard (IP) DC magnetic trap [47, 53] The coils of our trap are sketched in Fig. 3-1.

The first issue that arises in starting a magnetic trapping experiment is the choice of (ground) hyperfine states to be trapped. Magnetic trapping is achieved by creating a free space magnetic field configuration which has a minimum of the field strength. Choice of atomic states is thus restricted to “low field seeking” states, in which the magnetic moment of the atom is anti-aligned with the magnetic field, and the ground state energy increases with increasing field strength¹.

¹High field seeking states cannot be trapped, because we cannot create a magnetic field maximum in

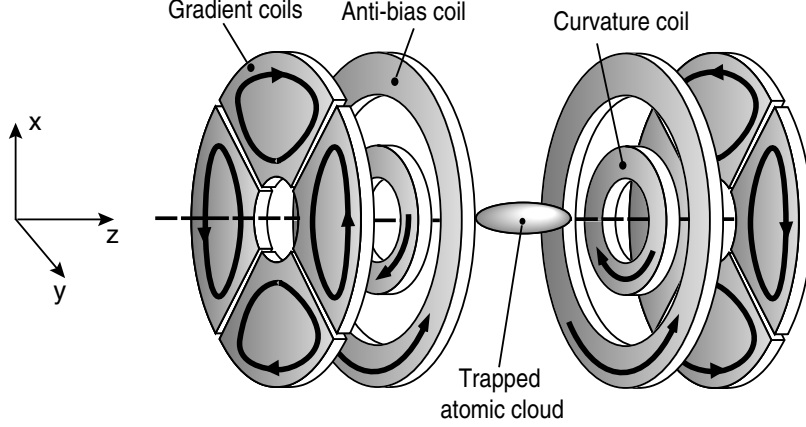


Figure 3-1: Ioffe-Pritchard magnetic trap coils. “Gradient coils” produce a two-dimensional quadrupole field in the radial plane. “Curvature” and “anti-bias” coils together produce a large curvature and a small offset “bias” field along the axial direction. Anti-bias coils are mounted in a Helmholtz configuration and produce a uniform field which opposes the field produced by the smaller curvature coils. This cancels most of the axial bias field, while leaving the axial curvature intact. In this way, high trapping frequencies can be achieved along both the axial and the radial direction. Technical details of our trap are described in the Diploma thesis of Christian Schunck [8].

Hyperfine ground states of ^{23}Na and ^6Li , as a function of the magnetic field, are shown in Fig. 3-2. If we ignore the small nuclear contribution, all of the atom’s magnetic moment comes from the one unpaired electron. At low magnetic field, the energy of an $|F, m_F\rangle$ state is:

$$E = g_F m_F \mu_B B \quad (3.1)$$

In the ground state of all alkali atoms, the g factor universally takes a simple form:

$$g_{F=I\pm 1/2} = \pm \frac{1}{(I + 1/2)} \quad (3.2)$$

and the states which are magnetically trappable are those in which $g_F m_F > 0$.

Since all of our work relies on being able to evaporatively cool sodium to BEC, let us start from there. We have three low field seeking states to choose from, $|F, m_F\rangle = |2, 2\rangle$, $|2, 1\rangle$, and $|1, -1\rangle$. State $|2, 0\rangle$ is only weakly magnetically trappable, due to the quadratic Zeeman shift. Mixtures of states are unstable against a variety of spin exchange collisional

free space. Using index notation ($i, j = 1, 2, 3$), a stationary point of the magnetic field strength is given by $\partial_i B^2 = 2B_j \partial_i B_j = 0$. At a local maximum, second derivatives in all directions are negative. However, the sum of second derivatives is $\partial_i^2 B^2 = 2(\partial_i B_j)^2 + 2B_j \partial_i^2 B_j = 2(\partial_i B_j)^2 \geq 0$. The second term in the last equation is zero because in free space we can describe the field by a scalar potential, $B_j = \partial_j \Omega$, and hence $\partial_i^2 B_j = \partial_i^2 \partial_j \Omega = \partial_j \partial_i^2 \Omega = \partial_j \partial_i B_i = \partial_j \vec{\nabla} \cdot \vec{B} = 0$. Since the sum of the second derivatives is positive, clearly they cannot be all negative.

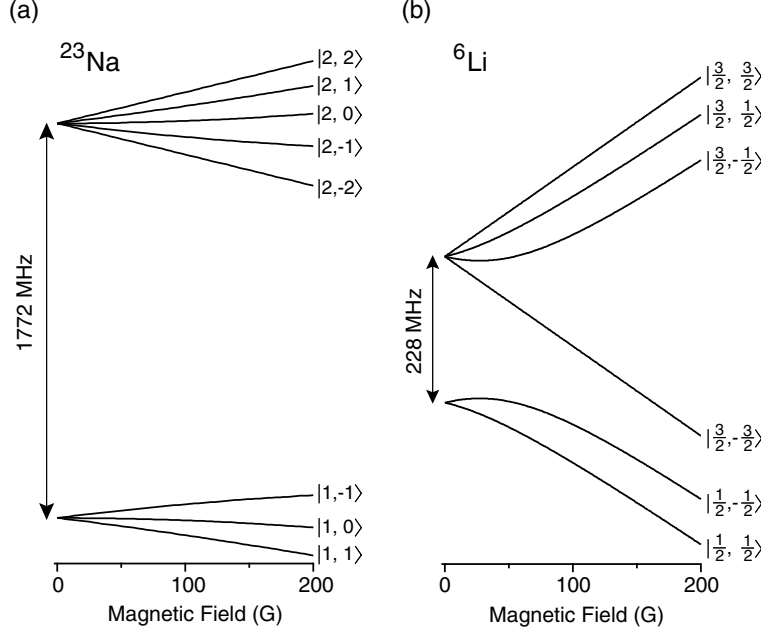


Figure 3-2: Hyperfine structures of ^{23}Na and ^6Li . The states are labelled in the low field, $|F, m_F\rangle$ basis. (a) Sodium is magnetically trappable in the $|1, -1\rangle$, and in the $|F = 2, m_F \geq 0\rangle$ states. Previously, sodium was evaporatively cooled to BEC only in the $|1, -1\rangle$, lower hyperfine state. (b) Due to finite trap depth of $\sim k_B \times 330 \mu\text{K}$ in the $|1/2, -1/2\rangle$ state, lithium can be efficiently loaded into the magnetic trap only in the upper, $F = 3/2$ hyperfine state.

processes, so we need to consider only single states. Pure $|2, 1\rangle$ is also unstable against spin exchange collisions², and hence not an option for evaporative cooling. This leaves us with only two options. Traditionally, we produced sodium BECs in the $|1, -1\rangle$ state. The only other state in which BECs could in principle be produced is $|2, 2\rangle$. However, condensation of sodium in the upper hyperfine state is considerably more difficult than in the lower one, and had not been previously achieved. As we will see in Section 3.3, this route was actually not completely blocked. However, we initially tried to avoid it.

Now let us look at ^6Li . The trappable states are $|3/2, 3/2\rangle$, $|3/2, 1/2\rangle$ and $|1/2, -1/2\rangle$. At temperatures below the p -wave threshold, any single state is stable, since the particles do not interact at all. However, any combination of these states will engage in drastic inelastic collisions³.

Taking into account the possible spin exchange collisions between sodium and lithium atoms, *i.e.* ensuring that the total projection of the spin is conserved in the collision, and that collisions which would require energies equal to the hyperfine splitting are energetically

²*e.g.* $|2, 1\rangle + |2, 1\rangle \rightarrow |2, 1\rangle + |1, 1\rangle + h \times 1.77 \text{ GHz}$ of released energy.

³The spin exchange rate coefficients in ^6Li are anomalously high, in the $10^{-9} \text{ cm}^3/\text{s}$ range [54]. The rate of spin flip collisions is given by the product of the rate coefficient and the gas density, and is independent of particle velocities.

forbidden, we arrive at a simple (and predictable) conclusion - the only two truly safe combinations of states are:

$$|1, -1\rangle + |1/2, -1/2\rangle$$

and

$$|2, 2\rangle + |3/2, 3/2\rangle$$

We initially favored the former.

However, for its many nice properties, ${}^6\text{Li}$ has one relatively serious problem, which is indicated in Fig. 3-2. So far, I did not give a quantitative meaning to the term “low magnetic field”. The characteristic magnetic field at which the $\vec{I} \cdot \vec{J}$ hyperfine interaction is decoupled, and Eq. 3.1 stops being valid, is set by the species dependent hyperfine constant. Due to a rather low hyperfine constant, in ${}^6\text{Li}$ this field is only a few tens of Gauss, and the quadratic Zeeman shift becomes important sooner than we would have liked. Most importantly, we see that the $|1/2, -1/2\rangle$ state is low field seeking only at very moderate field values. Since the external magnetic field couples $|1/2, -1/2\rangle$ only with $|3/2, -1/2\rangle$, the exact solution of this (Breit-Rabi [55]) problem involves simply diagonalizing a 2×2 matrix. This gives:

$$E_{|1/2, -1/2\rangle} = \text{const.} - \frac{1}{2}h\nu_{\text{hf}} \sqrt{1 - \frac{2}{3}x + x^2} \quad (3.3)$$

where $\nu_{\text{hf}} = 228$ MHz is the hyperfine splitting, and $x = 2\mu_B B / (h\nu_{\text{hf}})$. We see that the magnetic moment, $-\partial E / \partial B$, vanishes in this state at $x = 1/3$, or $B \approx 27$ G. The maximum magnetic trap depth for this state is then given by $E(x = 1/3) - E(x = 0) \approx k_B \times 330 \mu\text{K}$.

This presents a serious problem for magnetic trapping of ${}^6\text{Li}$ in this state. Both in our own, and in experience of others [18, 49], it is hard to cool lithium optically below about $300 \mu\text{K}$, even if the atom number is compromised. This means that most of the $|1/2, -1/2\rangle$ atoms “loaded” into the magnetic trap actually immediately spill out. Further, atoms are usually transferred from the MOT into an IP trap with a finite offset magnetic field, making the trap for the $|1/2, -1/2\rangle$ state shallower still. In practice, things can be even worse. For example, the magnetic trap and the MOT are not perfectly mode-matched, and the transfer leads to heating of the cloud. These concerns were supported by our experimental findings, and after some initial failed attempts, we gave up on trying to magnetically trap a significant number of laser-cooled ${}^6\text{Li}$ atoms in this state.

Now, allowing for slight oversimplification, the conclusions of our state analysis so far could be summarized as follows:

- (1) ${}^{23}\text{Na}$ can be evaporated to BEC only in the $F = 1$, lower hyperfine state.
- (2) ${}^6\text{Li}$ can be efficiently magnetically trapped only in the $F = 3/2$, upper hyperfine state.
- (3) A mixture of $F = 1$ sodium and $F = 3/2$ lithium atoms is not stable.

On the face of it, this does not look good. In order to cool ${}^6\text{Li}$ into quantum degeneracy, we had to alter at least one of our three conclusions. To this day, we still believe that Conclusion 2 stands firm. Section 3.2 describes how we produced our first quantum degenerate ${}^{23}\text{Na}$ - ${}^6\text{Li}$ mixtures, by at least quantitatively working around Conclusion 3. In Section 3.3, I will describe how we made Conclusion 1 completely obsolete. This allowed us to produce far superior degenerate Fermi samples, and Bose-Fermi mixtures, as described in Section 3.4.

3.2 Sympathetic cooling with sodium in the $F = 1$ state

Here I describe our first successful sympathetic cooling experiments, with sodium evaporated in the $F = 1$, lower hyperfine state. In this way, we produced a respectable degenerate Fermi gas, with $> 10^5$ atoms at a temperature of $0.5 T_F$ [1]. The degenerate ${}^6\text{Li}$ samples were produced in peaceful coexistence with ${}^{23}\text{Na}$ BECs of $\sim 2 \times 10^6$ atoms, with the lifetime of the degenerate mixture as long as 10 s. This was the first time that anyone had cooled a mixture of two different chemical elements into simultaneous quantum degeneracy.

However, these achievements have been completely overshadowed by our later cooling experiments (see Section 3.4 and publication [2]), and this cooling strategy is unlikely to ever be used again. Here I describe these infant steps for two reasons. The first one is historic (or nostalgic). The second reason is the lingering sense of wonder - I am still not convinced that these experiments were supposed to work. Some remaining confusions are discussed at the end of this section.

In the early days of our sympathetic cooling experiments, just about the only thing we were sure of was that we knew how to make large sodium condensates in the $F = 1$ state. Since the high heat capacity refrigerator for cooling of fermions was supposed to be the main strength of our experiment, we were reluctant to compromise it by moving sodium to the upper hyperfine state. Evaporation in the $F = 2$ state has been attempted in the past, both in our group and at NIST, and was found to be much more difficult than $F = 1$ evaporation. These efforts were abandoned without $F = 2$ condensates ever being produced.

Therefore, we decided to bet on the ${}^6\text{Li}$ sympathetic cooling strategy depicted in Fig. 3-3. While we did not expect the combination of $F = 1$ sodium and $F = 3/2$ lithium atoms to be stable against inelastic spin-exchange collisions at high densities and over long times, we hoped that this mixture might allow us enough time for at least some initial cooling. If we could cool lithium atoms in the upper hyperfine state down to at least $\sim 50 \mu\text{K}$, then we could transfer them into the $|1/2, -1/2\rangle$ state, thereby producing a stable ${}^{23}\text{Na}$ - ${}^6\text{Li}$ mixture. Cooling could then be safely continued.

At this point we knew absolutely nothing about the inter-species collisional properties of our mixture. However, while the rates for elastic and spin-exchange collisions are both

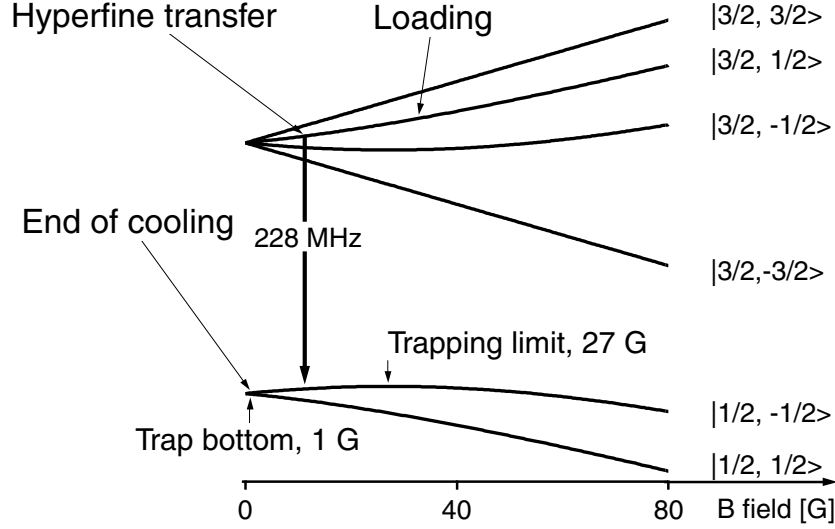


Figure 3-3: ${}^6\text{Li}$ cooling path. The atoms are loaded into the magnetic trap in the upper hyperfine state, at a temperature of $\sim 700\,\mu\text{K}$. After the initial cooling stage to $50\,\mu\text{K}$, the atoms are transferred into the $|1/2, -1/2\rangle$ state, and further cooled to a final temperature of $\sim 330\,\text{nK}$.

proportional to the gas density, the former is proportional to particle velocities, and the latter is velocity independent. Therefore, it seemed at least plausible that the elastic collisions dominate at high temperatures. It turned out that we were lucky enough with ${}^{23}\text{Na}$ - ${}^6\text{Li}$ collisional properties for this approach to work.

In these experiments, we collected about 2×10^7 lithium atoms or 6×10^9 sodium atoms in single-species MOTs. In a two-species MOT, lithium atom number was reduced by a factor of about 4^4 . The temperature of the lithium cloud was $\sim 700\,\mu\text{K}$.

After the MOT phase, we optically pumped lithium into the upper hyperfine state. At the time, we did only hyperfine (F) optical pumping, with a single laser beam resonant with the $F = 1/2$, lower hyperfine ground state. We did not attempt any Zeeman (m_F) pumping, for reasons I will touch upon below in Section 3.2.1. The transfer efficiency of lithium into the magnetic trap was (only) about 12%. Part of the reason for such inefficient transfer was that at the time, the MOT stage was still followed by 4 ms of polarization gradient “molasses” cooling of sodium. Molasses require a much more precise alignment and balancing of light beams than the MOT. We could never simultaneously achieve perfect enough alignment for both species, and the lithium light was always damaging to the transfer. To cut our losses, we simply turned off the lithium light, and let the lithium cloud

⁴These numbers are clearly at odds with our current two-species MOT described in Ch. 2. Everything was still sub-optimal in these early days. I hope that the system parameters I report today will appear as bafflingly sub-par a year or two from now.

into free expansion for 4 ms. This reduced the transfer efficiency by about a factor of 2. The transfer efficiency of sodium atoms into the magnetic trap was about 33%, without any optical pumping, since in the dark-SPOT most of the atoms are collected in the (three) $F = 1$ states. We have thus magnetically trapped $\sim 6 \times 10^5$ ^6Li and $\sim 2 \times 10^9$ ^{23}Na atoms.

At this point, we started the first cooling stage, trying to reach a temperature of $\sim 50 \mu\text{K}$ as quickly as possible. Being too conservative with the evaporation rate would cause unnecessary additional spin-exchange losses - once the system has thermalized, waiting around for the inelastic losses to kill it did not seem like a very good idea.

We evaporated sodium on the $|F, m_F\rangle = |1, -1\rangle \rightarrow |2, -2\rangle$ hyperfine transition near 1.77 GHz. In standard BEC experiments, sodium is evaporated on the $|1, -1\rangle \rightarrow |1, 0\rangle$ RF transition. However, using this transition for evaporation would also cause unwanted direct evaporation of lithium atoms. The 1.77 GHz microwave field is on the other hand completely invisible to ^6Li .

After 5 s of evaporation, the mixture was cooled to $\sim 50 \mu\text{K}$ ⁵, with only about half the lithium atoms lost. At this point, we found that a substantial fraction of lithium atoms was in the $|3/2, 1/2\rangle$ state, which was yet another stroke of luck. This allowed us to transfer lithium atoms to the $|1/2, -1/2\rangle$ state on a single-photon RF transition at 228 MHz, which is to first order independent of the magnetic field⁶.

However, not all $F = 3/2$ atoms were in the $|3/2, 1/2\rangle$ state, or at least not all were successfully transferred into the $|1/2, -1/2\rangle$ state. Consequently, spin-exchange collisions between lithium atoms in different hyperfine states led to a rapid loss of atoms from the trap. To avoid this, we followed the RF pulse with a light pulse resonant with the $F = 3/2$ state, which optically pumped the atoms into either $|1/2, -1/2\rangle$, or the untrapped $|1/2, 1/2\rangle$ state. In this way, the overall efficiency of our hyperfine transfer was $\sim 50\%$.

The evaporation was then resumed for another 10 s. We observed efficient sympathetic cooling of the $|1/2, -1/2\rangle$ atoms, and cooled both gases into quantum degeneracy without further observable losses in the lithium atom number.

Fig. 3-4 displays the effect of sympathetic cooling on the ^6Li cloud. The three absorption images of the trapped ^6Li gas were taken after the ^{23}Na evaporation was terminated at different trap depths. Cooling (from top to bottom) is seen in the shrinking of the density distribution, and an increase in the peak optical density. At this point, cooling is conservative in the lithium atom number.

In order to determine the temperature of the lithium clouds, we performed two-dimensional

⁵This temperature was determined from the sodium cloud. The density of the lithium cloud at this point was too low to provide enough signal-to-noise for direct temperature measurement. We took it on faith that lithium was also cooled. Our hopes were confirmed by efficient trapping upon transfer of lithium into the lower hyperfine state.

⁶A similar two-stage cooling and hyperfine transfer of ^6Li was previously used by the group of Christophe Salomon [18]. However, in their case ^6Li was sympathetically cooled with ^7Li , and in the first cooling stage both atoms were trapped in the upper hyperfine states ($|2, 2\rangle$ for ^7Li). In this case, all ^6Li atoms were in the $|3/2, 3/2\rangle$ state, and a two-photon transition had to be employed to transfer them into $|1/2, -1/2\rangle$.

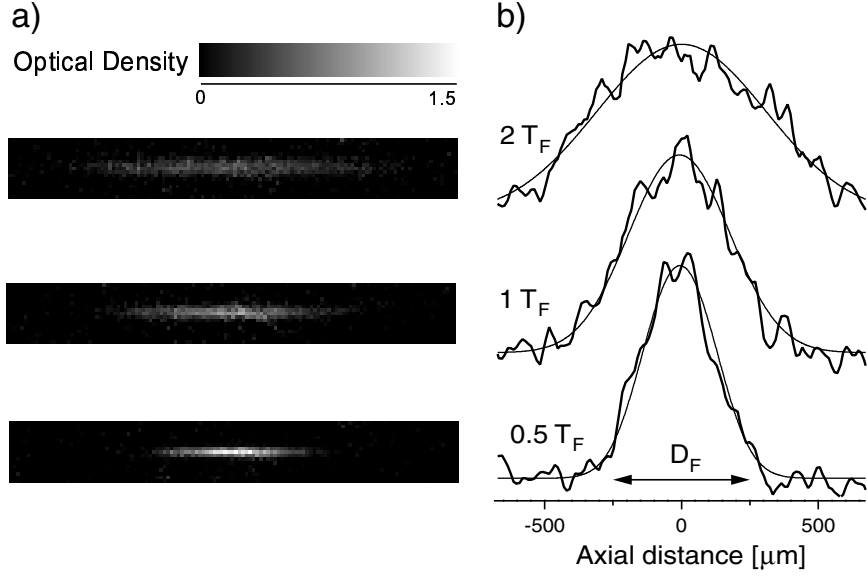


Figure 3-4: Onset of Fermi degeneracy. Three pairs of images (top to bottom) correspond to $T/T_F = 2, 1$, and 0.5 . (a) Column densities of the ${}^6\text{Li}$ cloud recorded by absorption imaging. (b) Axial line density profiles and the Fermi-Dirac fits to the data are plotted. The arrow indicates the size of the Fermi diameter, D_F .

fits to the cloud column densities using a semi-classical (Thomas-Fermi) distribution for trapped non-interacting fermions [56]. In this approach, the probability that an atom has position \vec{r} and momentum \vec{p} is obtained from the Fermi-Dirac distribution for the total (kinetic and potential) energy of the particle. The fitting function for the spatial distribution of atoms in the trap is then obtained by integrating out the momentum degrees of freedom. This approach is valid at all temperatures, as long as the number of particles in the system is large [56], and we do not need to take into account the exact form of the eigenstates of the harmonic trapping potential.

Fig. 3-4(b) shows projected line densities along the axial direction of the ${}^6\text{Li}$ cloud, and the Thomas-Fermi fits to the data. The arrow indicates the size of the axial real-space Fermi diameter

$$D_F = 2\sqrt{\frac{2k_B T_F}{m\omega_z^2}} \quad (3.4)$$

where ω_z is the axial trapping frequency and T_F is determined from the fitted atom number, $N_{\text{Li}} = 1.4 \times 10^5$. D_F represents the minimum size the cloud would assume at zero temperature.

Encouraged by the seemingly low rate for spin-exchange collisions between $F = 3/2$ lithium and $F = 1$ sodium atoms, we also tried to cool this mixture all the way to degeneracy. To our surprise even this worked, again leaving us with $> 10^5$ lithium atoms at $T \sim 0.5T_F$.

In this case all the surviving atoms were in the $|3/2, 1/2\rangle$ state.

3.2.1 Some remaining confusions...

We were very pleased with these results, but we never quite understood the population dynamics of different lithium m_F states in the magnetic trap. Before returning to the main story line, I briefly discuss some remaining puzzles.

During the loading phase we made no deliberate bias towards $|3/2, 3/2\rangle$ or $|3/2, 1/2\rangle$ state. Even the polarization of the optical pumping beam was not carefully controlled⁷. Initially, part of the reason for this was that we did not know which state we preferred. Later, the main reason for not studying this in detail was that the experiment seemed to work, and we had more important things to do, such as to rush and start studying interacting Fermi systems [3].

In the experience of Christophe Salomon’s group [57], and according to theoretical calculations [54], only one of the two states should have survived a fast (< 1 s) inelastic “clean-up”. In case of bosons, one can easily analyze possible spin-exchange collisions, and conclude that it is always the stretched state that survives. In the case of ^6Li , if we ignore for now the presence of sodium in the trap, the winner of the clean-up should simply be the state which is more populated to start off. So it could be either of the two, and the result would depend on the uncontrolled outcome of optical pumping. The high shot-to-shot and day-to-day reproducibility of our experiments does not support complete randomness.

Now, at the $50\,\mu\text{K}$ point, we discovered that the sample is sensitive to the RF frequency corresponding to the zero-field hyperfine splitting of $\sim 228\text{ MHz}$. Given the finite bias magnetic field of $B_0 \sim 1\text{ G}$ in our trap, this conclusively proved the presence of $|3/2, 1/2\rangle$ atoms in the sample. The fact that in this way we could not transfer all the atoms into the $|1/2, -1/2\rangle$ state indicates, but does not really prove that $|3/2, 3/2\rangle$ atoms were also present in the sample. If theorists tell us that presence of one state excludes the presence of the other one, we would have no hard proof to refute this.

On the other hand, if sympathetic cooling in the $F = 3/2$ state was continued for further 10 s, we were left with pure $|3/2, 1/2\rangle$ samples. At this point we could transfer all the atoms into the $|1/2, -1/2\rangle$ state. The $|3/2, 1/2\rangle \rightarrow |1/2, -1/2\rangle$ transition is (at least to first order) field independent and hence temperature insensitive. It is then hard to believe that the inefficiency of the same transfer at $50\,\mu\text{K}$ is purely technical.

Now let us add sodium into the picture. Given the much higher density of the sodium cloud, it is plausible that lithium spin-state dynamics are dominated by $^6\text{Li}\text{-}^{23}\text{Na}$ and not $^6\text{Li}\text{-}^6\text{Li}$ collisions. It then seems quite reasonable that the large sodium cloud in $|1, -1\rangle$ pumped the lithium atoms towards lower m_F values. However, if the sodium cloud actually drove the $|3/2, 3/2\rangle \rightarrow |3/2, 1/2\rangle$ transition, then it is not clear why it did not further

⁷By this I mean that the direction of the ambient magnetic field was not controlled.

convert $|3/2, 1/2\rangle \rightarrow |3/2, -1/2\rangle$ with similar efficiency, and expelled all lithium atoms from the trap.

While these puzzles intrigue me personally, it would be dishonest to say that they “will be the topic of further work”. We have since designed a far superior (and better understood) cooling strategy, and I doubt that anyone will ever go back to study these issues.

3.3 Condensation of ^{23}Na in the $F = 2$ hyperfine state

Immediately after producing our first degenerate Fermi clouds [1], we started our first studies of ^6Li in the strongly interacting regime [3]. However, it became increasingly obvious that our modestly sized samples would not offer a sufficient signal-to-noise ratio for a variety of standard techniques of BEC research, such as velocimetry using long expansion times or Bragg spectroscopy. We therefore felt that all future experiments would benefit in a qualitative way if we stepped back to improve our cooling methods and produce larger, and if possible colder, Fermi samples.

To this end, we decided to reexamine the possibility of the evaporative cooling of sodium in the $F = 2$, upper hyperfine state. Potential benefits for sympathetic cooling of ^6Li were obvious - if we magnetically trapped both species in their stretched states, we would create a mixture which is stable against spin-exchange collisions at all densities. This would bring us closer to the sympathetic cooling strategy promised in Section 2.2.

Condensation in the upper hyperfine state of sodium is more difficult than in the lower state for the following two reasons:

(1) Sodium atoms collected in the dark-SPOT are (essentially) all in the $F = 1$ state, distributed approximately evenly among the three m_F states. Efficient loading of the magnetic trap in the upper hyperfine state thus requires efficient optical pumping in a cloud with a density $\geq 10^{11} \text{ cm}^{-3}$. This is notoriously hard. In fact, the dark-SPOT was invented in order to create laser-cooled samples with optical density much larger than 1 [48]⁸.

(2) The experimentally measured three-body loss rate coefficient in the upper hyperfine state is $\sim 1.6 \times 10^{-29} \text{ cm}^3/\text{s}$ [58], about an order of magnitude higher than in the lower hyperfine state. This result was obtained by transferring optically trapped $F = 1$ BECs into the upper hyperfine state, and then studying them.

Neither of these reasons was however really prohibitive, as we will see below.

3.3.1 Magnetic trap loading

Our method for loading sodium into the magnetic trap in the $|2, 2\rangle$ state is sketched in Fig. 3-5.

⁸In $F = 1$ BEC experiments, $\sim 33\%$ of the atoms are transferred into the magnetic trap in the $|1, -1\rangle$ state, and we have traditionally been unsuccessful at increasing this transfer efficiency by optical Zeeman pumping.

After the dark-SPOT laser light and magnetic fields were turned off, a guide magnetic field of 3 G was applied, and the atoms were optically pumped for 2 ms, using σ^+ polarized light. The polarization gradient cooling stage was eliminated from the experimental procedure, in order to enhance the efficiency of lithium loading into the magnetic trap (See Section 3.2). We found that this did not have any adverse effects for sodium cooling.

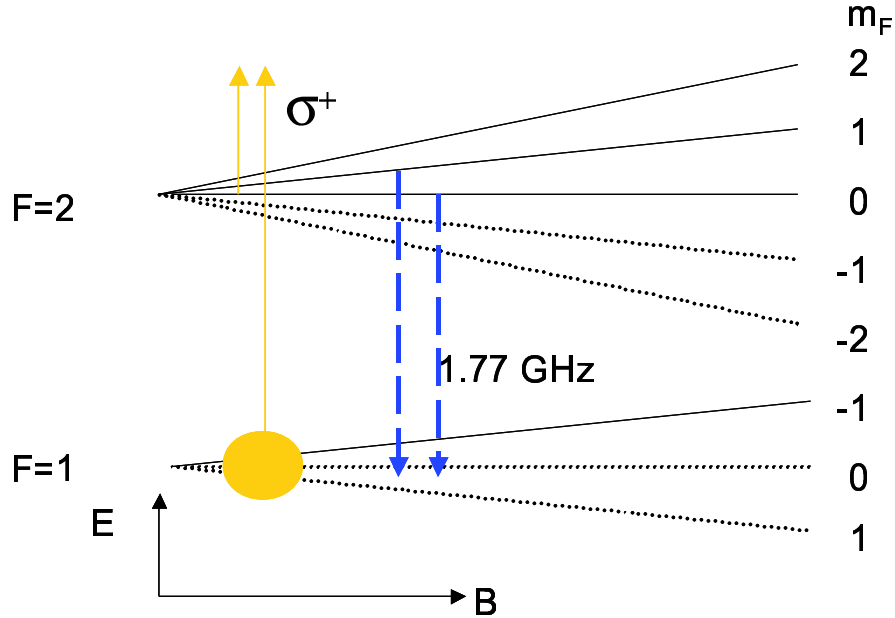


Figure 3-5: Loading of $|F = 2, m_F = 2\rangle$ sodium atoms into the magnetic trap from a dark-SPOT. Full lines: atoms are optically pumped from the $F = 1$ ground state using two σ^+ polarized light beams. Dashed lines: in the magnetic trap, the unwanted $|F = 2, m_F = 0, 1\rangle$ atoms are transferred into the untrapped $|F = 1, m_F = 0, 1\rangle$ states in order to prevent inelastic spin-exchange collisions with the $|2, 2\rangle$ atoms.

To achieve both F (hyperfine) and m_F (Zeeman) pumping, two light beams were used, resonant with the $F = 1$ and $F = 2$ ground states. Frequencies of the two pumping beams were optimized empirically, and the highest fraction of atoms we could pump into the $|2, +2\rangle$ state was about 30 %.

In optimizing the optical pumping frequencies we found a little surprise. The magnetic trap loading was most efficient if both beams were resonant with $F' = F$ transitions (Fig. 3-6), where F' denotes the total spin of the excited state, as usual.

It makes perfect sense that the m_F -pumping “ $F = 2$ ” beam is kept resonant with the $F = 2 \rightarrow F' = 2$ transition. In this way, $|2, 2\rangle$ is a dark state. If the cycling $F = 2 \rightarrow F' = 3$ transition was used, this would ensure that $F = 2$ atoms do not fall back into the $F = 1$ ground state, but it would also make $|2, 2\rangle$ atoms visible to the light, and would lead to unnecessary heating of the cloud.

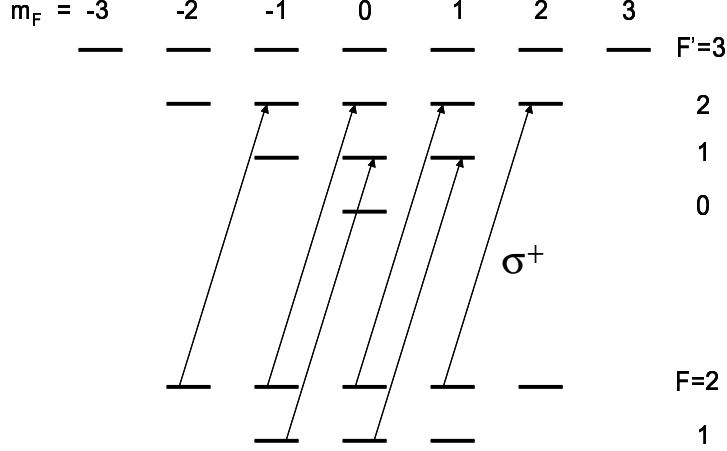


Figure 3-6: Frequencies for sodium optical pumping. Magnetic trapping was surprisingly most efficient if the $F = 1 \rightarrow F' = 1$ transition was used for hyperfine pumping. Zeeman pumping was (sensibly) done on the $F = 2 \rightarrow F' = 2$ transition.

However, keeping the hyperfine-pumping $F = 1$ beam resonant with the $F' = 1$ makes very limited sense, since this also makes $|1, 1\rangle$ a dark state. Of course, light polarizations are never perfect, and this state is not really dark. Still, for all $F = 1$ states, Clebsch-Gordan coefficients tell us that optical pumping into the $F = 2$ ground state would be more efficient if $F = 1 \rightarrow F' = 2$ transition was used, in disagreement with our observations.

After the optical pumping stage, the atoms were loaded into the IP magnetic trap with a radial gradient of 164 G/cm, and axial curvature of 185 G/cm². As I discussed earlier, sodium atoms in all three $|F = 2, m_F \geq 0\rangle$ states are (at least weakly) magnetically trap-pable (Fig. 3-2(b)), but only pure $|2, 2\rangle$ samples are stable against inelastic spin-exchange collisions. A crucial step in preparing the samples for efficient evaporation was to actively re-move $|F = 2, m_F = 0, 1\rangle$ atoms from the trap, before they engaged in inelastic collisions with the $|2, 2\rangle$ atoms. The atoms were loaded into a weak magnetic trap, with a high bias field of $B_0 = 80$ G. This field splits the $F = 2$ Zeeman sub-levels by $(1/2)\mu_B B_0 \sim k_B \times 2.8$ mK. Since this splitting was larger than the temperature of the cloud, the different states could be resolved in microwave spectroscopy, and the $|F = 2, m_F = 0, 1\rangle$ atoms could be selectively transferred to the untrapped $|F = 1, m_F = 0, 1\rangle$ lower hyperfine states (Fig. 3-5). This transfer was done with a microwave sweep near the ²³Na hyperfine splitting of 1.77 GHz. In this way, all the $|2, +2\rangle$ atoms initially loaded into trap could be preserved.

Further, we were able to “recycle” some of the untrapped atoms by optically pumping them out of the $F = 1$ ground states, and thus giving them a “second chance” to fall into the $|2, +2\rangle$ state. The final setup consisted of two microwave sweeps, the first of 0.8 s duration with the optical pumping light on, and the second of 2.4 s duration without the light. In this way, the overall transfer efficiency from the dark-SPOT to the magnetic trap

was improved to about 35 %, comparable to our standard $F = 1$ BEC experiments [47]. Starting with $\sim 10^{10}$ ^{23}Na atoms collected in the dark-SPOT, we loaded $> 3 \times 10^9$ $|2, 2\rangle$ atoms into the magnetic trap.

At this point, the magnetic trap was tightened by reducing the bias field to 3.8 G in 2.4 s. Resulting trapping frequencies were 204 Hz radially, and 34 Hz axially. This provided good conditions for forced runaway evaporation of sodium. Evaporation was done on the $|2, +2\rangle \rightarrow |1, +1\rangle$ microwave transition near 1.77 GHz. As in Section 3.2, the motivation for using microwave evaporation was to ensure that ^6Li is not evaporated in sympathetic cooling experiments.

3.3.2 Avoiding three-body losses

After 15 s of evaporation, the sodium atoms reached a temperature of $T \sim 10 \mu\text{K}$. Up to this point, we did not observe any significant three-body losses. This was verified by interrupting the evaporation, and observing that the lifetime of the cloud was still longer than 10 s.

However, if the evaporation was pushed further, three-body losses became significant. We could still condense sodium after further 15 s of evaporation, but the BEC was limited to $\leq 10^6$ atoms, and had a lifetime of only ~ 200 ms.

In order to eliminate the problem of three-body losses, at this point we reduced the cloud density by adiabatically reducing the trapping frequencies. The three-body loss rate is proportional to the square of the gas density, n^2 . Therefore, to increase the characteristic decay time of the cloud from a few hundred milliseconds to a few seconds, it is sufficient to decrease the density by a factor of 3 – 5. In a classical gas, during adiabatic decompression, density scales simply as the product of the inverse oscillator lengths in three dimensions, and so:

$$n_{\text{cl}} \propto \bar{\omega}^{3/2} \quad (3.5)$$

In a weakly interacting BEC, balancing the mean-field energy ($\propto n$), and the potential energy in the trapping potential ($\propto \bar{\omega}^2 n^{-2/3}$) gives:

$$n_{\text{BEC}} \propto \bar{\omega}^{6/5} \quad (3.6)$$

In either case, reducing $\bar{\omega}$ by a factor of about 3 suffices. We reduced the trapping frequencies to 49 Hz radially, and 18 Hz axially. After this adiabatic decompression of the cloud and 15 s of further evaporation, we could produce almost pure $|2, 2\rangle$ BECs containing up to 10 million atoms. The lifetime of the BEC in the weak trap was longer than 3 s.

3.4 Sympathetic cooling with sodium in the $F = 2$ state

Once we established evaporation of sodium in the $F = 2$ state, the benefits for sympathetic cooling of lithium were immediate and dramatic.

3.4.1 Boost in the ${}^6\text{Li}$ atom number

As described in Ch. 2, we collected $\sim 10^{10}$ ${}^{23}\text{Na}$ and $\sim 10^8$ ${}^6\text{Li}$ atoms in a two-species MOT. After the MOT stage, during the 2 ms of optical pumping for sodium, we also optically pumped ${}^6\text{Li}$ into the stretched $|3/2, 3/2\rangle$ state. Again, two σ^+ polarized laser beams were used, resonant with the $F = 1/2$ and $3/2$ ground states. In case of ${}^6\text{Li}$, the excited state is not resolved, so the discussion of dark states during the optical pumping does not arise. Due to the small optical density of the ${}^6\text{Li}$ cloud coming out of a bright MOT, most of the atoms could be pumped into the stretched state.

This was pretty much all we had to do. At this point we simply evaporated sodium the same way as in Section 3.3, and observed essentially ideal sympathetic cooling of lithium. During the typical 30 s of evaporative/sympathetic cooling, we observed no significant inelastic loss of lithium atoms. Here, the residual losses could arise from three-body collisions or dipolar relaxation, since spin-exchange collisions have been completely eliminated. However, in our case, the final number of degenerate ${}^6\text{Li}$ atoms was at least half of the number initially loaded into the trap. We did not study this in detail, but such a small loss rate is not inconsistent with the only loss process being the unavoidable collisions with the background gas in the vacuum chamber.

At the same time, we (again) observed a favorable rate of elastic collisions between the two species. The inter-species thermalization time was “shorter than 1 s” [2]. This loose upper bound really means that, as long the number of sodium atoms was larger than the number of lithium atoms, at no time did we observe any lag in lithium temperature behind the sodium one.

At the end of evaporation, we still had up to $\sim 7 \times 10^7$ ${}^6\text{Li}$ atoms in the trap. Since our primary interest was cooling of fermions, we evaporated all sodium atoms in order to get lithium to the lowest possible temperatures. In this way, even in our largest ${}^6\text{Li}$ samples, we achieved temperatures below $0.5 T_F$.

This meant that a year after our first sympathetic cooling experiments, we produced ${}^6\text{Li}$ samples with 500 times more atoms, at about the same temperature (measured relative to T_F). The increase in atom number came from several sources, which I recapitulate here. The balance roughly works out, even though some of these estimates are somewhat provisional:

(1) By getting better at simultaneously aligning and balancing the MOT laser beams for the two species, we improved the number of atoms in the single-species ${}^6\text{Li}$ MOT by a factor of $\sim 5 - 10$.

(2) By learning how to minimize the light-assisted losses, we gained another factor of ~ 2 in the lithium atom number in the two-species MOT.

(3) Eliminating polarization gradient cooling of sodium from the experimental procedure increased the transfer efficiency of lithium atoms into the magnetic trap by a factor of ~ 2 .

(4) We further increased the transfer efficiency of lithium into the magnetic trap by a factor of $\sim 3 - 5$ by better optical pumping. In $F = 1$ sympathetic cooling strategy, optical pumping probably could not have been improved, since (it seems that) the non-stretched $|3/2, 1/2\rangle$ state was preferred for magnetic trapping.

(5) By eliminating spin-exchange losses and the imperfect hyperfine transfer of lithium atoms during the evaporative/sympathetic cooling, we gained another factor of $\sim 3 - 4$.

3.4.2 Trading-in the ^6Li atom number for deeper quantum degeneracy

At this point, we had achieved more than we hoped for in terms of increasing the size of our degenerate Fermi samples. However, we also wanted to reduce their temperature. With our new sympathetic cooling strategy, we had ^6Li atoms to spare, and suddenly became limited by the finite size of our ^{23}Na refrigerator.

In order to go deeper into quantum degeneracy, we deliberately reduced the number of ^6Li atoms, in order to increase the ratio of the heat capacity of our sodium refrigerator to the heat capacity of the lithium cloud. This tradeoff turned out to be very favorable. By reducing the lithium number only slightly, to $\sim 3 \times 10^7$, we could achieve temperatures in the range $0.05 - 0.2 T_F$. An example of our coldest Fermi samples is shown in Fig. 3-7.

As before, temperatures were extracted from absorption images of the clouds, using a semiclassical (Thomas-Fermi) fit to the Fermi-Dirac distribution [1, 56]. One difference is that in contrast to Section 3.2, the clouds were now imaged after ~ 10 ms of free expansion from the trap. The quoted temperature range reflects both the shot-to-shot and day-to-day reproducibility of our experiments, and the fact that the Fermi distribution is only weakly sensitive to the temperature in the ultra-degenerate limit.

Comparing Fig. 3-7 with Fig. 3-4 should make it rather obvious how much we improved our Fermi system since our early experiments, both in terms of the offered signal-to-noise for absorption imaging, and in terms of the level of quantum degeneracy. Our new ^6Li clouds had a high enough optical density for crisp absorption imaging even after ballistic expansion to a size larger than one millimeter (Fig. 3-7(a)). While in Fig. 3-4(b), the size of the coldest cloud is “comparable” to the axial Fermi diameter D_F [1], in Fig. 3-7(b) the two are virtually indistinguishable.

Note that after time t of free expansion from the trap, the (axial) Fermi diameter of the cloud is given by:

$$D_F(t) = D_F(0) \sqrt{1 + \omega_z^2 t^2} = 2 \sqrt{\frac{2k_B T_F}{m \omega_z^2}} (1 + \omega_z^2 t^2) = 2v_F t \sqrt{\frac{1 + \omega_z^2 t^2}{\omega_z^2 t^2}} \quad (3.7)$$

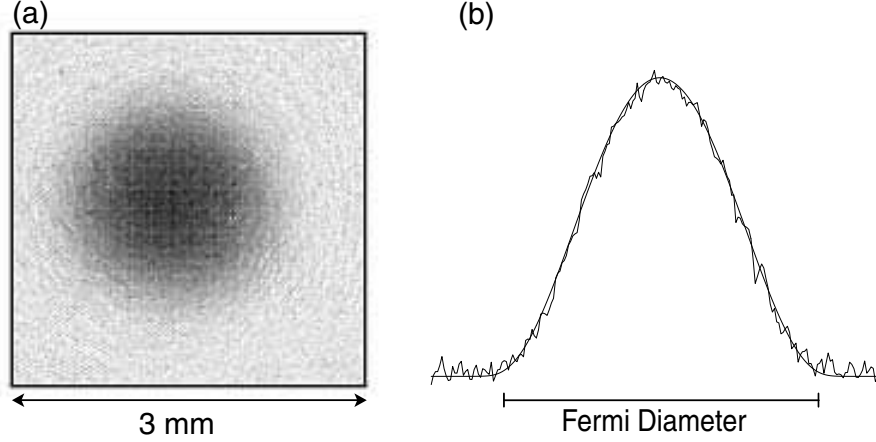


Figure 3-7: Large and ultra-degenerate Fermi sea. (a) Absorption image of 3×10^7 ^6Li atoms released from the trap and imaged after 12 ms of free expansion. (b) Axial (vertical) line density profile of the cloud in (a). A semiclassical fit (thin line) yields a temperature $T = 93 \text{ nK} = 0.05 T_F$. At this temperature, the high energy wings of the cloud do not extend visibly beyond the Fermi energy, indicated in the figure by the momentum-space Fermi diameter.

where $v_F = \sqrt{2k_B T_F / m}$ is the Fermi velocity. In absorption imaging, we always record the spatial extent of the cloud. However, for long expansion times, this becomes the direct measure of the momentum distribution.

3.4.3 Two-species degenerate mixture

In optimizing the sympathetic cooling of ^6Li we always evaporated sodium completely. Since large lithium clouds present a severe heat capacity “payload”, we could not simultaneously condense sodium and produce our best degenerate Fermi samples. However, we could make a reasonable compromise and produce a two-species quantum degenerate Bose-Fermi mixture with several million atoms of each species (Fig. 3-8). The mixture was stable, with a lifetime of several seconds.

In order to optimize the cooling strategy for either single- or two-species experiments, we implemented a dual-imaging technique, in which both ^6Li and ^{23}Na clouds were imaged onto the same CCD camera using separate light pulses. The times of free expansion of the two gases after the release from the magnetic trap could be varied independently.

3.5 Summary of sympathetic cooling experiments

There are two ^{23}Na and three ^6Li hyperfine ground states which are magnetically trappable and, at least on their own, stable against spin-exchange collisions. During our search for the ideal sympathetic cooling experiment, we have cooled all five of these states into quantum

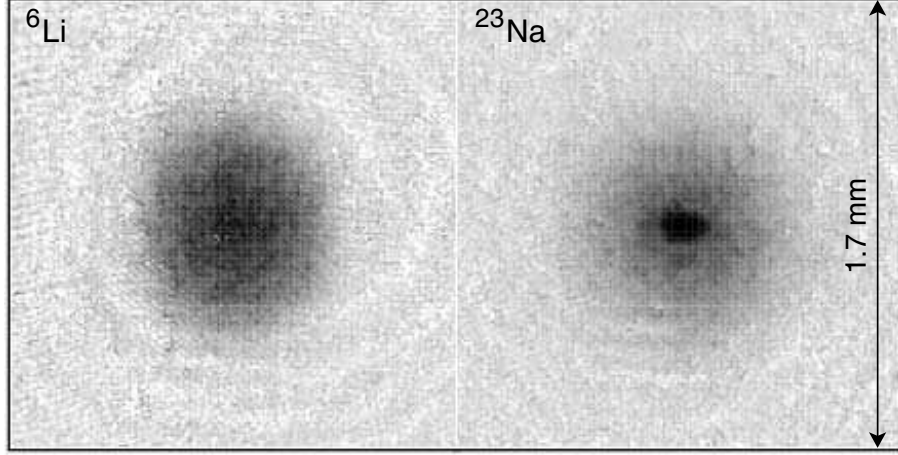


Figure 3-8: Two-species mixture of degenerate Bose and Fermi gases. For the displayed image, the expansion times were $t_{\text{Li}} = 8 \text{ ms}$ and $t_{\text{Na}} = 25 \text{ ms}$ and the atom numbers were $N_{\text{Li}} \sim 10^7$ and $N_{\text{Na}} \sim 6 \times 10^6$. Sodium was cooled below the condensation temperature, corresponding to $\sim 0.2 T_F$ for the lithium cloud. Condensation of sodium is seen in the characteristic anisotropic expansion of the BEC [10].

degeneracy.

While we have produced respectable degenerate Fermi samples in all three magnetically trappable lithium states, the $|3/2, 3/2\rangle$ state, cooled with sodium in the $|2, 2\rangle$ state, gave us by far the best results. In this state, we have now produced degenerate Fermi samples comparable in size with the largest alkali BECs [46].

In our coldest lithium samples we reached a temperature of $0.05 T_F$, currently the lowest ever achieved. At present, we would not know how to conclusively extract even lower temperatures. Hence, while I believe that lower temperatures will soon be reached by all experimental groups, we will also need to develop better fitting (or detection) methods in order to extract them.

In achieving all this, at no point did we have to perform any detailed studies of the collisions between ^{23}Na and ^6Li , either elastic or inelastic. To this day, the most accurate statement we can make about the inter-species collisions in our experiments is that they are favorable. Essentially everything we tried worked at least as well as we hoped. I cannot stress enough how fortunate this position is for a sympathetic cooler.

Chapter 4

Interactions in ${}^6\text{Li}$ spin mixtures

The true long term interest in degenerate Fermi gases lies in the studies of the strongly interacting spin mixtures. For most part, we will be interested in the simplest interacting Fermi system, involving two different spin states. The unique appeal of these systems stems from the fact that the strength of the interactions is widely tunable, as we will see in this chapter. A particular “Holy Grail” of this field is the attainment of novel regimes of fermionic superfluidity [31–42]. However, with the number of new theoretical proposals constantly growing, other interesting many-body states may be within reach.

As we will see in Ch. 5, production and studies of strongly interacting fermionic spin mixtures involves a whole new set of experimental tools. Despite these difficulties, we have recently witnessed a rapid progress in achieving and characterizing the strongly interacting regime in both ${}^{40}\text{K}$ [22, 24, 27, 29] and ${}^6\text{Li}$ [3, 5, 23, 25, 26, 28, 59]. Our own contributions to this research [3–5] will be described in Chs. 6 through 8.

In this chapter I briefly introduce the relevant theoretical background - the types of collisions occurring in the system, and the resonant control of interactions in the vicinity of Feshbach resonances. I conclude by briefly indicating why in these systems a superfluid transition may occur at surprisingly modest levels of degeneracy.

4.1 Language of collisions

Collisions in ultracold gases are discussed in a host of review papers [60, 61] and books [62–65]. Here I discuss some main concepts without mathematically rederiving any well known results.

4.1.1 Inelastic, elastic, and coherent collisions

We can distinguish three types of collisions in an atomic gas - inelastic, elastic, and coherent:

(1) Inelastic collisions involve a transfer of energy between internal and external degrees of freedom. Some examples of such collisions were mentioned in Ch. 3. In three-body

recombination, two atoms form a molecule, and share the released binding energy with a third one. In spin-exchange collisions, the change in Zeeman and/or the hyperfine energy of one or both particles is converted into kinetic energy. As a rule of thumb, the internal energy scale is much larger than the external one in ultracold gases. Products of inelastic collisions are therefore most commonly lost from the trap, even when they are in principle trappable. In rare cases when the released energy is still smaller than the trap depth, inelastic processes lead to the heating of the sample.

(2) Elastic collisions conserve the total kinetic energy and momentum of the two colliding particles, but can change the momenta of each particle. These collisions are responsible for establishing thermal equilibrium in the sample. In a two-state mixture of fermions below the p -wave threshold, the only interactions will be s -wave collisions between two atoms in different spin states.

(3) Coherent collisions are a subset of elastic collisions in which the incoming and the outgoing (two-particle) state are identical. These collisions do not change the momentum distribution in the sample, but they do contribute to the (many-body) ground state energy. In our case, the only allowed coherent collision process is forward scattering, with both particles preserving their momenta. The exchange interaction, in which the particles would interchange their momenta, is forbidden because the particles are distinguishable and the outgoing state would be different from the incoming one.

4.1.2 Elastic scattering amplitude

In the s -wave limit, two-body collisions at a finite energy are described by the scattering amplitude:

$$f = -\frac{a}{1 + ika} = -\frac{a}{1 + k^2 a^2}(1 - ika) \quad (4.1)$$

where a is the scattering length and $\hbar k$ is the relative momentum of the colliding particles. All the details of the scattering potential are encoded in the value of a . Positive/negative values of a correspond to repulsive/attractive interactions.

The total cross-section for elastic collisions is then given by:

$$\sigma = 4\pi|f|^2 = \frac{4\pi a^2}{1 + k^2 a^2} \quad (4.2)$$

4.1.3 Weakly interacting limit

In the weakly interacting limit, $ka \ll 1$, Eqs. 4.1 and 4.2 reduce to the more familiar expressions $f = -a$ and $\sigma = 4\pi a^2$. In this limit, the deBroglie wavelength of the particles is longer than a , so it seems reasonable that the detailed structure of the scattering potential is not important. Further, for fermions, the typical distance between particles in a gas must be even larger than the deBroglie wavelength. We can then safely, though with some

effort [60], model the interaction with an effective short range potential of the form:

$$V(\vec{r}) = \frac{4\pi\hbar^2 a}{m} \delta(\vec{r}) = U_0 \delta(\vec{r}) \quad (4.3)$$

This result also agrees with the Born approximation. Intuitively, if the scattering amplitude is (proportional to) the Fourier transform of the scattering potential, and it has no k dependence, then clearly the potential must be a δ function.

Now we can trivially see that the mean-field energy felt by a test particle moving through a sea of scatterers with density n is:

$$\frac{4\pi\hbar^2 a}{m} n \quad (4.4)$$

In analogy with the index of refraction, or the interaction self-energy of a particle, we intuitively expect that $\text{Re}(f)$ determines the change in the particle's energy, while $\text{Im}(f)$ determines its lifetime, or the total rate of scattering out of a state. The latter is formally expressed through the optical theorem:

$$\sigma = 4\pi|f|^2 = \frac{4\pi\text{Im}(f)}{k} \quad (4.5)$$

Therefore, even in this limit, we should formally preserve the small imaginary part of $f = -a(1 - ika)$.

In our language, $\text{Re}(f)$ describes the coherent collisions and the mean-field, while $\text{Im}(f)$ describes all the other, velocity changing, elastic collisions. Therefore, $\text{Re}(f)$ controls the ground state properties of a many-body system, while $\text{Im}(f)$ controls the dynamic properties such as the thermalization rate.

4.1.4 Strongly interacting limit

As we will see in Section 4.2, a sensitively depends on the details of the interatomic potential and can be orders of magnitude larger than the range of the potential R . Therefore, even in the “low energy” s -wave limit, given by $kR \ll 1$, it is still possible that $k|a| \gg 1$. In this limit, scattering is still isotropic, but it does depend on the energy of colliding particles.

For $k|a| \rightarrow \infty$, the elastic cross-section approaches a “unitarity limited” value of:

$$\sigma = \frac{4\pi}{k^2} \quad (4.6)$$

More intriguingly, we see that for $k|a| \gg 1$:

$$\text{Re}(f) \rightarrow -\frac{1}{k^2 a} \quad (4.7)$$

actually decreases with increasing $|a|$.

In a degenerate Fermi gas, atoms will have a spread of relative momenta set by the Fermi momentum $\hbar k_F = \sqrt{2mk_B T_F}$. Therefore, obtaining both the total rate of elastic collisions and the total interaction energy will involve averaging over the momentum distribution [9, 26]. In this case, even for values of $|a|$ up to $\sim 10/k_F$, the average value of $\text{Re}(f)$ is comparable to $-\text{sgn}(a)1/k_F$. Similar considerations apply to a classical gas, with the relative momentum spread given by the temperature.

4.2 Feshbach resonances

One of the many flexibilities offered by dilute atomic gases is that the strength of inter-atomic interactions can be externally controlled. In the language of conventional condensed matter systems, this is somewhat analogous to having an experimental knob which controls the electron charge. In fact, the freedom offered to an atomic experimentalist is even greater, as we can change not only the strength of interactions, but also their nature - from repulsive to attractive. This tunability of interactions relies on the existence of so-called Feshbach resonances [66]. These scattering resonances occur if the total energy of two colliding atoms is shifted into degeneracy with a quasi-bound molecular state. This mechanism has been demonstrated in atomic Bose gases [67–70], and has been used to dramatically alter their properties [71–75]. In experiments with degenerate Fermi gases, the ability to control the inter-species interactions is a crucial component in the search for novel regimes of superfluidity [37, 40, 42].

In this section I outline the main features of resonant scattering in general, and Feshbach resonances in particular.

4.2.1 Scattering resonances

In order to see how the scattering length can be strongly modified by small changes in the scattering potential, consider the exactly solvable toy model shown in Fig. 4-1. Here, two particles of equal mass m interact via a spherical box potential of depth V_0 and range R (Fig. 4-1(a)), and we assume that their kinetic energy in the center of mass frame is (close to) zero. Discrete bound (molecular) states of the potential are indicated by dashed lines. Fig. 4-1(b) shows the corresponding scattering length as a function of the potential depth V_0 [60]:

$$a = R - \frac{\tan(k_0 R)}{k_0} \quad (4.8)$$

where $k_0 = \sqrt{mV_0}/\hbar$. We see that for most values of $k_0 R$ (larger than $\sim 2^1$), the scattering length is roughly constant and has a typical “background” value of $a \sim R$. In alkali atoms,

¹Real interatomic (molecular) potentials have many bound states, so we need not be concerned with the low $k_0 R$ values.

this is typically a few nanometers.

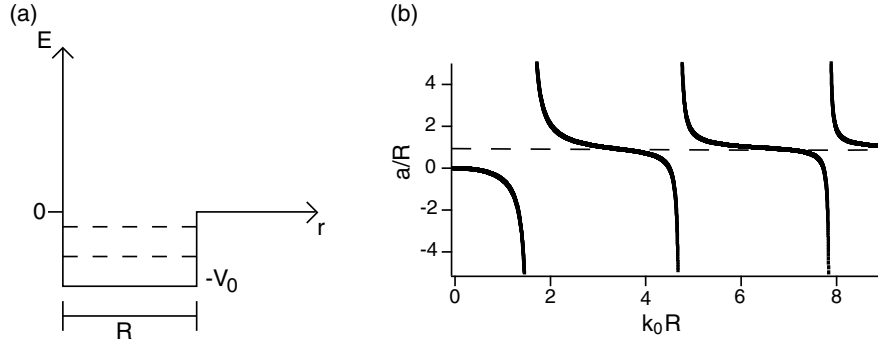


Figure 4-1: Cartoon of scattering resonances. (a) A model scattering box potential of depth $V_0 = \hbar k_0^2/m$ and range R . (b) The corresponding scattering length as a function of $k_0 R$. Away from the discrete resonances, the dashed line reasonably approximates the plateaus at $a \approx R$.

However, we also see a number of discrete resonances at $k_0 R = (2n + 1)\pi/2$, where n is an integer. Each of these resonances exactly corresponds to an appearance of a new bound state in the scattering potential. We can also see the general “topology” of a resonance - a weakly bound state corresponds to a diverging positive a , while a virtual “about to be bound” state gives a diverging negative a .

To bring our discussion closer to reality, now consider the more realistic interatomic van der Waals potential shown in Fig. 4-2. Here I include the centrifugal barrier for partial waves with angular momentum $l > 0$. We will eventually be interested in s -wave scattering, but this slight dishonesty will ease the intuitive introduction of some resonance concepts. The same qualitative analysis as for Fig. 4-1 applies here, and we can also make a few further remarks:

(1) Now we also have “bound” states of the potential with positive energies, giving rise to scattering resonances at finite kinetic energy. These states however are not truly bound, but have a finite lifetime given by the tunnelling rate through the potential barrier.

(2) Neglecting the interaction with the further detuned bound states, we know from standard second order perturbation theory that the virtual scattering leads to “repulsion” of the incoming state and the closest bound state. This immediately reproduces our mathematical observation that a weakly bound state leads to repulsive interaction ($a > 0$), and the reverse holds for a bound state slightly above the incoming energy.

(3) Exactly on resonance, non-degenerate perturbation theory breaks down. The proper eigenstates of the system are then the symmetric and the anti-symmetric superposition of the incoming and the bound state. The interaction splits these two states symmetrically. Waving our hands, we can then argue that the incoming/outgoing state contains equal parts of these two states, and hence does not experience any energy shift. This can intuitively

explain why very close to resonance, while a diverges², $\text{Re}(f) \rightarrow 0$ (Eq. 4.7). We also recover our analogy with the optical index of refraction, whose real part vanishes exactly on resonance.

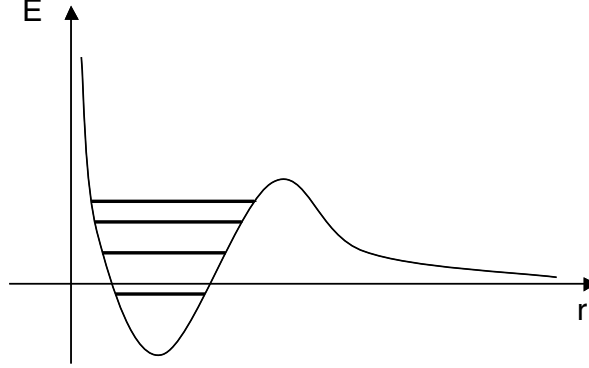


Figure 4-2: Shape scattering resonance. Scattering is resonantly enhanced whenever the incoming energy coincides with the energy of a (quasi-)bound state. This mechanism occurs for partial waves with $l > 0$.

This type of scattering resonance is known as the “shape” resonance, since it depends on the shape of the scattering potential and (crudely) occurs when the deBroglie wavelength of the incoming particle is commensurate with the range of the potential. Such a resonance for p -wave scattering in ^{40}K was observed by DeMarco *et al.* [76].

4.2.2 Tuning the scattering length with a magnetic field

Figure 4-3 indicates how scattering resonances can also occur for s -wave scattering, and how they can be reached by applying an external magnetic field. This effect is known as the Feshbach resonance [65, 66].

So far, I have discussed collisions between two particles ignoring their internal degrees of freedom. The molecular potential curves, such as shown in Fig. 4-2, actually depend on the spin configurations of the colliding particles. S -wave Feshbach resonances are mediated by coupling between two different spin configurations, or collision “channels”. In Fig. 4-3, molecular potential curves are sketched for two different (two-particle) spin configurations. The atomic sample is prepared in the lower energy, “open” channel. The energy difference between the two curves is set by some internal energy scale, and as such it is usually much larger than the typical external energies in an ultracold gas. This is why the higher energy spin channel is “closed”.

A Feshbach resonance occurs if the energy in the open channel coincides with one of the bound states of the closed channel. The coupling between the two channels takes place at intermediate distances of order R . Generally, the molecular states ($r \ll R$) and the free

²This is also not strictly true, if we introduce the finite width of the bound state.

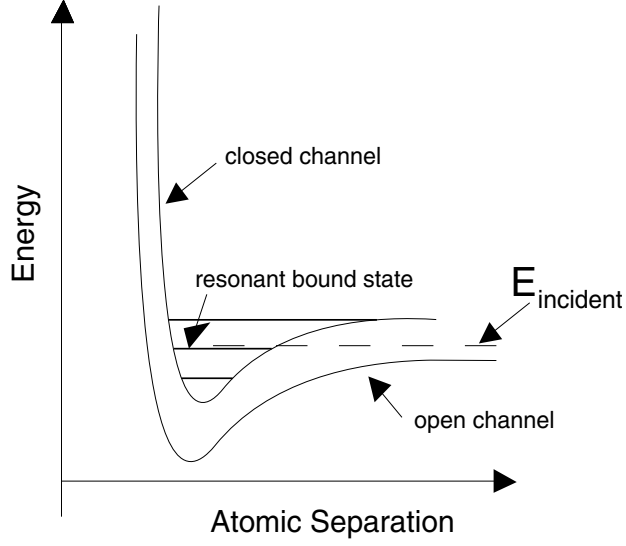


Figure 4-3: Feshbach resonance. Tunability of the scattering length by magnetic field.

particle states ($r \gg R$), have different good (magnetic) quantum numbers. In the cross-over region, $r \sim R$, the decoupled channels drawn in Fig. 4-3 do not represent an exact diagonalization of the total hamiltonian. This channel-coupling interaction here takes the role which the tunnelling had for a shape resonance.

The beauty of the Feshbach resonances is that, since the two channels correspond to different internal atomic (or molecular) states, they respond differently to externally applied electro-magnetic fields. Specifically, if the two channels have different total magnetic moments, we can tune their relative energies simply by applying an external magnetic field. The energy distance to the closest bound state is then given by:

$$E - E_0 = \Delta\mu(B - B_0) \quad (4.9)$$

where $\Delta\mu$ is the difference between the magnetic moments for the closed and the open channel, and E_0 and B_0 are the energy, and the magnetic field position of the resonance.

In the vicinity of the resonance, we can assume that only the distance to the closest bound state varies appreciably, while the contributions to a from the distant states are energy independent. We then traditionally write the dependence of a on the magnetic field B as [65, 77]:

$$a = a_{\text{nr}} \left(1 + \frac{\Delta B}{B - B_0} \right) \quad (4.10)$$

where a_{nr} is the non-resonant, background contribution from the distant states. The mag-

netic field width of the resonance:

$$\Delta B \propto \frac{1}{a_{\text{nr}} \Delta \mu} \quad (4.11)$$

is defined as the range of fields around the resonance for which the resonant contribution to a dominates the background contribution.

Again, Eq. 4.10 can intuitively be understood as the result of non-degenerate second order perturbation theory.

4.2.3 Strongly interacting limit revisited

Near the resonance, we can ignore the background contribution to a in Eq. 4.10, and consider only the resonant form of the scattering length $a = a_{\text{nr}} \Delta B / (B - B_0)$. Substituting this form into Eq. 4.1, at finite k we obtain:

$$\begin{aligned} \text{Re}(f) &= -\frac{1}{a_{\text{nr}} k^2} \frac{B - B_0}{\Delta B} \frac{1}{1 + \left(\frac{B - B_0}{a_{\text{nr}} k \Delta B} \right)^2} \\ \sigma = \frac{4\pi \text{Im}(f)}{k} &= \frac{4\pi}{k^2} \frac{1}{1 + \left(\frac{B - B_0}{a_{\text{nr}} k \Delta B} \right)^2} \end{aligned} \quad (4.12)$$

These equations now indeed pleasingly resemble the dispersive (real) and absorptive (imaginary) parts of the optical index of refraction.

From an experimental point of view, we may also choose to redefine ΔB as the magnetic field range in which the gas characterized by a typical k (or k_F) is strongly interacting, $ka \geq 1$. This inequality holds for $|B - B_0| < \Delta B'$, with $\Delta B' = k a_{\text{nr}} \Delta B$. Equation 4.12 then simplifies to:

$$\begin{aligned} \text{Re}(f) &= -\frac{1}{k} \frac{B - B_0}{\Delta B'} \frac{1}{1 + \left(\frac{B - B_0}{\Delta B'} \right)^2} \\ \sigma = \frac{4\pi \text{Im}(f)}{k} &= \frac{4\pi}{k^2} \frac{1}{1 + \left(\frac{B - B_0}{\Delta B'} \right)^2} \end{aligned} \quad (4.13)$$

4.2.4 Adiabatic creation of diatomic molecules

Finally, note that an adiabatic (Landau-Zener) sweep of the magnetic field through the Feshbach resonance can be used to permanently transform an ultracold atomic gas into a gas of diatomic molecules. The sweep should be done from the “atomic” to the “molecular” side of the resonance, *i.e.* from the attractive ($a < 0$) to the repulsive ($a > 0$) side. This is a two-body process and does not involve any inelastic release of energy. The process is also reversible - an adiabatic sweep in the opposite direction will convert the molecules back into atoms.

Using this method, Regal and Jin [29] have recently created molecules from a ^{40}K Fermi gas. Diatomic ^6Li molecules have subsequently been created in the group of Christophe Salomon [30], and in our group (unpublished). In Bose atomic gases, the same method was applied to ^{87}Rb [78], ^{133}Cs (group of Rudi Grimm, unpublished) and ^{23}Na (our next door neighbors, unpublished).

4.3 High temperature superfluidity of ^6Li ?

As most papers concerning degenerate Fermi gases, and this thesis, keep reminding us, the Holy Grail of this field is the attainment of novel regimes of fermionic superfluidity. Here I very briefly outline why we, as the field, are hopeful that this transition may occur at temperatures which are already experimentally reachable.

In a conventional superconductor, electrons pair into spin singlets due to an effective attractive s -wave interaction, which is mediated by the exchange of phonons. The maximum phonon energy is given by the Debye temperature T_D , and hence the electron-electron interaction can be attractive only within $k_B T_D$ of the Fermi surface. The characteristic vibrational energies in a crystal, or a molecule, are $\sim \sqrt{m_e/m}$ times smaller than the electronic energies. Here, m_e and m are the electron and the atom (ion) mass, respectively. In a metal, the Fermi energy of the electrons is of the same order as a typical electronic energy in an atom or a ground-state molecule, a few eV ³. Therefore, we can estimate $T_D \sim \sqrt{m_e/m} T_F$. In the standard (Cooper) derivation of the superconducting gap parameter or pairing temperature, we assume that at energies up to $k_B T_D$, the effective electron-electron attraction is of constant strength V [20, 79]. The result for the superconducting critical temperature can then be written as:

$$T_c \sim \sqrt{\frac{m_e}{m}} T_F e^{-\frac{1}{N_0 V}} \quad (4.14)$$

where $N_0 = (m_e/2\pi^2\hbar^2)k_F$ is the density of states at the Fermi energy.

In ultracold Fermi gases, the most promising pairing mechanism is a direct, attractive s -wave interaction between atoms in two different spin states. In this case, the interaction is attractive at all energies up to E_F . In the weak-coupling regime, the strength of the attractive interaction is given by $(4\pi\hbar^2/m)a$, with $a < 0$. If we then blindly translate the Cooper result (Eq. 4.14) into atomic physics, we obtain:

$$T_c \sim T_F e^{-\frac{\pi}{2k_F|a|}} \quad (4.15)$$

We see two reasons for the potential enhancement of T_c/T_F . First, the prefactor in Eq. 4.15 is larger than in Eq. 4.14 by a factor $\sqrt{m/m_e} \sim 10^2$. This will be true even for

³All of these energies correspond to the localization to approximately one Bohr radius. This is the typical size of the lattice spacing in a crystal, the size of an atom, or the size of a molecule.

more complicated pairing mechanisms, as atomic systems have only one characteristic mass scale.

Second, the exponent in Eq. 4.15 is “widely tunable”. This statement should however be taken with a grain of salt, since it is not clear how the theory can be extended into the strong-coupling regime $k_F a \gg 1$. As we have already seen in this chapter, while a is widely tunable, we should certainly not hope for the properly calculated exponent of Eq. 4.15 to be smaller than unity, or even $\pi/2$. Nonetheless, we can see that it might be reasonable to hope for a transition on the $10^{-1} T_F$ scale.

Several authors have theoretically studied the superfluid transition in the strongly interacting regime, near a Feshbach resonance [37, 40, 42], and have concluded that the transition temperature may indeed be as high as $0.5 T_F$.

In this regime, a cross-over between a BCS state and a BEC of tightly bound diatomic molecules could also be studied [42].

Chapter 5

Experiments with ${}^6\text{Li}$ in the vicinity of Feshbach resonances

In this chapter I briefly introduce the experimental methods and the types of measurements we use for studying strongly interacting ${}^6\text{Li}$ spin mixtures. For a complementary discussion and further technical details, I also refer the reader to the (concurrently written) PhD thesis of Subhadeep Gupta [9].

5.1 Prediction of Feshbach resonance(s) in ${}^6\text{Li}$

In order to design a Feshbach resonance experiment and access its feasibility, we need to rely on theoretical predictions for magnetic field positions and widths of the resonances. Examples of experimentally relevant questions are:

- (1) Do resonances occur at magnetic fields which can be relatively easily generated in the lab?
- (2) What internal atomic (ground) states are involved and how can they be trapped at the relevant magnetic fields?
- (3) What are the widths of the resonances, and hence what level of magnetic field stability and spatial uniformity is required in order to resolve them?

Theoretical predictions of Feshbach resonances crucially depend on the details of the interatomic potentials, which are generally not well known. Such predictions are thus constantly evolving, as they get further constrained by new experimental results. However, even preliminary calculations are usually accurate enough to design an experiment.

At the time we started our experiments, we were guided by the calculations of Houbiers *et al.* [54] (Fig. 5-1). For the two lowest ground states of ${}^6\text{Li}$, a broad inter-state s -wave resonance was expected to occur in the vicinity of 800 G. At high magnetic fields, these two states correspond to $|m_J, m_I\rangle = |-1/2, 1\rangle$ (lowest state) and $|-1/2, 0\rangle$ (second to lowest). For simplicity, we shall label them $|1\rangle$ and $|2\rangle$ at all magnetic fields (Fig. 5-1(b)).

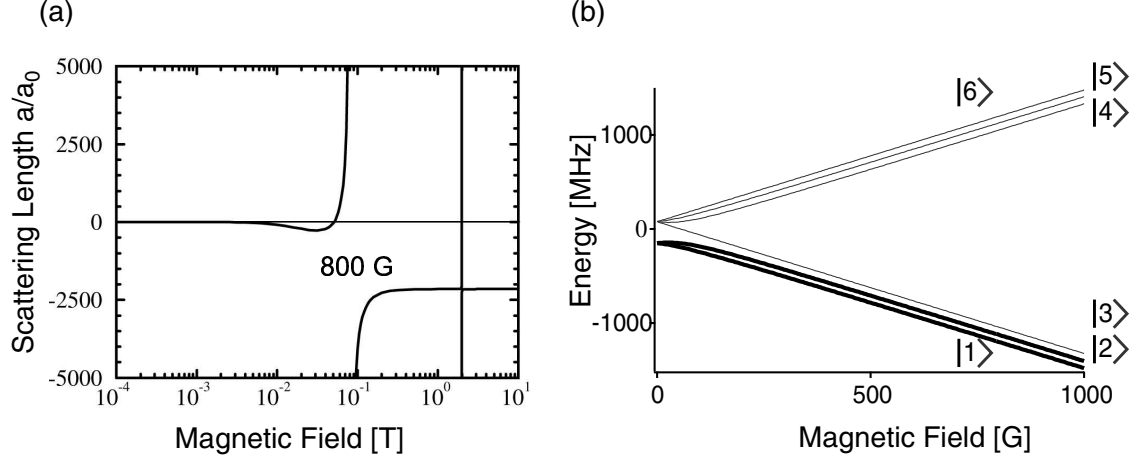


Figure 5-1: Predicted Feshbach resonance in ${}^6\text{Li}$. (a) For the two lowest hyperfine states of ${}^6\text{Li}$, $|1\rangle$ and $|2\rangle$, the inter-state s -wave scattering length a_{12} is predicted to have a broad resonance at ~ 800 G (taken from [54]). a_0 is the Bohr radius. (b) Electronic ground states of ${}^6\text{Li}$ in the relevant range of magnetic fields. Since the $\vec{I} \cdot \vec{J}$ hyperfine interaction is essentially completely decoupled by the external magnetic field, we see two m_I triples corresponding to $m_J = \pm 1/2$. The six states are labelled according to increasing energy.

Magnetic fields of ~ 800 G are relatively moderate, and the (unusually) large width of the resonance, of the order of 100 G, does not pose any stringent requirements for magnetic field stability.

Similar Feshbach resonances should occur for mixtures of any two $m_J = -1/2$ states. However, we intuitively expect that the combination of two lowest states is most stable against any inelastic processes [39]. This makes it particularly appealing for studies of strongly interacting Fermi systems, and possible observation of superfluidity.

5.2 Experimental methods

5.2.1 Generation of uniform high magnetic fields

Uniform magnetic fields up to ~ 1000 G can be generated by the anti-bias coils of our IP magnetic trap (Fig. 3-1). These coils generate a field of 2.06 G/A, and are powered by a commercial 500 A DC power supply.

We have recently built a new magnetic trap, taking extra care that the anti-bias coils are mounted in an almost perfect Helmholtz configuration [8]. This ensures that the applied magnetic fields are essentially uniform across the few millimeter long atomic clouds. Our estimate is that for the highest applied fields, the residual field curvature results in < 1 G field variation across the atomic sample.

5.2.2 Optical trapping

States $|1\rangle$ and $|2\rangle$ are both high field seeking at high magnetic fields (Fig. 5-1). A strongly interacting mixture of these two states can thus be studied only in an optical dipole trap (ODT) [80].

An optical dipole trapping potential is created by the negative AC Stark shift of the ground state energy in the presence of a red detuned laser beam [43]. Our ODT is formed by a focus of a single laser beam at 1064 nm, which is aligned with the axis of the magnetic trap. Since the detuning of the trapping laser is much larger than the energy difference between different ground states, all the states experience the same trapping potential.

The ODT light is produced by a commercial fiber-amplified Nd:YAG laser. The maximum laser power available for trapping is ~ 4 W, and the beam is focused to $1/e^2$ radius of $16\ \mu\text{m}$. For ^6Li ground states, this yields a maximum trap depth of $k_B \times \sim 600\ \mu\text{K}$, and maximum trapping frequencies of $\sim 18\ \text{kHz}$ radially, and $\sim 280\ \text{Hz}$ axially. This gives a Fermi temperature as function of lithium atom number equal to:

$$T_F \sim 400\ \text{nK} \times N^{1/3} \quad (5.1)$$

We usually operate our ODT at about $1/4$ of the maximum power, which corresponds to a trap depth lower by a factor of 4, and trapping frequencies and Fermi temperature lower by a factor of 2.

5.2.3 Preparation of interacting spin mixtures

Our degenerate Fermi samples are prepared in the magnetic trap in the state $|6\rangle$, equal to $|F = 3/2, m_F = 3/2\rangle$ at low magnetic field (see Ch. 3). At the end of the cooling cycle, all the ^{23}Na atoms are evaporated away, and the ^6Li atoms are transferred into the optical trap by adiabatically ramping up the ODT laser power, and then turning off the magnetic trap coils. We have not yet perfected this process, and the transfer is not perfectly adiabatic. After the transfer, our single-state Fermi samples are usually only moderately degenerate, with a typical temperature of $0.5 - 1\ T_F$.

After the transfer into the ODT, the cloud is transferred at (close to) zero magnetic field into the $|1\rangle$ state, equal to $|F = 1/2, m_F = 1/2\rangle$ at low fields. $|6\rangle \rightarrow |1\rangle$ is a single photon transition at $\sim 228\ \text{MHz}$. States $|6\rangle$ and $|2\rangle = |F = 1/2, m_F = -1/2\rangle$ are not coupled by a single photon, since this transition requires $\Delta m_F = -2$. It is therefore easy to be sure that an adiabatic RF sweep around $228\ \text{MHz}$ produces a pure $|1\rangle$ sample.

At high magnetic fields, different m_I states within the same m_J triplet (Fig. 5-1) are split approximately by $|a_{\text{hf}} m_J m_I| \sim 76\ \text{MHz}$. Here, $a_{\text{hf}} = \nu_{\text{hf}}/(I + 1/2)$ is the hyperfine constant, equal to $152\ \text{MHz}$ in ^6Li . Starting with a pure $|1\rangle$ sample, we can create different spin mixtures of states $|1\rangle$ and $|2\rangle$ (and $|3\rangle$) at high magnetic fields using single photon RF transitions near $\sim 76\ \text{MHz}$.

Once an interacting spin mixture is formed in a finite depth ODT, plain evaporative (re)cooling of the sample sets in [9] (see Fig. 5-2 below). Forced evaporative cooling could also be implemented by gradually lowering the ODT power [19].

5.2.4 Spin selective imaging at high magnetic fields

In order to image lithium clouds at high magnetic fields, we have set up an additional part of the laser system which generates appropriately detuned imaging laser beams (see Appendix A.3). Alternatively, magnetic fields could be switched off right before imaging [3]. However, the ability to image the clouds at high fields has several advantages.

Switching off our magnetic fields takes $\sim 50 - 100 \mu\text{s}$, due to the relatively large inductance of our magnetic coils¹. This cannot be considered instantaneous, and the ability to probe the dynamics of the system at shorter timescales could be important. For example, this time is comparable to the inverse radial trapping frequency in the ODT, and hence to the timescale on which the field-dependent interaction energy is converted into kinetic energy if the gas is released from the trap [28]. In a strongly interacting system, other relevant timescales, such as the inverse mean field energy or the coherence time of a (hypothetical) superfluid state, could be even shorter. Hence, a superfluid state formed at some high magnetic field could decay after the field is turned off without allowing enough time to image the system at low magnetic fields.

Further, at high magnetic fields, states $|1\rangle$, $|2\rangle$, and $|3\rangle$ are separated in energy by more than the optical linewidth of 6 MHz. This allows for state selective imaging of spin mixtures - spatially overlapping clouds in different spin states can be imaged simultaneously with separate light beams onto different parts of the same CCD camera. Examples of such images are shown in Fig. 5-2.

Finally, high field imaging also provides a good calibration of our magnetic fields.

5.3 What to look for?

According to our classification of collisions in a gas (Ch. 4), there are fundamentally three types of experiments one can perform in the strongly interacting regime - those that study (1) inelastic, (2) elastic, and (3) coherent collisions. Ultimately, from a condensed matter physics point of view, the last type of experiments is the most interesting. However, studies of inelastic and (incoherent) elastic collisions are also essential for characterizing the interaction properties of the system, and designing the optimal experimental conditions for future studies of novel many-body states.

¹This is a consequence of the fact that the geometry of our steel vacuum chamber forces us to have relatively large magnetic coils [8]. In contrast, in the group of Christophe Salomon, a small vacuum glass cell allows for small magnetic coils and switch-off times shorter than $20 \mu\text{s}$ [28, 57].

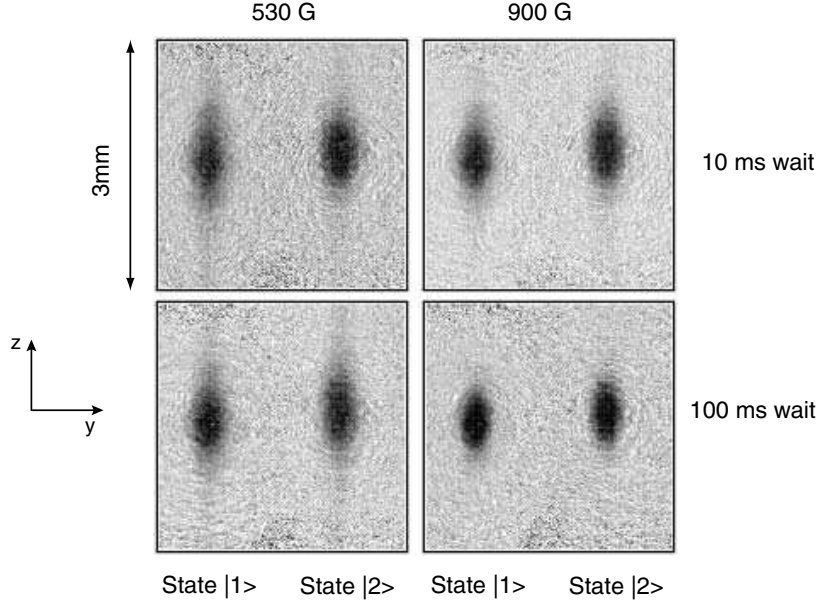


Figure 5-2: Spin selective imaging of the optically trapped $|1\rangle - |2\rangle$ mixture. Spatially overlapping clouds in states $|1\rangle$ and $|2\rangle$ are simultaneously imaged onto different parts of the same CCD camera. Here we also see the effects of mutual cooling as a function of the magnetic field and hold time in the ODT. At 530 G, $a_{12} \sim 0$ [23, 59], and cooling is inefficient. At 900 G, cooling is seen in the shrinking size and increasing density of the clouds.

Each of the following three chapters is dedicated to one of the three types of collisions:

(1) Inelastic collisions can be probed by studying the decay of a trapped cloud, as we will see in Ch. 6.

(2) Rates of elastic collisions can be studied by perturbing the system in some way, and then observing how the collisions drive it back towards the equilibrium. As we will see, this can be simply done by observing the expansion of the gas released from the trap. It has recently been proposed that expansion measurements can also be used to observe the superfluid transition in a degenerate Fermi gas [81]. We have however argued that this would be very hard under current experimental conditions [4]. These two topics are covered in Ch. 7.

(3) Interaction energy of the system caused by the coherent collisions can also be extracted from the expansion measurements [25, 26, 28], since it is converted into kinetic energy during the expansion. This method was particularly nicely used by the group of Christophe Salomon [28]. They have prepared $|1\rangle - |2\rangle$ ^6Li spin mixtures at high magnetic fields, and then let the gas expand, either in the presence of the magnetic field, or with the magnetic field turned off at the beginning of the expansion. In the former case, the total kinetic energy of the expanding gas is equal to the sum of in-trap kinetic and interaction energy. In

the latter case, the interaction energy is taken out of the system, and only the in-trap kinetic energy is measured. The interaction energy can then be extracted from the comparison of the two measurements. Alternatively, coherent collision shifts of the atomic energy levels can be measured spectroscopically. We have taken the latter approach, as I will describe in Ch. 8.

Chapter 6

Inelastic losses near a Feshbach resonance

Our first experiment with the interacting $|1\rangle - |2\rangle$ ${}^6\text{Li}$ spin mixtures was a study of inelastic losses at magnetic fields up to 900 G [3]. This field range encompasses the predicted Feshbach resonance for the inter-species scattering length a_{12} (Fig. 5-1) [54]. Details of this experiment were reported in the following publication:

*K. Dieckmann, C. A. Stan, S. Gupta, Z. Hadzibabic, C. H. Schunck, and W. Ketterle, "Decay of an Ultracold Fermionic Lithium Gas near a Feshbach Resonance," Phys. Rev. Lett. **89**, 203201 (2002) [3].*

Enhancement of the scattering length near a Feshbach resonance generally also leads to an increased rate of inelastic losses [82–84]. One loss mechanism which we expect to be enhanced is the three-body recombination [85]. Near the resonance, atoms spend a large fraction of their time in the off-resonant molecular state. This increases the chances of a collision with a third atom, and subsequent quenching into a permanently bound molecule. Further, the rate of collisions with a third atom is proportional to the elastic cross-section, and hence also enhanced. In a two-state Fermi system, this process should be at least somewhat suppressed, as it necessarily involves two identical fermions being in close proximity [86, 87]. For the two lowest states of ${}^6\text{Li}$, this is expected to be the only resonantly enhanced loss process [39].

There are two reasons for starting off the studies of the strongly interacting regime by looking at inelastic losses:

(1) This is a very economic way to explore a wide range of magnetic fields and experimentally locate the resonances. All we have to do is to expose the spin mixture to different magnetic fields, and observe the number of atoms that remains in the trap after some fixed time. Historically, this method has proved very useful for the first observation of a Feshbach

resonance in a BEC [67].

(2) Based on our experience with BECs near Feshbach resonances, we know that strong inelastic losses could preclude the studies of the coherent properties of an interacting system at high densities [82]. It is therefore important to verify/ensure that a strongly interacting Fermi system has a long enough lifetime compared to for example the expected time needed for formation of Cooper pairs [34, 45].

6.1 Note on the experimental procedure

At the time when we performed these experiments, the experimental procedure was different from the standard/current one described in Ch. 5. Sympathetic cooling of lithium was still done with sodium in the $F = 1$ state (Section 3.2), and we still had not implemented spin selective absorption imaging at arbitrary magnetic fields.

The ^6Li clouds were therefore sympathetically cooled and transferred into the ODT in the $|2\rangle$ state, at a temperature $T \sim T_F$, and a typical peak density of $\sim 3 \times 10^{13} \text{ cm}^{-3}$. $|1\rangle - |2\rangle$ mixtures were then created by non-adiabatic RF sweeps at low magnetic fields. At low magnetic fields, the two states are nearly degenerate (on the scale of the optical linewidth), but have different magnetic moments (Fig. 3-2). The spin composition of the samples could thus be calibrated by spatially separating the two states with a Stern-Gerlach magnetic field gradient [9]. In this way, the rate of the non-adiabatic RF sweep could be adjusted so that an equal mixture was produced.

Either spin mixtures, or pure states, were then exposed to magnetic field pulses of duration 50 ms–2 s. After switching off the high magnetic field, the total number of remaining atoms was recorded by absorption imaging.

Attempts to perform Stern-Gerlach analysis of the samples after the inelastic decay had taken place were flawed by poor signal to noise ratio. We therefore could not monitor the spin compositions during the decay.

Absorption imaging of either state on the cycling $m_J = -1/2 \rightarrow -3/2$ transition (Appendix A.3) could be done only at select fields near 700 G, using a primitive setup which redirected the red detuned light used for Zeeman slowing (Section 2.4.4) into the imaging system. This method was used for calibrating the magnetic fields created by our coils.

6.2 Two decay resonances of the $|1\rangle - |2\rangle$ spin mixture

The results of our measurements for an equal mixture of states $|1\rangle$ and $|2\rangle$ are summarized in Fig. 6-1 [3]. In contrast to our expectations, we observed two decay resonances, one narrow at ~ 550 G, and one broad at ~ 680 G.

Soon after we completed these measurements, an improved theoretical calculation showed that a second narrow resonance is indeed expected to occur close to 550 G [23] (Fig. 6-2).

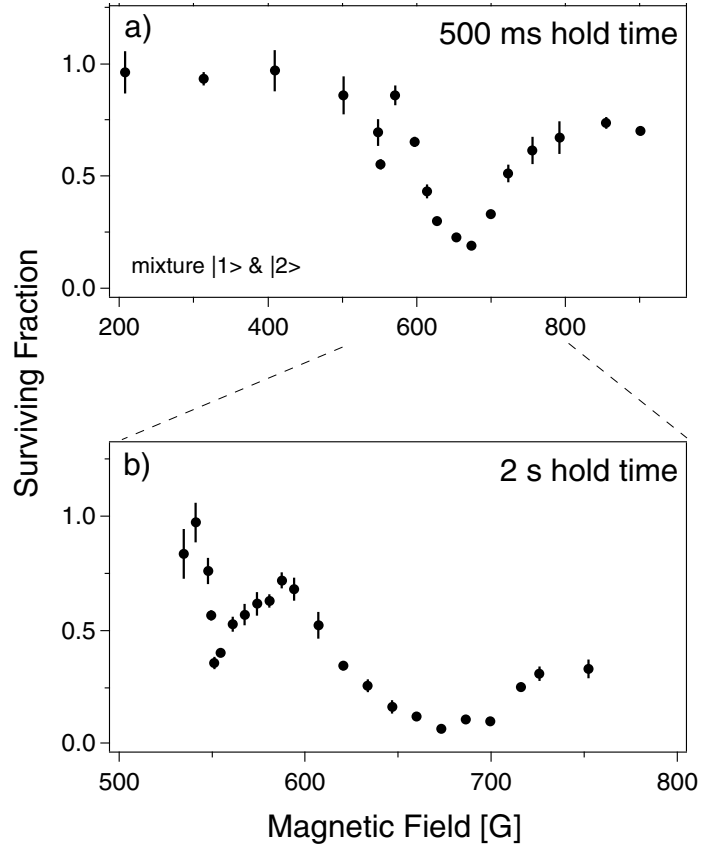


Figure 6-1: Magnetic field dependence of inelastic losses in a ^6Li $|1\rangle - |2\rangle$ spin mixture. (a) The fraction of atoms remaining in the system after the magnetic field was applied for 500 ms. Two decay resonances are observed, at 550 G and 680 G. (b) The two resonances are shown with higher density of data points, and for 2 s magnetic field pulses. Each data point is an average of three measurements.

6.3 Relative positions of the decay and the Feshbach resonances

The updated calculations however still predicted the broad Feshbach resonance at ~ 860 G, relatively far from our inelastic loss peak. The new calculations included the measurement of the “zero crossing” of a_{12} at ~ 530 G [23, 59] (Fig. 6-2). Note that the same experiment in which the zero crossing was measured [23], also observed a loss peak on the low field side of the predicted resonance, at ~ 650 G [23]. Later measurements by the group of Christophe Salomon [28] also showed a similar discrepancy. In that experiment, both inelastic and elastic interactions were studied in more detail (See Ch. 7). While the elastic cross section appeared to peak at a magnetic field in agreement with the predicted Feshbach resonance, the losses peaked at a lower field in agreement with our measurements. The shift of the decay resonance with respect to the elastic Feshbach resonance thus appears to be real.

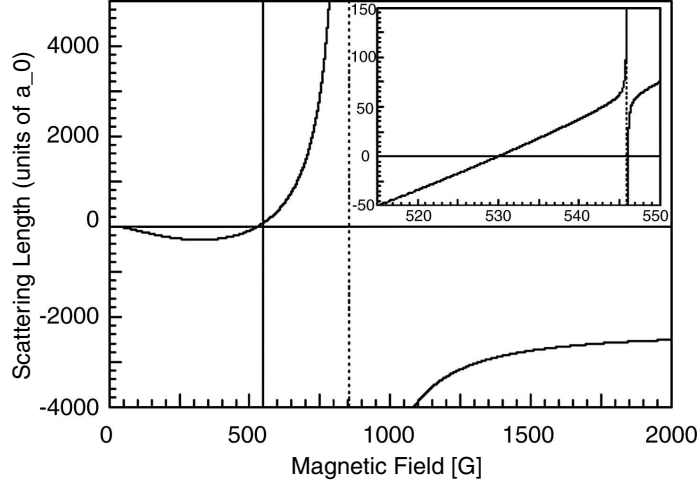


Figure 6-2: Updated prediction of the ${}^6\text{Li } a_{12}$ Feshbach resonances, taken from [23]. The calculations include the measured zero crossing of a_{12} at 530 G [23, 59]. The two resonances correspond to two different molecular hyperfine sub-levels of the same vibrational state.

Recently, several authors have theoretically studied this somewhat surprising observation [86, 88–91]. However, we maybe should not be too worried as long as the shift does not exceed the width of the resonance. This is particularly true if only the recombination into the closest molecular level, *i.e.* the one responsible for the resonance, is resonantly enhanced. For example, in that case the decay should occur only on the positive side of the resonance ($a > 0$), since only then the molecular state lies below the incident collision energy, and the process is exothermic. The exact amount of released energy, compared to the Fermi energy, or the trap depth, can also be relevant. For example, the products of recombination may stay trapped or not, the other atoms may have enough energy to break apart a weakly bound molecule, and so forth. The released energy is zero exactly on resonance, and grows as the magnetic field is tuned to lower values. Therefore, as we move away from the resonance, the probability of the inelastic process decreases, but the amount of released energy increases. Without understanding the details, it then seems plausible that different tuning of these two relevant parameters may conspire to produce a shift of the measured loss peak of the order of the resonance width.

Finally, note that the ~ 800 G ${}^6\text{Li}$ resonance is by far the broadest one ever studied. It is therefore quite plausible that the observed effects are not particular to this resonance, but its large width allowed us to resolve them for the first time.

6.4 The main good news

Remaining mysteries aside, the most important conclusion of these measurements was that the observed losses did not seem prohibitive for further studies of the strongly interacting

^6Li spin mixtures. Even at the resonance peak, losses took place on a timescale larger than 100 ms. This time is longer than any other expected relevant timescale in the system, such as the inverse trapping frequency, inverse Fermi energy, elastic collision rate, expected inverse superfluid gap energy [37, 40], or the expected time needed for the formation of the Cooper pairs [34, 45].

Chapter 7

Elastic collisions and the expansion measurements

Enhancement of the elastic collisions near a Feshbach resonance can conveniently be characterized by releasing the gas from an anisotropic trapping potential, and monitoring the expansion of the cloud [92, 93]. In the collisionally dense, *classical* hydrodynamic regime, the spatial anisotropy of the trapped gas is reversed during the expansion [25, 27, 28, 94]. Such expansion measurements will be discussed in Section 7.1.

The first observation of an anisotropic expansion of a *degenerate* Fermi gas near a Feshbach resonance [25], has attracted a lot of attention because of a recent proposal that this may also be a signature of the superfluid transition [81] (Section 7.2). The ability to experimentally differentiate the two physical effects strongly depends on the possibility that, at low temperatures, the classical hydrodynamic behavior is suppressed by Pauli blocking of elastic collisions. In Section 7.3, I discuss the role of Pauli blocking in a degenerate Fermi gas in general, and during the expansion in particular.

Parts of this chapter are based on our theoretical paper:

S. Gupta, Z. Hadzibabic, J. R. Anglin, and W. Ketterle, "Collisions in zero temperature Fermi gases," cond-mat/0307088 (2003). [4]

in which we have argued that making the distinction between the two types of hydrodynamic behavior may be very difficult under current experimental conditions. Mathematical details of the calculations reported in [4] will be given in the PhD thesis of Subhadeep Gupta [9].

7.1 Hydrodynamic expansion of a classical gas

Trapped atomic gases are usually “collisionless”, in the sense that the mean free path for classical elastic collisions is much larger than the size of the cloud. For a classical gas, or a moderately degenerate Fermi gas, with peak density n_0 , we can write this condition as:

$$l_0 = \frac{1}{\sqrt{2}n_0\sigma} \gg R_{r,z} = \sqrt{\frac{k_B T}{m\omega_{r,z}^2}} \quad (7.1)$$

where l_0 is the mean free path, and $R_{r,z}$ is the cloud size in the radial/axial direction. Alternatively, condition 7.1 is equivalent to the rate of collisions being much lower than the trapping frequencies, $n_0\sigma\sqrt{k_B T/m} \ll \omega_{r,z}$.

The hydrodynamic parameter, which I define as the ratio:

$$\varphi_{r,z} = \frac{R_{r,z}}{l_0} \quad (7.2)$$

roughly corresponds to the number of collisions per particle during one trapping period. In the collisionless regime, $\varphi \ll 1$.

If the cloud density or the elastic cross section are increased, the gas may cross over into the hydrodynamic regime, $\varphi \gg 1$. This regime has only recently been experimentally realized, both for Bose [94–96], and for Fermi gases [24, 25, 28, 97, 98].

For a gas trapped in an anisotropic potential, cross-over into the hydrodynamic regime, and hence the rate of elastic collisions, can be studied by simply releasing the gas from the trap, and observing the spatial distribution during the expansion [92, 93]. For the usual case of cylindrically symmetric traps, the shape of an expanding cloud is characterized by the (radial to axial) aspect ratio:

$$\lambda(t) = \frac{R_r(t)}{R_z(t)} \quad (7.3)$$

where for a trapped gas, we have:

$$\lambda_0 \equiv \lambda(0) = \frac{\omega_z}{\omega_r} = \frac{\varphi_r}{\varphi_z} \quad (7.4)$$

and for our cigar shaped optical trap (Section 5.2.2), $\lambda_0 \approx 0.015$.

In the collisionless regime, the gas will expand ballistically. For long expansion times, $\omega_{r,z}t \gg 1$, we have:

$$R_{r,z}(t) = R_{r,z}(0)\sqrt{1 + \omega_{r,z}^2 t^2} = \sqrt{\frac{k_B T}{m}} t \sqrt{1 + \frac{1}{\omega_{r,z}^2 t^2}} \rightarrow \sqrt{\frac{k_B T}{m}} t \quad (7.5)$$

The spatial distribution will thus become isotropic, $\lambda_\infty \equiv \lambda(t \rightarrow \infty) = 1$. This simply

reflects the isotropic momentum distribution in the trap.

In the hydrodynamic regime, elastic scattering during the expansion will redistribute the particle momenta from the direction of greater collisional density (in our case axial) to the directions of smaller collisional density (in our case radial). In this case, the spatial distribution after long expansion times will be anisotropic, with the cloud aspect ratio inverted [92, 93]. In the fully hydrodynamic regime ($\varphi \rightarrow \infty$), and for $\lambda_0 \rightarrow 0$, we expect $\lambda_\infty \sim 0.38/\lambda_0$ [81]. For our optical trap, this corresponds to $\lambda_\infty \sim 25$. In principle, we expect $\lambda_\infty > 1$ even for infinitesimal values of φ . However, the effect is likely to be experimentally observable only for $\varphi_z \geq 1$.

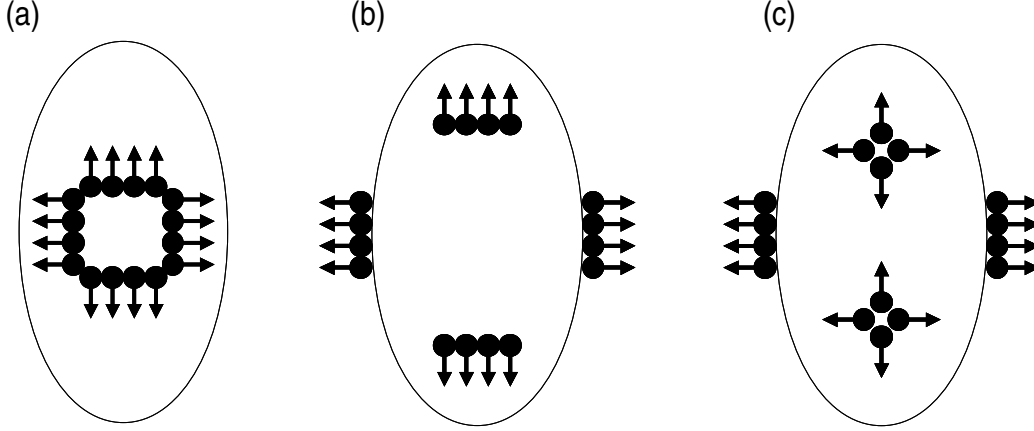


Figure 7-1: Ballistic and hydrodynamic expansion of a classical gas. The ellipse indicates the cigar shape of the trapped cloud with $\lambda_0 < 1$. We concentrate on 16 atoms which start the expansion from the center of the cloud, with velocities indicated by the arrows. (a) Isotropic momentum distribution of a trapped gas. (b) Momentum distribution of a ballistically expanding cloud. We always have 4 atoms moving in each direction. (c) Momentum distribution of an expanding cloud which is collisionless in the radial (horizontal) direction, but hydrodynamic in the axial (vertical) direction. After one collision time, we have 12 atoms travelling radially, and only 4 travelling axially.

The two types of expansion are simplistically illustrated in Fig. 7-1 for our trap geometry. In Fig. 7-1(a), the gas is still trapped, and the momentum distribution is isotropic, locally and globally. In Fig. 7-1(b), the gas expands ballistically. *Globally*, the momentum distribution remains isotropic. However, note that *locally*, the momentum distribution becomes anisotropic - on the top of the image, we have atoms moving upwards, and so forth. In Fig. 7-1(c), the gas expands (partially) hydrodynamically. For simplicity, suppose that $\varphi_z \gg 1 \gg \varphi_r$. In this case, radially moving atoms leave the cloud without undergoing any collisions. On the other hand, the atoms initially moving in the axial direction do undergo collisions. Consequently, their momentum distribution becomes *locally* isotropic. This leads to an anisotropic *global* momentum distribution, with more atoms moving radially than axially. Qualitatively, the same arguments will hold as long as $\varphi_z/\varphi_r = 1/\lambda_0 > 1$.

The anisotropic expansion of our strongly interacting ${}^6\text{Li}$ spin mixture is shown in Fig. 7-2 (unpublished). Our data lie in the intermediate, “cross-over” regime, between a fully hydrodynamic ($\varphi \rightarrow \infty$) and a collisionless ($\varphi \rightarrow 0$) expansion. In the limits of $\varphi \rightarrow 0$ or ∞ , the expansion of the gas (obviously) does not explicitly depend on the elastic cross section σ . However, in the intermediate regime, the aspect ratio of the cloud after a fixed expansion time could be used to extract φ , and hence σ [93]. This method is unlikely to yield a “precision” measurement of σ , due to the systematic uncertainties in determining the gas density. However, variation of φ with the applied magnetic field can be used to characterize a Feshbach resonance. This method was used for ${}^6\text{Li}$ in [28], and for ${}^{40}\text{K}$ in [27].

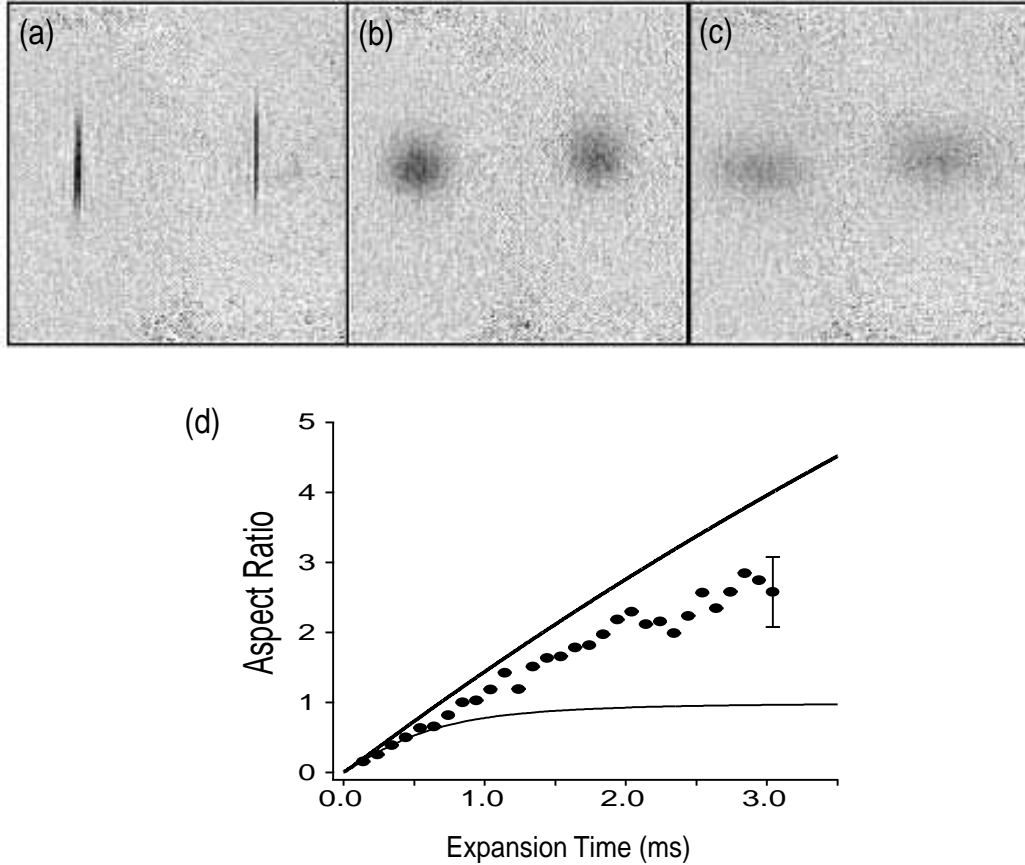


Figure 7-2: Anisotropic expansion of a strongly interacting ${}^6\text{Li}$ spin mixture. An equal $|1\rangle - |2\rangle$ mixture, with $\sim 1.5 \times 10^6$ atoms in each state, was released from the optical trap at a temperature $T \sim 0.5 T_F$, and in the presence of an external magnetic field of 900 G. (a-c) The two states are simultaneously imaged for expansion times $t = 0$, $900 \mu\text{s}$, and $1500 \mu\text{s}$. (d) Evolution of the cloud aspect ratio $\lambda(t)$, with $\lambda_0 = 0.015$, and 1 ms corresponding to 13 radial trapping periods. The upper curve corresponds to a fully hydrodynamic expansion, with $\lambda_\infty \approx 25$ [81]. The lower curve corresponds to a ballistic expansion, with $\lambda_\infty = 1$. Our data lie in between these two limits.

7.2 Superfluid *vs.* classical hydrodynamics in a degenerate Fermi gas

The hydrodynamic evolution of a classical gas plotted in Fig 7-2 is predicted from the scaling solutions to the hydrodynamic equations of motion [81, 92, 93]:

$$\begin{aligned}\frac{\partial}{\partial t}n &= -\nabla \cdot (n\vec{v}) \\ m\frac{\partial}{\partial t}\vec{v} &= -\nabla \left(\mu + V + \frac{1}{2}mv^2 \right)\end{aligned}\tag{7.6}$$

where μ and V are the chemical and the external potential. The crucial assumption in writing down these equations is that the gas is always in local equilibrium, and can be described in terms of the local macroscopic variables - density n , and the velocity field \vec{v} .

Let me make two comments about the applicability of the hydrodynamic equations of motion:

(1) We generally expect this approach to provide a good description of the long-wavelength and low-frequency behavior of the system. At short distances and high frequencies, we need to describe the system in terms of the distribution functions for the $(6N)$ microscopic degrees of freedom. In a classical gas, the separation between “long” and “short” distances is set by the mean free path. Likewise, “high” and “low” frequencies are separated by the collision rate. In our discussion of the expansion measurements, we have qualified the gas as hydrodynamic if the lengthscale (cloud size) and the timescale (trapping frequency) relevant for our specific problem could be considered long¹.

(2) The applicability of the hydrodynamic equations of motion hinges only on our ability to describe the system in terms of the local macroscopic variables, and not on the exact mechanism which ensures the local equilibrium. In a classical gas, the establishment of the local thermodynamic equilibrium depends on the collisions between atoms. On the other hand, an atomic BEC is classically collisionless. Yet, in this case, the presence of the macroscopic (superfluid) order validates a hydrodynamic description [65, 99]. The system is fully described by the macroscopic wave function $\psi = |\psi|e^{i\varphi}$, which has only two degrees of freedom, the amplitude and the phase. These two variables define the local density $n = |\psi|^2$, and the velocity field $\vec{v} = (\hbar/m)\nabla\varphi$. In this system, the role of the mean free path l_0 is taken over by the healing length

$$\xi = \sqrt{\frac{\hbar^2}{2m\mu}}\tag{7.7}$$

where $\mu = (4\pi\hbar^2/m)na$ is the mean field chemical potential. In both systems, these length-

¹Of course, in our system, these are the largest length and timescale available. Therefore, our definition of the hydrodynamic condition is the least stringent possible.

scales (l_0, ξ) determine the distance over which the gas can respond to an external perturbation, and restore the equilibrium. Likewise, the role of the collision rate is taken over by the frequency associated with the mean field, μ/\hbar . Again, these are the timescales on which the two systems can respond to an external perturbation, such as a change in boundary conditions. Therefore, a BEC will expand hydrodynamically as long as the healing length is smaller than the size of the cloud. As in the classical case (Eq. 7.1), it is trivial to verify that this criterion is identical to μ/\hbar being larger than the trapping frequencies.

If the requirements for the local equilibrium of the system are (somehow) fulfilled, the resulting hydrodynamic equations take a rather universal form. The only differences between different systems arise from different equations of state, which determine the local pressure. For example, in a degenerate Fermi gas released from the trap, the chemical potential giving the local pressure is given by the (kinetic) Fermi energy, and scales as $n^{2/3}$. On the other hand, in an expanding weakly interacting BEC, the local chemical potential is given by the mean field energy, and scales as n . The exact solutions thus might depend on the system, but some general features are ubiquitous. For example, as long as we can identify a force field which is proportional to the density gradient, this will inevitably lead to the reversal of spatial anisotropy of the gas during the expansion.

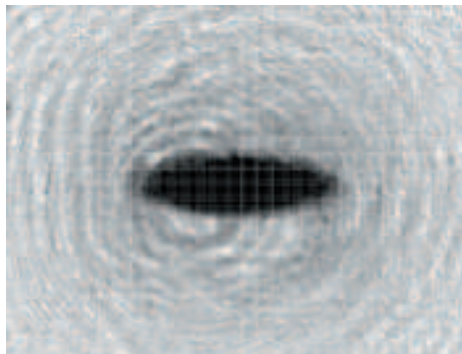


Figure 7-3: Superfluid hydrodynamic expansion of a weakly interacting ^{23}Na BEC. The cigar shaped (magnetic) trap is oriented as in Figs. 7-1 and 7-2. As in the case of classical hydrodynamics, the aspect ratio of the cloud is inverted during the expansion.

The familiar anisotropic expansion of a weakly interacting BEC (Fig. 7-3) is used as a “smoking gun” for condensation. Since a fermionic superfluid is also predicted to obey hydrodynamic equations [35, 81, 100, 101], it has recently been proposed [81] that the same effect can be used as a qualitative and unambiguous signature of the superfluid transition in a degenerate Fermi gas. The potential simplicity of this detection method is very exciting. One could for example observe a sudden onset of the anisotropic expansion as a function of the temperature or the spin composition of the cloud.

However, for such a signature to be unambiguous, we would have to be able to distinguish it from classical hydrodynamics. This is difficult for two reasons:

(1) In this case, the two types of the hydrodynamic expansion are predicted to be identical [81].

(2) All current efforts to achieve superfluidity are concentrating on the strongly interacting regime in the vicinity of a Feshbach resonance.

This issue has become very important now that hydrodynamic expansion of Fermi gases has been observed. Further, hydrodynamic expansion of ^6Li was observed in an equal $|1\rangle - |2\rangle$ mixture at $T \sim 0.1 T_F$, and a magnetic field of 910 G [25]. At least some theories would suggest that these conditions satisfy all the criteria for a superfluid transition (see Section 4.3). However, in the same experiment, hydrodynamic behavior was observed over a wide range of temperatures, up to $\sim 3.5 T_F$, without any observable changes. We, and other groups [27, 28], have since observed the same behavior at various temperatures and for different spin compositions.

Classical and superfluid hydrodynamics could be distinguished at very low temperatures, when the Pauli blocking suppresses the elastic collisions [25, 102]. However, this argument does not apply to expansion measurements, as we will see in the next section.

7.3 Pauli blocking of collisions during the expansion of a degenerate Fermi gas

Pauli blocking prevents scattering of atoms into already occupied states, and limits the total rates of (incoherent) elastic scattering at low temperatures. Coherent collisions on the other hand are not affected by Pauli blocking, since they do not involve any change in occupation numbers of different momentum states.

In a trapped gas, Pauli blocking may have significant consequences for the rates of evaporative cooling [103–105], thermalization of an impurity in the gas² [106, 107], or damping of collective excitations [98, 108].

In equilibrium at zero temperature, no elastic collisions occur even in an interacting ($a_{12} \neq 0$) spin mixture. At a small but finite T , the total rate of collisions is determined by the small number of energetically accessible unoccupied states.

However, if the Fermi surface is deformed from its equilibrium shape, collisions will occur even at $T = 0$. This will have important implications on our interpretation of expansion measurements in a degenerate Fermi gas. Before addressing that specific example, I discuss this issue in a more general context.

7.3.1 Effects of the Fermi surface deformation on Pauli blocking

Two examples of the deformation (or excitation) of a $T = 0$ Fermi surface are illustrated in Fig. 7-4. Such excitations necessarily lead to opening up of energetically accessible states,

²In a two-state mixture, an “impurity” can simply be an atom in the other spin state.

and to the elastic collisions which aim to restore the equilibrium. As in the case of a finite temperature, the total rate of collisions will depend on the number of the available final states, and hence on the extent of the deformation. For example, in the small amplitude limit, we may find that the collective excitations of the system are not damped at all, because the gas remains essentially collisionless at all times [108]. However, for larger deformations, the gas will behave increasingly more classically [4].

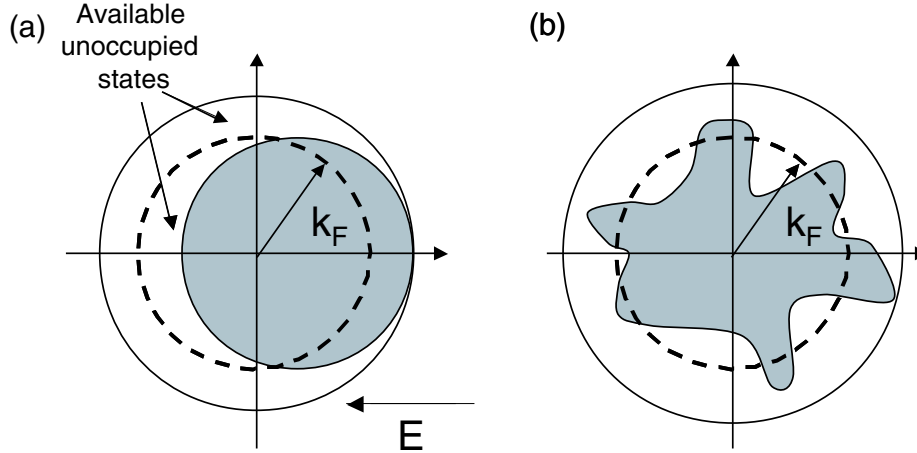


Figure 7-4: Opening up of final states for elastic scattering at zero temperature. (a) The momentum space Fermi sphere (shaded area) is displaced from its equilibrium position (dashed circle). All the states within the large thin-line circle are energetically accessible. The unshaded area within this circle represents states which are also unoccupied and hence available as final states for elastic collisions. This excitation is analogous to applying an external electric field E on an electron gas in a metal. (b) The same analysis applies for an arbitrary deformation of the Fermi surface.

As a simple example, let us consider the case of a linear displacement of the Fermi surface (Fig. 7-4(a)). This situation may remind us of applying an external electric field E on a (normal) metal at zero temperature. If the relaxation time due to elastic collisions is τ , the drift velocity of the electrons will be limited to $Ee\tau/m$, despite the constantly applied acceleration. If the applied electric field changes sign on a timescale $1/\omega \ll \tau$, collisions will not play any role. The electrons will then exhibit undamped oscillations, but only because they never attempt to exceed the maximum drift velocity. In this case the typical drift velocity is $Ee/(m\omega) \ll Ee\tau/m$. Now, if the collision rate is actually Pauli limited, τ will decrease with increasing E . Therefore, the same frequency oscillation may be damped or not, depending on its amplitude. In this simple example, we considered a driven off-resonant oscillation. However, the same thinking will apply to damping of the normal modes of the system.

Atomic systems are quite different from the electron gas in a metal, and most other conventional condensed matter systems, in that drastic deformations of the Fermi surface

are easily accessible and quite common. For example, it is easy to displace a trapped gas from its equilibrium position to a distance comparable to the size of the cloud, *i.e.* its real space Fermi diameter. If the gas is then released to exhibit a dipole oscillation in the trap, the common drift velocity of the atoms will be comparable to the Fermi velocity.

Some of these thoughts have been experimentally confirmed by DeMarco and Jin [98], in an experiment quite analogous to our electron gas discussion. There, two trapped clouds in different spin states of ^{40}K were set into relative oscillation inside the magnetic trap. In the degenerate regime ($T \sim 0.4 T_F$), Pauli suppression of collisions was observed. However, if the amplitude of the oscillation was increased to $\sim 10\%$ of the cloud size, the collisional behavior became essentially classical.

7.3.2 Deformation of the Fermi surface during the expansion

Free expansion of the gas released from an anisotropic trap is an extreme example of the deformation of the Fermi surface. First, let us consider a collisionless expansion of a $T = 0$ gas. For example, let us assume that we have an equal mixture of two spin states, but for now we set $a_{12} = 0$.

At $t = 0$, the system is in equilibrium, and the local momentum space Fermi surface is isotropic at all spatial positions:

$$\sum_i \frac{p_i^2}{2m} = E_F - \sum_i \frac{1}{2} m \omega_i^2 x_i^2 \quad (7.8)$$

To find the local momentum distributions during the ballistic expansion, we replace $x_i \rightarrow x_i - (p_i/m)t$, and obtain:

$$\sum_i \frac{1 + \omega_i^2 t^2}{2m} \left(p_i - \frac{m x_i}{t} \frac{\omega_i^2 t^2}{1 + \omega_i^2 t^2} \right)^2 = E_F - \sum_i \frac{1}{2} \frac{m \omega_i^2 x_i^2}{1 + \omega_i^2 t^2} \quad (7.9)$$

At all positions, the momentum space Fermi surface evolves into ellipsoids, as illustrated in Fig. 7-5. At long times, the center of the momentum ellipsoid at a particular position is given by $\vec{p} = m\vec{x}/t$. This is just the momentum which a particle starting from the center of the trap would need in order to arrive at \vec{x} in time t . The spread of the momenta at (\vec{x}, t) then reflects the spread of the initial positions of the atoms in the trapped cloud. Therefore, for $\omega_{r,z} t \gg 1$, the local momentum space Fermi surface at all positions assumes the shape of the original trapped cloud. The volume of the momentum space ellipsoid gives the local real space density, and the overall shrinking of the momentum distributions describes the decay of the gas density during the expansion.

Deformations of the Fermi surface shown in Fig. 7-5 clearly open up final states for elastic scattering, as shown in Fig. 7-6.

In [4], we have proposed a way to quantify the effectiveness of Pauli blocking during

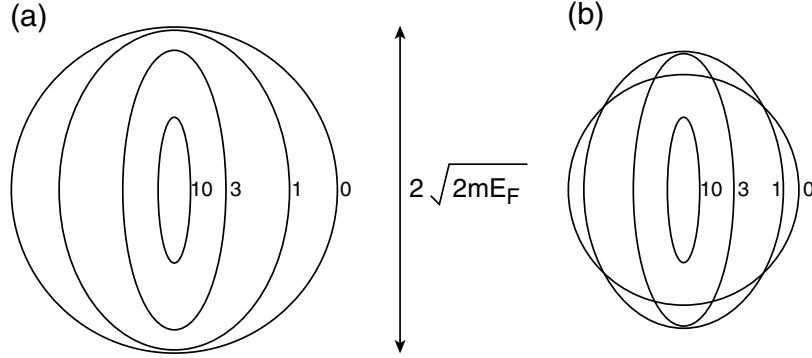


Figure 7-5: Local momentum-space Fermi surface of a ballistically expanding gas. As usual, we consider a cigar shaped trap, here with $\lambda_0 = 0.2$. Fermi surfaces are plotted for expansion times $\omega_r t = 0, 1, 3$, and 10 . Results of Eq. 7.9 are plotted for two different spatial locations - (a) the trap origin, and (b) a position radially displaced by $\sqrt{E_F/(m\omega_r^2)}$. In (b), the changing origin of the momentum space ellipsoid is subtracted.

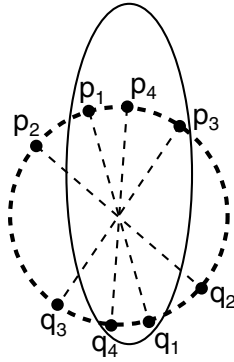


Figure 7-6: Allowed and forbidden elastic collisions during the expansion. The ellipse indicates the identical Fermi surfaces for the two spin states, labelled by momenta \vec{p} and \vec{q} . Process $(\vec{p}_1, \vec{q}_1) \rightarrow (\vec{p}_2, \vec{q}_2)$ is allowed due to the Fermi surface deformation. $(\vec{p}_1, \vec{q}_1) \rightarrow (\vec{p}_3, \vec{q}_3)$ is classically allowed, but suppressed by Pauli blocking. $(\vec{p}_1, \vec{q}_1) \rightarrow (\vec{p}_4, \vec{q}_4)$ does not change the momentum distribution, because the reverse process has the same rate.

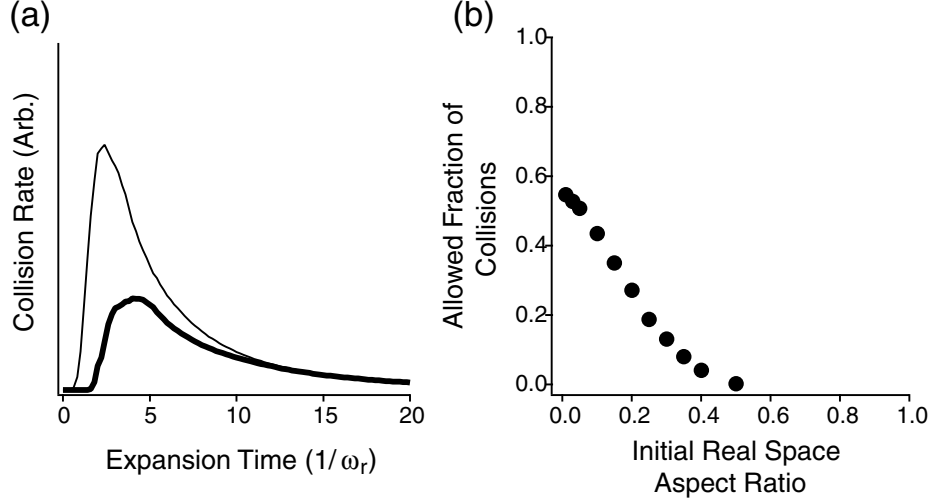


Figure 7-7: Fraction of Pauli allowed elastic collisions during the expansion. (a) Rates of classically (thin line) and Pauli (thick line) allowed elastic collisions. Only the collisions which change the momentum distribution are included. The plotted rates are calculated for $\vec{x} = \vec{p}_1 = 0$, and provide an upper bound for the effectiveness of Pauli blocking [4]. For this particular plot, the trap aspect ratio is $\lambda_0 = 0.03$. (b) The two collision rates are integrated over time, and the ratio is plotted as a function of λ_0 .

the expansion. We allowed the Fermi surface to propagate ballistically, as in Fig. 7-5, and at each time t , we compared the number of allowed collisions in a $T = 0$ Fermi gas, and the total number of energetically allowed collisions. In the notation of Fig. 7-6, the former includes only the processes similar to $(\vec{p}_1, \vec{q}_1) \rightarrow (\vec{p}_2, \vec{q}_2)$, while the latter also includes the processes of the $(\vec{p}_1, \vec{q}_1) \rightarrow (\vec{p}_3, \vec{q}_3)$ kind, which are allowed only if we completely ignore the Pauli blocking. Our results are plotted in Fig. 7-7. We found that for small values of λ_0 , the fraction of energetically allowed collisions which are not suppressed by the Pauli blocking exceeds $1/2$.

Our results show that, in the perturbative limit of small σ , only a fraction of collisions is suppressed by Pauli blocking. This implies that for a larger σ , collisions will occur at a high rate, and transform the ballistic expansion into a more hydrodynamic expansion.

In the strongly interacting limit, the shape of the Fermi surface will not evolve ballistically, because collisions *will* occur and make it locally more isotropic. It may seem that this would increase the level of Pauli suppression, and invalidate our results at least quantitatively. This is true, but in this case, “the deed is already done”, and the gas expands anisotropically.

The point of our calculations is therefore that the idea that the gas expands ballistically *because* of the Pauli blocking is not consistent, and can be reduced to a contradiction.

Therefore, if the gas is strongly interacting, it is hard to rule out classical hydrodynamics as an interpretation of anisotropic expansion, even at $T = 0$. Certainly we cannot hope for

this approach to give us a simple qualitative tool for observing a superfluid transition.

7.4 Conclusions and one final thought

Expansion measurements provide a simple tool to observe the enhanced rate of elastic collisions near a Feshbach resonance, and the resulting classical hydrodynamic behavior.

However, the exciting proposal that the hydrodynamic expansion can be used as a “smoking gun” signature of fermionic superfluidity does not seem easily applicable to current experimental efforts.

On the other hand, if the hydrodynamic expansion was observed in a weakly interacting gas, this would probably be accepted as an unambiguous signature of superfluidity. In the limit of weak enough interactions, expansion will be classically collisionless even if we completely ignore Pauli blocking. However, this would pose unrealistic requirements on the cooling of the system. Using Eqs. 7.1 and 7.2, and applying them to a degenerate Fermi gas, we find that $\varphi_z \ll 1$ requires:

$$k_F a \ll \sqrt{\frac{3\pi}{4\sqrt{2}} 6^{1/3}} \frac{\lambda_0^{1/3}}{N^{1/6}} \approx \frac{\lambda_0^{1/3}}{N^{1/6}} \quad (7.10)$$

where N is the number of atoms in each state. For a pancake shaped trap ($\lambda_0 > 1$), $\varphi_r \ll 1$ is the more stringent requirement, and similarly reads:

$$k_F a \ll \frac{1}{\lambda_0^{1/6} N^{1/6}} \quad (7.11)$$

In our experiments, $N^{-1/6} \sim 0.07 - 0.1$. Even if the number of atoms was drastically reduced, for all current and reasonable future experiments, $N^{-1/6} < 0.2$. The trap aspect ratio constrains $k_F a$ further, in our case $\lambda_0^{1/3} \approx 0.25$. This factor could be brought somewhat closer to unity, however relatively significant trap anisotropy is needed in order for λ_∞ to be observably different from 1.

Therefore, even most (unreasonably) optimistically, we would need $k_F a \ll 0.2$. In this limit, we can estimate the resulting superfluid critical temperature from the standard Cooper result:

$$T_c \ll 4 \times 10^{-4} T_F \quad (7.12)$$

This is very far from our current experimental ability.

Chapter 8

RF Spectroscopy of coherent collision energy shifts

This chapter focuses on our spectroscopic studies of the interaction energy arising from coherent s -wave collisions in spin mixtures of ${}^6\text{Li}$. At the end of the thesis, I attach two manuscripts which provide further details of our work:

*S. Gupta, Z. Hadzibabic, M. W. Zwierlein, C. A. Stan, K. Dieckmann, C. H. Schunck, E. G. M. van Kempen, B. J. Verhaar, and W. Ketterle, “Radio-frequency Spectroscopy of Ultracold Fermions,” Science **300**, 1723 (2003) [5].* Included in Appendix D.

M. W. Zwierlein, Z. Hadzibabic, S. Gupta, and W. Ketterle, “Spectroscopic insensitivity to cold collisions in a two-state mixture of fermions,” cond-mat/0306627 (2003) [6]. Included in Appendix E.

The interaction energy in a two-state mixture of fermions can shift the relative energy of the two internal atomic levels away from its single-particle, vacuum value. This is illustrated in Fig. 8-1.

The resulting shifts of the spectroscopic lines, *suggested* by Fig. 8-1, are known as “clock shifts” [109], because they limit the accuracy of the current atomic clocks based on bosonic atoms¹ [110, 111]. We would like to use the spectroscopic measurements to characterize the interaction energy in the strongly interacting ${}^6\text{Li}$ spin mixtures. In this case, spectroscopy is performed in the radio-frequency (RF) domain, near the $|1\rangle - |2\rangle$ energy splitting of ~ 76 MHz.

However, as we will see in Section 8.1, in a two-state mixture of fermions, the clock shift is *absent* [5, 112], even if the equilibrium energy levels of the two states *are* shifted by different amounts [6]. While this is actually a problem for our (main) purposes, this

¹In the case of bosons, both intra- and inter-state collisions occur. However, the basic idea illustrated in Fig. 8-1 is still valid.

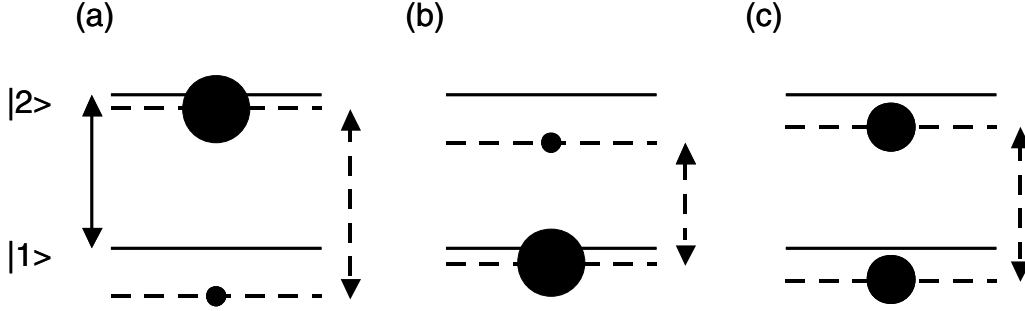


Figure 8-1: Equilibrium shifts of the energy levels in an interacting two-state mixture of fermions. Full lines and arrow indicate the vacuum energy levels and their separation. Dashed lines and arrows indicate the shifted energy levels and their separations. The mean field energy of atoms in one state is proportional to the density of atoms in the other one. Different populations in the two states are represented by differently sized circles. The figures are drawn for an attractive interaction, $a_{12} < 0$. In (a), $n_2 > n_1$, and hence the level separation is increased. In (b), the situation is reversed. In (c), $n_1 = n_2$, and the difference between the energy levels is equal to the vacuum value.

robust elimination of density dependent frequency shifts is potentially relevant for future improvements of atomic clocks.

In Section 8.2, we will see how the interaction energy shifts can be observed if the spectroscopic methods are extended to three atomic levels. Using this approach, we have studied ^6Li spin mixtures in both the weakly and the strongly interacting regime. In the weakly interacting regime, our method reproduces the expected interaction energies calculated within the mean field approximation. Our observations in the strongly interacting regime are at present not completely understood, and will be briefly discussed in Section 8.2.1.

8.1 Spectroscopic insensitivity to coherent collisions in a two-level system

In the limit of low density and weak interactions, the energy shifts of different atomic states are well described in the mean field approximation. In a two-state ($|1\rangle - |2\rangle$) statistical mixture of fermions, the total interaction energy density is given by:

$$\mathcal{E}_{\text{int}} = V_{12}n_1n_2, \quad V_{12} = \frac{4\pi\hbar^2}{m}a_{12} \quad (8.1)$$

The two equilibrium energy levels are then shifted by the interactions according to $\delta\mu_{1(2)} = V_{12}n_{2(1)}$, and the frequency (energy) separation of the two levels differs from the vacuum value by:

$$\hbar\Delta\nu = \Delta E_{\text{int}} = \delta\mu_2 - \delta\mu_1 = V_{12}(n_1 - n_2). \quad (8.2)$$

Our measurements of the $|1\rangle - |2\rangle$ transition frequency in the limits $n_1 = 0$ and $n_2 = 0$ are shown in Fig. 8-2 [5]. The experiments were performed at a gas density of $\sim 3 \times 10^{13} \text{ cm}^{-3}$, and a magnetic field of 570 G, where (theoretical) $a_{12} \sim 150 a_0$. Equation 8.2 then predicts $\Delta\nu = \pm 5 \text{ kHz}$ for the two spectra, but the observed lines are separated only by $0.04 \pm 0.35 \text{ kHz}$. Therefore, within our experimental precision, no clock shift is observed. As I outline below, this effect can be understood relatively easily, but this was the first time it was experimentally confirmed.

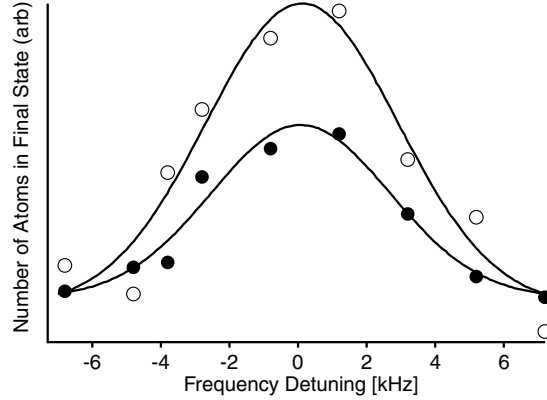


Figure 8-2: Absence of the clock shift in a pure fermionic state. RF transitions were driven between states $|1\rangle$ and $|2\rangle$ on a system prepared purely in state $|1\rangle$ (filled circles), and purely in state $|2\rangle$ (open circles). Mean-field interactions would result in 5 kHz shifts for the two curves in opposite directions. Gaussian fits to the data (solid lines) are separated by $(0.04 \pm 0.35) \text{ Hz}$. This gives a (conservative) clock shift suppression factor of 30. The widths of the spectra are dominated by the frequency broadening of the $140 \mu\text{s}$ RF pulses.

In these experiments, RF pulses were applied to pure single-state samples. Since the RF field causes a coherent evolution of the system, it simply acts as a rotation in the two-dimensional Hilbert space, and does not change the purity of the state. In other words, during the RF transfer, the superposition of the two spin states has the same relative phase for all the atoms. The atoms thus stay indistinguishable, and cannot interact in the s -wave regime. We then conclude that in the experiments shown in Fig. 8-2, there was no mean field energy in the system, so it is not surprising that no clock shift was observed.

The interaction energy in the system is established only when the coherence of the two-state superposition is lost, and a purely statistical mixture of the two states is formed. This is an implicit assumption of Eqs. 8.1 and 8.2².

²We believe that the dominant source of decoherence in our system is the residual spatial inhomogeneity of the applied magnetic field. The (vacuum) energy difference between the two states depends on the magnetic field, albeit weakly (see Fig. 5-1). Therefore, the relative phase of the superposition state evolves differently in different parts of the cloud, and atoms with different “trap oscillations histories” accumulate a different phase. Once the uncertainty in the accumulated phase becomes of order π , the system acquires the properties of a statistical mixture. Typical decoherence times in our experiments are on the $\sim 10 - 100 \text{ ms}$ scale. See [9] for a further discussion of this topic.

However, in Fig. 8-3, we see that the resonance shifts are absent in a two-state system of fermions even after the system has fully decohered, and the mean field energy has fully developed [6]. As we have explained in [6], this is again a direct consequence of the coherent nature of the RF excitation, and is indeed not dependent on the coherence of the sample on which the spectroscopy is performed. Our argument is outlined in the following section.

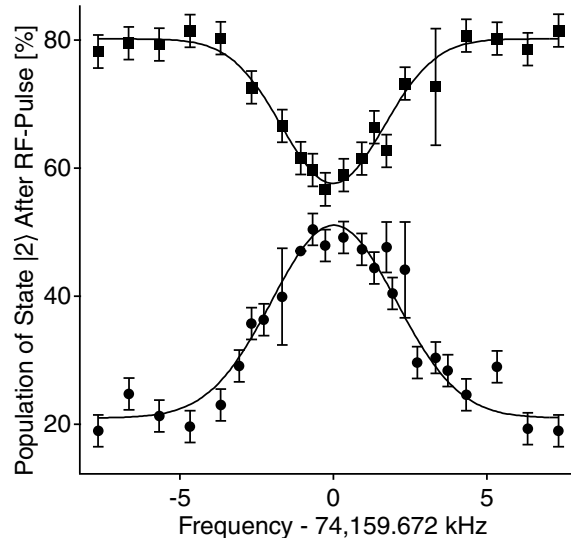


Figure 8-3: Absence of the resonance shifts in a decohered two-state mixture of fermions. The resonance curves were measured for fully decohered 80%/20% mixtures of states $|1\rangle$ and $|2\rangle$. The experimental parameters were $n_1 + n_2 \sim 5 \times 10^{13} \text{ cm}^{-3}$ and $B = 320 \text{ G}$. At this field, $a \sim -300 a_0$, and Eq. 8.2 predicts the splitting of the two lines of $\sim 20 \text{ kHz}$. However, the measured splitting is only $(34 \pm 146) \text{ Hz}$.

8.1.1 Bloch sphere representation of the RF transitions

In Fig. 8-4, the two experiments of Figs. 8-2 and 8-3 are (qualitatively) represented on a spin-1/2 Bloch sphere. The average properties of the many-body state are described by the three coordinates of the Bloch vector $\vec{m} = m_z \hat{e}_z + \vec{m}_\perp$. The population difference in the two states, or the “magnetization” of the sample, is given by $m_z = (n_2 - n_1)/2$, while the coherence in the system is measured by \vec{m}_\perp . Fully decohered statistical mixtures are represented by vectors with polar angle $\theta = 0$, or equivalently $\vec{m}_\perp = 0$ ³.

The length of the Bloch vector measures the purity of the state, and hence the entropy of the system. The key point is that the RF field just rotates the Bloch vector, and preserves its length $|\vec{m}|$. In other words, a unitary transformation cannot change the entropy.

In Fig. 8-4(a), state B is created by applying an RF pulse on a pure sample A. This corresponds to the experiment of Fig. 8-2. As I already explained, in this case there is no interaction energy in the system during the RF pulse, and no frequency shift is expected [5].

³State A in Fig. 8-4(a) is a trivial special case of a pure state.

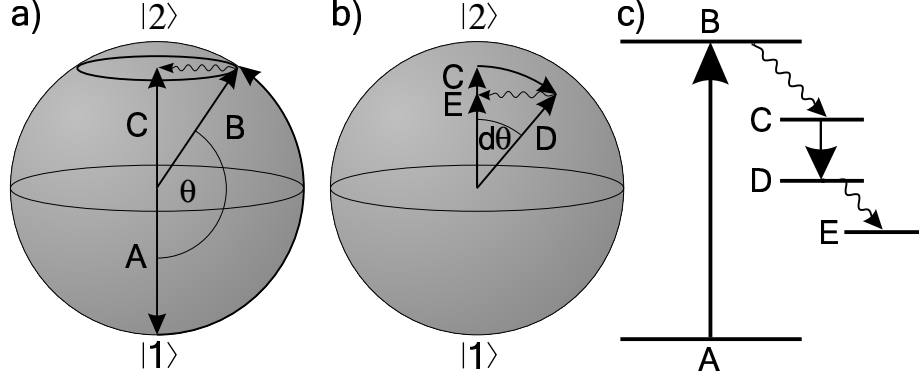


Figure 8-4: Bloch sphere representation of the RF transitions. (a) corresponds to the experiment in Fig. 8-2. An RF pulse rotates a pure state A into another pure state B. Subsequently, the superposition state decoheres into a “ring” distribution, represented by its average, C. (b) corresponds to the experiment in Fig. 8-3. Here, a second RF pulse transforms the fully decohered state C into a partially coherent state D. The final state E is reached only after further decoherence. (c) Transfers $A \rightarrow B$ and $C \rightarrow D$ are coherent and reversible. $B \rightarrow C$ and $D \rightarrow E$ are irreversible.

State C is formed through subsequent decoherence of state B. In B and C, the magnetization m_z is the same, but in C the mean-field has fully developed.

The experiment of Fig. 8-3 is performed on a C-like state. In this case, the equilibrium energy levels *are* shifted according to Eq. 8.2. However, we now understand that the RF field cannot connect two fully decohered states with different magnetizations, such as C and E. Instead, in order to change m_z , while preserving $|\vec{m}|$, we must tilt the Bloch vector away from the vertical axis, and reintroduce some level of coherence into the system. Therefore, in Fig. 8-4(b), it is the energy of the transformation $C \rightarrow D$, that needs to be calculated in order to find the correct resonant RF frequency. So let us do that.

The inter-state s-wave interaction is described by the second-quantized hamiltonian density:

$$H_{\text{int}} = V_{12} \psi_1^\dagger(\mathbf{r}) \psi_2^\dagger(\mathbf{r}) \psi_2(\mathbf{r}) \psi_1(\mathbf{r}). \quad (8.3)$$

The mean field expectation value of this hamiltonian is:

$$\mathcal{E}_{\text{int}} = \langle H_{\text{int}} \rangle = V_{12} (n_1 n_2 - n_{12} n_{21}) \quad (8.4)$$

where $n_1 = \langle \psi_1^\dagger \psi_1 \rangle$, $n_2 = \langle \psi_2^\dagger \psi_2 \rangle$, and we have introduced “coherences” $n_{12} = \langle \psi_1^\dagger \psi_2 \rangle$ and $n_{21} = \langle \psi_2^\dagger \psi_1 \rangle$. In a fully coherent sample $n_{12} n_{21} = n_1 n_2$, while in a fully decohered sample $n_{12} = n_{21} = 0$.

In terms of the coordinates of the Bloch vector, we can rewrite:

$$\begin{aligned} n_1 n_2 &= \left(\frac{n_1 + n_2}{2} \right)^2 - m_z^2 \\ n_{12} n_{21} &= m_\perp^2 \end{aligned} \tag{8.5}$$

The interaction energy is then given by:

$$\mathcal{E}_{\text{int}} = V_{12} \left(\frac{n^2}{4} - |\vec{m}|^2 \right) \tag{8.6}$$

where $n = n_1 + n_2$ is the constant total particle density. We see that the interaction energy depends *only* on $|\vec{m}|$. In a partially or fully decohered sample, $|\vec{m}| < n/2$, and the system is interacting. However, even then, the RF pulse does not *change* the total interaction energy. Hence, the RF photons do not need to supply any extra energy, and the resonance frequency is universally equal to the vacuum value.

8.1.2 Comparison with bosons

In [6], we have extended the above analysis to the RF spectroscopy of thermal bosons. This calculation is included in Appendix E, and (even) further details will be given in the PhD thesis of Martin Zwierlein.

In the case of thermal bosons, RF spectroscopy also measures frequency shifts *different* from the equilibrium shifts of the energy levels. By now, this should not surprise us.

In a coherent superposition of two states, both the forward and the exchange inter-state scattering is allowed. The contribution to the mean field energy is then twice larger than in a decohered sample, where the particles are distinguishable, and the only coherent (inter-state) collision process is the forward scattering.

However, analogous to the Fermi case, RF methods always measure the coherent result, independent of the level of coherence in the sample. In this case, this corresponds to a “coherent factor of 2”. This effect has recently been observed by the group of Eric Cornell [113], and was initially qualified as a “mystery” [114].

Using the Bloch sphere representation, we have provided an intuitive resolution of this puzzle. One should however note that the mystery was formally resolved by more sophisticated calculations which have preceded our work [115–119].

8.2 Spectroscopy of cold collisions in a three-level system

In order to spectroscopically observe the effects of coherent collisions in ^6Li spin mixtures, we have implemented a three-level method illustrated in Fig. 8-5. Here, a superposition of states $|1\rangle$ and $|2\rangle$ is created by an RF drive, and allowed to decohere into a statistical mixture [5, 9]. We then perform RF spectroscopy of the $|2\rangle \rightarrow |3\rangle$ transition. This technique

was independently introduced by the group of Debbie Jin for studies of interactions in ^{40}K [27].

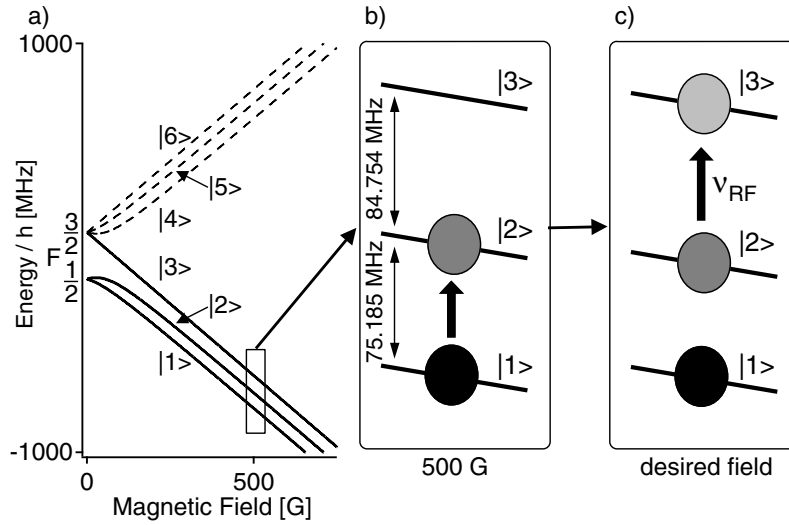


Figure 8-5: RF spectroscopy in a three-level system. (a) Hyperfine structure of the ground state of ^6Li . (b and c) Experimental scheme: (b) A statistical mixture of atoms in states $|1\rangle$ and $|2\rangle$ is prepared at 500 G. (c) RF spectroscopy of the $|2\rangle \rightarrow |3\rangle$ transition is performed at various magnetic fields.

The discussion of Section 8.1 is still completely applicable to the $|2\rangle - |3\rangle$ two-level system, and the interactions between atoms in these two states do not affect the spectroscopic measurements.

However, any superposition, or a statistical mixture, of states $|2\rangle$ and $|3\rangle$ is (equally and completely) orthogonal to state $|1\rangle$. Hence, during the RF transfer, the interaction energy of the $|2\rangle - |3\rangle$ atoms, due to forward scattering with $|1\rangle$ atoms, depends only on the relative populations of the two states. In the mean field approximation, this contribution to the interaction energy density is given by:

$$\frac{4\pi\hbar^2}{m}n_1(a_{12}n_2 + a_{13}n_3) \quad (8.7)$$

In contrast to Eq. 8.1, here we do not have to assume anything about the coherence of the $|2\rangle - |3\rangle$ system.

In the language of the $|2\rangle - |3\rangle$ Bloch sphere, this interaction energy now depends on m_z rather than $|\vec{m}|$. Since m_z does change during the RF transfer, the effects of the interactions are observable spectroscopically. We expect the $|2\rangle \rightarrow |3\rangle$ resonance to be shifted according to:

$$\Delta\nu = \frac{2\hbar}{m}n_1(a_{13} - a_{12}) \quad (8.8)$$

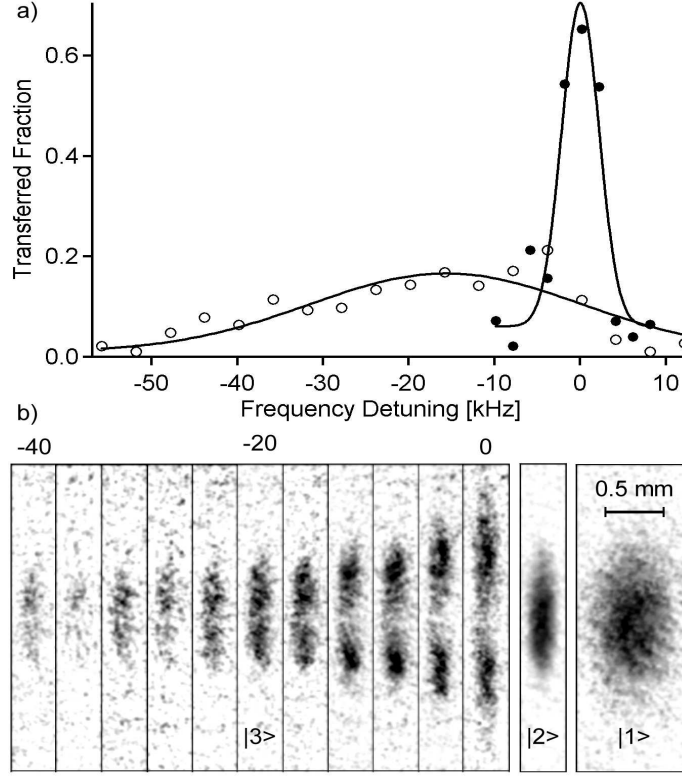


Figure 8-6: Spectroscopic measurement of the interaction energy at 480 G. (a) Fraction of atoms transferred from $|2\rangle$ to $|3\rangle$ in the center of the cloud, with $|1\rangle$ atoms absent (filled circles), and present (open circles). Solid lines are gaussian fits to the data. (b) Absorption images of state $|3\rangle$ for the interaction perturbed resonance. Images of states $|2\rangle$ and $|1\rangle$ are shown only for zero RF detuning. States $|3\rangle$ and $|2\rangle$ were imaged simultaneously to observe their complementary spatial structure. State $|1\rangle$ was imaged after $760\ \mu\text{s}$ expansion time to record its population.

An example of a spectroscopic measurement using the three-level method is shown in Fig. 8-6. Two spectra were taken at $B = 480\ \text{G}$, one with $n_1 = 0$, and one with $n_1 \sim 2.4 \times 10^{13}\ \text{cm}^{-3}$. The $n_1 = 0$ measurement was used to calibrate the vacuum resonance frequency ν_0 . In the interacting system ($n_1 \neq 0$), the spectrum is both shifted and broadened. To reduce the effect of the spatial inhomogeneity of n_1 , only the central part of the cloud was used to compute the fraction of atoms transferred from $|2\rangle$ to $|3\rangle$ [5].

Figure 8-6(b) displays the absorption images of the $|3\rangle$ cloud for $n_1 \neq 0$, and different applied RF frequencies. While the radial density distribution is averaged out during the $140\ \mu\text{s}$ RF pulse and the $120\ \mu\text{s}$ expansion time, the axial distribution is clearly visible. For zero detuning from ν_0 , only the atoms in the low density wings of the cloud are transferred. As we tune the RF frequency away from ν_0 , the transfer efficiency in the wings decreases, while the transfer efficiency in the center of the cloud initially grows and peaks for a detuning of $\sim -15\ \text{kHz}$.

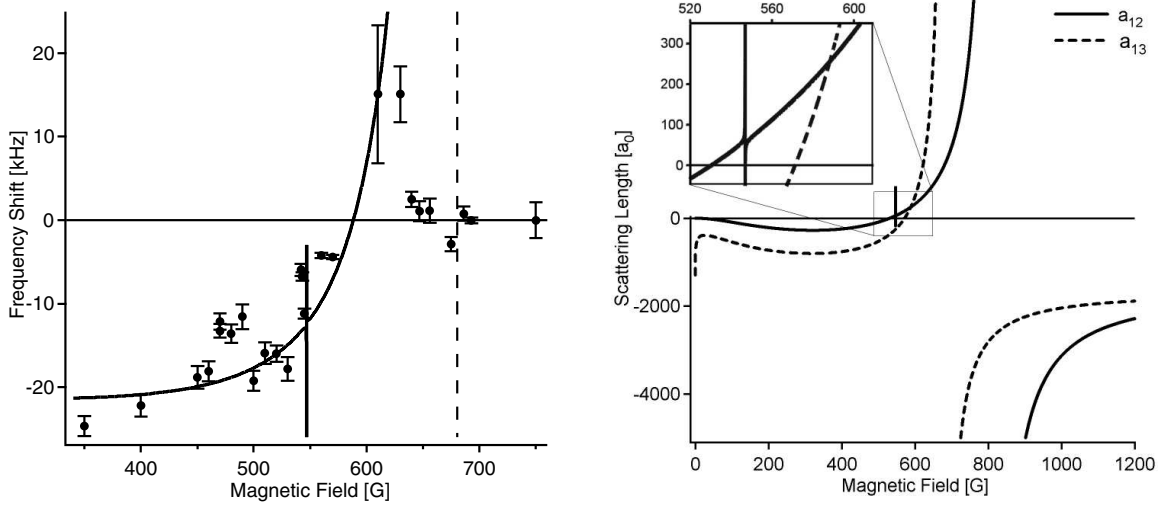


Figure 8-7: Spectroscopic frequency shifts as a function of the magnetic field. (a) Frequency shifts of the $|2\rangle \rightarrow |3\rangle$ resonance due to the presence of atoms in state $|1\rangle$. The fit at low fields (solid line) uses Eq. 8.8 with $n_1 = 2.2 \times 10^{13} \text{ cm}^{-3}$ and the theoretical calculations of the scattering lengths. The dashed line indicates the position of the predicted a_{13} resonance. (b) The latest calculations of the a_{12} and a_{13} s -wave scattering lengths as a function of the magnetic field [120]. a_{12} has a narrow Feshbach resonance at 550 G and a wide one at 810 G. a_{13} has a wide Feshbach resonance at 680 G.

The summary of our measurements at different magnetic fields is shown in Fig. 8-7(a). At low fields, the data are fitted using the mean field prediction of Eq. 8.8, with the latest calculations of a_{12} and a_{13} [5, 120], shown in Fig. 8-7(b)⁴. However, in the most interesting region, above ~ 630 G, our results are clearly strongly deviating from the mean field description of a weakly interacting system.

8.2.1 Strongly interacting and high density limit

The mean field result of Eq. 8.8 relies on two assumptions:

- (1) That the two-body interactions are weak, $k|a| \ll 1$. In this limit, the interactions are energy independent, and $\text{Re}(f) \approx -a$.
- (2) That the effective gas density is low, $|na^3| \ll 1$.

Near the Feshbach resonance, both of these assumptions can be invalidated. Further, in a degenerate Fermi gas, the two conditions are qualitatively the same, since $n \sim k_F^3$.

In Ch. 4, we have seen how the strong two-body interactions can be properly described for all values of ka . However, we do not know how to properly account for the simultaneous breakdown of the low-density approximation. This is a job for the many-body theorists [21].

⁴Note that this is the third plot of the $|1\rangle - |2\rangle$ Feshbach resonance in this thesis (see Figs. 5-1 and 6-2). As I mentioned at the beginning of Ch. 5, the theoretical predictions are constantly updated by the new experimental inputs. The calculations displayed here make use of all the presently available ^6Li experimental data.

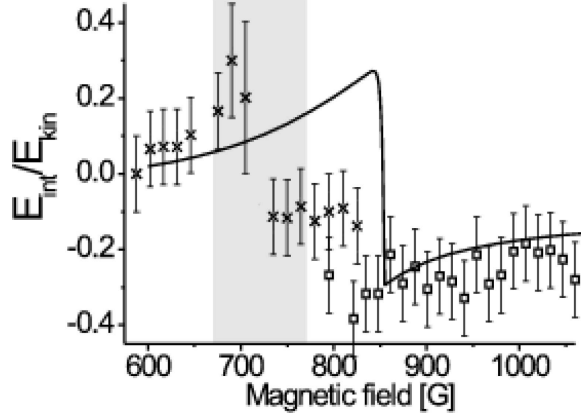


Figure 8-8: Expansion measurements of the $|1\rangle - |2\rangle$ interaction energy by Bourdel *et al.*, taken from [28]. The ratio of interaction to kinetic energy is plotted as a function of the magnetic field. Crosses and squares correspond to measurements in differently prepared samples, while the solid curve shows a mean field calculation. See [28] for details.

It seems natural that in the limit $|a| \rightarrow \infty$, this scale does not enter the problem explicitly, and is replaced by some real length scale, such as $1/k$ or the inter-particle separation. In a degenerate Fermi gas, these two scales are the same, $1/k_F$. The question is whether in this limit, the physics is still sensitive to the sign of a . If we just treat the two-body interaction properly in the unitarity limit, and average $\text{Re}(f)$ over the momentum distribution, we will conclude that it is. As I mentioned in Ch. 4, we find $\langle \text{Re}(f) \rangle \sim -\text{sgn}(a)(1/k_F)$ [9, 26]. Using this result, we can at least qualitatively explain our measurements in the 630 – 680 G region. For these magnetic fields, both a_{12} and a_{13} are large and positive. Therefore, the two contributions to the frequency shift of the $|2\rangle \rightarrow |3\rangle$ transition saturate at a common large value, and exactly cancel.

However, for fields above 680 G, a_{12} and a_{13} are large, and have opposite signs. Therefore, the two frequency shifts should add up to a large negative value. However, we still observe essentially no shifts. Our observations are at least qualitatively consistent with the expansion measurements of the interaction energy in a $|1\rangle - |2\rangle$ mixture by Bourdel *et al.* [28], shown in Fig. 8-8. In that experiment, the interaction energy was found to be constant and negative for magnetic fields up to 80 G below the a_{12} resonance. Also, the change of the sign of the interaction energy was abrupt, similar to the sudden disappearance of the frequency shift at ~ 630 G in our measurements (Fig. 8-7(a)). In order to explain our data, we would have to assume that the two contributions to the $|2\rangle \rightarrow |3\rangle$ frequency shift have the same sign and magnitude at all fields above 630 G.

Some many-body theorists have suggested that in the high density regime, $|na^3| \gg 1$, the interaction energy should indeed be universally negative and constant in the vicinity of a Feshbach resonance, on both of its sides [121, 122]. Other authors have proposed that this effect could be related to the presence of molecules on the positive side of the

resonance [28, 30]. However, my general feeling is that the experimental observations are still not well understood.

Chapter 9

Conclusions and outlook

*The bartender says we don't serve robots
And the robot says, oh but someday you will*
D.C. Berman, *Frontier Index*

The ongoing quest for fermionic superfluidity in a gaseous system is currently one of the most exciting research topics in all of atomic physics. The eventual attainment of this goal will involve many demanding experimental steps. Ultimately, we need to create a stable, deeply degenerate spin mixture of fermions, in which the interactions are strong and attractive. In this thesis, I have described our progress in achieving these tasks.

The first part of the thesis described our advances in the cooling of ^6Li fermions deep into quantum degeneracy. The success of our lithium cooling strategy relied on the use of a large ^{23}Na bosonic cloud as a refrigerant for sympathetic cooling. In order to improve our refrigerator, we have also achieved first condensation of sodium in the upper, $F = 2$ hyperfine state by evaporative cooling. This allowed us to magnetically trap and cool a mixture of sodium and lithium atoms which is stable against inelastic spin-exchange collisions at all densities. At present, our system produces the largest and the coldest Fermi samples, as well as the largest Bose-Fermi mixtures [2].

In the second part of the thesis I have discussed our studies of strongly interacting fermions [3–6]. We have produced and studied optically trapped spin-mixtures of ^6Li in the vicinity of the magnetic field Feshbach resonances, where the phase transition to a superfluid state is predicted to occur.

In our first study of this regime, we have investigated the stability of the system against inelastic losses. We have shown that, in contrast to bosonic gases, a mixture of the two lowest ground states of ^6Li exhibits sufficient stability in the strongly interacting regime to allow further studies and the possible observation of superfluidity [3]. In these experiments, we have also identified a new Feshbach resonance, which was not theoretically predicted prior to our work [23].

In the second set of experiments, we have established RF spectroscopy as a method to measure the interaction energy in ^6Li spin-mixtures arising from coherent collisions between atoms. As part of this work, we have also demonstrated the absence of mean field “clock shifts” in a two-state mixture of fermions [5, 6], which may be important for future improvements of atomic clocks. Interaction energy shifts could be observed by extending our scheme to a three-level system [5].

Our spectroscopic measurements of the interaction energy shifts in the strongly interacting regime have yielded some surprises, with the interaction energy seemingly being universal to a surprisingly high degree, independently of both the strength and the repulsive or attractive nature of the two-body interactions. While our findings are consistent with other experiments [28], they still present a challenge to the theorists.

Experimentally, the next challenge is to combine the deep degeneracy of our magnetically trapped ^6Li samples, with the tunability of interactions in the optically trapped spin-mixtures.

However, we will also need further theoretical insight in order to progress. Most importantly, we need to identify an effective and unambiguous way to detect the superfluid phase transition. With several groups, including ours, already reaching the conditions at which the transition may occur, this issue is becoming increasingly urgent. We are currently considering whether our RF spectroscopic methods can be used to observe the pair breaking energy in the superfluid state [123, 124].

Finally, we should expect several related research avenues to open in parallel with the ongoing efforts to achieve superfluidity in a (quasi-)uniform gas. Here I briefly mention three topics which will almost certainly be important in the near future:

Bose-Fermi mixtures

So far, most Bose-Fermi experiments have concentrated on studies of the degenerate Fermi gas, and bosons have mostly been used only as a refrigerant for fermions. Studies of non-trivial physics in Bose-Fermi mixtures have been limited to theory [125] and a single experimental paper, which explored collapse of a harmonically trapped ^{40}K degenerate Fermi gas due to attractive interactions with a ^{87}Rb Bose cloud [126]. Future studies of the degenerate mixtures may open a whole new parameter space for finding exotic many-body states.

Optical lattices

Ultimately, the most exciting studies of strongly correlated systems will almost certainly involve optical lattice trapping potentials. In the case of bosons, this technique has already yielded fascinating results in the observation of the superfluid to Mott insulator transition [127]. Optical lattices may soon become important both for the research with Bose-Fermi mixtures, and for alternative ways of achieving fermionic superfluidity [41].

Molecules

We have recently learned that diatomic ^6Li molecules created by sweeping the magnetic field through a Feshbach resonance have a lifetime of almost a second [30]. This is a very pleasant surprise, given that they are in the last bound, highly excited vibrational state, and we would expect them to undergo a rapid inelastic relaxation. This surprising metastability may offer a window of opportunity for evaporative cooling and Bose-Einstein condensation of molecules. Conversion of molecules back into strongly correlated atomic pairs may be another way of achieving the superfluid state. Finally, it would be as exciting to condense the molecules in their ground state. This is a serious experimental challenge for the future.

Appendix A

^6Li laser system baedeker

This appendix was written as a more technical companion to Section 2.4.4. As such, it is rather a collection of loosely connected topics, than a coherent story. The first section introduces the basics of diode lasers. The second section describes our scheme for referencing the master laser to a ^6Li atomic resonance. In the third section, I calculate the frequencies needed for imaging of ^6Li at high magnetic fields. Finally, I provide a technical drawing of the actual setup of the laser system.

A.1 Diode Lasers

A.1.1 Free Running Diode Lasers

Laser diodes are the central ingredient of our laser system. Here we introduce some of their basic characteristics and share some practical experiences. Our experience is limited to 670 nm laser diodes, and may not be more widely applicable. For a more general introduction to diode lasers and their uses in atomic physics, one can refer to the review article by Carl Wieman and Leo Hollberg [128]. A comprehensive source on lasers in general is the book by Anthony Siegman [129].

Main Properties

When current is injected into the depletion region of a $p-n$ semiconductor junction, electron-hole pairs are recombined and photons corresponding to the band gap of the semiconductor material are emitted. The gain profile of the material can be up to 20 nm broad, but mode competition will select one or a few modes near its peak. This is the basic principle behind the operation of a diode laser, although more complicated layered semiconductor structures are used in commercial products.

A diode laser basically consists of a semiconductor diode mounted on a temperature stabilizing block. Mounts based on a Peltier element are commercially available and contain a temperature monitor and contacts for current injection.

At this point only the cleaved surfaces of the semiconductor serve as the laser mirrors. The size of this laser cavity is typically $d \sim 1$ mm, corresponding to mode spacing of $\Delta\nu = c/2d \sim 100$ GHz. We measure the linewidth of the laser to be in the 100 MHz range, much larger than the 6 MHz natural linewidth of ^6Li . To make things worse, the diode may not be lasing in a single mode, and will certainly not stay on a single mode over long times. The maximum power that this type of laser can output in a continuous wave mode is about 50 mW.

The laser linewidth should be distinguished from the “cold” cavity mode width. The latter measures the range of frequencies that the cavity will support and is given simply by the single photon lifetime inside the cavity. A cavity that is as leaky as reflective has a finesse no better than 2 or 3, and the corresponding mode width should be several tens of GHz.

Temperature Control

The band gap of the diode semiconductor material, and hence the wavelength of the emitted light can be somewhat tuned by changing the temperature. In our experience, typical temperature dependence of 670 nm diodes is about 0.15 nm/K, with higher temperatures corresponding to longer wavelengths. Without much complication, diodes can be operated at least 30 K away from room temperature, giving a temperature tuning range of about ± 5 nm.

Commercially available controllers can stabilize the temperature stable to better than 0.01 K.

Current Control

A typical diode requires a threshold injection current of about 50 mA to start lasing. This threshold marks the separation between the stimulated and the spontaneous emission regimes, and between a laser and a simple LED. The laser’s maximum output power is reached at about 100 mA.

The ~ 1 mW/mA scaling can be directly linked to the fact that a red photon has about 3×10^{-19} J of energy, while the charge of the electron is 1.6×10^{-19} C. The fact that this rule of thumb does hold reasonably well also tells us that conversion of electron-hole pairs into photons is a pretty efficient process, certainly in the several tens of percent ballpark. This high efficiency can be characteristic only of direct gap semiconductors. In indirect gap materials, photon emission relies on phonon assistance, and they should make rather poor lasers.

The threshold current increases with increasing temperature. Therefore, in order to achieve a satisfactory power output, we generally operate heated diodes at a higher current than is advised by the manufacturer. This is generally OK, if we keep the following warning in mind. The slope of power vs. current beyond the threshold point, which measures the

conversion efficiency, generally does not change with temperature. We can keep increasing the current as long as this slope remains constant. Eventual decrease in the slope with increasing current can be interpreted as a “runaway threshold” behavior - higher current increases the local junction temperature through Joule heating and hence increases the threshold point even though the temperature is nominally set to the same value. We interpret this as a warning to stop pushing the current further.

Since the injection current affects the local heating of the junction, varying its value will tune not only the intensity but also the frequency of the light. This dependence is on a GHz/mA scale.

Like their temperature counterpart, current controllers are also commercially available, and will keep the chosen injection current stable to better than 0.1 mA.

Beam Shape

The cross-section of a diode’s active region, perpendicular to the direction of propagation, is of rectangular shape, with an aspect ratio of about 3. In this way, the gain is bigger along one axis and the emitted light has a well defined linear polarization along that direction. Dimensions of the active region are rather small, of the order of $1\text{ }\mu\text{m}$. Correspondingly, the output beam has rather large diffraction limited divergence angles, of the order of 10° . Thus the beam needs to be immediately collimated with a short focal length lens.

Our diodes have divergence angles along the directions parallel and orthogonal to the polarization axis of about 8° and 20° respectively. Using a 4.5 mm lens, we collimate the laser beams to an elliptical, $5 \times 2\text{ mm}$ shape. By adjusting the position of the lens carefully the beam can usually be collimated over a distance of several meters. Since usually a circular beam profile is preferred, we then use a combination of two prisms, known as an anamorphic prism pair, to expand the short axis of the beam by a factor of 2.5, without affecting the long one.

Reliability and Lifetime

People much more experienced than us know that there are 1001 ways to kill a diode [128]. So far we have been fortunate not to discover too many of them.

In our experience, the fate of a laser diode has been determined in the first few hours of operation. Or attempted operation. Occasionally a diode would appear to work fine, but would be impossible to collimate. This might be a sign that it has been electrocuted before it was mounted. Sometimes a nicely collimated diode will turn out to have a bad mode hop that makes it impossible to use at the desired wavelength. Further, sometimes the manufacturer will specify only the nominal wavelength of the diode, and not the measured value for the particular sample. The two can be different by several nanometers, and the experimentalist can be in for a bad surprise. As a general rule, one should try to purchase many replacement diodes and try them out. Given their low cost (usually below \$100), this

is not a big problem. Once a good diode is found, and then carefully operated, it can give thousands of hours of reliable operation.

One safe way to kill a diode is to run too much current through it or to allow high transients during switching. Fortunately, commercial current controllers have the option to limit the maximum current, and have built in “soft” switches. Short of power failure during operation, this should provide enough safety. If one is forced to heat the diode in order to tune its wavelength, the threshold current will increase, and the output power at the manufacturer recommended operating current will drop. It is then naturally tempting to increase the current. We have certainly done this for diodes heated up to 50°C , and have always managed to recover the nominal output power. We would however suggest that the current is increased carefully, and the power is constantly monitored, watching out for the runaway threshold behavior we described earlier. Similarly, if cooling of the diode is needed, it should probably be checked whether the maximum current should be reduced.

Another common wisdom is that heating a diode will shorten its lifetime “drastically”. However the issue of what exactly are the time scales involved does not seem to be an exact science.

Optical Isolators

Finally, it is important to note that laser diodes are very sensitive to optical feedback. Since the internal feedback is weak due to a poor cavity, the laser will be affected by any external light that falls within the very broad gain profile of the diode material. Controlled feedback can be used to improve the laser characteristics, as we will discuss in the following sections. However, it is crucial to protect the diode from any accidental uncontrolled feedback. Part of the laser’s own light reflected back into the diode from somewhere in the optics setup, can disrupt and even kill the diode. Protection of the diode is conventionally done by placing a “Faraday isolator” immediately in front of the laser. In brief, the central part of an isolator is a crystal, surrounded by a permanent magnet, which rotates the laser polarization through 45° . This part is sandwiched between two polarizers positioned at 45° with respect to each other. The key point is that polarization is rotated in the same sense independent of the direction of light propagation [130]. Therefore the isolator acts as an optical diode. In the forward direction, all the light (with polarization aligned with the input polarizer) is transmitted, whereas the backwards travelling light is blocked with isolation up to 40 dB.

Summary

To summarize, the basic (670 nm) diode laser setup consists of a diode mounted on a cooling/heating block, temperature and current controllers, collimating and beam shaping optics, and an optical isolator. Its output is a circular 5 mm beam, with linear polarization,

power up to 30 mW distributed over several modes, linewidth of about 100 MHz, and no long term stability.

A.1.2 Grating Stabilization

One way to improve the spectral characteristics of a free running laser diode is to put it into an external cavity. A Littrow configuration illustrated in Fig. A-1 is an example of a solution in this spirit. A collimated laser beam is incident on a holographic grating aligned so that the first diffraction order is reflected back into the diode. The zeroth order, containing about 50% of the diode power, constitutes the output of the laser. Therefore the cavity is now essentially formed by the back facet of the diode and the grating, and has a typical size of $L \sim 1$ cm. Cavity modes are now separated by about 10 GHz, and are a few GHz wide. The linewidth of our TuiOptics DL100 grating stabilized laser is about 1 MHz.

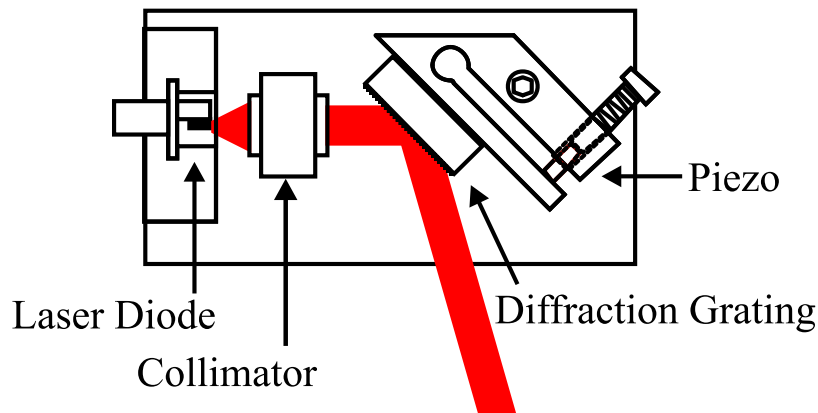


Figure A-1: Grating stabilized laser system in a Littrow configuration.

One new scale now appearing is the gain profile of the grating, which is broadened by the fact that only a finite number of grating periods is illuminated by the laser beam. For a 5 mm beam, about 10^4 grating periods are used, and thus the grating resolution (essentially given by the ratio of optical wavelength and the number of grating periods) is around 50 GHz.

Coarse wavelength selection of this type of a laser is done by rotating the grating, which is mounted in such a way that the changes in the length of the cavity match the changes in the wavelength selected by the grating angle. As long as the laser's behavior is governed by the external cavity, its wavelength can be pulled up to 7 nm away from the free running value. The quantitative measure of the grating feedback is the lowering of the threshold current from the free running value by up to 10 %. At the next level of precision, different modes can be selected by varying the laser temperature and current. The summary of different frequency scales is given in Fig. A-2. Good lasing at the desired frequency is achieved when the different gain and mode profiles overlap as shown.

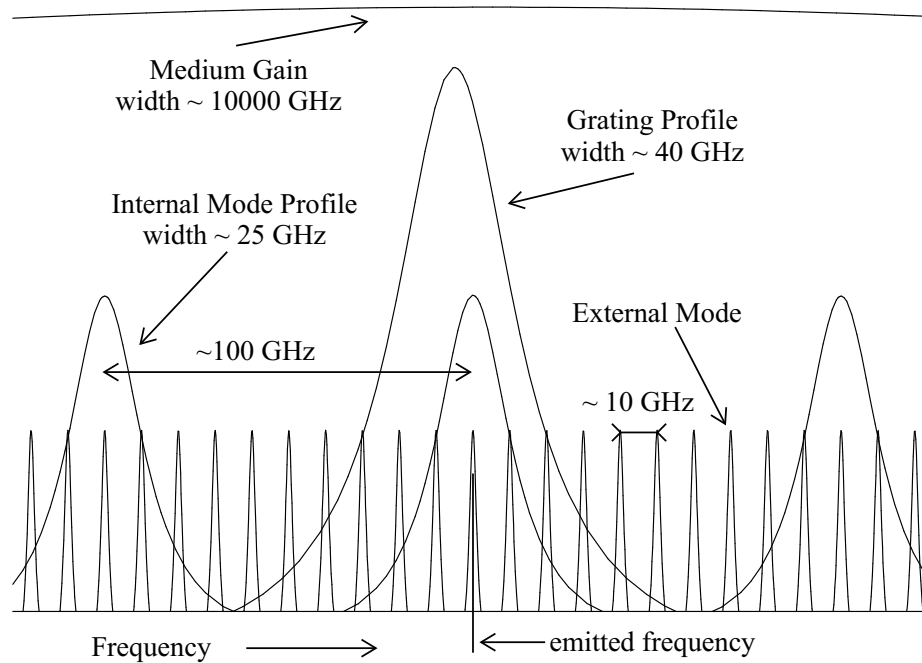


Figure A-2: Summary of frequency scales in a grating stabilized laser.

Once the desired wavelength has been selected to within several GHz and the feedback has been optimized, the final tuning can be done by applying voltage to the piezoelectric transducer at the back of the grating mount. This method can also be used to scan the laser frequency over the same range, at rates up to 1 kHz.

Generally speaking, grating (re)alignment needs to be done maybe twice a year. The fact that it needs to be done at all is a sign of either (generally unpredictable) diode aging effects, or the fact that the laser has been accidentally bumped into. Temperature of the diode is changed somewhat more often, probably in order to compensate for smaller aging effects. Playing with the current and the grating voltage is a daily procedure, taking not more than a few minutes.

A.1.3 Injection Locking

Another way to improve the spectral characteristics of a free running laser diode is to inject a small amount of high spectral quality light into it. As long as the injection light is compatible with the (rather loose) constraints of the diode gain profile and internal resonator, it will easily win the mode competition.

Optical isolators usually use polarizing beam splitter cubes as their input and exit polarizers. This provides an excellent entrance port for the seeding light. If light of appropriate polarization is sent into the exit polarizer from the side, it will be reflected into the isolator.

Further, since it has the opposite polarization from the light that would have entered it *en face*, it will be rotated in such a way that it will exit the polarizer at the entrance end without being attenuated. In addition, due to imperfect polarization, a small amount of slave light is rejected by the exit polarizer, and can be used as a perfect counter propagating tracer beam for alignment. We have replaced the exit polarizers of our optical isolators with free standing polarizing beam splitter cubes to provide easier optical access, and overlap of the seeding and the slave light. This arrangement is sketched in Fig. A-3.

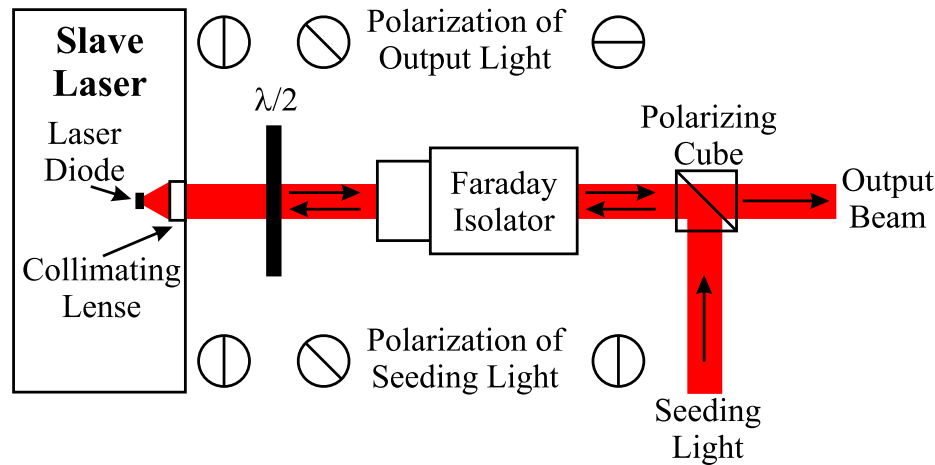


Figure A-3: Seeding of a diode laser.

Effects of seeding are best monitored with a Fabry-Perot spectrum analyzer. The first sign that the seeding beam is entering the slave diode is visible heating, pushing the slave frequency to the red. If this effect is maximized, we can be pretty sure that the spatial overlap of the two beams is optimized. At that point, a narrow spectral line will already appear among the broad features of a free running slave. Varying the slave current slightly will then transfer all the laser power into the seeded mode. As with the grating stabilization, good injection locking will also manifest itself in a reduction of the threshold current, and hence an increase in the power output.

For long term seeding stability, it is favorable that the distance between the master laser and the slave is minimal. At the same time, for good alignment of the seeding beam, it is best that it is overlapped with the tracer beam over the longest possible distance. This conflict can be resolved in the following manner. We align the slave laser output with some distant object. An obvious choice is the tracer beam of the wavemeter, with which the laser needs to be aligned anyway. Then we crudely align the seeding beam, so that it goes nicely through the optical isolator, and into the slave's collimating package. At that point, if we turn down the slave current, the small reflection of the seeding beam off the collimating lens is visible and almost aligned with the wavemeter tracer beam. By then

carefully aligning the two, we are certain that the seeding beam is also perfectly overlapped with the slave beam. At this point simply turning up the slave current will almost invariably reveal good seeding.

A.2 Locking of the master laser to the ^6Li atomic resonance

For long term stability we lock our Master laser to the ^6Li atomic vapor resonance. At room temperature, the Doppler width of the atomic vapor is on a GHz scale, and some form of Doppler free spectroscopy needs to be employed. We use optical pumping spectroscopy, which is a slight variation on the textbook saturated absorption method. The setup is summarized in Fig. A-4. The pump and the probe beam are counter propagated through a ^6Li vapor cell and the transmission of the probe beam as a function of the laser frequency is recorded by a photodiode.

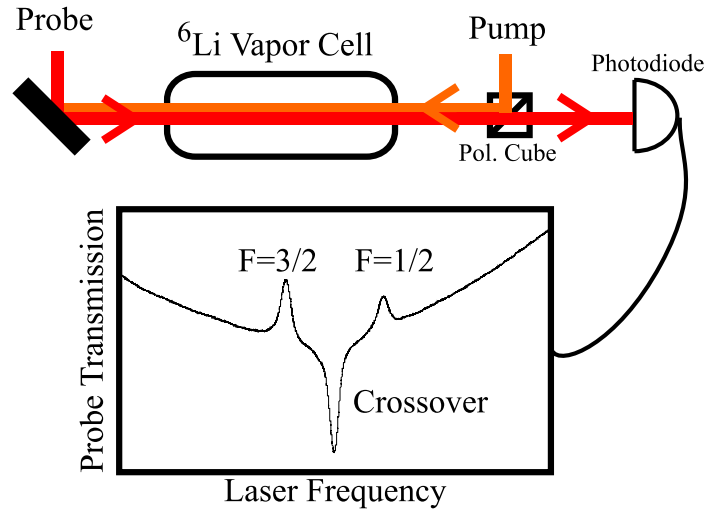


Figure A-4: Saturated absorption spectroscopy setup. Three Doppler free features are seen on top of the broad Doppler profile.

Optical Pumping Spectroscopy in a Three Level System

The origins of the Doppler free features seen in Fig. A-4 are visually summarized in Fig. A-5. At a general frequency, pump and probe beams are resonant with different velocity classes and there is no effect on the probe absorption. This gives the $\sim \text{GHz}$ broad Doppler profile. If the laser is resonant with one of the two atomic lines, both beams are competing for the zero velocity atoms and the absorption of the probe is reduced. These are the standard Lamb dips, except that the absorption reduction comes not from the fact that atoms spend a large fraction of the time in the excited state, but simply from the fact that they are pumped over into the other ground state. When the laser is tuned half way between the two resonances, the pump and the probe talk to the same velocity class, in two different ground

states. This way, the pump beam will actually increase the population of the ground state that the probe is resonant with, and the probe absorption will be enhanced. This feature is known as the crossover peak. Since atoms in both ground states contribute to it, the crossover is actually the most pronounced feature and is the one we use for locking. Atoms contributing to this feature have a Doppler shift of 114 MHz, corresponding to a velocity of about 70 m/s. Since this is much less than the width of the thermal distribution, their population is essentially the same as that of the zero velocity atoms, and this does not result in any relative reduction of the signal.

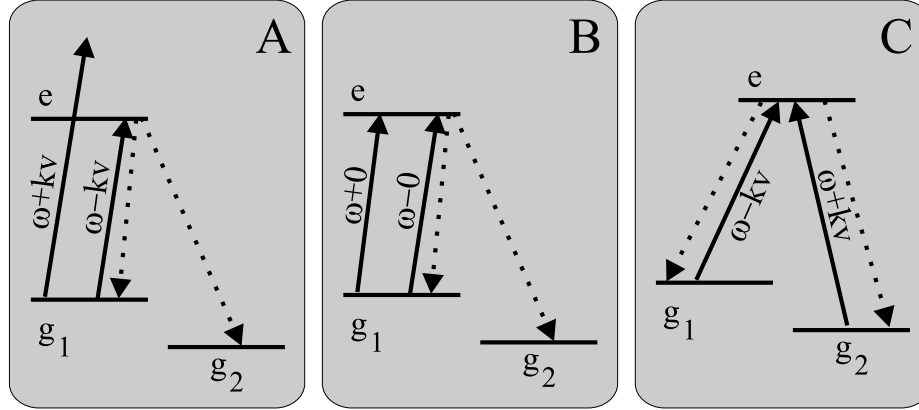


Figure A-5: Principle of saturated absorption (or optical pumping) Doppler free spectroscopy. (A) Broad Doppler background: The velocity class that is resonant with the probe beam is not resonant with the pump. (B) Lamb dip: The laser is on one of the two resonances - the probe and the pump both compete for the zero velocity class atoms. (C) Crossover peak: The laser is half way between the two resonances - the pump puts more atoms in resonance with the probe.

⁶Li Vapor Cell

Lithium vapor cells require a bit more effort than those of most other alkali gases. Firstly, in order to get a sufficient vapor pressure for a good locking signal, lithium must be heated to about 350 °C. Secondly, lithium is on rather bad terms with glass, and it is important to keep the vapor away from the windows that are used for optical access. Our first cell, an all-glass design based on work by Libbrecht *et al.* [131], had a lot of problems with coating of the windows with lithium, and was eventually shelved. Our final design is a simple 40 cm long metal cell with plain vacuum windows. A few grams of lithium metal is placed in the middle part of the cell, which is wrapped in tape heaters. In order to keep lithium away from the windows we load the cell with about 100 mTorr of argon buffer gas. The optimal argon pressure was empirically determined so that lithium fluorescence is well localized to the central part of the cell, while the pressure broadening of the Doppler free features is not too drastic, roughly within 20 MHz.

The Lock Point

The offset between the desired laser frequency and the crossover line is chosen by AOMs inserted into both the pump and the probe beam. For tuning up to tens of MHz, it is sufficient to change the frequency of one of the beams. The pump and the probe will then have different frequencies, but all our previous arguments still hold, just with the “zero velocity” being redefined to mean the “velocity corresponding to half the difference between the pump and the probe frequencies”. As long as this is much less than the width of the thermal distribution, everything will be fine. To this end, the pump AOM is set up in a double pass configuration, so that the lock point can easily be changed without changing the alignment of the setup (see Fig. A-8).

As the lock point, we choose the frequency of the MOT cooling transition, about 25 MHz below the $F = 3/2 \rightarrow F' = 5/2$ cycling transition.

The error signal

In order to lock the master frequency, we need an ‘error signal’, proportional to the difference between the current frequency and the lock point. The absorptive signal shown in Fig. A-4 is not suitable for this. While one could choose to lock to the slope of the crossover peak, the lock point would then depend on laser power and the vapor pressure in the gas cell. Instead, we lock to the position of the crossover peak, by turning the absorptive signal into a dispersive one. To achieve this, the pump frequency is modulated at a rate of 50 kHz, with an adjustable amplitude $\Delta\omega \sim 5$ MHz. A (Stanford Research Systems) lock-in amplifier is used to provide the oscillator signal to the pump AOM. The probe absorption signal is then fed into the lock-in amplifier which integrates out its 50 kHz Fourier component in phase with the oscillator signal. The value of this Fourier component is the measure of the local slope of the absorptive signal, and in the limit of small $\Delta\omega$, this essentially corresponds to differentiation. Measured absorptive and dispersive signals are shown in Fig. A-6. Less than 1 mW of master laser power is more than sufficient to obtain the displayed signal to noise ratio. The lock-in integration time is 1 ms, and thus the error signal contains only components up to 1 kHz. This is somewhat limiting, but we have found in practice that it is sufficient.

Feedback to the Laser

Error signal from the lock-in amplifier is fed back to the laser, via a home built electronic PI (Proportional - Integral) gain box with a bandwidth of 1 kHz. The “restoring force” on the laser is mostly provided by the piezoelectric transducer attached to the grating. The response time of the transducer is about 1 ms, in agreement with the bandwidth of our error signal. We have however found that some feedback to the current controller increases the laser stability, and tightens the lock from about 4 MHz to about 1 MHz.

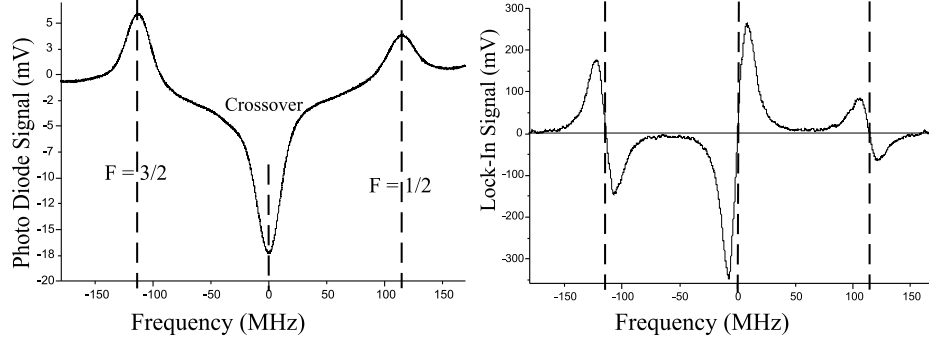


Figure A-6: Measured absorptive and dispersive Doppler free spectral features. The absorptive signal from a photodiode, and the dispersive signal from the lock-in amplifier are recorded on a digital oscilloscope.

A.3 Imaging frequencies at high magnetic fields

Ground, and $2P_{3/2}$ excited states of ^6Li at high magnetic fields are shown in Fig. A-7. In the following calculations, all the frequencies are referenced to the frequency of the zero field cooling transition $F = 3/2 \rightarrow F' = 5/2$, $h\nu_0 = E_e - E_g$. Further, all the calculations are done with the precision of the natural linewidth, $\Gamma = 6$ MHz.

Let us start with the ground states. We are interested in imaging states $|1\rangle$, $|2\rangle$, and $|3\rangle$ of the ground state $m_J = -1/2$ manifold. I will label their energies $E_{1,2,3}$ and reference them to the zero field energy of the $F = 3/2$ state, E_g .

State $|3\rangle$ is stretched, so we simply have $E_3 = E_g - h \times 1.4 \text{ MHz/G } B$. For the states $|1\rangle$ and $|2\rangle$, we solve the standard Breit-Rabi problem, and get:

$$E_1 = E_g - h \times 114 \text{ MHz} - h \times 114 \text{ MHz} \sqrt{1 + \frac{2}{3}x + x^2}$$

$$E_2 = E_g - h \times 114 \text{ MHz} - h \times 114 \text{ MHz} \sqrt{1 - \frac{2}{3}x + x^2}$$

where $x = B \times (1.4 \text{ MHz/G}) / 114 \text{ MHz}$. For best results, one should plot this one a computer. However, for fields above ~ 350 G, $114 \text{ MHz}/x^2 < \Gamma$, so we can expand to order $1/x$:

$$\sqrt{1 \pm \frac{2}{3}x + x^2} \approx x \pm \frac{1}{3} + \frac{4}{9x}$$

Further, for fields above ~ 350 G, we can, with Γ precision, replace $114 \text{ MHz} \times 4/(9x)$ with 6 MHz. So finally, for imaging purposes, we have:

$$\begin{aligned} E_1 &= E_g - h \times 1.4 \text{ MHz/G } B - h \times 158 \text{ MHz} \\ E_2 &= E_g - h \times 1.4 \text{ MHz/G } B - h \times 82 \text{ MHz} \\ E_3 &= E_g - h \times 1.4 \text{ MHz/G } B \end{aligned} \tag{A.1}$$

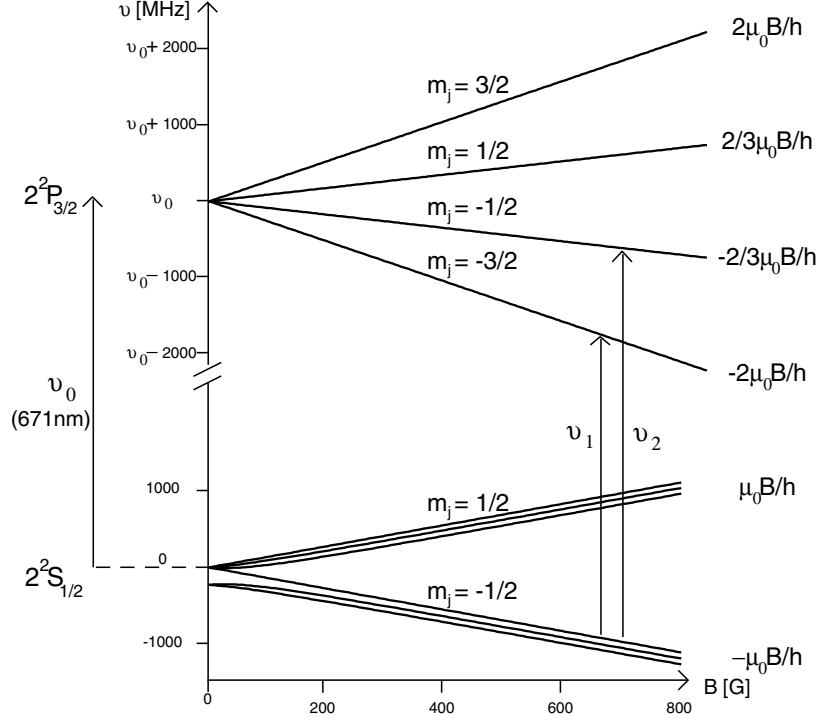


Figure A-7: Optical transitions in ${}^6\text{Li}$ at high magnetic fields. Atoms in the three $m_J = -1/2$ ground states can be imaged on the transitions to the excited states $m_J = -3/2$ (ν_1) or $m_J = -1/2$ (ν_2). Transitions to the $m_J = 1/2$ states are too far detuned from all the frequencies already available in the laser system.

Now let us look at the excited states. The hyperfine constant in the excited state of lithium is only ~ 1 MHz, and the resulting hyperfine structure is not resolved at low fields (see Section 2.4). Likewise, at high fields, different m_I states within the same m_J manifold are not resolved. The two transitions which are easiest to reach with AOMs are those to $m_J = -1/2$ and $m_J = -3/2$. We label the energies of these states $E_{-1/2}$ and $E_{-3/2}$, and reference them to the zero field energy of all F' states, E_e .

In ${}^6\text{Li}$, the fine splitting of the $2P$ state is also rather small, about 10 GHz. Therefore, at fields of interest, the $\vec{L} \cdot \vec{S}$ interaction already starts being decoupled. Hence, the $m_J = -1/2$ state has a small upwards quadratic shift because it is repelled from the $m_J = -1/2$ state of the $J = 1/2$ manifold. So, again we solve a simple Breit-Rabi problem, and then expand in the small parameter, except now the small parameter is B , rather than $1/B$. The $m_J = -3/2$ state is stretched, so no effort is required there. This calculation gives:

$$\begin{aligned} E_{-1/2} &= E_e - h \times \frac{2}{3} \times 1.4 \text{ MHz/G } B + h \times 0.44 \text{ MHz/G}^2 B^2 \\ E_{-3/2} &= E_e - h \times 2 \times 1.4 \text{ MHz/G } B \end{aligned} \quad (\text{A.2})$$

Subtracting Eq. A.1 from Eq. A.2, and remembering that $(E_e - E_g)/h = \nu_0$ is the MOT cooling frequency (tuned to resonance), we obtain all the needed frequency with sufficient

precision to be able to image the atoms. A further tuning of the imaging frequency, by a few MHz, can be done empirically.

Let us summarize all the six used frequencies:

$$\begin{aligned}
\nu_1^{-1/2} &= \nu_0 + \frac{1}{3} \times 1.4 \text{ MHz/G } B + 0.44 \text{ MHz/G}^2 B^2 + 158 \text{ MHz} \\
\nu_2^{-1/2} &= \nu_0 + \frac{1}{3} \times 1.4 \text{ MHz/G } B + 0.44 \text{ MHz/G}^2 B^2 + 82 \text{ MHz} \\
\nu_3^{-1/2} &= \nu_0 + \frac{1}{3} \times 1.4 \text{ MHz/G } B + 0.44 \text{ MHz/G}^2 B^2 \\
\nu_1^{-3/2} &= \nu_0 - 1.4 \text{ MHz/G } B + 158 \text{ MHz} \\
\nu_2^{-3/2} &= \nu_0 - 1.4 \text{ MHz/G } B + 82 \text{ MHz} \\
\nu_3^{-3/2} &= \nu_0 - 1.4 \text{ MHz/G } B
\end{aligned} \tag{A.3}$$

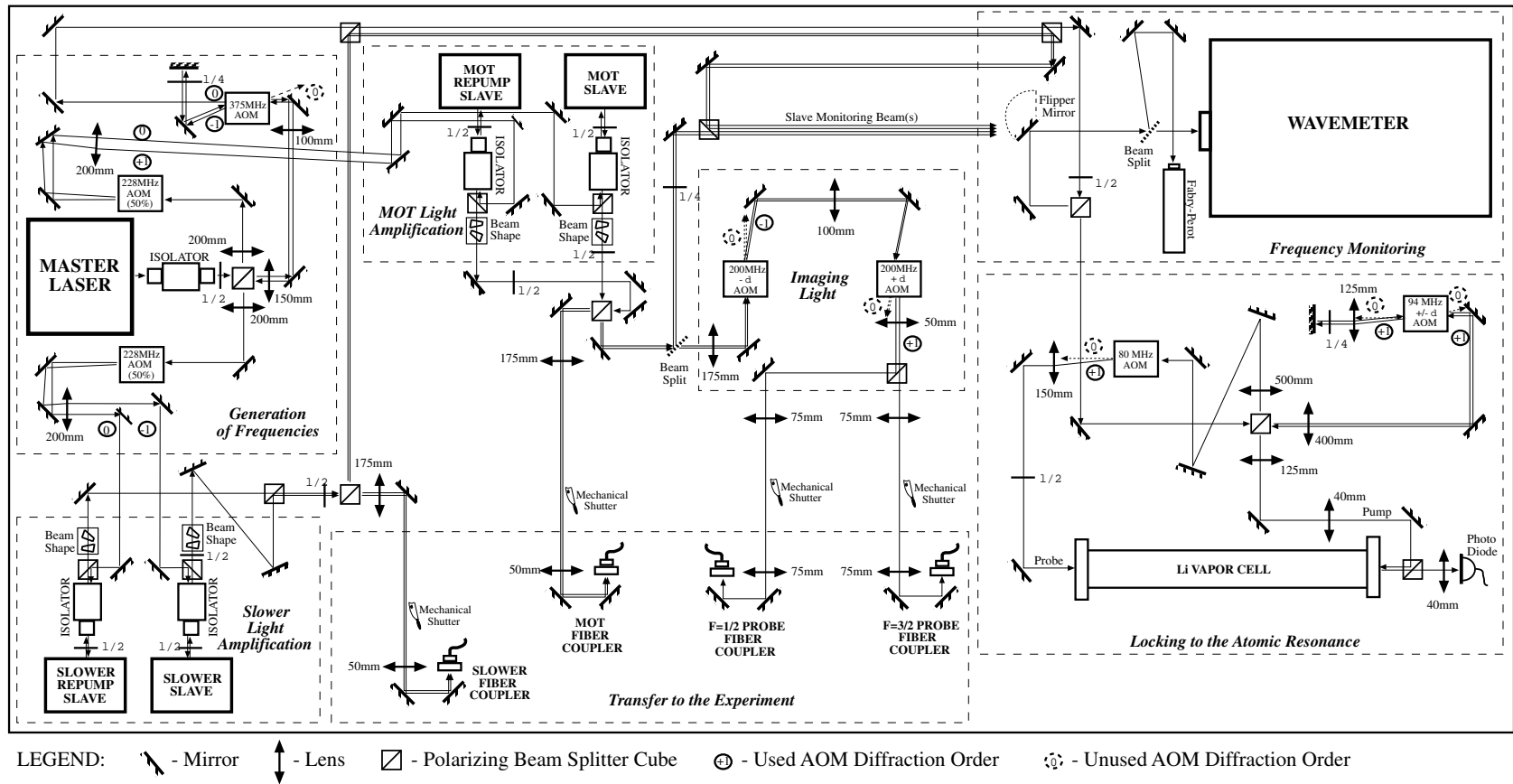
where the subscript labels the ground state, and the superscript labels the excited state.

A.4 Layout of the ^6Li laser system

Figure A-8 shows the real space arrangement of the ^6Li laser system, drawn roughly to scale. The dimensions of the optical table on which the system is assembled are 90×210 cm.

The part of the setup needed for imaging at high magnetic fields is not included, because it is currently being changed.

Figure A-8: Layout of the ^6Li laser system.



Appendix B

Two-Species Mixture of Quantum Degenerate Bose and Fermi Gases

This appendix includes the following paper [1]:

Z. Hadzibabic, C. A. Stan, K. Dieckmann, S. Gupta, M. W. Zwierlein, A. Görlitz, and W. Ketterle, “Two-Species Mixture of Quantum Degenerate Bose and Fermi Gases,” *Phys. Rev. Lett.* **88**, 160401 (2002).

Two-Species Mixture of Quantum Degenerate Bose and Fermi Gases

Z. Hadzibabic, C. A. Stan, K. Dieckmann, S. Gupta, M. W. Zwierlein, A. Görlitz,* and W. Ketterle

*Department of Physics, MIT-Harvard Center for Ultracold Atoms, and Research Laboratory of Electronics,
MIT, Cambridge, Massachusetts 02139*

(Received 26 December 2001; published 4 April 2002)

We have produced a macroscopic quantum system in which a ${}^6\text{Li}$ Fermi sea coexists with a large and stable ${}^{23}\text{Na}$ Bose-Einstein condensate. This was accomplished using interspecies sympathetic cooling of fermionic ${}^6\text{Li}$ in a thermal bath of bosonic ${}^{23}\text{Na}$. The system features rapid thermalization and long lifetimes.

DOI: 10.1103/PhysRevLett.88.160401

PACS numbers: 05.30.Fk, 32.80.Pj, 39.10.+j, 67.60.-g

Experimental methods of laser and evaporative cooling, used in the production of atomic Bose-Einstein condensates (BEC) [1], have recently been extended to realize quantum degeneracy in trapped Fermi gases [2–5]. What makes gaseous fermionic systems particularly appealing to investigate is the relative ease with which their properties can be varied. This allows the exploration of a vast range of experimental regimes, from noninteracting to strongly correlated. In the first case, purely quantum statistical effects can be studied, such as the implications of Pauli exclusion on scattering properties of the system. In the other extreme, exciting new regimes of BCS-like fermionic superfluidity may be within reach [6–9]. An additional area of interest is the production of a dilute quantum degenerate mixture of Bose and Fermi gases, akin to the strongly interacting ${}^4\text{He}$ - ${}^3\text{He}$ liquid. This would extend the list of possible experimental studies even further, to include effects such as interaction-driven phase separation [10] or BEC-induced interactions between fermions.

In this Letter, we report the production of a new macroscopic quantum system, in which a degenerate ${}^6\text{Li}$ Fermi gas coexists with a large and stable ${}^{23}\text{Na}$ BEC. We have achieved high numbers of both fermions ($>10^5$) and bosons ($>10^6$), and ${}^6\text{Li}$ quantum degeneracy characterized by a temperature of one-half the Fermi temperature (T_F). This provides us with the starting point for studies of the degenerate ${}^6\text{Li}$ Fermi gas, which is regarded as a particularly promising candidate for the BCS transition [6,7]. Further, favorable collisional properties make the ${}^6\text{Li}$ - ${}^{23}\text{Na}$ system very promising for studies of the degenerate Bose-Fermi mixtures, including the limitations to the cooling process [11,12]. It is also worth noting that, in our experiment, a mixture of two different atomic species has been simultaneously brought into quantum degeneracy for the first time.

Our experimental approach is based on sympathetic cooling of fermions in a large bosonic “refrigerator.” In contrast to the bosonic case, two-body elastic collisions are absent in a single-component Fermi gas at ultralow temperatures due to the Pauli exclusion principle. This lack of thermalization precludes direct implementation of forced evaporative cooling. Therefore, cooling of

fermions into the quantum degenerate regime must rely on collisions between distinguishable atoms. In two experiments which produced degenerate Fermi gases, mixtures of two fermionic spin states were simultaneously evaporated and mutually cooled [2,5]. Two groups have also demonstrated sympathetic cooling of ${}^6\text{Li}$ by the ${}^7\text{Li}$ bosonic isotope, thus also producing the first quantum degenerate Bose-Fermi mixtures. However, this system has a limitation that, in the upper hyperfine state, the ${}^7\text{Li}$ condensate is unstable [3], while scattering properties in the lower hyperfine state make sympathetic cooling inefficient, and limit the size of both ${}^6\text{Li}$ and ${}^7\text{Li}$ samples [4]. We have overcome both of these limitations by using a large ${}^{23}\text{Na}$ cloud, instead of ${}^7\text{Li}$, for sympathetic cooling of ${}^6\text{Li}$. Our work provides the natural progression in the search for an ideal Bose-Fermi system, where a “good” Bose-Einstein condensate is chosen, and then combined with a favorable fermionic species. Similar two-species experiments are currently being pursued by three other groups [13–15]. Given the vast variety of collisional properties among alkali gases, and a limited choice of favorable Bose-Fermi combinations, the properties of the ${}^6\text{Li}$ - ${}^{23}\text{Na}$ mixture are truly fortuitous. In our experiment, we have observed rapid interspecies thermalization, while low rates for both intra- and interspecies inelastic collisions result in a lifetime longer than 10 s. Both the presence of sufficient “good” (elastic) collisions needed for interspecies thermalization and the slow rate of “bad” (inelastic) collisions could not be taken for granted before our studies.

For this experiment, we have upgraded our ${}^{23}\text{Na}$ BEC apparatus [16] to allow for both lithium and sodium operation, while making minimal modifications to the original setup. The additional laser light needed for optical cooling of ${}^6\text{Li}$ was generated by a low power, diode laser system [17]. The lithium (671 nm) and sodium (589 nm) laser beams were overlapped using dichroic beam-splitters, and the spatial arrangement of the laser and atomic beams used to trap, cool, and detect lithium was identical to the original sodium setup. Specifically, a two-species magneto-optical trap (MOT) was loaded from a single two-species atomic beam, slowed in the same Zeeman slower previously used

in sodium-only experiments. The fact that the maximum spontaneous light force deceleration is twice as large for ^6Li as for ^{23}Na allowed us to slow lithium atoms without compromising the slowing efficiency for sodium.

To implement our experimental strategy, we have developed a two-species oven in which the vapors of ^6Li and ^{23}Na were mixed, and a single atomic beam containing both species was produced (Fig. 1). The main difficulty in designing such an oven is that, at the same temperature, the vapor pressure of lithium is 3 orders of magnitude lower than that of sodium. To achieve comparable atomic fluxes of both species, the alkali vapors must be produced in separate chambers, and then delivered to a mixing chamber, at controllable rates. In our design, the lithium chamber was also used for mixing. To operate the oven in either single- or two-species mode, we tuned the atomic fluxes independently by changing the temperatures of the alkali reservoirs. The maximum atom fluxes into the solid angle subtended by the MOT region were $3 \times 10^{11} \text{ s}^{-1}$ for ^6Li and $2 \times 10^{12} \text{ s}^{-1}$ for ^{23}Na .

Under typical operating conditions, 5 s of loading resulted in single-species MOTs with 2×10^7 lithium atoms or 6×10^9 sodium atoms. When both MOTs were operated simultaneously, interspecies light-assisted collisions reduced the number of lithium atoms by a factor of about 4, while the sodium atom number was not noticeably affected. The number of ^6Li atoms in the MOT was maximized when the trapping and the repumping light frequencies were tuned 25 MHz below the corresponding resonances. The resulting temperature of the lithium atoms was $\sim 700 \mu\text{K}$.

Since the ^{23}Na BEC is produced in the $|F, m_F\rangle = |1, -1\rangle$ lower hyperfine ground state, to avoid inelastic spin-exchange collisions, it is preferred to magnetically trap ^6Li in the corresponding $|1/2, -1/2\rangle$ state. (Here, F is the total angular momentum, and m_F is its projection along the quantization axis.) However, the maximum magnetic trap depth in the $|1/2, -1/2\rangle$ state is only $330 \mu\text{K}$ (see

Fig. 2), considerably lower than our MOT temperature. Further, due to the inefficiency of sub-Doppler cooling mechanisms, it is not possible to optically cool lithium to temperatures which would make magnetic trapping in this state efficient [17]. Therefore, to avoid drastic losses due to the limited trap depth, lithium atoms were optically pumped and then magnetically trapped in the $F = 3/2$ manifold. Before loading the magnetic trap, 4 ms were allowed for the sub-Doppler polarization gradient cooling of sodium, during which the lithium cloud was in free expansion. This reduced the transfer efficiency of lithium atoms into the trap by a factor of 2, limiting it to about 12%. We have thus magnetically trapped $\sim 6 \times 10^5$ ^6Li atoms in the upper hyperfine state and $\sim 2 \times 10^9$ ^{23}Na atoms in the lower one. At low energies, our cloverleaf magnetic trap is harmonic and axially symmetric. In the lower hyperfine states, the trapping frequencies for lithium (sodium) are $\omega_z = 2\pi \times 26$ (16) Hz axially and $\omega_r = 2\pi \times 354$ (221) Hz radially.

Once the atoms were loaded into the magnetic trap, we started the forced evaporative cooling of sodium [1]. A varying microwave field near 1.77 GHz was used to gradually lower the trap depth for ^{23}Na , selectively transferring the most energetic atoms into the untrapped $|2, -2\rangle$ state. This microwave field does not affect the ^6Li atoms, which were therefore not evaporated. Cooling of the lithium sample was instead achieved through thermal contact with sodium. We observed efficient sympathetic cooling of ^6Li in the *upper* hyperfine state by ^{23}Na in the *lower* one, and have successfully cooled this Bose-Fermi mixture into simultaneous quantum degeneracy. This observation indicates a surprisingly favorable ratio between

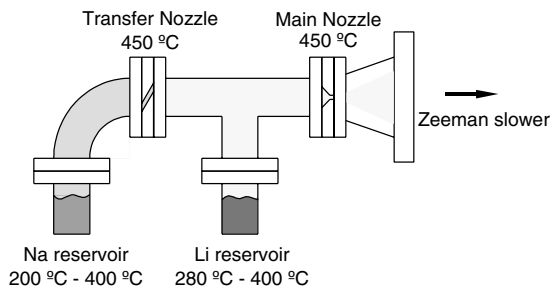


FIG. 1. Two-species oven. ^6Li and ^{23}Na vapors were produced in separate chambers to allow for independent control of the atom fluxes. The two species were mixed in the lithium chamber. The transfer nozzle has a conductance 40 times lower than the main nozzle, and limits the undesirable diffusion of lithium into the sodium chamber.

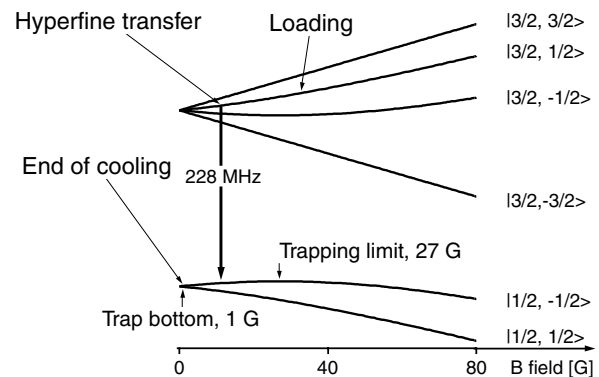


FIG. 2. ^6Li in the magnetic trap. Ground state energy levels: The six hyperfine states are labeled in the low magnetic field, $|F, m_F\rangle$ basis. The $|1/2, -1/2\rangle$ state becomes strong field seeking for fields above 27 G, limiting the trap depth to $330 \mu\text{K}$. Cooling path: Atoms in the $|3/2, 1/2\rangle$ upper hyperfine state were loaded into the magnetic trap at a temperature of $700 \mu\text{K}$. After the initial cooling stage to $50 \mu\text{K}$, the atoms were transferred to the $|1/2, -1/2\rangle$ state, and further cooled to a final temperature of 330 nK .

the good and bad interspecies collisions in this mixture. The losses due to inelastic spin-exchange collisions took place only on a time scale of several seconds, comparable to the total evaporation time of 15 s.

In order to produce a collisionally stable Bose-Fermi mixture, it is necessary to transfer the lithium atoms to the lower hyperfine state. To minimize the initial losses due to spin-exchange collisions, this transfer should take place as early in the cooling process as possible. On the other hand, before lithium atoms can be efficiently trapped in the lower hyperfine state, they must be cooled significantly below 330 μ K. Therefore, we implemented sympathetic cooling in two stages (see Fig. 2). We optimized the initial evaporation stage to reach a temperature of ~ 50 μ K in 5 s, while losing less than half of the lithium atoms, and maintaining the conditions for efficient sodium evaporation. At this point, we found that a substantial fraction of lithium atoms was in the $|3/2, 1/2\rangle$ state. They could thus be transferred to the $|1/2, -1/2\rangle$ state on a single-photon rf transition at 228 MHz, which is, to first order, independent of the magnetic field. This simplification over a similar hyperfine transfer previously employed in [4] was not expected. After the rf pulse was applied, the remaining $F = 3/2$ atoms were optically pumped into untrapped hyperfine states, and expelled from the trap. If this “cleanup” light pulse was omitted, spin-exchange collisions between lithium atoms in different hyperfine states led to a rapid loss of atoms from the trap [18]. The overall efficiency of our hyperfine transfer was $\sim 50\%$. The evaporation was then resumed for another 10 s. We observed efficient sympathetic cooling of the $|1/2, -1/2\rangle$ atoms, and cooled both gases into quantum degeneracy without observable losses in the lithium atom number.

Figure 3(a) displays the effect of sympathetic cooling on the ^6Li cloud. Absorption images of the trapped ^6Li gas were taken after the ^{23}Na evaporation was terminated at different trap depths, and the sample was allowed to equilibrate for 1 s. Cooling (from top to bottom) is seen in the shrinking of the density distribution and an increase in the peak optical density. In contrast to standard evaporative cooling, and the mutual cooling between two Fermi species, the total number of atoms remains constant.

Quantitative analysis of the ^6Li clouds is depicted in Fig. 3(b). We performed two-dimensional fits to the recorded column densities using both a simple Gaussian model and a semiclassical (Thomas-Fermi) distribution for trapped noninteracting fermions. In the latter approach, the probability that an atom has position \vec{r} and momentum \vec{p} is obtained from the Fermi-Dirac distribution for the total (kinetic and potential) energy of the particle. The fitting function for the spatial distribution of atoms in the trap is then obtained by integrating over the momentum degrees of freedom. While the Gaussian model gives a valid description of the gas only in the classical, high temperature limit, the Thomas-Fermi approach is valid at all temperatures, as long as the number of particles in

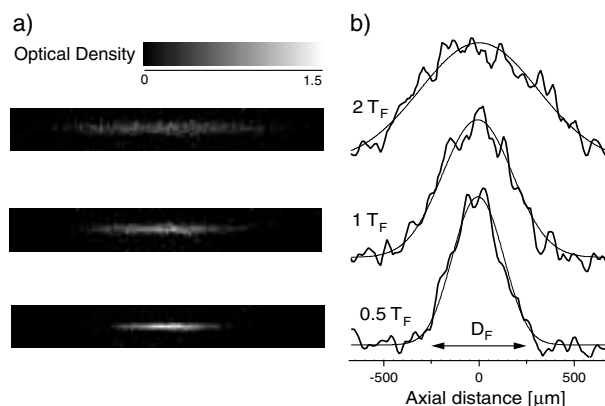


FIG. 3. Onset of Fermi degeneracy. Three pairs of images (top to bottom) correspond to $T/T_F = 2, 1$, and 0.5 . (a) Column densities of the ^6Li cloud were recorded by absorption imaging. (b) Axial line density profiles and the Thomas-Fermi fits to the data are plotted. The arrow indicates the size of the Fermi diameter, D_F .

the system is large [19]. Indeed, at higher temperatures, the two fits performed equally well, and yielded the same temperature. However, at a temperature of about 400 nK, the classical fits started to fail. This was indicated by the relative growth of the reduced χ^2 values, by up to 20% above the corresponding values for the fermionic fits. For the coldest samples, Gaussian fits also overestimated the temperature by $\sim 15\%$. From the fitted number of atoms in the system ($N_{\text{Li}} \sim 1.4 \times 10^5$, $T_F \approx 670$ nK), we found that the noticeable inadequacy of the classical fits occurred at $\sim 0.6 T_F$, which is a clear signature of the Fermi degeneracy. Figure 3(b) shows projected line densities along the axial direction of the ^6Li cloud and the Thomas-Fermi fits to the data. The arrow indicates the size of the Fermi diameter, $D_F = 2\sqrt{2k_B T_F / (m\omega_z^2)}$, for the fitted atom number. The spatial extent of the coldest cloud ($T \approx 330$ nK $\approx 0.5 T_F$) is already comparable to the minimum size the system would assume at zero temperature. Typical densities of the coldest lithium samples were $\sim 10^{12}$ cm^{-3} .

In Fig. 4, the temperature of the ^6Li cloud is plotted as a function of the final ^{23}Na trap depth. The coldest lithium samples were produced in coexistence with almost pure sodium condensates with $\sim 2 \times 10^6$ atoms. The lifetime of this degenerate mixture was limited to about 10 s by the three-body decay of the BEC, while the lithium cloud had a lifetime longer than 100 s. The lifetime of either species was not detectably affected by the presence of the other one. Even after sodium was lost from the trap, the energy of the lithium cloud did not increase noticeably (< 5 nK/s) during its slow decay. We also compared the ^6Li temperatures with the temperatures of the ^{23}Na cloud, extracted from the thermal wings of the bosonic density distribution. In hotter samples, the two agreed to within 10%. However, for the coldest samples we observed a discrepancy between the two temperatures. The lowest measurable temperature

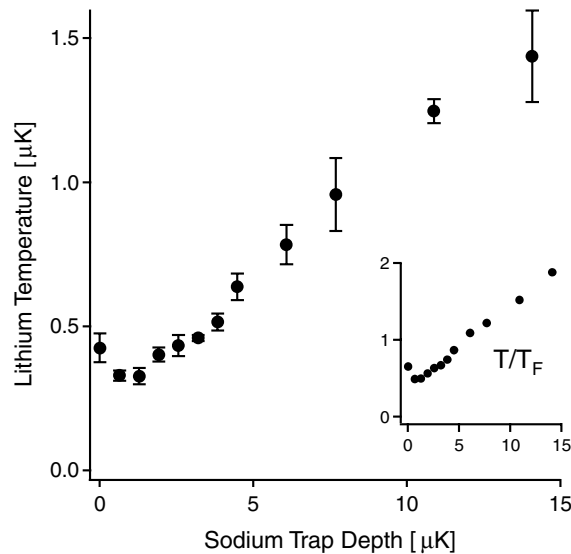


FIG. 4. Temperatures of the ^6Li cloud as a function of the ^{23}Na trap depth. Each data point is an average of three measurements. The error bars indicate the shot-to-shot fluctuations, while the uncertainties of the fits are comparable or smaller. In the case when sodium was completely evaporated from the trap (c.f. zero trap depth data point), the very last stage of sympathetic cooling became inefficient due to the vanishing heat capacity of the bosonic reservoir. The inset shows the same temperature data scaled to the Fermi temperature.

of sodium was $T \approx 170$ nK, about half the corresponding lithium value. We verified that, in these samples, extending the thermalization time at the end of evaporation up to 10 s did not lower the lithium temperature any farther. The reasons for the observed temperature discrepancy are worthy of further investigation. Simple spatial separation of the two clouds due to different gravitational sags can be readily ruled out. However, some form of phase separation of the two species [10], or constant heating of the fermionic cloud [12], could play a role.

In conclusion, we have produced a system in which a ^6Li Fermi sea coexists with a ^{23}Na BEC. This provides us with a starting point for studies of the degenerate Bose-Fermi mixtures. In particular, the observed temperature difference between the two spatially overlapped species might provide further insight into the limits of sympathetic cooling. Further, by loading the degenerate Fermi cloud into an optical trap, effects of magnetically tunable interactions between lithium atoms in different spin states can be studied [18]. A particularly appealing prospect is the observation of the BCS transi-

tion to a fermionic superfluid state, for which ^6Li is a very promising candidate.

We thank Florian Schreck for useful discussions and Christian Schunck for experimental assistance. This research was supported by NSF, ONR, ARO, NASA, and the David and Lucile Packard Foundation. M. W. Z. acknowledges the support of the Studienstiftung des deutschen Volkes and the Ecole Normale Supérieure, Paris.

*Current address: Universität Stuttgart, 5. Phys. Inst., Stuttgart, Germany.

- [1] *Bose-Einstein Condensation in Atomic Gases*, Proceedings of the International School of Physics "Enrico Fermi," Course CXL, edited by M. Inguscio, S. Stringari, and C. Wieman (IOS Press, Amsterdam, 1999).
- [2] B. DeMarco and D. S. Jin, *Science* **285**, 1703 (1999).
- [3] A. G. Truscott, K. E. Strecker, W. I. McAlexander, G. B. Partridge, and R. G. Hulet, *Science* **291**, 2570 (2001).
- [4] F. Schreck, L. Khaykovich, K. L. Corwin, G. Ferrari, T. Bourdel, J. Cubizolles, and C. Salomon, *Phys. Rev. Lett.* **87**, 080403 (2001).
- [5] S. R. Granade, M. Gehm, K. M. O'Hara, and J. E. Thomas, *Phys. Rev. Lett.* **88**, 120405 (2002).
- [6] H. T. C. Stoof, M. Houbiers, C. A. Sackett, and R. G. Hulet, *Phys. Rev. Lett.* **76**, 10 (1996).
- [7] M. Houbiers, R. Ferwerda, H. T. C. Stoof, W. I. McAlexander, C. A. Sackett, and R. G. Hulet, *Phys. Rev. A* **56**, 4864 (1997).
- [8] M. A. Baranov and D. S. Petrov, *Phys. Rev. A* **58**, R801 (1998).
- [9] M. Holland, S. J. J. M. F. Kokkelmans, M. L. Chiofalo, and R. Walser, *Phys. Rev. Lett.* **87**, 120406 (2001).
- [10] K. Mølmer, *Phys. Rev. Lett.* **80**, 1804 (1998).
- [11] E. Timmermans and R. Côté, *Phys. Rev. Lett.* **80**, 3419 (1998).
- [12] E. Timmermans, *Phys. Rev. Lett.* **87**, 240403 (2001).
- [13] J. Goldwin, S. B. Papp, B. DeMarco, and D. S. Jin, *Phys. Rev. A* **65**, 021402(R) (2002).
- [14] G. Modugno, G. Ferrari, G. Roati, R. J. Brecha, A. Simoni, and M. Inguscio, *Science* **294**, 1320 (2001).
- [15] M. Mudrich, S. Kraft, K. Singer, R. Grimm, A. Mosk, and M. Weidemüller, *physics/0111213*.
- [16] M. O. Mewes, M. R. Andrews, N. J. van Druten, D. M. Kurn, D. S. Durfee, and W. Ketterle, *Phys. Rev. Lett.* **77**, 416 (1996).
- [17] U. Schünemann, H. Engler, M. Zielonkowski, M. Weidemüller, and R. Grimm, *Opt. Commun.* **158**, 263 (1998).
- [18] M. Houbiers, H. T. C. Stoof, W. I. McAlexander, and R. G. Hulet, *Phys. Rev. A* **57**, R1497 (1998).
- [19] D. A. Butts and D. S. Rokhsar, *Phys. Rev. A* **55**, 4346 (1997).

Appendix C

Fifty-fold improvement in the number of quantum degenerate fermionic atoms

This appendix includes the following manuscript [2]:

Z. Hadzibabic, S. Gupta, C. A. Stan, C. H. Schunck, M. W. Zwierlein, K. Dieckmann, and W. Ketterle, “Fifty-fold improvement in the number of quantum degenerate fermionic atoms,” *cond-mat/0306050* (2003).

Fifty-fold improvement in the number of quantum degenerate fermionic atoms

Z. Hadzibabic, S. Gupta, C.A. Stan, C.H. Schunck, M.W. Zwierlein, K. Dieckmann, and W. Ketterle
*Department of Physics, MIT-Harvard Center for Ultracold Atoms, and Research Laboratory of Electronics,
 MIT, Cambridge, MA 02139*

(June 3, 2003)

We have produced a quantum degenerate ${}^6\text{Li}$ Fermi gas with up to 7×10^7 atoms, an improvement by a factor of fifty over all previous experiments with degenerate Fermi gases. This was achieved by sympathetic cooling with bosonic ${}^{23}\text{Na}$ in the $F = 2$, upper hyperfine ground state. We have also achieved Bose-Einstein condensation of $F = 2$ sodium atoms by direct evaporation.

PACS numbers: 05.30.Fk, 32.80.Pj, 39.25.+k, 67.60.-g

Over the last few years, there has been significant progress in the production of quantum degenerate atomic Fermi gases (${}^{40}\text{K}$ [1,2] and ${}^6\text{Li}$ [3–6]) and degenerate Bose-Fermi mixtures (${}^7\text{Li}$ - ${}^6\text{Li}$ [3,4], ${}^{23}\text{Na}$ - ${}^6\text{Li}$ [6], and ${}^{87}\text{Rb}$ - ${}^{40}\text{K}$ [2]). These systems offer great promise for studies of new, interaction-driven quantum phenomena. The ultimate goal is the attainment of novel regimes of BCS-like superfluidity in a gaseous system [7–10]. The current efforts to induce and study strong interactions in a Fermi gas [11–20] are complemented with the ongoing efforts to improve fermion cooling methods, which would lead to lower temperatures and larger samples.

The main reason why studies of degenerate Fermi gases are still lagging behind the studies of atomic Bose-Einstein condensates (BECs), is the complexity of cooling methods. The Pauli exclusion principle prohibits elastic collisions between identical fermions at ultra-low temperatures, and makes evaporative cooling of spin-polarized fermionic samples impossible. For this reason, cooling of fermions must rely on some form of mutual or sympathetic cooling between two types of distinguishable particles, either two spin states of the same atom [1,5], or two different atoms [2–4,6]. A key element in fermion cooling is the design of better “refrigerators” for sympathetic cooling.

In this Letter, we report the first production of degenerate Fermi samples comparable in size with the largest alkali BECs [21]. We successfully cooled up to 7×10^7 magnetically trapped ${}^6\text{Li}$ atoms to below half the Fermi temperature (T_F). This is an improvement in atom number by a factor of 50 over the largest previously reported Fermi sea [20]. Further, in samples containing up to 3×10^7 atoms, we observed temperatures as low as $0.05 T_F$, the lowest ever achieved. At these temperatures, the fractional occupation of the lowest energy state differs from unity by less than 10^{-8} .

As in our previous work [6], ${}^6\text{Li}$ atoms were magnetically trapped in the $F = 3/2$, upper hyperfine ground state, and sympathetically cooled by bosonic ${}^{23}\text{Na}$. The crucial improvement was our achievement of forced evaporation of sodium in the $|F, m_F\rangle = |2, +2\rangle$, upper hyperfine ground state, producing large and stable BECs with up to 10^7 atoms. This allowed us to create a magneti-

cally trapped ${}^{23}\text{Na}$ - ${}^6\text{Li}$, Bose-Fermi mixture which is stable against spin-exchange collisions at all densities, and dramatically boosted our fermion atom number.

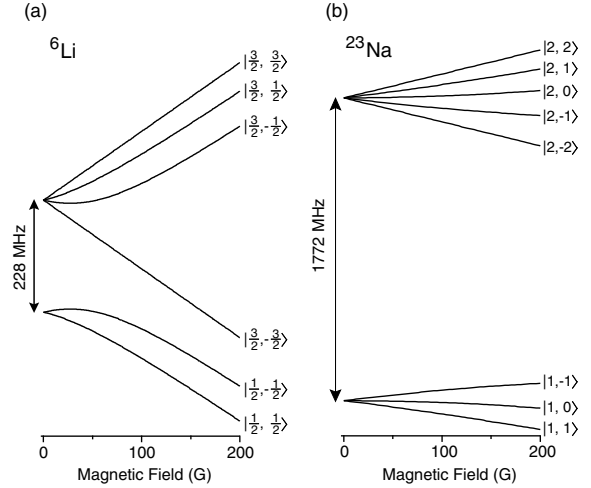


FIG. 1. Hyperfine structures of ${}^6\text{Li}$ and ${}^{23}\text{Na}$. The states are labelled in the low field, $|F, m_F\rangle$ basis. (a) Due to finite trap depth of $\sim k_B \times 300 \mu\text{K}$ in the $|1/2, -1/2\rangle$ state, lithium can be efficiently loaded into the magnetic trap only in the upper, $F = 3/2$ hyperfine state. (b) Sodium is magnetically trappable in the $|1, -1\rangle$, and in the $|F = 2, m_F \geq 0\rangle$ states. Previously, sodium has been evaporatively cooled to BEC only in the $|1, -1\rangle$, lower hyperfine state.

The criteria for designing sympathetic cooling experiments include the heat capacity of the refrigerator, and the inter-species collisional properties, both elastic and inelastic. Large and stable ${}^{23}\text{Na}$ condensates are an appealing choice for sympathetic cooling of fermions. Further, a favorable mass ratio allows for simultaneous Zeeman slowing of ${}^{23}\text{Na}$ and ${}^6\text{Li}$ [6], and for simultaneous magnetic trapping without large differences in the gravitational sag. The inter-species collisional properties are generally not predictable, and have to be tested experimentally. In order to minimize all possible inelastic processes, the natural choice is to magnetically trap both species in their lower hyperfine ground states. However, at temperatures reachable by laser cooling ($\geq 300 \mu\text{K}$), ${}^6\text{Li}$ can be efficiently magnetically trapped only in the

upper hyperfine state, $F = 3/2$ [4,6] (Fig. 1(a)). On the other hand, until now sodium has been successfully evaporated only in the lower, $F = 1$ hyperfine state. This was a limiting factor for sympathetic cooling of ^6Li , since the mixture of sodium in the lower, and lithium in the upper hyperfine state is not stable against spin-exchange collisions. The inelastic loss rate increases as the temperature is lowered and the density grows. In our previous work [6], we partially overcame this problem by transferring lithium atoms into the lower hyperfine state after an initial sympathetic cooling stage to $\sim 50\ \mu\text{K}$. By achieving forced evaporative cooling and Bose-Einstein condensation of sodium in the $F = 2$ state, we have now realized a more robust sympathetic cooling strategy, and dramatically improved the size and temperature of a degenerate Fermi system.

We loaded $\sim 3 \times 10^9$ sodium and up to 10^8 lithium atoms in their upper hyperfine states from a two-species magneto-optical trap (MOT) into the magnetic trap. The adverse effect of light assisted collisions in a two-species MOT [6,22] was minimized by slightly displacing the two MOTs with respect to each other. During the typical 30 s of evaporative/sympathetic cooling, we observed no significant inelastic loss of lithium atoms (by three-body collisions or dipolar relaxation), the final number of degenerate atoms being at least half of the number initially loaded into the trap. On the other hand, we observed a favorable rate of elastic collisions between the two species, with the inter-species thermalization time being shorter than 1 s. Therefore, sodium atoms in the upper hyperfine state have ideal properties as a refrigerant for ^6Li .

Since our primary interest was cooling of fermions, we evaporated all sodium atoms in order to get lithium to the lowest possible temperatures. Even in our largest ^6Li samples, of $\sim 7 \times 10^7$ atoms, we achieved temperatures below $0.5 T_F$. Temperatures in the range $0.05 - 0.2 T_F$ could be achieved by reducing the ^6Li atom numbers only slightly, to $\sim 3 \times 10^7$. Such big clouds had a high enough optical density for crisp absorption imaging even after ballistic expansion to a size larger than one millimeter (Fig. 2(a)).

Temperatures were extracted from absorption images of expanding clouds released from the trap, using a semiclassical (Thomas-Fermi) fit to the Fermi-Dirac momentum distribution [6,23] (Fig. 2(b)). The quoted temperature range reflects both the shot-to-shot and day-to-day reproducibility, and the fact that the Fermi distribution is very insensitive to the temperature in this ultra-degenerate limit.

In these experiments, the ^6Li atom number was adjusted during the loading phase. Somewhat lower temperatures could possibly be achieved if the maximum lithium atom number was loaded into the magnetic trap, and then the hottest part of the cloud was selectively removed by direct evaporation once the sodium atom num-

ber dropped to the point where the heat capacities of the two species become comparable. However, at this point it appears unlikely that temperatures below $0.05 T_F$ could be conclusively extracted in order to differentiate the two strategies.

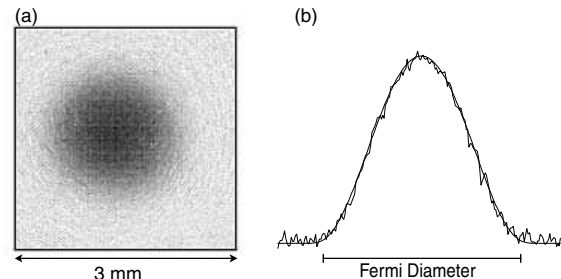


FIG. 2. Large and ultra-degenerate Fermi sea. (a) Absorption image of 3×10^7 ^6Li atoms released from the trap and imaged after 12 ms of free expansion. (b) Axial (vertical) line density profile of the cloud in (a). A semiclassical fit (thin line) yields a temperature $T = 93\ \text{nK} = 0.05 T_F$. At this temperature, the high energy wings of the cloud do not extend visibly beyond the Fermi energy, indicated in the figure by the momentum-space Fermi diameter.

We also produced two-species degenerate Bose-Fermi mixtures with several million atoms in each species (Fig. 3). The mixture was stable, with a lifetime of several seconds, limited only by the three-body decay of the sodium cloud.

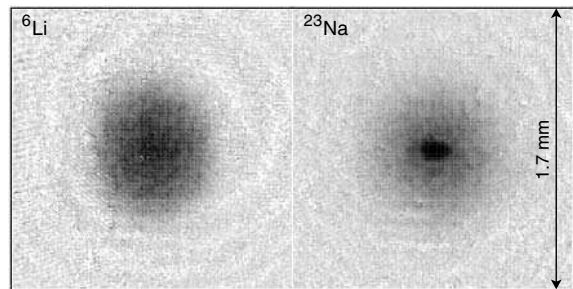


FIG. 3. Two-species mixture of degenerate Bose and Fermi gases. After release from the magnetic trap, both ^6Li and ^{23}Na clouds were imaged onto the same CCD camera using separate light pulses. The times of free expansion of the two gases could be varied independently. This dual-imaging technique allowed for optimizing the cooling strategy for either single- or two-species experiments. For the displayed image, the expansion times were $\tau_{Li} = 8\ \text{ms}$ and $\tau_{Na} = 25\ \text{ms}$, and the atom numbers were $N_{Li} \sim 10^7$ and $N_{Na} \sim 6 \times 10^6$. Sodium was cooled below the condensation temperature, corresponding to $\sim 0.2 T_F$ for the lithium cloud.

In the rest of the paper, we summarize the numerous steps which were introduced to prepare sodium in the $F = 2$ state as a refrigerant.

In contrast to ^{87}Rb , condensation of sodium by evaporative cooling was previously achieved only in the lower, $|1, -1\rangle$ hyperfine state. $F = 2$ sodium condensates could thus be studied only by transferring optically trapped $F = 1$ BECs into this state [24,25]. Condensation in the upper hyperfine state of sodium is more difficult than in the lower state for two reasons: (1) The requirement for efficient optical pumping in dense laser-cooled samples, and (2) an order of magnitude higher three-body loss rate coefficient [24].

The basic setup of our experiment is described in [6]. In 10 s, we collected typically $\sim 10^{10}$ ^{23}Na atoms, and $\sim 10^8$ ^6Li atoms in a magneto-optical trap (MOT). Typical MOT temperatures were 0.7-1 mK. Sodium was collected in a dark-SPOT variant of the MOT [26], and therefore most of the atoms were in the $F = 1$ hyperfine state. Lithium was collected in a “bright” MOT, with about 2/3 of the atoms in the $F = 3/2$ state.

Before the transfer into the magnetic trap, the atoms were optically pumped into the stretched hyperfine ground states, $|2, +2\rangle$ for ^{23}Na , and $|3/2, +3/2\rangle$ for ^6Li . A magnetic guide field of 3 G was applied, and the atoms were optically pumped for 2 ms, using σ^+ polarized light. To achieve both F (hyperfine) and m_F (Zeeman) pumping, two light beams were used for each species, resonant with the $|F = I \pm 1/2\rangle \rightarrow |F' = I \pm 1/2\rangle$ transitions. Here, I is the nuclear spin ($I = 3/2$ for ^{23}Na , and $I = 1$ for ^6Li), and F' is the total spin in the excited electronic state. In this way, almost all the lithium atoms could be pumped into the $|3/2, +3/2\rangle$ state. On the other hand, the density of sodium atoms in the dark-SPOT is $\geq 10^{11} \text{ cm}^{-3}$, and Zeeman pumping is notoriously difficult at such high densities. In our experiments, the fraction of atoms pumped into the $|2, +2\rangle$ state was limited to about 30 %, with most of the remaining atoms distributed among the other m_F sub-levels of the $F = 2$ manifold.

After the optical pumping stage, the atoms were loaded into a Ioffe-Pritchard magnetic trap with a radial gradient of 164 G/cm, and axial curvature of 185 G/cm². Sodium atoms in all three $|F = 2, m_F \geq 0\rangle$ states are (at least weakly) magnetically trappable (Fig. 1(b)). However, only pure $|2, +2\rangle$ samples are stable against inelastic spin-exchange collisions. A crucial step in preparing the samples for efficient forced evaporation was to actively remove $|F = 2, m_F = 0, +1\rangle$ atoms from the trap, before they engaged in inelastic collisions with the $|2, +2\rangle$ atoms. The atoms were loaded into a weak magnetic trap, with a high bias field of 80 G. This field splits the $F = 2$ Zeeman sub-levels by $\sim k_B \times 2.8 \text{ mK}$. Since this splitting was larger than the temperature of the cloud, the different states could be resolved in microwave or rf spectroscopy, and the $|F = 2, m_F = 0, +1\rangle$ atoms could be selectively transferred to the untrapped $|F = 1, m_F = 0, +1\rangle$ lower hyperfine states. This transfer was done with a microwave sweep near the ^{23}Na hyperfine

splitting of 1.77 GHz. In this way, all the $|2, +2\rangle$ atoms initially loaded into trap could be preserved. We were even able to “recycle” some of the untrapped atoms by optically pumping them out of the $F = 1$ ground states, thus giving them a “second chance” to fall into the $|2, +2\rangle$ state. The final setup consisted of two microwave sweeps, the first of 0.8 s duration with the optical pumping light on, and the second of 2.4 s duration without the light. In this way, the overall transfer efficiency from the MOT to the magnetic trap was improved to about 35 %, comparable to our standard $F = 1$ BEC experiments [27].

After this purification of the $|2, +2\rangle$ sample, the magnetic trap was tightened by reducing the bias field to 3.8 G in 2.4 s. Resulting trapping frequencies were 204 Hz (400 Hz) radially, and 34 Hz (67 Hz) axially for the sodium (lithium) stretched state. This provided good conditions for forced runaway evaporation of sodium. Evaporation was done on the $|2, +2\rangle \rightarrow |1, +1\rangle$ microwave transition near 1.77 GHz. In contrast to radio-frequency evaporation, this insured that ^6Li was far off resonance. Further, microwave evaporation avoided any undesirable aspects of “incomplete evaporation” into the $|F = 2, m_F = 0, +1\rangle$ states, which could lead to inelastic losses [28].

After 15 s of evaporation, the sodium atoms reached a temperature of $T \sim 10 \mu\text{K}$. At this point, to avoid three-body losses in the $|2, +2\rangle$ state [24], the trap was weakened to frequencies of 49 Hz (96 Hz) radially, and 18 Hz (35 Hz) axially for sodium (lithium). The final evaporation to BEC took another 15 s. In this way, in the absence of lithium atoms, we could produce almost pure $|2, +2\rangle$ BECs containing up to 10 million atoms. The lifetime of the BEC in the weak trap was longer than 3 s. In contrast to our previous work [24,25], studies of $F = 2$ condensates are now possible without the added complexity of an optical trap.

In conclusion, by creating a superior refrigerant for sympathetic cooling of ^6Li , we have produced the coldest and by far the largest quantum degenerate Fermi gas so far. With the number of atoms comparable with the largest alkali BECs, and the temperatures reaching the practical detection limit, we have fully exploited the potential of laser and evaporative cooling to engineer samples of ultracold fermions. In analogy with Bose-Einstein condensates, we expect these large samples to insure sufficient signal-to-noise ratio for all the standard techniques of BEC research, such as velocimetry using long expansion times, rf spectroscopy with Stern-Gerlach separation during ballistic expansion, direct non-destructive imaging of the trapped clouds, and Bragg spectroscopy. The next challenge is to maintain a similar combination of number and temperature for an interacting two-component Fermi gas [19].

We thank A. E. Leanhardt for critical reading of the manuscript. This work was supported by the NSF, ONR, ARO, and NASA.

-
- [1] B. DeMarco and D. S. Jin, *Science* **285**, 1703 (1999).
- [2] G. Roati, F. Riboli, G. Modugno, and M. Inguscio, *Phys. Rev. Lett.* **89**, 150403 (2002).
- [3] A. G. Truscott, K. E. Strecker, W. I. McAlexander, G. B. Partridge, and R. G. Hulet, *Science* **291**, 2570 (2001).
- [4] F. Schreck, L. Khaykovich, K. L. Corwin, G. Ferrari, T. Bourdel, J. Cubizolles, and C. Salomon, *Phys. Rev. Lett.* **87**, 080403 (2001).
- [5] S. R. Granade, M. E. Gehm, K. M. O'Hara, and J. E. Thomas, *Phys. Rev. Lett.* **88**, 120405 (2002).
- [6] Z. Hadzibabic, C. A. Stan, K. Dieckmann, S. Gupta, M. W. Zwierlein, A. Görlitz, and W. Ketterle, *Phys. Rev. Lett.* **88**, 160401 (2002).
- [7] M. Houbiers and H. T. C. Stoof, *Phys. Rev. A* **59**, 1556 (1999).
- [8] M. Holland, S. J. J. M. F. Kokkelmans, M. L. Chiofalo, and R. Walser, *Phys. Rev. Lett.* **87**, 120406 (2001).
- [9] Y. Ohashi and A. Griffin, *Phys. Rev. Lett.* **89**, 130402 (2002).
- [10] W. Hofstetter, J. I. Cirac, P. Zoller, E. Demler, and M. D. Lukin, *Phys. Rev. Lett.* **89**, 220407 (2002).
- [11] T. Loftus, C. A. Regal, C. Ticknor, J. L. Bohn, and D. S. Jin, *Phys. Rev. Lett.* **88**, 173201 (2002).
- [12] K. Dieckmann, C. A. Stan, S. Gupta, Z. Hadzibabic, C. H. Schunck, and W. Ketterle, *Phys. Rev. Lett.* **89**, 203201 (2002).
- [13] K. M. O'Hara, S. L. Hemmer, S. R. Granade, M. E. Gehm, J. E. Thomas, V. Venturi, E. Tiesinga, and C. J. Williams, *Phys. Rev. A* **66**, 041401 (2002).
- [14] C. A. Regal, C. Ticknor, J. L. Bohn, and D. S. Jin, *Phys. Rev. Lett.* **90**, 053201 (2003).
- [15] K. M. O'Hara, S. L. Hemmer, M. E. Gehm, S. R. Granade, and J. E. Thomas, *Science* **298**, 2179 (2002).
- [16] M. E. Gehm, S. L. Hemmer, S. R. Granade, K. M. O'Hara, and J. E. Thomas, *arXiv:cond-mat/0212499* (2002).
- [17] C. A. Regal and D. S. Jin, *arXiv:cond-mat/0302461* (2003).
- [18] T. Bourdel, J. Cubizolles, L. Khaykovich, K. M. F. Magalhães, S. J. J. M. F. Kokkelmans, G. V. Shlyapnikov, and C. Salomon, *arXiv:cond-mat/0303079* (2003).
- [19] S. Gupta, Z. Hadzibabic, M. W. Zwierlein, C. A. Stan, K. Dieckmann, C. H. Schunck, E. G. M. van Kempen, B. J. Verhaar, and W. Ketterle, *Science* (2003).
- [20] C. A. Regal, C. Ticknor, J. L. Bohn, and D. S. Jin, *arXiv:cond-mat/0305028* (2003).
- [21] J. R. Abo-Shaeer, C. Raman, J. M. Vogels, and W. Ketterle, *Science* **292**, 476 (2001).
- [22] V. Wippel, C. Binder, and L. Windholz, *Eur. Phys. J. D* **21**, 101 (2002).
- [23] D. A. Butts and D. S. Rokhsar, *Phys. Rev. A* **55**, 4346 (1997).
- [24] A. Görlitz, T. L. Gustavson, A. E. Leanhardt, R. Löw, A. P. Chikkatur, S. Gupta, S. Inouye, D. E. Pritchard, and W. Ketterle, *Phys. Rev. Lett.* **90**, 090401 (2003).
- [25] A. E. Leanhardt, A. Görlitz, A. P. Chikkatur, D. Kielpinski, Y. Shin, D. E. Pritchard, and W. Ketterle, *Phys. Rev. Lett.* **89**, 190403 (2002).
- [26] W. Ketterle, K. B. Davis, M. A. Joffe, A. Martin, and D. E. Pritchard, *Phys. Rev. Lett.* **70**, 2253 (1993).
- [27] M.-O. Mewes, M. R. Andrews, N. J. van Druten, D. M. Kurn, D. S. Durfee, and W. Ketterle, *Phys. Rev. Lett.* **77**, 416 (1996).
- [28] B. Desruelle, V. Boyer, S. G. Murdoch, G. Delannoy, P. Bouyer, and A. Aspect and M. Lécivain, *Phys. Rev. A* **60**, R1759 (1999).

Appendix D

Radio-Frequency Spectroscopy of Ultracold Fermions

This appendix includes the following paper [5]:

S. Gupta, Z. Hadzibabic, M. W. Zwierlein, C. A. Stan, K. Dieckmann, C. H. Schunck, E. G. M. van Kempen, B. J. Verhaar, and W. Ketterle, “Radio-Frequency Spectroscopy of Ultracold Fermions,” *Science* **300**, 1723 (2003).

Radio-Frequency Spectroscopy of Ultracold Fermions

S. Gupta,^{1*} Z. Hadzibabic,¹ M. W. Zwierlein,¹ C. A. Stan,¹
K. Dieckmann,¹ C. H. Schunck,¹ E. G. M. van Kempen,²
B. J. Verhaar,² W. Ketterle¹

Radio-frequency techniques were used to study ultracold fermions. We observed the absence of mean-field “clock” shifts, the dominant source of systematic error in current atomic clocks based on bosonic atoms. This absence is a direct consequence of fermionic antisymmetry. Resonance shifts proportional to interaction strengths were observed in a three-level system. However, in the strongly interacting regime, these shifts became very small, reflecting the quantum unitarity limit and many-body effects. This insight into an interacting Fermi gas is relevant for the quest to observe superfluidity in this system.

Radio-frequency (RF) spectroscopy of ultracold atoms provides the standard of time. However, the resonance frequencies of ultracold atoms are sensitive to interactions between atoms, leading to the so-called clock shifts of the unperturbed resonances (1). These shifts limit the accuracy of current atomic clocks (2, 3), but can also be used to characterize atomic interactions.

RF spectroscopy has previously been applied to cold atoms to determine the size and temperature of atom clouds (4, 5). RF methods have also been used for evaporative cooling, for preparing spinor Bose-Einstein condensates (BECs) (6, 7), and as an output coupler for atom lasers (5, 8). In all these experiments, shifts and broadenings due to atomic interactions were negligible. Recently, density-dependent frequency shifts of RF transitions were observed in rubidium (9) and sodium (10) BECs. These frequency shifts are proportional to the difference in mean-field energies of two internal atomic states and allow scattering lengths to be extracted. Mean-field shifts in BECs have also been observed by optical spectroscopy (11, 12).

Here, we apply RF spectroscopy to ultracold clouds of fermions and demonstrate several phenomena: (i) the absence of a clock shift in a two-level system because of fermionic antisymmetry, (ii) the emergence of mean-field shifts in a three-level system after the relaxation of pair correlations, (iii) the limitation of mean-field shifts because of the unitarity limit, and (iv) the universality of the

interaction energy in a dense cloud, independent of the attractive or repulsive nature of the two-particle interactions.

Research in ultracold fermions has advanced rapidly, with six groups now having cooled fermions into quantum degeneracy (13–18). A major goal of this research is to induce strong interactions by tuning magnetic fields to scattering resonances (called Feshbach resonances). Under these conditions, Cooper pairs of fermions may form, leading to superfluidity. This would establish a model system for studying Bardeen-Cooper-Schrieffer (BCS) pairing at densities nine orders of magnitude lower than in previous realizations in ³He and superconductors. We show that RF spectroscopy can be used to characterize interactions between fermions in the regime where superfluidity has been predicted (19, 20).

Our experimental technique for preparing ultracold fermions has been considerably improved since our earlier work (17, 21). Because the Pauli exclusion principle suppresses elastic collisions between identical fermions at low temperatures and prevents evaporative cooling, we cooled fermionic ⁶Li sympathetically with bosonic ²³Na loaded into the same magnetic trap. In contrast to previous work, we cooled both species in their upper hyperfine states (²³Na: $|F, m_F\rangle = |2, +2\rangle$, ⁶Li: $|F, m_F\rangle = |3/2, +3/2\rangle$, where F and m_F are the quantum numbers for the total spin and its z component, respectively. This led to a reduction of inelastic loss processes and boosted our final fermion atom numbers by two orders of magnitude. We could produce BECs that contained up to 10 million sodium atoms in the $|2, +2\rangle$ state by evaporatively cooling pure bosonic samples in the magnetic trap. For a Bose-Fermi mixture, the finite heat capacity of the bosons limited the final lithium temperature after the 30-s evaporation cycle to $\sim 0.3 T_F$ for 10 million fermi-

ons and $\sim T_F$ for 50 million fermions (22), where T_F is the Fermi temperature.

The spin states of ⁶Li of most interest for superfluid pairing are the two lowest states $|1\rangle$ and $|2\rangle$ ($|1/2, +1/2\rangle$ and $|1/2, -1/2\rangle$ at low field), which are predicted to have an inter-state s -wave (23) Feshbach resonance at ~ 800 G (24, 25). However, both states are high-field-seeking at these fields, which makes them unsuitable for magnetic trapping. We therefore transferred the atoms into an optical trap. For these experiments, 6 to 8 million $|3/2, +3/2\rangle$ lithium atoms were loaded into the optical trap at temperature $T \sim T_F \sim 35$ μ K (26). The atoms were then transferred to the lowest energy state $|1\rangle$, with an adiabatic frequency sweep around the lithium hyperfine splitting of 228 MHz. Magnetic fields of up to ~ 900 G were applied, a range that encompasses the $|1\rangle - |2\rangle$ Feshbach resonance. Using RF-induced transitions near 80 MHz, we could create mixtures of states $|1\rangle$, $|2\rangle$, and $|3\rangle$ ($|3/2, -3/2\rangle$ at low field) and explore interactions between fermions in these states.

Collisions between atoms cause a shift of their energy, which is usually described by the mean-field effect of all the other atoms on the atom of interest. For example, atoms in state $|2\rangle$ experience an energy shift, $[(4\pi\hbar^2)/(m)]n_1a_{12}$, that is due to the presence of atoms in state $|1\rangle$. Here \hbar is Planck’s constant h divided by 2π , m is the mass of the atom, n_1 is the density of $|1\rangle$ atoms, and a_{12} is the interstate scattering length between states $|1\rangle$ and $|2\rangle$. We use the convention that positive scattering length corresponds to a repulsive interaction. Density-dependent shifts of the resonance frequency for the transition that connects two states have been observed in laser-cooled (1) and Bose-condensed (9, 10) clouds.

In the case of ultracold fermions, only interactions between different internal states are allowed. For a system of density n , let us compare the energy of a gas prepared purely in state $|1\rangle$ to a gas in which one atom is transferred into state $|2\rangle$. The energy difference is $\hbar\nu_{12} + [(4\pi\hbar^2)/(m)]na_{12}$, where ν_{12} is the resonance frequency of the noninteracting system. Similarly, the energy difference between a gas prepared purely in state $|2\rangle$ and a gas in which one atom is transferred into state $|1\rangle$ is $\hbar\nu_{12} - [(4\pi\hbar^2)/(m)]na_{12}$.

However, these energy shifts should not affect the resonance for a coherent transfer out of a pure state. For fermions in the initial pure state, the pair-correlation function vanishes at zero distance because of the antisymmetry of the wave function. During any coherent transfer process, the state vectors of all the atoms rotate “in parallel” in Hilbert space; i.e., the superposition of the two spin states

¹Department of Physics, Massachusetts Institute of Technology (MIT)–Harvard Center for Ultracold Atoms, and Research Laboratory of Electronics, MIT, Cambridge, MA 02139, USA. ²Eindhoven University of Technology, Post Office Box 513, 5600 MB Eindhoven, Netherlands.

*To whom correspondence should be addressed. E-mail: deep@mit.edu

REPORTS

has the same relative phase for all atoms. Thus, the atoms remain identical and cannot interact in the *s*-wave regime. The mean-field energy is thus established only after the coherence of the superposition state is lost and the pair correlations have relaxed, forming a purely statistical mixture of the two states.

It is a consequence of Fermi statistics that spectroscopic methods do not measure the equilibrium energy difference between the initial and final state of the system, but rather measure the unperturbed resonance frequency. The expected absence of the clock shift has led to suggestions for the use of fermions in future atomic clocks (27). Our work presents an experimental demonstration of this phenomenon.

We determined the transition frequency between states $|1\rangle$ and $|2\rangle$, first starting with a pure state $|1\rangle$ and then with a pure state $|2\rangle$ sample. The absence of a splitting between these two lines proves the suppression of the clock shift. Fig. 1 shows an example of such measurements. The magnetic field was ramped up to 570 G with the cloud in state $|1\rangle$. At this field, $a_{12} \sim 150a_0$. Therefore, the expected equilibrium mean-field shifts were $\Delta\nu = \pm 5$ kHz for our mean density of $3 \times 10^{13} \text{ cm}^{-3}$ (28). The interaction between states $|1\rangle$ and $|2\rangle$ at this magnetic field was also observed in the mutual evaporative cooling of the two states in the optical trap. RF pulses 140 μs in duration were applied at frequencies near the unperturbed resonance $\nu_{12} \sim 76$ MHz. Atoms in states $|1\rangle$ and $|2\rangle$ could be monitored separately by absorption imaging, because they are optically resolved at this field. We observed a suppression of the clock shift by a factor of 30 (Fig. 1). Using the same method, we observed the absence of a clock shift at several other magnetic fields. In particular, we observed a suppression of more than three orders of magnitude at ~ 860 G (29).

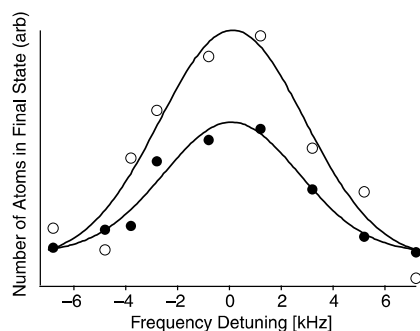


Fig. 1. Absence of the clock shift. RF transitions were driven between states $|1\rangle$ and $|2\rangle$ on a system prepared purely in state $|1\rangle$ (solid circles) and purely in state $|2\rangle$ (open circles). Mean-field interactions would have resulted in 5-kHz shifts for the two curves in opposite directions. Gaussian fits (solid lines) to the data are separated by 0.04 ± 0.35 kHz. This gives a clock-shift suppression factor of 30. Arb., arbitrary units.

P-wave interactions (23) could lead to a nonvanishing clock shift. However, at these low temperatures, they are proportional to T or T_F , whichever is higher, and are therefore strongly suppressed.

We can observe mean-field shifts and scattering lengths spectroscopically by driving transitions from a statistical mixture of two states to a third energy level. [While this work was in progress, use of a similar method to measure scattering lengths in fermionic ^{40}K was reported (30).] Specifically, we recorded the difference between the RF spectra for the $|2\rangle \rightarrow |3\rangle$ transition in the presence and in the absence of state $|1\rangle$ atoms. The presence of atoms in state $|1\rangle$ is then expected to shift the resonance by (31).

$$\Delta\nu = \frac{2\hbar}{m} n_1(a_{13} - a_{12}) \quad (1)$$

In our experimental scheme to determine the interaction energy at different magnetic fields (Fig. 2), the system was prepared by ramping up the magnetic field to 500 G with the atoms

in state $|1\rangle$. Either partial or complete RF transfer to state $|2\rangle$ was then performed. The number of atoms in state $|1\rangle$ was controlled by adjusting the speed of a frequency sweep around the $|1\rangle \rightarrow |2\rangle$ resonance. A fast, non-adiabatic sweep created a superposition of the two states, whereas a slow, adiabatic sweep prepared the sample purely in state $|2\rangle$. A wait time of 200 ms was allowed for the coherence between states $|1\rangle$ and $|2\rangle$ to decay and the system to equilibrate.

Typical parameters for the decohered $|1\rangle - |2\rangle$ mixture were mean-density $n_1 \sim 2.4 \times 10^{13} \text{ cm}^{-3}$ and $T \sim 0.7 T_F$. The magnetic field was then changed to the desired value, and the transition from state $|2\rangle$ to state $|3\rangle$ was driven with 140- μs RF pulses (Fig. 2C). We monitored the appearance of atoms in state $|3\rangle$ and the disappearance of atoms from state $|2\rangle$, using simultaneous absorption imaging. Fig. 2D shows the unperturbed and perturbed resonances at the magnetic field $B = 480$ G. The position of the unperturbed resonance

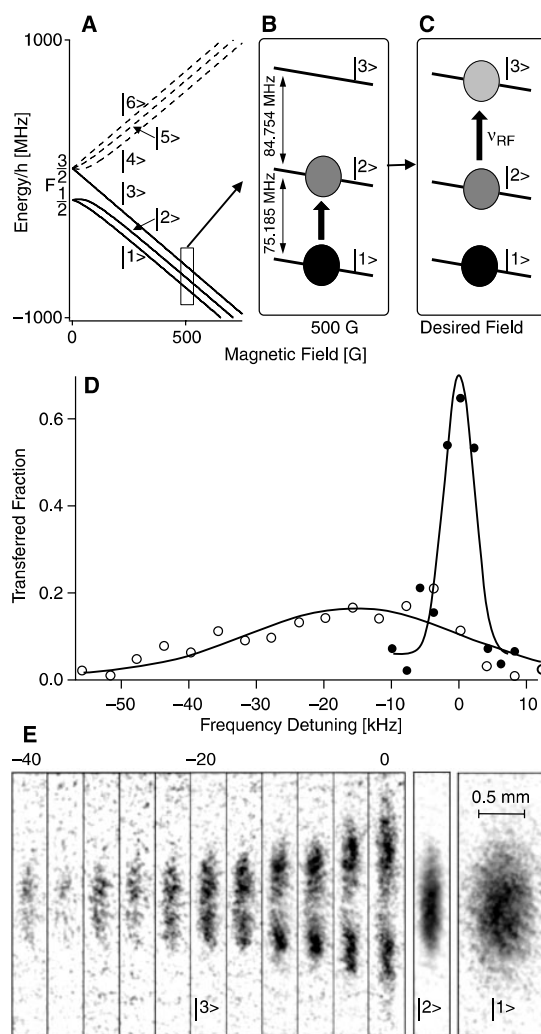


Fig. 2. Schematic of the mean-field measurement and representative spectra at 480 G. (A) Hyperfine structure of the ground state of ^6Li . (B and C) Experimental scheme: (B) Preparation of a mixture of atoms in states $|1\rangle$ and $|2\rangle$, and (C) RF spectroscopy of the $|2\rangle \rightarrow |3\rangle$ transition using a variable radio frequency (ν_{RF}). (D) The fraction of atoms transferred from $|2\rangle$ to $|3\rangle$, with $|1\rangle$ atoms absent (solid circles) and present (open circles). The mean-field shift is computed from Gaussian fits to the data (solid lines). (E) Spatial images of state $|3\rangle$ for the perturbed resonance. The optical trap was turned off immediately after the RF pulse and absorption images of the atoms were taken after 120 μs of expansion time. The central section of $\sim 150\text{-}\mu\text{m}$ vertical extent was used to extract the transferred fractions in (D). (E) also shows images of states $|2\rangle$ and $|1\rangle$ for zero RF detuning. States $|3\rangle$ and $|2\rangle$ were imaged simultaneously to observe their complementary spatial structure. State $|1\rangle$ was imaged after 760 μs of expansion time to record its density for normalization purposes.

ν_{23} also determines the magnetic field to an accuracy of <0.1 G. Fig. 2E shows absorption images of atoms in state $|3\rangle$, obtained for different values of the applied radio frequency. One can clearly see the spatial dependence and thus the density dependence of the mean-field shift: Close to the unperturbed resonance, the low-density wings of the cloud are predominantly transferred, whereas the high-density central part of the cloud is transferred only at sufficient detuning. To suppress spurious effects from this spatial dependence, only a small central part of the images was used to extract the transferred atomic fraction.

To ensure that our mean-field measurements were performed on a statistical mixture, we measured the time scale for decoherence in our system. The decay of the $|1\rangle - |2\rangle$ coherence at 500 G was observed by monitoring the $|2\rangle \rightarrow |3\rangle$ transfer at the measured unperturbed resonance ν_{23} , as a function of wait time (Fig. 3). For wait times that are small compared to the decoherence time of the $|1\rangle - |2\rangle$ superposition, the $|2\rangle \rightarrow |3\rangle$ RF drive places each atom in an identical three-state superposition. All mean-field shifts are then absent and the resulting transfer is unchanged from the unperturbed case. For longer wait times, the $|1\rangle - |2\rangle$ superposition decoheres and mean-field interactions set in. This shifts the resonance frequency of the $|2\rangle \rightarrow |3\rangle$ transition, reducing the transferred fraction at ν_{23} . The measured decoherence time of ~ 12 ms was attributed mainly to the sensitivity of ν_{12} to magnetic field variations across the cloud. These inhomogeneities cause the relative phase of the $|1\rangle - |2\rangle$ superposition in different parts of the trap to evolve at different rates, given by the local ν_{12} . Atoms that travel along different paths within the trap therefore acquire different phases between their $|1\rangle$ and $|2\rangle$ components. Being no longer in identical states, s -wave interactions between them are allowed. The inhomogeneities scale with B , whereas the sensitivity of the transition scales with $\partial\nu_{12}/\partial B$.

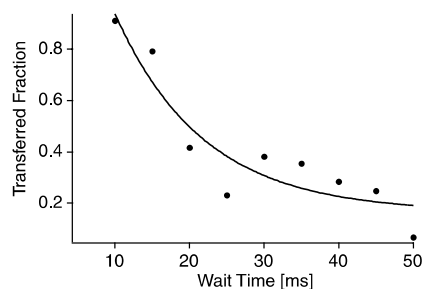


Fig. 3. Emergence of mean-field shifts due to decoherence at 500 G. Decoherence leads to a reduction of the $|2\rangle \rightarrow |3\rangle$ transfer at the unperturbed resonance ν_{23} . An exponential fit to the data (solid line) gives a time constant of 12 ms.

∂B . We would thus expect the decoherence time to vary inversely with the product of these two quantities. Our hypothesis is supported by our observation of longer decoherence times at higher fields, where $B \times \partial\nu_{12}/\partial B$ is lower.

Fig. 4A summarizes the results of our mean-field measurements for a wide range of magnetic fields up to 750 G. For magnetic fields up to 630 G, our data can be explained fairly well by using Eq. 1 with the theoretical calculations of the scattering lengths shown in Fig. 4B and an effective density of $n_1 = 2.2 \times 10^{13} \text{ cm}^{-3}$, which is consistent with the initial preparation of the system at 500 G. A narrow resonance of a_{12} at ~ 550 G (21, 25, 32) is indicated by the data but was not fully resolved. We also see additional structure near 470 G, which is not predicted by theory and deserves further study.

For fields above 630 G, the measured shifts strongly deviated from the predictions of Eq. 1, indicating a different regime of interactions. In the region between 630 G and 680 G, the two scattering lengths are expected to be large and positive, with $a_{13} \gg a_{12}$ (Fig. 4B). Eq. 1 would thus predict large positive mean-field shifts. In contrast, we observe very small shifts, indicating almost perfect cancellation of the two contributions. We also observe essentially no mean-field shifts between 680 G and 750 G, where the two scattering lengths are predicted to be very large in magnitude and of opposite signs, and in a simple picture should add up to a huge negative shift. These results are evidence for phenomena in a strongly interacting system, where

the scattering length becomes comparable to either the inverse wave vector of interacting particles or the interatomic separation.

Eq. 1 is valid only for low energies and weak interactions, where the relative wave vector of the two particles, k , satisfies $k \ll 1/|a|$. For arbitrary values of ka , the s -wave interaction between two atoms is described by replacing the scattering length a with the complex scattering amplitude f .

$$f = \frac{-a}{1 + k^2 a^2} (1 - ika) \quad (2)$$

The real part of f , $\text{Re}(f)$ determines energy shifts, and hence the ground state properties of an interacting many-body system. The imaginary part, $\text{Im}(f)$ determines the (inverse) lifetime for elastic scattering out of a momentum state, and hence the dynamic properties of the system such as thermalization rates. For $k|a| \rightarrow \infty$, the elastic cross-section $\sigma = 4\pi \text{Im}(f)/k$ monotonically approaches the well known “unitarity-limited” value of $4\pi/k^2$. On the other hand, the two-particle contribution to the mean-field energy, proportional to $-\text{Re}(f) = a/(1 + k^2 a^2)$ peaks at $|a| = 1/k$ and then, counter-intuitively, decreases as $1/|a|$ for increasing $|a|$. Averaging $\text{Re}(f)$ over a zero-temperature Fermi distribution with Fermi momentum $\hbar k_F$ limits its absolute value to $1.05/k_F$ and markedly weakens its dependence on the exact value of a in the $k_F|a| > 1$ regime (33). This results in a prediction for the mean-field energy that is sensitive to the sign of the scattering length, remains finite for $k_F|a| \gg 1$, and never exceeds $0.45 E_F$, where E_F is the Fermi energy. Hence,

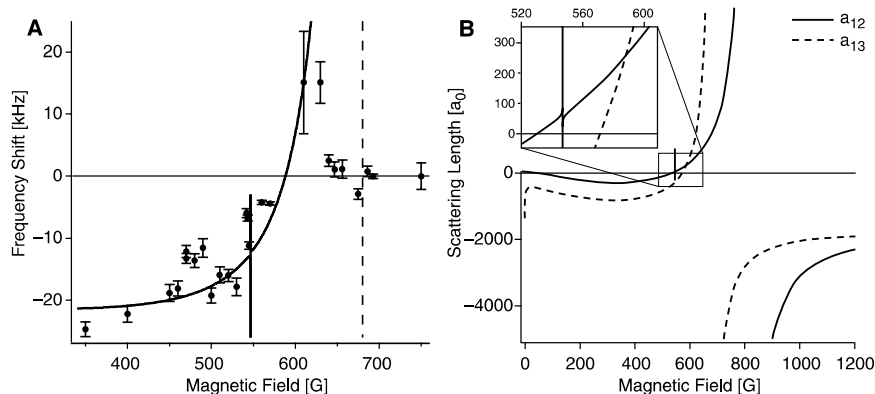


Fig. 4. Spectroscopic measurement of interaction energy. **(A)** Frequency shift versus magnetic field for the $|2\rangle \rightarrow |3\rangle$ resonance due to atoms in state $|1\rangle$. The shifts are computed by monitoring the arrival fraction in state $|3\rangle$ for 140- μ s RF pulses, except at 750 G. At 750 G, because of strong inelastic losses between $|3\rangle$ and $|1\rangle$ atoms, we monitored the loss of atoms in state $|2\rangle$ after applying RF sweeps 3 ms in duration and 2 kHz in width. All the data points are normalized to the same atom number in state $|1\rangle$. The fit at low fields (solid line) uses Eq. 1 with $n_1 = 2.2 \times 10^{13} \text{ cm}^{-3}$ and the theoretical calculations of the scattering lengths. The error bars reflect uncertainty in the state $|1\rangle$ atom number and the uncertainty in the Gaussian fits to the spectra. The dashed line indicates the position of the predicted a_{13} resonance. **(B)** s -wave scattering lengths a_{12} and a_{13} as a function of magnetic field, obtained from a highly model-independent quantum-scattering calculation. The calculation makes use of the presently available ^6Li experimental data (40) in a coupled channel approach to deduce accumulated phases that characterize the less well-known, short-range parts of the $^6\text{Li} + ^6\text{Li}$ scattering potential (32). a_{12} has a narrow Feshbach resonance at 550 G and a wide one at 810 G. a_{13} has a wide Feshbach resonance at 680 G.

this approach could qualitatively explain our results in the 630 to 680 G region, but it is in clear contradiction with negligible resonance shifts in the 680 to 750 G region (34).

We suggest that these discrepancies might be due to the fact that we are in the high-density regime, where $n|a|^3$ approaches unity. In a degenerate Fermi gas, the interparticle spacing is comparable to the inverse Fermi wave vector, $k_F^3 = 6\pi^2 n$. Hence, the unitarity limit coincides with the breakdown of the low-density approximation ($n|a|^3 \ll 1$) and higher order many-body effects can become important. Some recent many-body calculations (35–37) suggest that in the regime $k_F|a| \gg 1$ (or $n|a|^3 \gg 1$), the interaction energy is always negative and independent of both sign and magnitude of a . This suggests that whenever the scattering length is large, either positive or negative, the interaction energy is a universal fraction of the Fermi energy (33). This is a possible explanation for the small line shifts that we observed for fields higher than 630 G, where the interactions are strong in both states.

This picture is consistent with other recent experimental observations (30, 33, 38, 39). Expansion energy measurements in a mixture of states $|1\rangle$ and $|2\rangle$ of ^6Li (39) showed a negative interaction energy at 720 G, which is on the repulsive side of the predicted Feshbach resonance. RF spectroscopy in ^{40}K (30) has also shown some saturation of the mean field in the vicinity of a Feshbach resonance, which may reflect the unitarity limit.

In characterizing an interacting Fermi gas by RF spectroscopy, we have demonstrated absence of clock shifts in a two-level system and introduced a three-level method for measuring mean-field shifts. For strong interactions, we have found only small line shifts that may reflect both the unitarity limit of binary collisions and many-body effects. It would be very important to distinguish between two-body and many-body effects by studying the gas over a broad range of temperatures and densities. In a very dilute and very cold gas, the weakly interacting limit could be extended to very large values of $|a|$, thus allowing for direct verification of molecular calculations. This presents experimental challenges, because cooling changes the density and the temperature together. It would also be interesting to study similar phenomena in bosonic gases, in order to distinguish to what extent the high density many-body effects depend on quantum statistics. This insight into the physics of strongly interacting Fermi gases must be taken into account in the search for superfluidity in these systems.

References and Notes

1. K. Gibble, S. Chu, *Phys. Rev. Lett.* **70**, 1771 (1993).
2. C. Fertig, K. Gibble, *Phys. Rev. Lett.* **85**, 1622 (2000).
3. Y. Sortais *et al.*, *Phys. Scr.* **T95**, 50 (2001).
4. A. G. Martin, K. Helmerson, V. S. Bagnato, G. P. Lafyatis, D. E. Pritchard, *Phys. Rev. Lett.* **61**, 2431 (1988).

5. I. Bloch, T. W. Hänsch, T. Esslinger, *Phys. Rev. Lett.* **82**, 3008 (1999).
6. M. R. Matthews *et al.*, *Phys. Rev. Lett.* **81**, 243 (1998).
7. J. Stenger *et al.*, *Nature* **396**, 345 (1998).
8. M.-O. Mewes *et al.*, *Phys. Rev. Lett.* **78**, 582 (1997).
9. D. M. Harber, H. J. Lewandowski, J. M. McGuirk, E. A. Cornell, *Phys. Rev. A* **66**, 053616 (2002).
10. A. Görlitz *et al.*, *Phys. Rev. Lett.* **90**, 090401 (2003).
11. T. C. Killian *et al.*, *Phys. Rev. Lett.* **81**, 3807 (1998).
12. J. Stenger *et al.*, *Phys. Rev. Lett.* **82**, 4569 (1999).
13. B. DeMarco, D. S. Jin, *Science* **285**, 1703 (1999).
14. A. G. Truscott, K. E. Strecker, W. I. McAlexander, G. B. Partridge, R. G. Hulet, *Science* **291**, 2570 (2001).
15. F. Schreck *et al.*, *Phys. Rev. Lett.* **87**, 080403 (2001).
16. S. R. Granade, M. E. Gehm, K. M. O'Hara, J. E. Thomas, *Phys. Rev. Lett.* **88**, 120405 (2002).
17. Z. Hadzibabic *et al.*, *Phys. Rev. Lett.* **88**, 160401 (2002).
18. G. Roati, F. Riboli, G. Modugno, M. Inguscio, *Phys. Rev. Lett.* **89**, 150403 (2002).
19. M. Houbiers, H. T. C. Stoof, *Phys. Rev. A* **59**, 1556 (1999).
20. M. Holland, S. J. J. M. F. Kokkelmans, M. L. Chiofalo, R. Walser, *Phys. Rev. Lett.* **87**, 120406 (2001).
21. K. Dieckmann *et al.*, *Phys. Rev. Lett.* **89**, 203201 (2002).
22. Z. Hadzibabic *et al.*, preprint available at <http://arXiv.org/abs/cond-mat/0306050> (2003).
23. S-wave and p-wave interactions refer to two-body interactions with relative angular momentum 0 and \hbar , respectively.
24. M. Houbiers, H. T. C. Stoof, W. I. McAlexander, R. G. Hulet, *Phys. Rev. A* **57**, R1497 (1998).
25. K. M. O'Hara *et al.*, *Phys. Rev. A* **66**, 041401 (2002).
26. The transfer efficiency is limited by finite optical-trap depth and residual heating during the transfer.
27. K. Gibble, B. J. Verhaar, *Phys. Rev. A* **52**, 3370 (1995).
28. For our modest degeneracy, we can use a Gaussian approximation for the density distribution. The mean density is then lower than the peak density by a factor of $2\sqrt{2}$.
29. Our estimate uses the direct mean field measurement of Bourdel *et al.* (39), scaled to our parameters.
30. C. Regal, D. S. Jin, preprint available at <http://arXiv.org/abs/cond-mat/0302461> (2003).
31. Because of fermionic antisymmetry, there is no clock shift from interactions between atoms in states $|2\rangle$ and $|3\rangle$. Mean-field shifts arise only during a decoherence time (see later in the text) but are negligible if the population of atoms in state $|3\rangle$ is small.
32. E. G. M. van Kempen *et al.*, in preparation.
33. M. E. Gehm, S. L. Hemmer, S. R. Granade, K. M. O'Hara, J. E. Thomas, preprint available at <http://arXiv.org/abs/cond-mat/0212499> (2002).
34. For fields higher than 630 G, number losses generally reduced n_1 , and all the shifts in this region were scaled up by a factor of 1.1 to 2.7 but still remained negligible.
35. J. V. Steele, preprint available at <http://arXiv.org/abs/nuc1-th/0010066> (2000).
36. H. Heiselberg, *Phys. Rev. A* **63**, 043606 (2001).
37. R. Combescot, preprint available at <http://arXiv.org/abs/cond-mat/0302209> (2003).
38. K. M. O'Hara, S. L. Hemmer, M. E. Gehm, S. R. Granade, J. E. Thomas, *Science* **298**, 2179 (2002).
39. T. Bourdel *et al.*, preprint available at <http://arXiv.org/abs/cond-mat/0303079> (2003).
40. This includes the recent measurement of 800 ± 40 G for the resonance in a_{12} (39).
41. The work at MIT was supported by NSF, the Office of Naval Research, the Army Research Office, and NASA. The work at Eindhoven is part of the research program of the Stichting voor Fundamenteel Onderzoek der Materie, which is financially supported by the Nederlandse Organisatie voor Wetenschappelijk Onderzoek.

4 April 2003; accepted 25 April 2003

Published online 8 May 2003;

10.1126/science.1085335

Include this information when citing this paper.

The Interface Phase and the Schottky Barrier for a Crystalline Dielectric on Silicon

R. A. McKee,^{1*} F. J. Walker,^{1,2} M. Buongiorno Nardelli,^{1,3} W. A. Shelton,¹ G. M. Stocks¹

The barrier height for electron exchange at a dielectric-semiconductor interface has long been interpreted in terms of Schottky's theory with modifications from gap states induced in the semiconductor by the bulk termination. Rather, we show with the structure specifics of heteroepitaxy that the electrostatic boundary conditions can be set in a distinct interface phase that acts as a "Coulomb buffer." This Coulomb buffer is tunable and will functionalize the barrier-height concept itself.

When Schottky (1) and Mott (2) formulated the barrier-height theory for a metal-semiconductor junction and later when Anderson (3) formulated the band-edge offset problem for semiconductor-semiconductor junctions, there was no consideration given to interface states as contributions

to the electrostatic boundary conditions. The charge distribution at the interface was treated simply as a superposition of the bulk-terminated junction. Certainly these theories have been insightful, but they consistently misrepresent the barrier height or band-edge offsets because real interfaces, apparently from interfacial structure variations, modify the intrinsic band alignment (4–6).

Although the bulk-termination view of the problem has been enhanced over the years with an ever-increasing formalization of theoretical techniques (7–15), recent bond polarization ar-

¹Oak Ridge National Laboratory, Oak Ridge, TN 37831, USA. ²University of Tennessee (UT), Knoxville, TN 37996, USA. ³North Carolina State University, Raleigh, NC 27695, USA.

*To whom correspondence should be addressed. E-mail: mckee@ornl.gov

Appendix E

Spectroscopic insensitivity to cold collisions in a two-state mixture of fermions

This appendix includes the following manuscript [6]:

M. W. Zwierlein, Z. Hadzibabic, S. Gupta, and W. Ketterle, “Spectroscopic insensitivity to cold collisions in a two-state mixture of fermions,” cond-mat/0306627 (2003).

Spectroscopic insensitivity to cold collisions in a two-state mixture of fermions

Martin W. Zwierlein, Zoran Hadzibabic, Subhadeep Gupta, and Wolfgang Ketterle

*Department of Physics, MIT-Harvard Center for Ultracold Atoms, and Research Laboratory of Electronics,
MIT, Cambridge, MA 02139*

(Dated: June 24, 2003)

We have experimentally demonstrated the absence of spectroscopic resonance shifts in a mixture of two interacting Fermi gases. This result is linked to observations in an ultracold gas of thermal bosons. There, the measured resonance shift due to interstate collisions is independent of the coherence in the system, and twice that expected from the equilibrium energy splitting between the two states in a fully decohered cloud. We give a simple theoretical explanation of these observations, which elucidates the effect of coherent radiation on an incoherent mixture of atoms.

PACS numbers: 03.75.Ss, 05.30.Jp, 32.30.Bv, 34.20.Cf

The coherence properties of light and matter are intimately connected with the quantum statistics of the constituent particles. One quantitative measure of the coherence in a system is the two-particle correlation function at zero distance, $g^{(2)}$, which measures the probability that two particles are simultaneously detected. Intensity fluctuations in the incoherent light emitted by a light bulb lead to photon “bunching”, making this probability twice higher than in the coherent light of a laser. Identical fermions on the other hand exhibit “anti-bunching”, making such a probability zero.

Interactions in ultracold atomic gases crucially depend on the value of $g^{(2)}$ [1]. The reason is that s-wave scattering relies on particles overlapping in real space. The interaction energy in a many-body system is determined by coherent, or “cold” collisions, for which the outgoing and the incoming two-particle states are identical. Under this constraint, the two colliding particles can at most do two things - either preserve their momenta, or exchange them. We can thus distinguish four cases: (1) Two identical bosons in a thermal gas can collide in both ways, corresponding to $g^{(2)} = 2$, in analogy with a light bulb. (2) Two atoms in a Bose-Einstein condensate (BEC) have the same momenta and cannot undergo the exchange interaction. Here, $g^{(2)} = 1$, in analogy with laser light. (3) Two distinguishable particles, fermions or bosons, also cannot exchange their momenta because that would make the outgoing state different from the incoming one. Again, $g^{(2)} = 1$. (4) Two identical fermions cannot collide at all, so $g^{(2)} = 0$. In all cases, the mean-field energy of a particle with mass m is given by $g^{(2)}(4\pi\hbar^2/m)an$, where a is the s-wave scattering length, and n is the density of atoms it interacts with.

In experiments on ultracold hydrogen, mean-field shifts of the 1S-2S two-photon transition were used to prove the existence of a BEC [2]. However, quantitative interpretation of the shifts led to a vivid theoretical discussion about the coherence related “factors of 2” [3, 4, 5, 6]. More recently, Eric Cornell’s group at JILA performed Ramsey spectroscopy in a two-component, thermal gas of ^{87}Rb bosons to measure $g^{(2)}$ in the interstate collisional

shift [7]. Their measurements yielded $g^{(2)} = 2$, independent of the degree of coherence between the two states. The spectroscopic results thus seemed to correspond to the case of all particles being in an identical coherent superposition of the two internal states, even though the binary mixture was partially decohered and should have had a mean-field energy corresponding to $1 < g^{(2)} < 2$. The authors commented on this mystery [8]: “it is a pleasure to note that a two-level system can still yield surprises, 75 years after the advent of quantum mechanics.” The mystery can be formally resolved using a quantum Boltzmann equation [9, 10, 11, 12, 13].

Here, we experimentally address the relation between coherence and spectroscopic measurements in a binary mixture of ultracold *fermions*. We demonstrate that shifts of spectroscopic lines are absent even in a fully decohered binary mixture, in which the particles are distinguishable, and the many-body mean-field energy in the system has developed. We theoretically show that this is a direct consequence of the coherent nature of the RF *excitation*, and is not dependent on the coherence of the *sample* on which spectroscopy is performed. Our calculation intuitively explains both our results for fermions, and the JILA results for bosons.

In a recent paper [14], we demonstrated the absence of mean-field “clock-shifts” in a coherent two-state superposition of ^6Li fermions. In this case, RF spectroscopy was performed on a gas prepared purely in one internal state. Since an RF pulse acts as a rotation in the two-state Hilbert space, all the atoms stayed in an identical (superposition) state and could not interact. As long as the fermionic atoms were indistinguishable, $g^{(2)} = 0$, and the resonance was thus found to be unperturbed at $\nu_0 = \frac{E_{12}}{\hbar}$, where E_{12} is the energy difference between the internal states $|1\rangle$ and $|2\rangle$.

However, once decoherence sets in, for example due to inhomogeneous magnetic fields across the cloud, the spatial overlap between atoms in different states grows and mean-field energy density builds up:

$$\mathcal{E}_{\text{int}} = g^{(2)} V_{12} n_1 n_2, \quad V_{12} = \frac{4\pi\hbar^2}{m} a_{12}, \quad (1)$$

where n_1 and n_2 are the densities of particles in states $|1\rangle$ and $|2\rangle$, and a_{12} is the interstate s-wave scattering length. In a fully decohered cloud, we have a binary mixture of two distinct species of atoms, with a mean-field energy density $\mathcal{E}_{\text{int}} = V_{12}n_1n_2$. This interaction changes the equilibrium energy level of atoms in state $|1\rangle$ ($|2\rangle$) according to $\delta\mu_{1(2)} = V_{12}n_{2(1)}$. The difference in equilibrium mean-field energy of the two states is then

$$\Delta E_{\text{int}} = \delta\mu_2 - \delta\mu_1 = V_{12}(n_1 - n_2). \quad (2)$$

This suggests [7, 8, 14] that in a decohering sample, the resonant frequency for population transfer between the two states gradually changes from $\nu_{12} = \nu_0$ to $\nu_{12} = \nu_0 + \frac{1}{h}\Delta E_{\text{int}}$. Here, we show both experimentally and theoretically that this conclusion is wrong, and that the spectroscopic resonance frequency ν_{12} is always the unperturbed frequency ν_0 .

Our experimental setup was described in [14, 15]. Magnetically trapped ^6Li fermions were sympathetically cooled with ^{23}Na bosons, and then transferred into an optical dipole trap. About 10^7 atoms were trapped at a temperature of $35\text{ }\mu\text{K}$. The two-level system under consideration is formed by the two lowest ground state hyperfine levels, $|1\rangle$ and $|2\rangle$, corresponding to $|F, m_F\rangle = |1/2, 1/2\rangle$ and $|1/2, -1/2\rangle$ in the low field basis, respectively. A DC magnetic field of $B = 320\text{G}$ was applied to the sample in order to tune the interstate scattering length a_{12} to a large value of $\sim -300a_0$, where a_0 is the Bohr radius [14]. At this field, electronic and nuclear spins are mostly decoupled, and the two states experience approximately the same Zeeman shift. This greatly reduces the effect of magnetic field fluctuations, although the differential shift is still linear in B , unlike in [7].

We created a superposition of atoms in states $|1\rangle$ and $|2\rangle$ using a non-adiabatic RF sweep around the energy splitting of 74MHz . As the sample decohered, efficient evaporative cooling set in, confirming a large elastic scattering length. After 1 second, we were left with a fully decohered mixture at a mean density $n = 5 \times 10^{13}\text{cm}^{-3}$. The rate of the RF sweep was adjusted so that after decoherence and cooling, 80% of the atoms were in state $|2\rangle$. The mean-field interaction should thus have increased the energy splitting of the two levels by $h\delta\nu = \delta\mu_2 - \delta\mu_1 = V_{12}(n_1 - n_2) \approx h \times 10\text{kHz}$. Our experiments involving a third state [14] have confirmed the presence of such energy shifts.

Rabi spectroscopy in the interacting binary mixture was performed by applying $200\mu\text{s}$ RF pulses of different frequencies, and recording the final populations in the two states by simultaneous absorption imaging (Fig. 1). In order to eliminate the systematic uncertainty in the value of ν_0 , we performed a second experiment with the roles of states $|1\rangle$ and $|2\rangle$ reversed. According to Eq. 2, one would expect an opposite shift of the resonance.

Within our precision, no interaction shift of the resonance frequency was observed. Comparing the ex-

pected difference in mean-field shifts for the two experiments, $2\delta\nu = 20\text{kHz}$, with the measured line separation of $(34 \pm 146)\text{Hz}$, we arrive at an apparent value for $g^{(2)} = 0.002(7)$. This demonstrates the universal absence of a resonance shift in a two-level Fermi gas, independent of the coherence in the system.

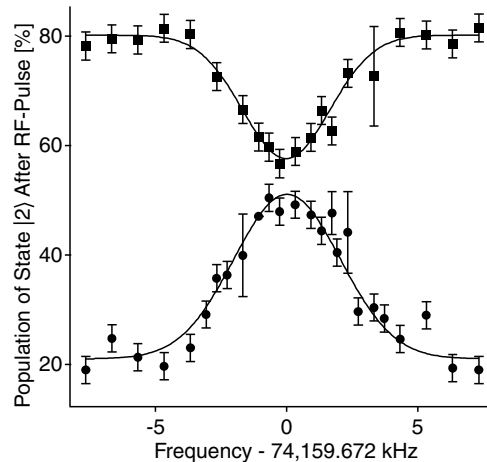


FIG. 1: Absence of mean-field shift of an RF transition in a binary Fermi system. The resonance curves were measured for fully decohered 80%/20% two-state mixtures of fermions. The measured frequency difference between the two lines is $(34 \pm 146)\text{Hz}$, even though Eq. 2 would predict a splitting of 20kHz .

Evidently, RF spectroscopy does not measure the expected difference in thermodynamic chemical potentials for the two states. Experiments with thermal bosons have posed a similar puzzle [7]. Here we explain that this is a direct consequence of the coherent nature of the RF excitation.

In Fig. 2, the average properties of the many-body state are described by the three coordinates of the spin-1/2 Bloch vector $\mathbf{m} = m_z\hat{e}_z + \mathbf{m}_\perp$: $m_z = \frac{n_2 - n_1}{2}$ represents the population difference in the two states, whereas the transverse component \mathbf{m}_\perp is a measure of the coherence in the system. In polar coordinates, the length of the Bloch vector measures the purity of the state and hence the entropy of the system. The polar angle θ encodes the coherence of the sample. Fully decohered statistical mixtures are represented by vectors with $\theta = 0$, or equivalently $\mathbf{m}_\perp = 0$, with state A being the special case of a pure state. In Fig. 2a, state B is created by applying an RF pulse on a pure sample A. In this case, there is no interaction energy in the system during the RF pulse, and no frequency shift is expected [14]. State C is formed through subsequent decoherence of state B. States B and C have the same number of particles in $|1\rangle$ and $|2\rangle$, but in C the mean-field has fully developed.

Our experiment is performed on a C-like state (Fig. 2b). Here we explain why Eq. 2 still does not give

the correct resonance frequency for an infinitesimal transfer of atoms between $|1\rangle$ and $|2\rangle$. The key point is that even though the sample is fully decohered, the applied RF pulse re-introduces coherence into the system. Let us consider two fully decohered states, C and E. Eq. 2 correctly gives the energy of the transformation $C \rightarrow E$. However, these two states have different entropies, as indicated by Bloch vectors of different lengths. An RF pulse is a unitary transformation of the system, and must preserve entropy. The true effect of the RF pulse is thus to change the relative populations of $|1\rangle$ and $|2\rangle$ by tilting the Bloch vector away from the z axis, into state D. It is the energy of *this* transformation, $C \rightarrow D$, that needs to be calculated in order to find the correct resonant RF frequency.

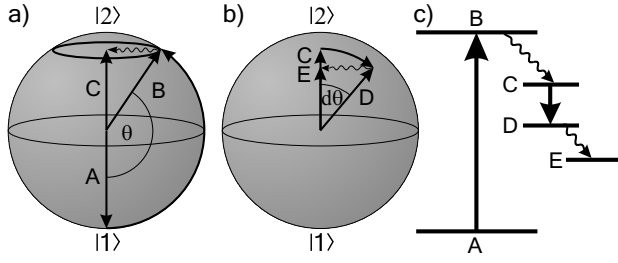


FIG. 2: Bloch sphere representation of RF transitions. a) An RF pulse rotates a pure state A into B. The superposition state decoheres into a “ring” distribution, represented by its average, C. b) A second RF pulse transforms the fully decohered state C into a partially coherent state D. The final state E is reached only after further decoherence. c) Transfers $A \rightarrow B$ and $C \rightarrow D$ are coherent and reversible. $B \rightarrow C$ and $D \rightarrow E$ are irreversible.

In the case of fermions, we can prove very generally that the resonance frequency will always be ν_0 , by showing that the interaction hamiltonian is invariant under rotations of the Bloch vector. The interstate s-wave interaction is described by the second-quantized hamiltonian density

$$H_{\text{int}} = V_{12} \psi_1^\dagger(\mathbf{r}) \psi_2^\dagger(\mathbf{r}) \psi_2(\mathbf{r}) \psi_1(\mathbf{r}). \quad (3)$$

Under a general rotation, described by polar angles θ, ϕ , the field operators $\psi_{1,2}^\dagger$ transform according to:

$$\begin{aligned} \psi_{1\theta,\phi}^\dagger &= \cos \frac{\theta}{2} e^{-i\phi/2} \psi_1^\dagger + \sin \frac{\theta}{2} e^{i\phi/2} \psi_2^\dagger \\ \psi_{2\theta,\phi}^\dagger &= -\sin \frac{\theta}{2} e^{-i\phi/2} \psi_1^\dagger + \cos \frac{\theta}{2} e^{i\phi/2} \psi_2^\dagger \end{aligned} \quad (4)$$

Using the standard fermionic anticommutation relations ($\psi_1 \psi_2 = -\psi_2 \psi_1$, $\psi_1 \psi_1 = 0$ etc.), it is easy to show that:

$$\begin{aligned} H_{\text{int}}^{\theta,\phi} &= V_{12} \psi_{1\theta,\phi}^\dagger(\mathbf{r}) \psi_{2\theta,\phi}^\dagger(\mathbf{r}) \psi_{2\theta,\phi}(\mathbf{r}) \psi_{1\theta,\phi}(\mathbf{r}) \\ &= V_{12} \psi_1^\dagger(\mathbf{r}) \psi_2^\dagger(\mathbf{r}) \psi_2(\mathbf{r}) \psi_1(\mathbf{r}) = H_{\text{int}} \end{aligned} \quad (5)$$

We therefore see that an RF-induced rotation on the Bloch sphere commutes with the interaction hamiltonian,

and hence does not change the energy of the many-body state. It is then obvious that the resonant frequency will always be ν_0 , independent of the coherence of the system.

We now present a more general calculation of the mean-field frequency shifts, which holds for both fermions and bosons. To reduce complexity and concentrate on the only controversial case of interstate interactions, we consider a fictitious boson with no intrastate interactions ($a_{11} = a_{22} = 0$). The mean-field expectation value of the hamiltonian in Eq. 3 is [16]

$$\begin{aligned} \mathcal{E}_{\text{int}} &= \langle H_{\text{int}} \rangle = V_{12}(n_1 n_2 + \epsilon n_{12} n_{21}), \\ g^{(2)} &= 1 + \epsilon \frac{n_{12} n_{21}}{n_1 n_2}, \end{aligned} \quad (6)$$

where $n_1 = \langle \psi_1^\dagger \psi_1 \rangle$ and $n_2 = \langle \psi_2^\dagger \psi_2 \rangle$ are the densities in the two states, we have introduced “coherences” $n_{12} = \langle \psi_1^\dagger \psi_2 \rangle$ and $n_{21} = \langle \psi_2^\dagger \psi_1 \rangle$, and $\epsilon = \pm 1$ for bosons/fermions. In a fully coherent sample $n_{12} n_{21} = n_1 n_2$ and $g^{(2)} = 1 + \epsilon$. As decoherence sets in, $g^{(2)}$ increases (decreases) from 0 (2) to 1 for fermions (bosons). For the most general case of a partially decohered sample, we can rewrite Eq. 6 in terms of the Bloch vector:

$$\begin{aligned} n_1 &= \frac{n}{2} - m_z, & n_2 &= \frac{n}{2} + m_z \\ n_{12} &= m_x + i m_y, & n_{21} &= m_x - i m_y \\ n_{12} n_{21} &= m_x^2 + m_y^2 = m_\perp^2, \end{aligned} \quad (7)$$

where n is the total particle density. This gives

$$\begin{aligned} \mathcal{E}_{\text{int}} &= V_{12} \frac{n^2}{4} - V_{12} m_z^2 + \epsilon V_{12} m_\perp^2 \\ &= V_{12} \frac{n^2}{4} + \epsilon V_{12} |\mathbf{m}|^2 - (1 + \epsilon) V_{12} m_z^2. \end{aligned} \quad (8)$$

Two states with same numbers of atoms in $|1\rangle$ and $|2\rangle$, but different levels of coherence, have the same m_z , but different $|\mathbf{m}_\perp|$ (e.g. states D and E in Fig. 2b). Again we see that two such states indeed have different interaction energies.

Now, let us evaluate the effect of coherence on the resonant RF frequency. A coherent RF excitation preserves entropy ($|\mathbf{m}| = \text{const.}$), and the total density n . In an infinitesimal tilt of the Bloch vector, the density of atoms transferred from $|1\rangle$ to $|2\rangle$ is $dn_2 = -dn_1 = dm_z$. Therefore, the change of interaction energy per transferred particle, and thus the shift in the resonant frequency $\Delta\nu$, comes out to be

$$\Delta\nu = \frac{1}{h} \frac{\partial \mathcal{E}_{\text{int}}}{\partial m_z} \bigg|_{n, |\mathbf{m}|} = \frac{1}{h} (1 + \epsilon) V_{12} (n_1 - n_2). \quad (9)$$

In analogy with a spinning top which precesses in the gravitational field, the resonant frequency for an infinitesimal tilt of the Bloch vector is also equal to the frequency of its free precession. In the traditional language of atomic physics, this analogy just reiterates that Rabi [14]

and Ramsey [7] spectroscopy measure the same characteristic frequency of the system. The striking result is that in contrast to the interaction energy (Eqs. 6, 8), the precession of the Bloch vector, or equivalently the RF frequency shift (Eq. 9), *does not* depend on the level of coherence in the sample. Equation 9 explains both our measurements with fermions, and the JILA experiment with thermal bosons [7].

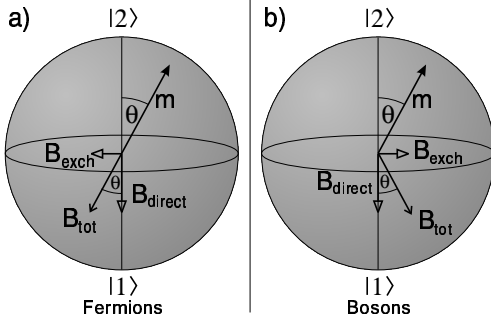


FIG. 3: Mean-field represented as effective magnetic field. a) Fermions: The exchange and direct interaction add up to form a magnetic field aligned with the average spin ($V_{12} < 0$ in the drawing). The net torque vanishes and the Bloch vector \mathbf{m} precesses at the unperturbed frequency ν_0 . b) Bosons: The exchange interaction has opposite sign than for fermions. It exerts a torque on the average spin equal to the torque induced by the direct interaction, as can be seen by comparing the two cross products with \mathbf{m} . The Bloch vector thus precesses at ν_0 plus twice the frequency shift due to direct interaction.

In order to further elucidate the role of coherences in the precession of the Bloch vector, we employ the interpretation of the mean-field energy as the interaction of the average spin with an effective magnetic field [12, 13]. Using Eq. 8, we obtain [17]

$$\mathcal{E}_{\text{int}} = \text{const.} - \frac{1}{2} \mathbf{B}_{\text{eff}} \cdot \mathbf{m}$$

$$\mathbf{B}_{\text{eff}} = 2V_{12} (m_z \hat{\mathbf{e}}_z - \epsilon \mathbf{m}_{\perp}). \quad (10)$$

In this picture, the precession of the spin due to interactions is driven by the torque $\mathbf{B}_{\text{eff}} \times \mathbf{m}$. The magnetic field along the z axis is induced by the direct interaction, and has the same sign for fermions and bosons (Fig. 3). The transverse magnetic field comes from the exchange interaction, and has opposite signs for fermions and bosons. For fermions, \mathbf{B}_{eff} is parallel to \mathbf{m} (Eq. 10) and hence does not cause any precession. Equivalently, the direct and exchange interaction exert torques equal and opposite to each other. For bosons, the two contributions add up to yield exactly twice the precession frequency given by the direct interaction alone. During decoherence, the exerted torque shrinks in proportion to the decaying transverse spin. Therefore, the precession frequency remains constant, no matter how small the coherences are.

In addition to the effects discussed here, interactions in inhomogeneous samples can lead to spin waves [9, 10, 12, 18, 19] both in bosonic and fermionic gases.

In conclusion, we have demonstrated the absence of the mean-field shift of RF transitions in a fully decohered, interacting binary mixture of fermions. This was explained by proving the invariance of the interaction energy under coherent Hilbert space rotations. This result is relevant for the potential use of a fermionic atom supplying the frequency standard in an atomic or optical clock, since it implies a robust elimination of the systematic errors due to density dependent frequency shifts. Previously, the absence of such clock shifts was explained by the absence of mean-field energy in a purely coherent superposition state [14]. Now we have shown that there is no spectroscopic shift even after decoherence has led to measurable mean-field energies. Further, we have presented a simple theoretical framework for calculating the precession frequency of the Bloch vector which describes an arbitrary spin state of either fermions or bosons. This resolves “The Mystery of the Ramsey Fringe that Didn’t Chirp” [8] with a simple and intuitive picture.

We thank Claudiu Stan and Christian Schunck for experimental assistance, and Michele Saba for critical reading of the manuscript. This work was supported by the NSF, ONR, ARO, and NASA.

-
- [1] W. Ketterle and H.-J. Miesner, Phys. Rev. A **56**, 3291 (1997).
 - [2] D. G. Fried, T. C. Killian, L. Willmann, D. Landhuis, S. C. Moss, D. Kleppner, and T. J. Greytak, Phys. Rev. Lett. **81**, 3811 (1998).
 - [3] R. Côté and V. Kharchenko, Phys. Rev. Lett. **83**, 2100 (1999).
 - [4] M. Ö. Oktel and L. S. Levitov, Phys. Rev. Lett. **83**, 6 (1999).
 - [5] M. Ö. Oktel, T. C. Killian, D. Kleppner, and L. S. Levitov, Phys. Rev. A **65**, 033617 (2002).
 - [6] C. J. Pethick and H. T. C. Stoof, Phys. Rev. A **64**, 013618 (2001).
 - [7] D. M. Harber, H. J. Lewandowski, J. M. McGuirk, and E. A. Cornell, Phys. Rev. A **66**, 053616 (2002).
 - [8] D. M. Harber, H. J. Lewandowski, J. M. McGuirk, and E. A. Cornell, in *Proceedings of the XVIII International Conference on Atomic Physics*, edited by H. R. Sadeghpour, E. J. Heller, and D. E. Pritchard (World Scientific, Cambridge, Massachusetts, USA, 2003), pp. 3–10.
 - [9] M. Ö. Oktel and L. S. Levitov, Phys. Rev. Lett. **88**, 230403 (2002).
 - [10] J. E. Williams, T. Nikuni, and C. W. Clark, Phys. Rev. Lett. **88**, 230405 (2002).
 - [11] A. S. Bradley and C. W. Gardiner, J. Phys. B: At. Mol. Opt. Phys. **35**, 4299 (2002).
 - [12] J. N. Fuchs, D. M. Gangardt, and F. Laloë, Phys. Rev. Lett. **88**, 230404 (2002).
 - [13] J. N. Fuchs, D. M. Gangardt, and F. Laloë, cond-

- mat/0304335 (2003).
- [14] S. Gupta, Z. Hadzibabic, M. W. Zwierlein, C. A. Stan, K. Dieckmann, C. H. Schunck, E. G. M. van Kempen, B. J. Verhaar, and W. Ketterle, *Science* **300**, 1723 (2003).
 - [15] Z. Hadzibabic, S. Gupta, C. A. Stan, C. H. Schunck, M. W. Zwierlein, K. Dieckmann, and W. Ketterle, cond-mat/0306050 (2003).
 - [16] This result can be derived using Wick's Theorem [20]. Abnormal averages like $\langle \psi_1 \psi_1 \rangle$ do not contribute in the case of fermions or thermal bosons.
 - [17] The factor of 1/2 reflects the self-interaction.
 - [18] H. J. Lewandowski, D. M. Harber, D. L. Whitaker, and E. A. Cornell, *Phys. Rev. Lett.* **88**, 070403 (2002).
 - [19] J. M. McGuirk, H. J. Lewandowski, D. M. Harber, T. Nikuni, J. E. Williams, and E. A. Cornell, *Phys. Rev. Lett.* **89**, 090402 (2002).
 - [20] A. L. Fetter and J. D. Walecka, *Quantum Theory of Many-Particle Systems* (McGraw-Hill, New York, 1971).

Bibliography

- [1] Z. Hadzibabic, C. A. Stan, K. Dieckmann, S. Gupta, M. W. Zwierlein, A. Görlitz, and W. Ketterle, “Two-Species Mixture of Quantum Degenerate Bose and Fermi Gases,” *Phys. Rev. Lett.* **88**, 160401 (2002).
- [2] Z. Hadzibabic, S. Gupta, C. A. Stan, C. H. Schunck, M. W. Zwierlein, K. Dieckmann, and W. Ketterle, “Fifty-fold improvement in the number of quantum degenerate fermionic atoms,” *cond-mat/0306050* (2003).
- [3] K. Dieckmann, C. A. Stan, S. Gupta, Z. Hadzibabic, C. H. Schunck, and W. Ketterle, “Decay of an Ultracold Fermionic Lithium Gas near a Feshbach Resonance,” *Phys. Rev. Lett.* **89**, 203201 (2002).
- [4] S. Gupta, Z. Hadzibabic, J. R. Anglin, and W. Ketterle, “Collisions in zero temperature Fermi gases,” *cond-mat/0307088* (2003).
- [5] S. Gupta, Z. Hadzibabic, M. W. Zwierlein, C. A. Stan, K. Dieckmann, C. H. Schunck, E. G. M. van Kempen, B. J. Verhaar, and W. Ketterle, “Radio-Frequency Spectroscopy of Ultracold Fermions,” *Science* **300**, 1723 (2003).
- [6] M. W. Zwierlein, Z. Hadzibabic, S. Gupta, and W. Ketterle, “Spectroscopic insensitivity to cold collisions in a two-state mixture of fermions,” *cond-mat/0306627* (2003).
- [7] D. M. Stamper-Kurn, Ph.D. thesis, Massachusetts Institute of Technology, 1999.
- [8] C. H. Schunck, Diploma Thesis, University of Heidelberg 2002 .
- [9] S. Gupta, Ph.D. thesis, Massachusetts Institute of Technology, 2003.
- [10] M. H. Anderson, J. R. Ensher, M. R. Matthews, C. E. Wieman, and E. A. Cornell, “Observation of Bose-Einstein Condensation in a Dilute Atomic Vapor,” *Science* **269**, 198 (1995).
- [11] C. C. Bradley, C. A. Sackett, J. J. Tollet, and R. G. Hulet, “Evidence of Bose-Einstein Condensation in an Atomic Gas with Attractive Interactions,” *Phys. Rev. Lett.* **75**, 1687 (1995).
- [12] K. B. Davis, M.-O. Mewes, M. R. Andrews, N. J. van Druten, D. S. Durfee, D. M. Kurn, and W. Ketterle, “Bose-Einstein Condensation in a Gas of Sodium Atoms,” *Phys. Rev. Lett.* **75**, 3969 (1995).
- [13] E. A. Cornell and C. E. Wieman, “Nobel Lecture: Bose-Einstein condensation in a dilute gas, the first 70 years and some recent experiments,” *Rev. Mod. Phys.* **74**, 875 (2002).

- [14] W. Ketterle, “Nobel lecture: When atoms behave as waves: Bose-Einstein condensation and the atom laser,” *Rev. Mod. Phys.* **74**, 1131 (2002).
- [15] B. DeMarco and D. S. Jin, “Onset of Fermi Degeneracy in a Trapped Atomic Gas,” *Science* **285**, 1703 (1999).
- [16] G. Roati, F. Riboli, G. Modugno, and M. Inguscio, “Fermi-Bose Quantum Degenerate ^{40}K - ^{87}Rb Mixture with Attractive Interaction,” *Phys. Rev. Lett.* **89**, 150403 (2002).
- [17] A. G. Truscott, K. E. Strecker, W. I. McAlexander, G. B. Partridge, and R. G. Hulet, “Observation of Fermi Pressure in a Gas of Trapped Atoms,” *Science* **291**, 2570 (2001).
- [18] F. Schreck, L. Khaykovich, K. L. Corwin, G. Ferrari, T. Bourdel, J. Cubizolles, and C. Salomon, “Quasipure Bose-Einstein Condensate Immersed in a Fermi Sea,” *Phys. Rev. Lett.* **87**, 080403 (2001).
- [19] S. R. Granade, M. E. Gehm, K. M. O’Hara, and J. E. Thomas, “Preparation of a degenerate, two-component fermi gas by evaporation in a single beam optical trap,” *Phys. Rev. Lett.* **88**, 120405 (2002).
- [20] L. N. Cooper, “Bound Electron Pairs in a Degenerate Fermi Gas,” *Phys. Rev.* **104**, 1189 (1956).
- [21] H. Heiselberg, “Bosons and Fermions near Feshbach resonances,” *cond-mat/0307726* (2003).
- [22] T. Loftus, C. A. Regal, C. Ticknor, J. L. Bohn, and D. S. Jin, “Resonant control of elastic collisions in an optically trapped Fermi gas of atoms,” *Phys. Rev. Lett.* **88**, 173201 (2002).
- [23] K. M. O’Hara, S. L. Hemmer, S. R. Granade, M. E. Gehm, J. E. Thomas, V. Venturi, E. Tiesinga, and C. J. Williams, “Measurement of the zero crossing in a Feshbach resonance of fermionic ^6Li ,” *Phys. Rev. A* **66**, 041401 (2002).
- [24] C. A. Regal, C. Ticknor, J. L. Bohn, and D. S. Jin, “Tuning p-wave interactions in an ultracold Fermi gas of atoms,” *Phys. Rev. Lett.* **90**, 053201 (2003).
- [25] K. M. O’Hara, S. L. Hemmer, M. E. Gehm, S. R. Granade, and J. E. Thomas, “Observation of a Strongly Interacting Degenerate Fermi Gas of Atoms,” *Science* **298**, 2179 (2002).
- [26] M. E. Gehm, S. L. Hemmer, S. R. Granade, K. M. O’Hara, and J. E. Thomas, “Mechanical Stability of a Strongly-Interacting Fermi Gas of Atoms,” *Phys. Rev. A* **68**, 011401(R) (2003).
- [27] C. A. Regal and D. S. Jin, “Measurement of Positive and Negative Scattering Lengths in a Fermi Gas of Atoms,” *Phys. Rev. Lett.* **90**, 230404 (2003).
- [28] T. Bourdel, J. Cubizolles, L. Khaykovich, K. M. F. Magalhães, S. J. J. M. F. Kokkelmans, G. V. Shlyapnikov, and C. Salomon, “Measurement of the Interaction Energy near a Feshbach Resonance in a ^6Li Fermi Gas,” *Phys. Rev. Lett.* **91**, 020402 (2003).

- [29] C. A. Regal, C. Ticknor, J. L. Bohn, and D. S. Jin, “Creation of ultracold molecules from a Fermi Gas of Atoms,” *Nature* **424**, 47 (2003).
- [30] J. Cubizolles, T. Bourdel, S. J. J. M. F. Kokkelmans, G. V. Shlyapnikov, and C. Salomon, “Production of Long-Lived Ultracold Li_2 Molecules from a Fermi Gas,” *cond-mat/0308018* (2003).
- [31] A. J. Leggett, “Cooper Pairing in Spin-Polarized Fermi Systems,” *Journal de Physique* **41**, C7 (1980).
- [32] H. T. C. Stoof, M. Houbiers, C. A. Sackett, and R. G. Hulet, “Superfluidity of spin polarized ^6Li ,” *Phys. Rev. Lett.* **76**, 10 (1996).
- [33] M. Houbiers, R. Ferwenda, H. T. C. Stoof, W. McAlexander, C. A. Sackett, and R. G. Hulet, “Superfluid state of atomic ^6Li in a magnetic trap,” *Phys. Rev. A* **56**, 4864 (1997).
- [34] M. Houbiers and H. T. C. Stoof, “Cooper-pair formation in trapped atomic Fermi gases,” *Phys. Rev. A* **59**, 1556 (1999).
- [35] M. A. Baranov and D. S. Petrov, “Critical temperature and Ginzburg-Landau equation for a trapped Fermi gas,” *Phys. Rev. A* **58**, R801 (1998).
- [36] R. Combescot, “Trapped ^6Li : A High T_c Superfluid?,” *Phys. Rev. Lett.* **83**, 3766 (1999).
- [37] M. Holland, S. J. J. M. F. Kokkelmans, M. L. Chiofalo, and R. Walser, “Resonance Superfluidity in a Quantum Degenerate Fermi Gas,” *Phys. Rev. Lett.* **87**, 120406 (2001).
- [38] J. N. Milstein, S. J. J. M. F. Kokkelmans, and M. J. Holland, “Resonance theory of the crossover from Bardeen-Cooper-Schrieffer superfluidity to Bose-Einstein condensation in a dilute fermi gas,” *Phys. Rev. A* **66**, 043604 (2002).
- [39] S. J. J. M. F. Kokkelmans, J. N. Milstein, M. L. Chiofalo, R. Walser, and M. J. Holland, “Resonance superfluidity: Renormalization of resonance scattering theory,” *Phys. Rev. A* **65**, 053617 (2002).
- [40] E. Timmermans, K. Furuya, P. W. Milonni, and A. K. Kerman, “Prospects of creating a composite Fermi-Bose superfluid,” *Phys. Lett. A* **285**, 228 (2001).
- [41] W. Hofstadter, J. I. Cirac, P. Zoller, E. Demler, and M. D. Lukin, “High-temperature superfluidity of fermionic atoms in optical lattices,” *Phys. Rev. Lett.* **89**, 220407 (2002).
- [42] Y. Ohashi and A. Griffin, “BCS-BEC crossover in a gas of Fermi atoms with a Feshbach resonance,” *Phys. Rev. Lett.* **89**, 130402 (2002).
- [43] H. J. Metcalf and P. van der Straten, *Laser Cooling and Trapping* (Springer-Verlag, New York, 1999).

- [44] W. Ketterle, D. S. Durfee, and D. M. Stamper-Kurn, in *Bose-Einstein condensation in atomic gases, Proceedings of the International School of Physics Enrico Fermi, Course CXL*, edited by M. Inguscio, S. Stringari, and C. Wieman (IOS Press, Amsterdam, 1999), pp. 67–176.
- [45] E. Timmermans, “Degenerate Fermion Gas Heating by Hole Creation,” *Phys. Rev. Lett.* **87**, 240403 (2001).
- [46] J. R. Abo-Shaeer, C. Raman, J. M. Vogels, and W. Ketterle, “Observation of Vortex Lattices in Bose-Einstein Condensates,” *Science* **292**, 476 (2001).
- [47] M.-O. Mewes, M. R. Andrews, N. J. van Druten, D. M. Kurn, D. S. Durfee, and W. Ketterle, “Bose-Einstein Condensation in a Tightly Confining dc Magnetic Trap,” *Phys. Rev. Lett.* **77**, 416 (1996).
- [48] W. Ketterle, K. B. Davis, M. A. Joffe, A. Martin, and D. E. Pritchard, “High Densities of Cold Atoms in a *Dark* Spontaneous Force Optical Trap,” *Phys. Rev. Lett.* **70**, 2253 (1993).
- [49] U. Schünemann, H. Engler, M. Zielonowski, M. Weidemüller, and R. Grimm, “Magneto-optic trapping of lithium using semiconductor lasers,” *Optics Comm.* **158**, 263 (1998).
- [50] L. Ricci, M. Weidemüller, T. Esslinger, A. Hemmerich, C. Zimmermann, V. Vuletic, W. König, and T. W. Hänsch, “A compact grating-stabilized diode laser system for atomic physics,” *Opt. Commun.* **117**, 541 (1995).
- [51] V. Wippel, C. Binder, and L. Windholz, “Cross-section for collisions of ultracold Li-7 with Na,” *Eur. Phys. J. D* **21**, 101 (2002).
- [52] G. D. Telles, W. Garcia, L. G. Marcassa, V. S. Bagnato, D. Ciampini, M. Fazzi, J. H. Müller, D. Wilkowski, and E. Arimondo, “Trap loss in a two-species Rb-Cs magneto-optical trap,” *Phys. Rev. A* **63**, 033406 (2001).
- [53] D. E. Pritchard, “Cooling Neutral Atoms in a Magnetic Trap for Precision Spectroscopy,” *Phys. Rev. Lett.* **51**, 1336 (1983).
- [54] M. Houbiers, H. T. C. Stoof, W. I. McAlexander, and R. G. Hulet, “Elastic and inelastic collisions of ^6Li atoms in magnetic and optical traps,” *Phys. Rev. A* **57**, R1497 (1998).
- [55] G. Breit and I. I. Rabi, “Measurement of the nuclear spin,” *Phys. Rev.* **38**, 2082 (1931).
- [56] D. A. Butts and D. S. Rokhsar, “Trapped Fermi gases,” *Phys. Rev. A* **55**, 4346 (1997).
- [57] F. Schreck, Ph.D. thesis, Université Paris VI, 2002.
- [58] A. Görlitz, T. L. Gustavson, A. E. Leanhardt, R. Löw, A. P. Chikkatur, S. Gupta, S. Inouye, D. E. Pritchard, and W. Ketterle, “Sodium Bose-Einstein Condensates in the $F = 2$ State in a Large-Volume Optical Trap,” *Phys. Rev. Lett.* **90**, 090401 (2003).

- [59] M. B. S. Jochim, G. Hendl, J. H. Denschlag, R. Grimm, A. Mosk, and M. Weidemüller, “Magnetic Field Control of Elastic Scattering in a Cold Gas of Fermionic Lithium Atoms,” *Phys. Rev. Lett.* **89**, 273202 (2002).
- [60] J. Dalibard, in *Bose-Einstein condensation in atomic gases, Proceedings of the International School of Physics Enrico Fermi, Course CXL*, edited by M. Inguscio, S. Stringari, and C. Wieman (IOS Press, Amsterdam, 1999), pp. 321–350.
- [61] D. J. Heinzen, in *Bose-Einstein condensation in atomic gases, Proceedings of the International School of Physics Enrico Fermi, Course CXL*, edited by M. Inguscio, S. Stringari, and C. Wieman (IOS Press, Amsterdam, 1999), pp. 351–390.
- [62] C. J. Joachin, *Quantum Collision Theory* (North Holland, Amsterdam, 1983).
- [63] K. Huang, *Statistical Mechanics* (Wiley, New York, 1987).
- [64] J. J. Sakurai, *Modern Quantum Mechanics* (Addison-Wesley, Reading, Massachusetts, 1994).
- [65] C. J. Pethick and H. Smith, *Bose-Einstein Condensation in Dilute Gases* (Cambridge University Press, Cambridge, 2002).
- [66] H. A. Feshbach, “A unified theory of nuclear reactions,” *Annals of Physics* **19**, 287 (1962).
- [67] S. Inouye, M. R. Andrews, J. Stenger, H.-J. Miesner, D. M. Stamper-Kurn, and W. Ketterle, “Observation of Feshbach resonances in a Bose-Einstein condensate,” *Nature* **392**, 151 (1998).
- [68] P. Courteille, R. S. Freeland, D. J. Heinzen, F. A. van Abeelen, and B. J. Verhaar, “Observation of a Feshbach resonance in cold atom scattering,” *Phys. Rev. Lett.* **81**, 69 (1998).
- [69] J. L. Roberts, N. R. Claussen, J. B. Jr., C. H. Greene, E. A. Cornell, and C. E. Wieman, “Resonant magnetic field control of elastic scattering in cold ^{87}Rb ,” *Phys. Rev. Lett.* **81**, 5109 (1998).
- [70] A. J. Kerman, V. Vuletić, C. Chin, and S. Chu, “Observation of Low-Field Feshbach Resonances in Collisions of Cesium Atoms,” *Phys. Rev. Lett.* **82**, 1406 (1999).
- [71] S. L. Cornish, N. R. Claussen, J. L. Roberts, E. A. Cornell, and C. E. Wieman, “Stable ^{85}Rb Bose-Einstein Condensates with Widely Tunable Interactions,” *Phys. Rev. Lett.* **85**, 1795 (2000).
- [72] E. A. Donley, N. R. Claussen, S. L. Cornish, J. L. Roberts, E. A. Cornell, and C. E. Wieman, “Dynamics of collapsing and exploding Bose-Einstein condensates,” *Nature* **89**, 203201 (2002).
- [73] K. E. Strecker, G. B. Partridge, A. G. Truscott, and R. G. Hulet, “Formation and propagation of matter-wave soliton trains,” *Nature* **417**, 150 (2002).
- [74] L. Khaykovich, F. Schreck, G. Ferrari, T. Bourdel, J. Cubizolles, L. D. Carr, Y. Castin, and C. Salomon, “Formation of a matter-wave bright soliton,” *Science* **296**, 1290 (2002).

- [75] T. Weber, J. Herbig, M. Mark, H.-C. Nägerl, and R. Grimm, “Bose-Einstein condensation of cesium,” *Science* **299**, 232 (2003).
- [76] B. DeMarco, J. L. Bohn, J. J. P. Burke, M. Holland, and D. S. Jin, “Measurement of p-Wave Threshold Law Using Evaporatively Cooled Fermionic Atoms,” *Phys. Rev. Lett.* **82**, 4208 (1999).
- [77] A. J. Moerdijk, B. J. Verhaar, and A. Axelsson, “Resonances in ultra-cold collisions of ^6Li , ^7Li and ^{23}Na ,” *Phys. Rev. A* **51**, 4852 (1995).
- [78] S. Dürr, T. Volz, A. Marte, and G. Rempe, “Observation of molecules produced from a Bose-Einstein condensate,” *cond-mat/0307440* (2003).
- [79] J. Bardeen, L. N. Cooper, and J. R. Schreiffer, “Theory of Superconductivity,” *Phys. Rev.* **108**, 1175 (1957).
- [80] D. M. Stamper-Kurn, M. R. Andrews, A. P. Chikkatur, S. Inouye, H.-J. Miesner, J. Stenger, and W. Ketterle, “Optical confinement of a Bose-Einstein condensate,” *Phys. Rev. Lett.* **80**, 2027 (1998).
- [81] C. Menotti, P. Pedri, and S. Stringari, “Expansion of an Interacting Fermi Gas,” *Phys. Rev. Lett.* **89**, 250402 (2002).
- [82] J. Stenger, S. Inouye, M. R. Andrews, H.-J. Miesner, D. M. Stamper-Kurn, and W. Ketterle, “Strongly enhanced inelastic collisions in a Bose-Einstein condensate near Feshbach resonances,” *Phys. Rev. Lett.* **82**, 2422 (1999).
- [83] J. L. Roberts, N. R. Claussen, S. L. Cornish, and C. E. Wieman, “Magnetic Field Dependence of Ultracold Inelastic Collisions near a Feshbach Resonance,” *Phys. Rev. Lett.* **85**, 728 (2000).
- [84] T. Weber, J. Herbig, M. Mark, H.-C. Nägerl, and R. Grimm, “Three-body recombination at large scattering lengths in an ultracold atomic gas,” *physics/0304052* (2003).
- [85] P. O. Fedichev, M. W. Reynolds, and G. V. Shlyapnikov, “Three-body recombination of ultracold atoms to a weakly bound s level,” *Phys. Rev. Lett.* **77**, 2921 (1996).
- [86] D. S. Petrov, “Three-body problem in Fermi gases with short-range interparticle interaction,” *Phys. Rev. A* **67**, 010703(R) (2003).
- [87] B. D. Esry, C. H. Greene, and H. Suno, “Threshold laws for three-body recombination,” *Phys. Rev. A* **65**, 010705(R) (2002).
- [88] R. Combescot, “Feshbach resonance in dense ultracold Fermi gases,” *cond-mat/0302209* (2003).
- [89] R. Combescot, “Shift of the molecular bound state threshold in dense ultracold Fermi gases with Feshbach resonance,” *New J. Phys.* **5**, 86 (2003).
- [90] G. M. Bruun and C. J. Pethick, “An effective theory of Feshbach resonances and many-body properties of Fermi gases,” *cond-mat/0304535* (2003).
- [91] T.-L. Ho and E. J. Mueller, “The Unitary Quantum Gas,” *cond-mat/0306187* (2003).

- [92] Y. Kagan, E. L. Surkov, and G. V. Shlyapnikov, “Evolution of a Bose gas in anisotropic time-dependent traps,” *Phys. Rev. A* **55**, R18 (1997).
- [93] P. Pedri, D. Guéry-Odelin, and S. Stringari, “Dynamics of a classical gas including dissipative and mean field effects,” *arXiv:cond-mat/0305624* (2003).
- [94] I. Shvarchuck, C. Buggle, D. S. Petrov, K. Dieckmann, M. Zielonkowski, M. Kemmann, T. Tiecke, W. V. Klitzing, G. V. Shlyapnikov, and J. T. M. Walraven, “Bose-Einstein Condensation into Nonequilibrium States Studied by Condensate Focusing,” *Phys. Rev. Lett.* **89**, 270404 (2002).
- [95] D. M. Stamper-Kurn, H.-J. Miesner, S. Inouye, M. R. Andrews, and W. Ketterle, “Collisionless and hydrodynamic excitations of a Bose-Einstein condensate,” *Phys. Rev. Lett.* **81**, 500 (1998).
- [96] M. Leduc, J. Leonard, F. P. dos Santos, E. Jahier, S. Schwartz, and C. Cohen-Tannoudji, “Hydrodynamic modes in a trapped gas of metastable helium above the Bose-Einstein transition,” *Acta Phys. Pol. B* **33**, 2213 (2002).
- [97] S. D. Gensemer and D. S. Jin, “Transition from collisionless to hydrodynamic behavior in an ultracold Fermi gas,” *Phys. Rev. Lett.* **87**, 173201 (2001).
- [98] B. DeMarco and D. S. Jin, “Spin Excitations in a Fermi Gas of Atoms,” *Phys. Rev. Lett.* **88**, 040405 (2002).
- [99] S. Stringari, “Collective excitations of a trapped Bose-condensed gas,” *Phys. Rev. Lett.* **77**, 2360 (1996).
- [100] A. Minguzzi and M. P. Tosi, “Scissors mode in a superfluid Fermi gas,” *Phys. Rev. A* **63**, 023609 (2001).
- [101] F. Zambelli and S. Stringari, “Moment of inertia and quadrupole response function of a trapped superfluid,” *Phys. Rev. A* **63**, 033602 (2001).
- [102] M. E. Gehm, S. L. Hemmer, K. M. O’Hara, and J. E. Thomas, “Unitarity-limited Elastic Collision Rate in a Harmonically-Trapped Fermi Gas,” *Phys. Rev. A* **68**, 011603(R) (2003).
- [103] W. Geist, A. Idrizbegovic, M. Marinescu, T. A. B. Kennedy, and L. You, “Evaporative cooling of trapped fermionic atoms,” *Phys. Rev. A* **61**, 013406 (1999).
- [104] M. Holland, B. DeMarco, and D. S. Jin, “Evaporative cooling of a two-component degenerate Fermi gas,” *Phys. Rev. A* **61**, 053610 (2000).
- [105] W. Geist and T. A. B. Kennedy, “Evaporative cooling of mixed atomic fermions,” *Phys. Rev. A* **65**, 063617 (2002).
- [106] G. Ferrari, “Collisional relaxation in a fermionic gas,” *Phys. Rev. A* **59**, R4125 (1999).
- [107] B. DeMarco, S. B. Papp, and D. S. Jin, “Pauli Blocking of Collisions in a Quantum Degenerate Atomic Fermi Gas,” *Phys. Rev. Lett.* **86**, 5409 (2001).
- [108] L. Vichi, “Collisional Damping of the Collective Oscillations of a Trapped Fermi Gas,” *J. Low Temp. Phys.* **121**, 177 (2000).

- [109] K. Gibble and S. Chu, “Laser-Cooled Cs Frequency Standard and a Measurement of the Frequency Shift due to Ultracold Collisions,” *Phys. Rev. Lett.* **70**, 1771 (1993).
- [110] C. Fertig and K. Gibble, “Measurement and Cancellation of the Cold Collision Frequency Shift in an ^{87}Rb Fountain Clock,” *Phys. Rev. Lett.* **85**, 1622 (2000).
- [111] Y. Sortais, S. Bize, M. Abgrall, S. Zhang, C. Nicolas, C. Mandache, P. Lemonde, P. Laurent, G. Santarelli, N. Dimarcq, P. Petit, A. Clairon, A. Mann, A. Luiten, S. Chang, and C. Salomon, “Cold atom clocks,” *Physica Scripta* **T95**, 50 (2001).
- [112] K. Gibble and B. J. Verhaar, “Eliminating cold-collision frequency shifts,” *Phys. Rev. A* **52**, 3370 (1995).
- [113] D. M. Harber, H. J. Lewandowski, J. M. McGuirk, and E. A. Cornell, “Effect of cold collisions on spin coherence and resonance shifts in a magnetically trapped ultracold gas,” *Phys. Rev. A* **66**, 053616 (2002).
- [114] D. M. Harber, H. J. Lewandowski, J. M. McGuirk, and E. A. Cornell, in *Proceedings of the XVIII International Conference on Atomic Physics*, edited by H. R. Sadeghpour, E. J. Heller, and D. E. Pritchard (World Scientific, Cambridge, Massachusetts, USA, 2003), pp. 3–10.
- [115] M. O. Oktel and L. S. Levitov, “Internal Waves and Synchronized Precession in a Cold Vapor,” *Phys. Rev. Lett.* **88**, 230403 (2002).
- [116] J. E. Williams, T. Nikuni, and C. W. Clark, “Collisional frequency shifts of absorption lines in an atomic hydrogen gas,” *Phys. Rev. Lett.* **88**, 230405 (2002).
- [117] A. S. Bradley and C. W. Gardiner, “Theory of Ramsey spectroscopy and anomalous segregation in ultracold rubidium,” *J. Phys. B: At. Mol. Opt. Phys.* **35**, 4299 (2002).
- [118] J. N. Fuchs, D. M. Gangardt, and F. Lalo, “Internal State Conversion in Ultracold Gases,” *Phys. Rev. Lett.* **88**, 230404 (2002).
- [119] J. N. Fuchs, D. M. Gangardt, and F. Lalo, “Large amplitude spin waves in ultra-cold gases,” *cond-mat/0304335* (2003).
- [120] E. G. M. van Kempen and et. al., “‘Scattering Calculations for Lithium’,” in preparation (2003).
- [121] J. V. Steele, “Effective Field Theory Power Counting at Finite Density,” *arXiv:nucl-th/0010066* (2000).
- [122] H. Heiselberg, “Fermi Systems with long scattering lengths,” *Phys. Rev. A* **63**, 043606 (2001).
- [123] P. Torma and P. Zoller, “Laser Probing of Atomic Cooper Pairs,” *Phys. Rev. Lett.* **85**, 487 (2000).
- [124] G. Bruun, P. Torma, M. Rodriguez, and P. Zoller, “Laser probing of Cooper-paired trapped atoms,” *Phys. Rev. A* **64**, 033609 (2001).
- [125] K. Mølmer, “Bose Condensates and Fermi Gases at Zero Temperature,” *Phys. Rev. Lett.* **80**, 1804 (1998).

- [126] G. Modugno, G. Roati, F. Riboli, F. Ferlaino, R. J. Brecha, and M. Inguscio, “Collapse of a degenerate Fermi gas,” *Science* **68**, 011601 (2002).
- [127] M. Greiner, O. Mandel, T. Esslinger, T. W. Hansch, and I. Bloch, “Quantum phase transition from a superfluid to a Mott insulator in a gas of ultracold atoms,” *Nature* **415**, 39 (2002).
- [128] C. E. Wieman and L. Hollberg, “Using diode lasers for atomic physics,” *Rev. Sci. Instrum.* **62**, 1 (1991).
- [129] A. E. Siegman, *Lasers* (University Science Books, Sausalito, 1986).
- [130] E. Hecht, *Optics* (Addison-Wesley, Reading, 1989).
- [131] K. G. Libbrecht, R. A. Boyd, P. A. Willems, T. L. Gustavson, and D. K. Kim, “Teaching Physics with 670nm Diode-lasers - Construction of Stabilized Lasers and Lithium Cells,” *Am. J. Phys.* **63**, 729 (1995).